Flüssigkristall-basierte Mikrowellenkomponenten mit schnellen Schaltzeiten: Material, Technologie, Leistungsverträglichkeit

Liquid Crystal Based Microwave Components with Fast Response Times: Material, Technology, Power Handling Capability

Vom Fachbrereich 18
Elektrotechnik und Informationstechnik
der Technischen Universität Darmstadt
zur Erlangung der Würde
eines Doktor-Ingenieurs (Dr.-Ing.)
genehmigte

Dissertation

von

Dipl.-Ing. Felix Gölden
geboren am 18.9.1977
in Darmstadt, Deutschland

Referent	:	Prof. Dr.-Ing. Rolf Jakoby
Korreferent	:	Prof. Dr.-Ing. habil. Peter Knoll

Tag der Einreichung	:	20.10.2009
Tag der mündlichen Prüfung	:	18.12.2009

D17
Darmstadt 2010

Vorwort

Die vorliegende Dissertation entstand während meiner Zeit als Stipendiat und als wissenschaftlicher Mitarbeiter am Fachgebiet Mikrowellentechnik der Technischen Universität Darmstadt. Da eine solche Arbeit nicht nur durch das einsame Schaffen einer einzelnen Person entsteht, sondern vielmehr im Zusammenspiel mit Kollegen und Partnern, möchte ich an dieser Stelle den Menschen danken, die zum Gelingen dieser Arbeit beigetragen haben.

Allen voran danke ich natürlich meinem Doktorvater Prof. Dr.-Ing. Rolf Jakoby sehr herzlich für das mir entgegengebrachte Vertrauen und die Bereitstellung einer höchst flexiblen und fruchtbaren Arbeitsumgebung. Herrn Prof. Dr.-Ing. habil. Peter Knoll von der Universität Karlsruhe danke ich für die Übernahme des Korreferats.

In den viereinhalb Jahren am Fachgebiet Mikrowellentechnik habe ich mich jederzeit sehr gut aufgehoben gefühlt, sowohl persönlich als auch fachlich. Das dies etwas Besonderes ist, steht außer Frage und dafür danke ich allen Kollegen. Ein besonderer Dank geht dabei an Herrn Dipl.-Ing. Alexander Gäbler für ein jederzeit offenes Ohr und die endlosen Diskussionen über Flüssigkristalle und andere Dinge. Herrn Dr.-Ing. Stefan Müller danke ich für die Einarbeitung in das interdisziplinäre Thema. Weiterhin danke ich den Herren Peter Kiesslich und Andreas Semrad für die überreichlich gewährte Unterstützung bei allen praktischen Aspekten meiner Arbeit. Herrn Dipl.-Ing. Holger Maune danke ich für die Durchsicht meines Manuskripts.

Außerdem möchte ich noch folgenden Personen danken:

- Herrn Prof. Dr. Wolfgang Haase und Herrn Dr. Artsiom Lapanik vom Eduard-Zintl-Institut für Anorganische und Physikalische Chemie der Technischen Universität Darmstadt für die wundervolle Zusammenarbeit und die vielen Einblicke in die Flüssigkristallchemie.

- Dr. V. Lapanik und Dr. V. Bezborodov vom Institut für angewandte Physik der Belarusian State University in Minsk für die Bereitstellung von Flüssigkristallen.

- Herrn Atsutaka Manabe und Herrn Mark Göbel von der Firma Merck KGaA für die Bereitstellung von Flüssigkristallen

- Frau Dr. Oksana Trushkevych vom Centre for Advanced Photonics and Electronics der University of Cambridge für die Zusammenarbeit auf dem Gebiet der Kohlenstoffnanoröhrchen/Flüssigkristall Mischungen.
- Herrn Dr. Klaus Seibert und Herrn Joachim Müller von der Firma W.L.Gore & Associates für die Zusammenarbeit bezügl. der ePTFE-Membranen

Zu guter Letzt danke ich meiner Familie für die immer vorhandene Unterstützung und besonders meiner Frau Eunjung für ihre Liebe und Unterstützung und dafür, dass sie das Manuskript mit Hingabe durchgearbeitet hat.

Berlin, 20. März 2010 Felix Gölden

Preface

This dissertation is the result of my time as Ph.D. Student at the Microwave Engineering Group at Technische Universität Darmstadt. Because such a work is not only the result of a single person's efforts but rather develops in co-operation with colleagues and partners, I would like to thank those people who contributed to this work.

First and foremost, I would like to give sincere thanks to my doctoral advisor Prof. Dr.-Ing. Rolf Jakoby for the trust placed in me and for providing a highly flexible and fruitful working environment. Prof. Dr.-Ing. habil. Peter Knoll I thank for taking over the part of second examiner.

In the four and a half years in the group, I felt at home at every time, both personally and professionally. This is certainly something special and for that I would like to thank all of the colleagues. A special thanks goes to Dipl.-Ing. Alexander Gäbler for being ready at all times to plunge into discussions about liquid crystals and other things. Dr.-Ing. Stefan Müller I thank for introducing me to the interdisciplinary topic. Peter Kiesslich und Andreas Semrad I thank for providing overabundant support concerning all the practical aspects of my work. I am thankful to Dipl.-Ing Holger Maune for reviewing my manuscript.

Furthermore, I would like to thank the following persons:

- Prof. Dr. Wolfgang Haase and Herrn Dr. Artsiom Lapanik from the Eduard-Zintl-Institut für Anorganische und Physikalische Chemie at Technische Universität Darmstadt for the wonderful cooperation and the insight into liquid crystal chemistry
- Dr. V. Lapanik and Dr. V. Bezborodov from the Institute of Applied Physics Problems, University of Minsk, for providing Liquid Crystal material
- Atsutaka Manabe and Mark Göbel from Merck KGaA, Darmstadt, for providing Liquid Crystal material
- Dr. Oksana Trushkevych from the Centre for Advanced Photonics and Electronics at the University of Cambridge for the cooperation concerning Carbon nanotube/Liquid Crystal mixtures
- Dr. Klaus Seibert and Joachim Müller from W.L.Gore & Associates for the cooperation concerning the ePTFE-Membranes

Last but not least, I want to thank my family for their continuing support and especially my wife Eunjung for her love and support and for working passionately through the manuscript.

Berlin, 20th March, 2010 Felix Gölden

Kurzfassung

Die vorliegende Arbeit befasst sich mit steuerbaren Mikrowellenkomponenten auf Basis von Flüssigkristallen (engl. Liquid Crystal, LC). Dabei wird die Tatsache ausgenutzt, dass LCs bei Frequenzen im GHz-Bereich wie auch bei optischen Frequenzen eine dielektrische Anisotropie entlang einer Vorzugsrichtung aufweisen. Durch das Anlegen eines elektrischen oder magnetischen Steuerfeldes, das dem Hochfrequenzfeld überlagert ist, kann die Vorzugsrichtung reorientiert und damit die für das Hochfrequenzfeld effektive Permittivität verändert werden.

Nachdem in einer vorangegangenen Promotionsarbeit die grundsätzliche Eignung von LCs für Mikrowellenanwendungen nachgewiesen werden konnte, ist die Motivation der vorliegenden Arbeit die Verwendung von LCs für Mikrowellenanwendungen, insbesondere für steuerbare Phasenschieber für rekonfigurierbare Gruppenantennen, weiter in Richtung eines kommerziellen Einsatzes voran zu treiben. Zu diesem Zweck werden sowohl Materialaspekte als auch Bauteil- bzw. Herstellungsaspekte betrachtet. Um die dielektrischen Eigenschaften, d.h. Verluste und die Anisotropie und damit die Steuerbarkeit, zu verbessern, wurden zahlreiche nematische Mischungen auf ihre Mikrowellenperformanz hin untersucht. Dadurch konnten bestimmte Komponenten identifiziert werden, die sowohl eine hohe Steuerbarkeit als auch niedrige dielektrische Verluste haben. Insbesondere sind dies auf Diphenylacetylen basierende Verbindungen sowie Quarterphenyl-Verbindungen. Mit Hilfe hochpräziser Messmethoden wird gezeigt, dass die Mikrowellenverluste stark von Molekülrelaxationen abhängen. Werden diese Relaxationen stark reduziert, können Materialien mit Verlustwinkeln von weniger als 0.006 und einer Steuerbarkeit von bis zu 25 % bei 30 GHz synthetisiert werden. Für ein passiv steuerbares Material sind dies herausragende Werte.

Um die bei auf LC basierenden Mikrowellenbauelementen mit LC-Schichtdicken von einigen 100 µm bisher üblichen Schaltzeiten von einigen Sekunden zu reduzieren, wurden zwei unterschiedliche Ansätze verfolgt. Zum einen ist dies die Stabilisierung des LC durch eine PTFE-Matrix. Durch diese Maßnahme konnten die Schaltzeiten deutlich auf unter 100 ms reduziert werden. Zum anderen wurde eine an die Displayherstellung angelehnte Methode entwickelt um dünne LC-Schichten auch in Mikrowellenbauelementen verwenden zu können. Mit den dabei hergestellten steuerbaren Kapazitäten konnte demonstriert werden, dass bei Schichtdicken von etwa 5 µm Schaltzeiten von unter 100 ms, bei Schichtdicken von etwa 1 µm sogar unter 5 ms, realisiert werden können. Basierend auf diesen steuerbaren Kapazitäten wurde ein steuerbarer Phasenschieber entwickelt, der eine Phasenschiebergüte von bis zu 60 Grad pro dB Einfügeverlust aufweist bei einer Schaltgeschwindigkeit von besser als 340 ms. Für dieses Bauteil wurden weiterhin resistive Steuerelektroden aus Indium-Zinn-Oxid verwendet.

Die Leistungsverträglichkeit von solchen Bauelementen wurde anhand von Ein- und Zweitonmessungen untersucht. Durch die Eintonmessungen konnte gezeigt werden, dass das Bauteilverhalten durch Selbstaktuierung bei hohen Leistungen beeinflusst werden kann, jedoch nur oberhalb einer bestimmten Schwellleistung. Mit den Zweitonmessungen wurde gezeigt, dass dieser Selbstaktuierungseffekt eine erhöhte Intermodulation bei kleinen Tonabständen (<1 kHz) bedingt. Für Tonabstände größer als 100 kHz können jedoch IP3 Werte von nahe 60 dBm erreicht werden.

Abstract

The present thesis is concerned with tunable microwave components based on Liquid Crystals (LC). Here, the fact is utilised that LC feature at GHz frequencies as well as at optical frequencies a dielectric anisotropy along a preferential direction. By means of an electric or magnetic control field, which superimposes the RF field, this preferential direction can be reoriented and thus the permittivity effective for the RF field can be controlled.

After in a preceding doctoral work the applicability of LC was demonstrated in principle, the motivation of the present work is to advance the usage of LC for microwave applications, particularly for tunable phase shifters for reconfigurable phased arrays, further toward commercial applicability. To this end, both material aspects as well as component and fabrication aspects are considered. In order to improve the dielectric properties, i.e. loss and anisotropy and hence the tunability, numerous nematic mixtures were investigated with respect to their microwave performance. Certain components could be identified which feature both high tunability and low loss. Particularly these compounds based on Diphenylacetylene or on Quarterphenyles. By employing high precision measurements it is shown that the dielectric loss strongly depends on molecular relaxations. If these relaxations are reduced, materials with loss tangents down to 0.006 and relative tunabilities of up to 25 % at 30 GHz can be synthesised. For passively tunable materials, these are exceptional values.

Two different approaches were pursued in order to reduce the so far for LC-based microwave devices with layer thicknesses of several 100 µm usual response times of several seconds. On the one hand, this is the stabilisation of the LC by means of a PTFE matrix which reduced the response times considerably down to 90 ms. On the other hand, a method resembling LC display assembly technology has been developed which allows realising thin LC layers also for microwave devices. Using the fabricated tunable capacitors it could be demonstrated that with a LC layer thickness of approx. 5 µm response times faster than 100 ms and with a layer thickness of approx. 1 µm response times faster than 5 ms can be achieved. Based on these tunable capacitors a tunable phase shifter is developed which features a phase shifter performance of up to 60 degrees per dB insertion loss at 20 GHz and a response time of faster than 340 ms. Additionally, for these devices resistive bias electrodes made of Indium-Tin-Oxide were employed.

The power handling capability of such devices was investigated by means of single and two tone measurements. With the single tone measurements it could be shown that the device characteristic is influenced at high power levels by self-actuation effects, however only above a certain threshold power. With the two tone measurements it could be shown that these self-actuation effects cause increased intermodulation at small tone distances (<1 kHz). However, for tone distances larger than 100 kHz IP3 values of about 60 dBm can be achieved.

Contents

Chapter 1

Introduction

Motivation

The key component necessary for realising reconfigurable antenna systems such as phased arrays or reflect arrays is a tunable phase shifter. The frequencies at which such antennas are operated are usually well above 10 GHz and range up to 100 GHz. Such antennas are for instance required for flexible inter-satellite communication in which e.g. a geostationary (GEO) satellite functions as a relay station from a low earth orbit (LEO) satellite to the surface of the earth. The GEO satellite, therefore, has to constantly track the trajectory of the LEO satellite. While this can be achieved using conventional mechanical beam steering, an electronic solution would offer reduction of weight and required space as no mechanical tilting of an antenna body is necessary. The concept of low profile reconfigurable antennas can also be applied to mobile ground stations which require a communication link to a satellite (LEO or GEO). As a further application of such antennas, 60 GHz wireless LAN is conceivable for which space division access schemes are then possible. Also scanning applications like automotive radar are realised using reconfigurable phased arrays but here the high reconfiguration speed is a strong requirement. The requirements common to all the aforementioned applications are low RF loss caused by the antenna module, low power consumption, reliability and, especially if a transmit path is included, linearity.

In order to realise components for the applications outlined above several technological approaches compete. On the one hand, these are various semiconductor solutions based on various material systems, mostly in Monolithic Microwave Integrated Circuit (MMIC) technology. Using Silicon Germanium (SiGe), tunable phase shifters have been demonstrated spanning frequencies up to 77 GHz [HR05, NKG$^+$06, KMR09]. SiGe based technology is actually a now well established for beam forming purposes at high frequencies [FWS$^+$09] and also offers the possibility to integrate amplifiers together with phase shifting elements. Furthermore, using CMOS MMICs circulators [ZS08] or tunable inductors [APE09] for the purpose of tunable phase shifters at ISM band frequencies have been reported. Alternatives are for instance MMICs based on High Electron Mobility Transistors [VCJ02] or PIN diodes which realise switch based phase

shifters [CKPZ90]. Depending on the material, semiconductor based solutions may need non-zero bias currents which may be contradictory to the usual requirement for powerless tuning.

Another very popular approach for passively tunable devices are ferroelectric dielectrics such as e.g. Barium Strontium Titanate (BST). Devices based on such dielectrics are reported e.g. in [MSK+00, MJM+01, HZL+07, ATH+02]. The working principle of this material system is the control of the dielectric permittivity by applying a bias voltage. Depending on the material, the operation frequencies range up to 40 GHz [VBB+07]. Due to the nature of ferroelectrics, devices with continuous tunability can be realised with them.

The RF MEMS (Micro-Electro-Mechanical Systems) technology offers also interesting solutions for tunable devices of all kinds. With this technology, various applications can be realised such as tunable filters [ATDR03] or phase shifters [MO06]. Depending on the realisation, RF MEMS are designed as switches or as continuously tunable capacitors. In [BR00], it is demonstrated that RF MEMS can be employed in high performance phase shifters up to W-band (110 GHz) frequencies.

A further alternative to the approaches outline above, the one this work is actually dedicated to, is Liquid Crystals (LCs) or more precisely, Nematic Liquid Crystals (NLCs). LC is today the dominant technology used for display applications for which the controllable anisotropy of the material is exploited in order to realise an optical switch or "valve". As the anisotropy is not limited to optical frequencies, LCs can be used as a tunable dielectric at microwave frequencies as well.

Early publications investigating LC at microwave frequencies [LML+93b, LML93a, LM92] proposed the use of this material for radar applications. The aforementioned works used rectangular waveguides for characterising the material. In [DLJH93] a so-called inverted microstrip line was used which uses NLC as the effective substrate for controlling the phase delay of a Transverse Electromagnetic Mode (TEM) waveguide. The latter approach was also used for realising tunable phase shifters for beam forming purposes (e.g. [WMS+03, MLP+03, KFN03, YS03, DKS+08]). As interest in the use of LCs in the microwave regime increased, classes other than nematic LCs were investigated [FKN+01, FKK+03].

All aforementioned works are, by their nature, demonstrations of the potential application of LCs for tunable microwave devices. Also the interest in using LC for tunable THz applications has emerged [CTPP03, PP07, NSYH06] and studies were undertaken in order to asses the applicability of nematic LCs at THz frequencies [KKFN04, TOY+07, OYK+07].

The present work explores the use of NLCs with particular focus on the realisation of tunable phase shifters. In that respect this work can be viewed as a consequent advancement of the results obtained in [Mül07], which demonstrated that tunable phase shifters can be realised based on LC and indeed exceed the performance of tunable phase shifters realised with other technologies, something which up to this point no work could show. In particular the present work explores the relationship between chemical components and the performance of NLCs in terms of tunability and dielectric loss. As a further important achievement, a new device concept and fabrication

scheme is developed which enables the design of LC based devices with response times like todays displays (i.e. in the millisecond-range) while a high microwave performance is maintained. Especially these response times of microwave devices, being in the order of seconds, were a major drawback of all works presented in the microwave region so far and they are certainly an obstacle for the transformation of the academic concept to a commercial product. With the devices developed in the present work, this obstacle is considerably lowered. Furthermore, the developed fabrication scheme is cost effective, as the fabrication process is compatible with that of LC displays. In terms of further investigating the applicability of LC based microwave devices, it is shown that such devices can, unlike semiconductor or ferroelectric solutions, feature very high linearity.

Structure of this work

Following this introduction, the second chapter will introduce the basics of Nematic LCs insofar as they are relevant to this work. Particularly, the anisotropic nature of LCs is described in detail along with other important concepts common to most LC devices.

The third chapter is dedicated to the investigation of LC materials and LC composites. Beside the investigation of the relationship between the chemical composition of LC mixtures and their microwave properties, the behaviour of porous PTFE sheets impregnated with LC is analysed. Furthermore, the impact of loading a LC host with carbon nanotubes is examined.

In the fourth chapter the fabrication scheme for realising thin LC layers is introduced. This enables to design parallel plate capacitors with LC as tunable dielectric. Based on this component a tunable phase shifter is developed. All devices based on these thin layers feature tuning response times which are in the same order as those of LC displays and therefore one to two orders of magnitude faster compared to previous works.

The response of LC under large signal conditions is investigated in the fifth chapter. Single tone excitation is used to study the self actuation effect and two tone excitation is used in order to examine intermodulation caused by LC.

This thesis closes with a conclusion in the sixth chapter which sums up the achieved results. An outlook is given which points out possible research to be pursued based on this work.

Chapter 2

Fundamentals of Liquid Crystal Devices

2.1 Dielectric Materials

On the microscopic scale, the dielectric behaviour of a specific material is described by the polarisability α_p of the molecules. α_p is a molecular property and has the SI unit Cs^2kg^{-1} or Cm^2V^{-1}. The induced dipole moment of a single molecule is given by

$$\vec{p} = \alpha_p \vec{E}_{local} \tag{2.1}$$

E_{local} is the so called local or molecular field which is experienced by the molecule [RMC80] and in general differs from the macroscopic field E. The relation between the molecular field $\vec{E}_{local}$ and the macroscopic field $\vec{E}$ is described by

$$\vec{E}_{local} = K\vec{E} \tag{2.2}$$

with K being the so called molecular field factor.

The macroscopic polarisation density can be calculated by multiplying the molecular dipole moment with the number density N of the material, i.e.

$$\vec{P} = N\vec{p} = N\alpha_p \vec{E}_{local} = N\alpha_p K\vec{E} = \chi_e \vec{E}. \tag{2.3}$$

As for the local field the relation

$$\vec{E}_{local} = \vec{E} + \frac{\vec{P}}{3\varepsilon_0}$$

holds [Jac65, RMC80, YW06], the macroscopic polarisation $\vec{P}$ is given by

$$\vec{P} = \frac{N\alpha_p \vec{E}}{1 - N\alpha_p/(3\varepsilon_0)}.$$

The molecular field factor is accordingly

$$K = \frac{1}{1 - N\alpha_p/(3\varepsilon_0)}.$$

$\vec{P}$ is related to the macroscopic dielectric displacement $\vec{D}$ and the relative permittivity ε_r according to

$$\vec{D} = \varepsilon_0 \varepsilon_r \vec{E} = \varepsilon_0 \vec{E} + \vec{P}$$

which leads to the Clausius-Mossotti equation in Eqn. (2.4) [RMC80, CON$^+$04].

$$\frac{\varepsilon_r - 1}{\varepsilon_r + 2} = \frac{N\alpha_p}{3\varepsilon_0} \tag{2.4}$$

The above fundamental relations imply that the material in question is isotropic which enables using α_p and K as scalars. For most materials this is however not the case and only materials with molecules having spherical symmetry are an exception. As particularly LC molecules do not feature spherical symmetry, both α_p and K have to be written in tensor form, that is Eqn. (2.2) rewrites as $\vec{E}_{local} = \mathbf{T}^K \vec{E}$ and Eqn. (2.3) as $\vec{P} = N\mathbf{T}^{\alpha_p}\vec{E}_{local}$. Before discussing the general anisotropic dielectric behaviour of LCs in more detail, the basic properties of nematic LCs are introduced in the next section.

2.2 Properties of Liquid Crystals

2.2.1 Ordering of a Bulk of Liquid Crystal

Fig. 2.1 shows schematically how LC molecules behave in a bulk. The molecules are represented by rods which represents both their physical shape and the anisotropic behaviour. Also due to this the molecules tend to align in parallel, i.e. they feature orientational order but no translational order. If the respective phase of the LC features an ordering like in Fig. 2.1(b), the phase is called nematic. The level of ordering is however temperature dependent. This is quantitatively described by the so called order parameter S. The general behaviour of S is such that it approaches one for very low temperatures (Fig. 2.1(a)) and decreases with increasing temperature. At a certain temperature, the so called clearing point, the molecule configuration changes from a relatively ordered, obviously anisotropic configuration (Fig. 2.1(b)), into the so called isotropic phase in which all molecules are oriented randomly (Fig. 2.1(c)). This happens suddenly, i.e. at the clearing point the order parameter drops from a value unequal zero to zero.

For purely nematic LC compounds or mixtures, the nematic phase can also change to a crystalline or glass phase. This happens usually at low temperatures but also depends on the material. The temperature at which crystallisation happens can usually not precisely be specified as

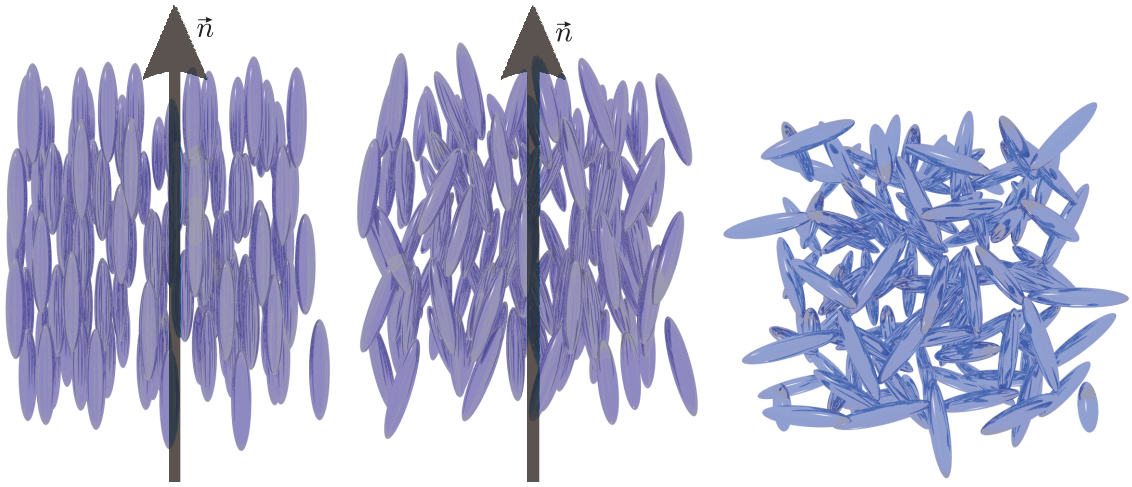

Figure 2.1: The ordering of nematic liquid crystal molecules depending on the order parameter S. The arrow indicates the director $\vec{n}$. (a) All molecules point in the same direction which means that the system is perfectly ordered, i.e. $S = 1$. (b) A preferential direction of the molecules exists and S takes a value between 0 and 1. (c) No ordering is present, i.e. $S = 0$.

the crystallisation point strongly depends on the LC material itself and the material the LC is contained in. This is very much in contrast to the clearing point which can be clearly identified in experiments. Due to the fact that the material crystallises at some temperature, $S = 1$ can actually never be reached.

In the nematic phase, the preferential, i.e. the average direction of the molecules is described by the director $\vec{n}$ (Figs. 2.1(a) and 2.1(b)). The director is a macroscopic quantity and for a bulk of LC molecules generally expressed in the form of a vector field. Although the arrows in Figs. 2.1(a) and 2.1(b) are pointing in a specific direction (up in this case), the mathematical representation of the system permits them to point in the opposite direction as the system is symmetric with respect to a plane on which $\vec{n}$ is normal. The physical behaviour of the director will be described in more detail in section 2.4.

2.2.2 Definition and Description of the Order Parameter S

As mentioned above, the order of a bulk of liquid crystal depends on temperature. How ordered a given system actually is can be generally described by order parameters. While there are many order parameters defined which account for whether the material is uniaxial, biaxial, ferroelectric, etc., the most important and for nematic liquid crystals most commonly used one S, shall be described here.

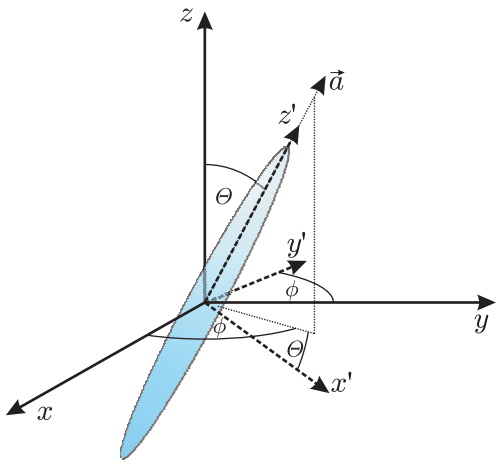

Figure 2.2: The coordinate system commonly used for a single LC molecule. The molecules coordinate system is defined by the axes x', y' and z'. The direction in which the molecule points is described by the unit vector $\vec{a}$ which is defined on the xyz coordinate system. The director $\vec{n}$ is aligned with the z-axis.

Fig. 2.2 defines the working coordinate system of a single rod-like molecule with respect to the director. The director is assumed to be aligned with the z-axis. The probability to find the unit vector $\vec{a}$ within the solid angle $d\Omega$ is given by $f(\theta,\varphi)d\Omega$ with $d\Omega = \sin\theta d\theta d\phi$ [YW06]. Due to the assumed uniaxiallity, $f(\theta,\varphi)$ only depends on θ so φ will not be explicitly used in the following.

The order parameter S depending on the temperature T is generally defined as (e.g. [GP93])

$$S(T) = \langle P_2(\cos\theta)\rangle = \int_0^{\pi} P_2(\cos\theta) f(\theta,T)\sin\theta d\theta. \tag{2.5}$$

$P_2(x) = \frac{1}{2}(3x^2\theta - 1)$ is the second order Legendre-polynomial which accounts, as opposed to the first order polynomial P_1, for the system's symmetry with respect to a plane on which $\vec{n}$ is normal ($\vec{n} = -\vec{n}$). The angle brackets denote the expected value which is identical both temporal and spatial.

Maier and Saupe [GP93] derived an expression for the order parameter by assuming the following so called nematic potential

$$V_n(\theta,T) = -\nu S(T)\cdot\left(\frac{1}{2}(3\cos^2\theta - 1)\right) \tag{2.6}$$

where T is the absolute temperature. The approach in Eqn. (2.6) is based on the consideration of a single molecule which is surrounded by a bulk of other molecules which are more or less ordered around the director. The latter fact is represented by including the order parameter S. Rotating the molecule away from the direction of $\vec{n}$ changes the potential. Details about this approach can be found in [Gie03].

The parameter ν is an interaction constant which was assumed to be independent on temperature in the original Maier-Saupe theory. It was found later that this assumption is not true [GP93] but the impact on the actual derivation of the order parameter is not too high.

Taking the nematic potential in Eqn. (2.6) the orientation probability in terms of θ (see Fig. 2.2) is determined by the Boltzmann distribution

$$f(\theta,T) = \frac{e^{-\frac{V_n(\theta,T)}{k_B T}}}{Z(T)} = \frac{1}{Z(T)} e^{S(T)\cdot\left(\frac{1}{2}(3\cos^2\theta-1)\right)\frac{\nu}{k_B T}} \tag{2.7}$$

The parameter $Z(T)$ is the so called partition function [YW06] and acts as the normalization of the distribution. k_B is Boltzmann's constant. As $Z(T)$ is the sum of all possible states with respect to the orientation θ of a molecule, it is calculated according to

$$Z(T) = \int_0^{\pi} e^{-\frac{V_n(\theta,T)}{k_B T}} \sin\theta d\theta. \tag{2.8}$$

Finally, substituting Eqn. (2.7) in Eqn. (2.5), a self consistent equation can be written down:

$$S(T) = \frac{1}{Z(T)} \int_0^{\pi} P_2(\cos\theta) e^{S(T)\cdot\left(\frac{1}{2}(3\cos^2\theta-1)\right)\frac{\nu}{k_B T}} \sin\theta d\theta. \tag{2.9}$$

By defining a normalized temperature $T_n = k_B T/\nu$ Eqn. (2.9) can be rewritten as

$$S(T_n) = \frac{1}{Z(T_n)} \int_0^{\pi} P_2(\cos\theta) e^{S(T_n)\cdot\left(\frac{1}{2}(3\cos^2\theta-1)\right)\frac{1}{T_n}} \sin\theta d\theta. \tag{2.10}$$

This equation cannot be solved analytically in terms of S. It is however possible to solve it numerically. Doing so, one obtains a curve as plotted in Fig. 2.3. As can be seen from the

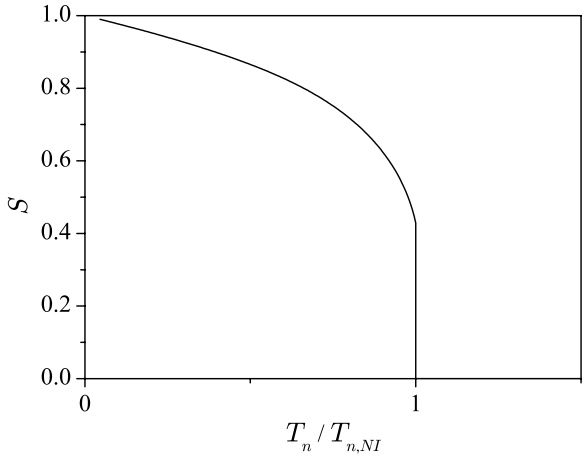

Figure 2.3: The order parameter S as a function of temperature normalised with respect to the transition normalised temperature $T_{n,NI}$

plot, the order parameter drops suddenly to zero at a certain temperature, i.e. the phase changes

from nematic (Fig. 2.1(b)) to isotropic (Fig. 2.1(c)). This happens exactly at $T_{n,NI} = 0.22019$ [GP93, YW06] which marks the nematic to isotropic transition. The value of $T_{n,NI}$ is universal and is determined by energy minimization considerations. The temperature scale in Fig. 2.3 can be rescaled to a °C scale according to

$$T^{\circ C} = \frac{T_n}{T_{n,NI}}(T_{NI} - T_0) + T_0.$$

T_{NI} is the clearing point and T_0 the absolute zero temperature, both in °C.

Although $S(T_n)$ and hence $S(T)$ with T_{NI} scaled according to $T_{n,NI}$ is universal, it offers only an estimation of the real behaviour of LCs, particularly because of the rather simple approach and the assumed constant ν. Measurements of the order parameter with methods like nuclear magnetic resonance spectroscopy [HW03] usually differ slightly from the theoretical values. However the given $S(T)$ gives a good starting point to explain certain experimental results both qualitatively and quantitatively.

For describing the order parameter versus temperature, the Landau-deGennes theory can also be employed [YW06, GP93, Mül07]. This theory includes additional parameters which allow to fit the respective function to a measurement which makes this theory less suitable for general explanations of LC behaviour, especially in this work. Furthermore the order parameter can take values larger than one if the parameters are not correctly chosen. Nevertheless, this theory describes an additional phenomenon not predicted by the Maier-Saupe theory. In a certain temperature interval around the clearing point both phases, i.e. the nematic and the isotropic, can exist. This interval spans usually 1-3 °C, depending on the material. However, because this effect was found to be negligible in the scope of this work, the Landau-deGennes theory is not further described here.

Lastly, it should be mentioned that the aforementioned crystalline state is neither described by the Maier-Saupe theory nore by the Landau-deGennes theory as the order parameter is defined down to 0 K. In order to be able to apply the theory to measurements, it is assumed that the actual characteristics of the order parameter as shown in Fig. 2.3 are not influenced by the crystallisation point but rather that the model stops being valid from the temperature at which crystallisation occurs. The actual configuration of the molecules in the crystalline state can usually not directly be given as the molecules form arbitrary crystals.

2.3 Dielectric and Magnetic Properties of LCs

In the following, the dielectric and magnetic properties are reviewed with particular focus on the anisotropic nature of these quantities. The magnetic properties are introduced first as their description is simpler compared to the dielectric properties.

2.3.1 Magnetic Properties

LC materials are mostly diamagnetic which stems particularly from the benzene rings present in almost all LC molecules [GP93]. From the molecular point of view, a current builds up in the ring structures when the magnetic field is perpendicular to the ring which in turn leads to an increased energy state. On the other hand, if the field is in parallel to the ring, no current is induced and the energy of the molecules is not increased. Because of that a host of molecules will always try to align parallel to a magnetic field.

The so called molecular magnetic polarisabilities, which describe the origin of the above mentioned behaviour qualitatively, are defined as $\kappa_\perp$ and $\kappa_{||}$ [YW06]. The subscripts $\perp$ and $||$, respectively, refer to the directions perpendicular and parallel to the molecule long axis. Referring to Fig. 2.2 these are the directions perpendicular and parallel to the z'-axis. With these two parameters, the tensor of the molecular magnetic polarisabilities

$$\tilde{\mathbf{T}}^{\kappa} = \begin{pmatrix} \kappa_\perp & 0 & 0 \\ 0 & \kappa_\perp & 0 \\ 0 & 0 & \kappa_{||} \end{pmatrix}$$

can be defined in the $x'y'z'$ coordinate system. Using the rotation matrix

$$\mathbf{R} = \begin{pmatrix} \cos(\Theta)\cos(\phi) & -\sin(\phi) & \sin(\Theta)\cos(\phi) \\ \cos(\Theta)\sin(\phi) & \cos(\phi) & \sin(\Theta)\sin(\phi) \\ -\sin(\Theta) & 0 & \cos(\Theta) \end{pmatrix},$$

which represents the orientation of a single molecule with respect to the director or the $z-$*axis* (Fig. 2.2), the basis $x'y'z'$ of the tensor $\tilde{\mathbf{T}}^{\kappa}$ can be transformed to align with the cartesian coordinate system *xyz*. This transformation yields the tensor

$$\mathbf{T}^{\kappa} = \mathbf{R}\tilde{\mathbf{T}}^{\kappa}\mathbf{R}^{-1}.$$

As the magnetic interaction among the molecules is weak [YW06, GP93], i.e. the local field experienced by the molecule is approximately the same as the macroscopic field, the macroscopic magnetic susceptibility χ_m can be obtained by simply multiplying the molecular property κ by the number density N of the material, that is in tensorial form one obtains $\mathbf{T}^{\chi_m} = N\mathbf{T}^{\kappa}$ [Jeu79]. Calculating $\langle \mathbf{T}^{\chi_m} \rangle$, that is element by element, one obtains the matrix

$$\langle \mathbf{T}^{\chi_m} \rangle = \begin{pmatrix} \chi_{m,\perp}^{S=1} + \frac{1}{3}(1-S)\Delta\chi_m^{S=1} & 0 & 0 \\ 0 & \chi_{m,\perp}^{S=1} + \frac{1}{3}(1-S)\Delta\chi_m^{S=1} & 0 \\ 0 & 0 & \chi_{m,\perp}^{S=1} + \frac{1}{3}(2S+1)\Delta\chi_m^{S=1} \end{pmatrix} \quad (2.11)$$

with $\Delta\chi_m = \chi_{m,||}^{S=1} - \chi_{m,\perp}^{S=1}$ [YW06]. It should be noted that $\chi_{m,||}^{S=1}$ and $\chi_{m,\perp}^{S=1}$ in Eqn. (2.11) are the values which would be macroscopically obtained if one was able to characterise the material at

$S = 1$ as they directly stem from molecular and therefore order parameter independent properties. The macroscopic values for $\chi_{m,\perp}$ and $\chi_{m,||}$ are consequently

$$\chi_{m,\perp} = \chi_{m,\perp}^{S=1} + \frac{1}{3}(1-S)\Delta\chi_m^{S=1} \tag{2.12}$$

$$\chi_{m,||} = \chi_{m,\perp}^{S=1} + \frac{1}{3}(2S+1)\Delta\chi_m^{S=1} \tag{2.13}$$

From Eqns. (2.12) and (2.13), it can directly be seen that $\Delta\chi_m = \chi_{m,||} - \chi_{m,\perp} \propto S$. As the magnetic susceptibility of nematic LCs is very close to zero at microwave frequencies [Mül07], it is not considered in the experiments and analysis presented in this work. However, the fact that there is a finite, though very small, $\Delta\chi$ is utilised for reorienting the molecules with magnetic fields.

For the dielectric properties, which play the major role in this work, the description of the anisotropy and its dependence on the order parameter is more complex as will be shown in the next section.

2.3.2 Dielectric Properties

As already hinted in section 2.1, a direct and simple relation between the molecular and the macroscopic properties is not given when it comes to the anisotropic permittivity of LCs. In the following, the derivation of the effective perpendicular and parallel permittivities as a function of the order parameter is described insofar as it is relevant to this work. A detailed treatment can be found e.g. in [Jeu79] or in [YW06].

From section 2.1, the macroscopic polarisation density is

$$\vec{P} = N\mathbf{T}^{\alpha_p}\mathbf{T}^{K}\vec{E}. \tag{2.14}$$

Both $\mathbf{T}^{\alpha_p}$ and $\mathbf{T}^{K}$ are molecular tensors [Jeu79] which enables to write

$$\tilde{\mathbf{T}}^{\alpha_p} = \begin{pmatrix} \alpha_{p,\perp} & 0 & 0 \\ 0 & \alpha_{p,\perp} & 0 \\ 0 & 0 & \alpha_{p,||} \end{pmatrix}$$

and

$$\tilde{\mathbf{T}}^{K} = \begin{pmatrix} K_{\perp} & 0 & 0 \\ 0 & K_{\perp} & 0 \\ 0 & 0 & K_{||} \end{pmatrix}.$$

Both tensors above are defined in the molecules coordinate system $x'y'z'$, which is why they are diagonal. The subscripts $\perp$ and $||$ refer again to the directions perpendicular and parallel to the

molecule long axis. Aligning the tensors with the laboratory coordinates *xyz* (Fig. 2.2) in order to use them in Eqn. (2.14) is accomplished by calculating $\mathbf{T}^{\alpha_p} = \mathbf{R}\tilde{\mathbf{T}}^{\alpha_p}\mathbf{R}^{-1}$ and accordingly $\mathbf{T}^{K} = \mathbf{R}\tilde{\mathbf{T}}^{K}\mathbf{R}^{-1}$. Eqn. (2.14) can then be written as

$$\vec{P} = N\mathbf{R}\tilde{\mathbf{T}}^{\alpha_p}\tilde{\mathbf{T}}^{K}\mathbf{R}^{-1}\vec{E} = \mathbf{T}^{\chi_e}\vec{E}.$$

Expanding this equation yields

$$\mathbf{T}^{\chi_e} = N\begin{pmatrix} \alpha_{p,\perp}K_\perp \cdot(\cos^2\Theta\cos^2\phi+\sin^2\phi) + \alpha_{p,||}K_{||}\sin^2\Theta\cos^2\phi & \cos\phi\sin\phi\sin^2\Theta \cdot(\alpha_{p,||}K_{||}-\alpha_{p,\perp}K_\perp) & \cos\phi\cos\Theta\sin\Theta \cdot(\alpha_{p,||}K_{||}-\alpha_{p,\perp}K_\perp) \\ \cos\phi\sin\phi\sin^2\Theta (\alpha_{p,||}K_{||}-\alpha_{p,\perp}K_\perp) & \alpha_{p,\perp}K_\perp \cdot(\cos^2\Theta\sin^2\phi+\cos^2\phi) + \alpha_{p,||}K_{||}\sin^2\Theta\sin^2\phi & \cos\Theta\sin\phi\sin\Theta \cdot(\alpha_{p,||}K_{||}-\alpha_{p,\perp}K_\perp) \\ \cos\phi\cos\Theta\sin\Theta \cdot(\alpha_{p,||}K_{||}-\alpha_{p,\perp}K_\perp) & \cos\Theta\sin\phi\sin\Theta \cdot(\alpha_{p,||}K_{||}-\alpha_{p,\perp}K_\perp) & \alpha_{p,\perp}K_\perp\sin^2\Theta + \alpha_{p,||}K_{||}\cos^2\Theta \end{pmatrix}$$

The above equation represents the macroscopic electric susceptibility of a material having anisotropic molecules with the orientation (Θ,ϕ). As the orientation has an underlying statistic (see Eqn. (2.7)), calculating the expected value of $\mathbf{T}^{\chi_e}$ will give the electric susceptibility which is effectively experienced by an electric field. Using $\langle\sin^2\Theta\rangle = (2-2S)/3$, $\langle\cos^2\Theta\rangle = (2S+1)/3$, $\langle\cos^2\phi\rangle = \langle\sin^2\phi\rangle = 1/2$, $\langle\sin\Theta\rangle = \langle\cos\Theta\rangle = 0$, $\langle\sin\phi\rangle = \langle\cos\phi\rangle = 0$ and $\langle\sin\phi\cos\phi\rangle = 0$ [YW06][1] one obtains:

$$\langle\mathbf{T}^{\chi_e}\rangle = \frac{N}{3}\begin{pmatrix} \alpha_{p,\perp}K_\perp(2+S) + \alpha_{p,||}K_{||}(1-S) & 0 & 0 \\ 0 & \alpha_{p,\perp}K_\perp(2+S) + \alpha_{p,||}K_{||}(1-S) & 0 \\ 0 & 0 & \alpha_{p,\perp}K_\perp(2-2S) + \alpha_{p,||}K_{||}(1+2S) \end{pmatrix} \tag{2.15}$$

Eqn. (2.15) describes therefore the electric susceptibility of a bulk of LC the director of which is aligned with the *z*-axis. The relative permittivity tensor can simply be calculated according to

$$\mathbf{T}^{\varepsilon_r} = \mathbf{I} + \frac{1}{\varepsilon_0}\mathbf{T}^{\chi_e} \tag{2.16}$$

with $\mathbf{I}$ being the identity matrix. The effective anisotropy $\mathbf{T}^{\varepsilon_r}_{33} - \mathbf{T}^{\varepsilon_r}_{11}$ and hence $\mathbf{T}^{\varepsilon_r}_{33} - \mathbf{T}^{\varepsilon_r}_{22}$ is

$$\Delta\varepsilon_r = \frac{N}{\varepsilon_0}(\alpha_{p,||}K_{||} - \alpha_{p,\perp}K_\perp)S.$$

The problem at this point is to find a way how to apply Eqn. (2.16) for this work's purpose as both $\tilde{\mathbf{T}}^{\alpha_p}$ and $\tilde{\mathbf{T}}^{K}$ are generally unknown and not accessible by measurements. Nevertheless in the

[1] It is also possible to calculate the expected values explicitly using the LC statistics presented in section 2.2.2

literature several justifications can be found which allow to treat the terms $\alpha_{p,||}K_{||}$ and $\alpha_{p,\perp}K_{\perp}$ as molecular properties which are related to the macroscopic susceptibility by the number density N, i.e. that neither $\tilde{\mathbf{T}}^{\alpha_p}$ nor $\tilde{\mathbf{T}}^{K}$ depends on the order parameter [Jeu79, YW06]. According to [Jeu79] particularly $\tilde{\mathbf{T}}^{K}$ does not change significantly over the nematic range and also not in the isotropic phase near the clearing point. The following relation can be established:

$$\mathbf{T}^{\varepsilon_r}(S=1) = \begin{pmatrix} \varepsilon_{r,\perp}^{S=1} & 0 & 0 \\ 0 & \varepsilon_{r,\perp}^{S=1} & 0 \\ 0 & 0 & \varepsilon_{r,||}^{S=1} \end{pmatrix} \tag{2.17}$$

Using Eqn. (2.17), Eqn. (2.16) can be rewritten such that one obtains

$$\varepsilon_{r,\perp} = \frac{1}{3}\left(\varepsilon_{r,\perp}^{S=1}(2+S) + \varepsilon_{r,||}^{S=1}(1-S)\right) \tag{2.18}$$

$$\varepsilon_{r,||} = \frac{1}{3}\left(\varepsilon_{r,\perp}^{S=1}(2-2S) + \varepsilon_{r,||}^{S=1}(1+2S)\right). \tag{2.19}$$

Eqns. (2.18) and (2.19) are very important as they explain how the material related properties $\varepsilon_{r,\perp}^{S=1}$ and $\varepsilon_{r,||}^{S=1}$ contribute to the measurable quantities. They also establish the foundation for the explanation of the parallel loss tangent which will be presented in section 3.1.3. It must however be noted that the values $\varepsilon_{r,\perp}^{S=1}$ and $\varepsilon_{r,||}^{S=1}$ cannot be measured as perfect order in the LC is not achievable. It should be noted that the parallel and perpendicular parts of the permittivity are defined with respect to the director or the z-axis in Fig. 2.2, respectively.

Finally, for the sake of completeness, the calculation rule for the electric displacement field $\vec{D}$ shall be given as it will be used throughout this work. For that purpose the director $\vec{n}$ is assumed to be aligned with the $x'y'z'$ coordinate system in Fig. 2.2 and the electric fields are expressed in the xyz frame. Analogous to the considerations for a single molecule, the permittivity tensor of the director in the xyz frame is

$$\mathbf{T}_{\vec{n}}^{\varepsilon_r} = \mathbf{R}\begin{pmatrix} \varepsilon_{r,\perp} & 0 & 0 \\ 0 & \varepsilon_{r,\perp} & 0 \\ 0 & 0 & \varepsilon_{r,||} \end{pmatrix}\mathbf{R}^{-1} = \begin{pmatrix} \varepsilon_{r,xx} & \varepsilon_{r,xy} & \varepsilon_{r,xz} \\ \varepsilon_{r,xy} & \varepsilon_{r,yy} & \varepsilon_{r,yz} \\ \varepsilon_{r,xz} & \varepsilon_{r,yz} & \varepsilon_{r,zz} \end{pmatrix} \tag{2.20}$$

2.3.3 Benchmark Values of Tunable Materials

In order to characterise the dielectric performance of tunable material the so called tunability can be defined. For nematic LCs this is

$$\tau_{LC} = \frac{\varepsilon_{r,||} - \varepsilon_{r,\perp}}{\varepsilon_{r,||}}. \tag{2.21}$$

In Eqn. (2.21) it is assumed that $\varepsilon_{r,||} > \varepsilon_{r,\perp}$ which is in the microwave region always given. Incorporating the dielectric loss tangent $\tan\delta$ a material efficiency can be defined according to

$$\eta_{LC} = \frac{\tau_{LC}}{\max(\tan\delta)}. \tag{2.22}$$

As will be seen later on, the loss tangent differs depending on whether the material is used in perpendicular ($\tan\delta_\perp$) or parallel ($\tan\delta_{||}$) configuration.

For optical frequencies, usually not the permittivity but rather the index of refraction n is employed. For the corresponding applications the optical anisotropy Δn sis defined according to

$$\Delta n = n_{||} - n_\perp = \sqrt{\varepsilon_{r,||}} - \sqrt{\varepsilon_{r,\perp}}.$$

2.4 The Elastic Continuum Theory of Liquid Crystals

2.4.1 The Oseen-Frank Energy

The continuum theory of liquid crystals is a formulation in terms of energies. It is a macroscopic approach based on the director $\vec{n}$ which has elastic properties. Any deformation of the director leads to an increase of the energy of the system. This energy is of the Gibbs energy type, i.e. it is assumed that, whatever deformations the LC molecules undergo, there is no change in temperature or pressure [YW06].

Three fundamental types of deformations can exist in nematic liquid crystals. These types are called splay, twist and bend deformations. The nature of these deformations is shown in Fig. 2.4. The contribution to the system's energy of each of these deformation types can be computed

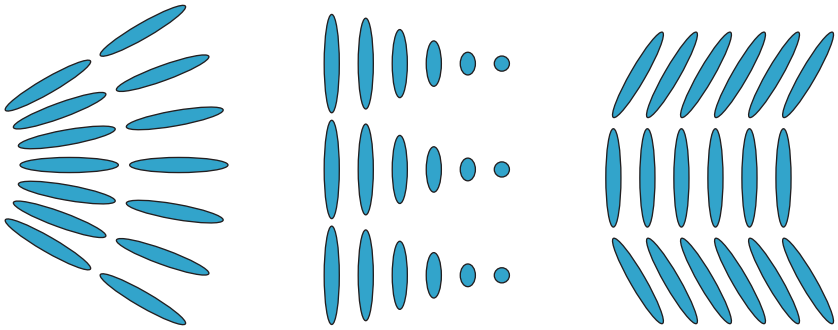

Figure 2.4: The three fundamental elastic deformations in nematic liquid crystals: (a) splay (b) twist (c) bend

according to Eqns. (2.23) to (2.25):

$$f_{splay} = \frac{1}{2} K_{11} \left(\nabla \cdot \vec{n}\right)^2 \tag{2.23}$$

$$f_{twist} = \frac{1}{2} K_{22} \left(\vec{n} \cdot \nabla \times \vec{n}\right)^2 \tag{2.24}$$

$$f_{bend} = \frac{1}{2} K_{33} \left(\vec{n} \times \nabla \times \vec{n}\right)^2 \tag{2.25}$$

These three terms are combined to the Oseen-Frank elastic energy:

$$f_{elastic} = f_{splay} + f_{twist} + f_{bend} \tag{2.26}$$

with $f_{elastic}$ being an energy density. The terms K_{11}, K_{22} and K_{33} are called elastic constants, which have to be determined experimentally. For this work's purpose the values of these constants are not needed and the equations above are presented in order to be able to make certain qualitative derivations. Usually the constants are experimentally determined using commercially available tools such as listed e.g. in [Ins07].

2.4.2 Response to Electric and Magnetic Fields

In the following, the theory of the response of a bulk of LC to an applied electric field is reviewed. Although limited here to the electric field case, the theory can be modified easily for magnetic fields essentially by replacing the electric field and material quantities with the respective magnetic ones. The latter is insofar relevant to this work as for the material characterisation magnetic fields are used for controlling the orientation of the LC.

In order to calculate the response to an electric field the energy density of the electric field must be calculated [KW93]:

$$f_{electr} = \frac{1}{8\pi} \vec{E} \cdot \vec{D} = \frac{\varepsilon_\perp}{8\pi} \langle \vec{E}^2 \rangle + \frac{\Delta\varepsilon \langle (\vec{n} \cdot \vec{E})^2 \rangle}{8\pi} \tag{2.27}$$

Here, $\langle\rangle$ denotes the time average. Eqn. (2.27) is also given in other literature (e.g. [GP93,SS74]) however, mostly static fields are assumed or implied and the author of [KW93] is one of the few who explicitly states that Eqn. (2.27) is also valid for optical fields. A linear material is assumed in the equation. Eqn. (2.27) is obviously given in electrostatic cgs units (see [Kho07] and [Jac65]). In SI units Eqn. (2.27) yields

$$f_{electr} = \frac{1}{2} \varepsilon_0 (\langle \vec{E}^2 \rangle \varepsilon_{r,\perp} + \Delta\varepsilon_r \langle (\vec{n} \cdot \vec{E})^2 \rangle) = \frac{1}{2} \varepsilon_0 \langle \vec{E}^2 \rangle (\varepsilon_\perp + \Delta\varepsilon \cos^2 \vartheta) \tag{2.28}$$

with ϑ being the angle between the electric field and the director. In Eqns. (2.27) and (2.28), the effective value of the electric field is the quantity that governs the behaviour of the director. As will be seen later, the equations implicate that the director can be distorted by a signal having any arbitrary frequency.

A system defined by a specific LC and an electric field will adjust the director orientation such that the functional of the total free energy

$$R = \int_{Vol} f_{elastic} - f_{electr} \tag{2.29}$$

is minimized. The integral has to be calculated for the entire volume of the considered LC bulk. The electric energy f_{electr} is counted negative to comply with the definition of the Gibbs free energy. In order to understand that, one can consider a system as shown in Fig. 2.5(a). Here,

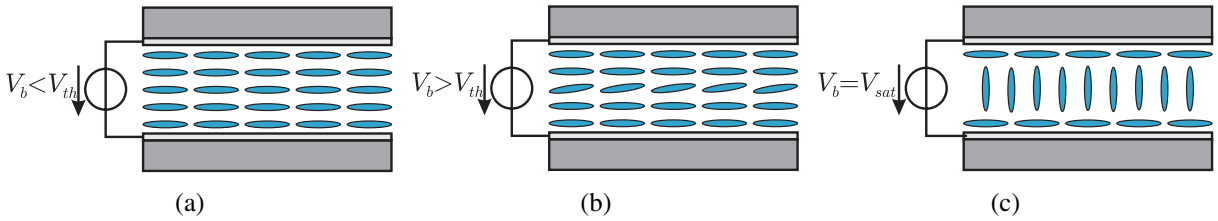

Figure 2.5: The orientation of the director in a Freedericks type cell. (a) With a voltage below the threshold voltage V_{th} there is no change of the director. (b) With $V_b > V_{th}$ the center molecules start to rotate. (c) Saturation is reached at V_{sat}

the voltage source is connected to a parallel plate capacitor filled with LC at an arbitrary point in time. The director directly at the electrodes is assumed to be fixed parallel to the electrodes. At the moment the voltage source is connected, the system assumes a new state. Electrical work will be done in order to move charges to the electrodes of the parallel plate capacitor. In that sense this work is deducted from the free electrical energy stored in the voltage source, i.e. electrical work is done to the parallel plate capacitor. Unlike an elastic deformation of the director, this process is not reversible. If the director is distorted by whatever means, the elastic energy increases which lets the total free energy increase (Eqn. (2.29)).

From Eqn. 2.29, an important property can be derived: The Freedericks transition voltage. Assuming a structure as shown in Fig. 2.5(a) this is the voltage above which the LC molecules, and therefore the director, start turning. In other words, only from this voltage an effect on the director is detectable. The reason for the existance of such a threshold can be explained using Eqn. 2.29. If a certain low voltage is applied to the capacitor, the free energy will be reduced accordingly. If $\Delta\varepsilon = \varepsilon_{||} - \varepsilon_{\perp} > 0$ is assumed, the free energy would be reduced further if the molecules did rotate in parallel to the field. However, as the molecules are fixed at the electrodes this would lead to a director distortion which in turn would increase the free energy. At a certain voltage the reduction of the free energy by the electrical work (increased by the higher permittivity of the rotated director) is larger than the free energy increase caused by a distortion. This is the so called Freedericks threshold voltage V_{th}.

The threshold voltage can be calculated according to (see e.g. [GP93, YW06])

$$V_{th} = \pi\sqrt{\frac{K_{11}}{\varepsilon_0\Delta\varepsilon}}. \tag{2.30}$$

This equation is valid only for configurations as shown in Fig. 2.5 which have only or are dominated by splay deformations (hence K_{11}). For twist configurations, as they are used in display cells with the director twisted by 90 ° on one electrode, more than one type of director distortion is involved and the respective formula is then more complex. Most experiments in the

scope of this work use director and surface alignment configurations which only lead to splay distortion. It should be noted that V_{th} is independent on the thickness of the LC layer.

While the threshold voltage can be calculated analytically, the saturation voltage must be defined according to the respective application. The reason for that is that only at infinite bias voltage the director in the entire LC bulk is perfectly aligned with the electric field and therefore true bias saturation is reached. However, a reasonable approximation for a saturation can be given under the assumption of a parallel plate capacitor as shown in Fig. 2.5 as this topology represents the tunable devices used in this work quite accurately. The approach chosen here is semi-analytical and uses the same equations and assumptions commonly given in the literature for the derivation of the threshold voltage. Therefore only the differential equation needed to compute the director distribution in the 1D case is required. This equation is obtained using the Euler-Lagrange equation on Eqn. (2.29) [BC94, CH97, Som06].

$$\frac{\varepsilon_0 \Delta\varepsilon E_z^2}{K_{11}} \sin\Theta\cos\Theta - \frac{\partial^2\Theta}{\partial z^2} = \frac{V^2}{V_{th}^2}\pi^2 \sin\Theta\cos\Theta - \frac{\partial^2\Theta}{\partial \tilde{z}^2} = 0. \tag{2.31}$$

The coordinates are defined in the xyz frame (Fig. 2.2). The terms in the equation above have the physical meaning of torques. $\tilde{z} = z/d$, which makes it possible to express the field strength E_z by the bias voltage V_b. d is accordingly the thickness of the LC layer. Eqn. (2.31) uses the threshold voltage as given in Eqn. (2.30) as a parameter and is therefore universal. It should be noted that for Eqn. (2.31) the so called one constant approximation ($K_{11} = K_{22} = K_{33}$) [GP93] is made. Otherwise the differential equation would be more complex and even numerically difficult to handle. Eqn. (2.31) is a boundary value problem with $\Theta(\tilde{z} = 0) = 90^\circ$ and $\Theta(\tilde{z} = 1) = 90^\circ$. The solution of this problem for various ratios of V_b/V_{th} is shown in Fig. 2.6(a)[2].

The graph shows the deflection $\Theta(\tilde{z})$ of the director vs. the $\tilde{z}$ coordinate, i.e. from the bottom electrode to the top electrode. Due to the formulation as a boundary value problem, and as also can be seen from Fig. 2.6(a), the deflection at the boundaries is always zero. This consideration is also referred to as strong anchoring.

Next, a measure needs to be found for assessing the tuning efficiency of an ideal parallel plate capacitor i.e. a criterion has to be defined for the saturation voltage. As mentioned before and as obvious from Fig. 2.6(a), it takes infinite bias voltage in order to fully orient the director. Nevertheless it is important to know how much bias voltage is necessary to obtain e.g 90 or 95 % tunability.

For that purpose an infinitely large parallel plate capacitor is considered. The dielectric is LC and assumes for instance a configuration in between that in Figs. 2.5(b) and 2.5(c). As the structure is infinitely large, the equipotential lines are parallel to the electrodes which makes the electric field $\vec{E}$ perpendicular to the electrodes. Due to the fact that $\mathbf{T}_{\vec{n}}^{\varepsilon_r}$ (Eqn. (2.20)) is not diagonal for $\Theta \neq 0$, the dielectric displacement field will not be parallel to $\vec{E} = (0, 0, E_z)$.

[2]The numeric solution can for instance be obtained using the MATLAB function `bvp4c`. In order to enable the solver to find the solution, an initial value $\Theta \neq 0$ must be supplied as otherwise $\frac{V}{V_{th}}\pi^2 \sin\Theta\cos\Theta = 0$ which is a trivial solution to the differential equation and corresponds to a non-existent excitation torque.

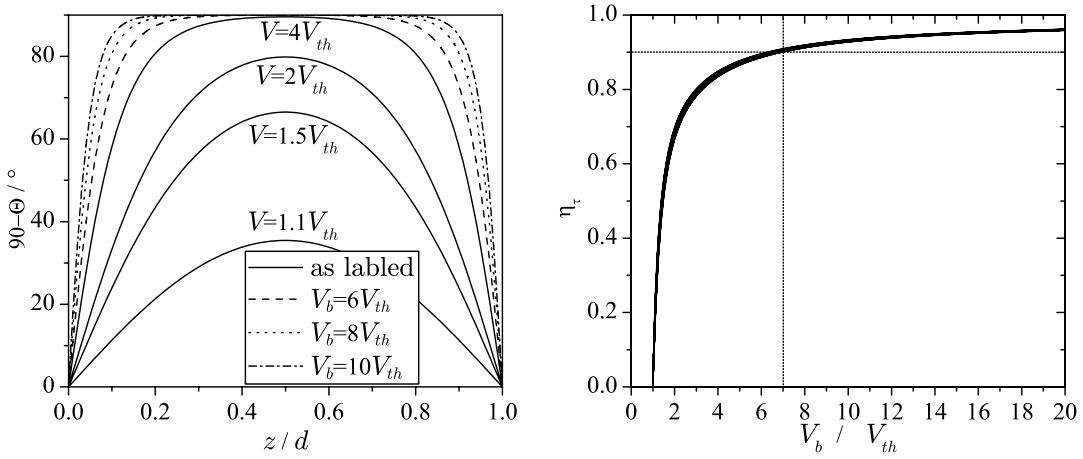

Figure 2.6: (a) The deflection of the director vs. the coordinate $\tilde{z}$. (b) The tuning efficiency vs. the applied bias voltage

Using Gauss's law, i.e.

$$\oint \vec{D} d\vec{A} = Q_e$$

with $d\vec{A}$ being a surface element of a volume and Q_e the charge inside the volume, it is possible to write down the absolute value of the charge density $q_e = D_z$ on either electrode because D_z is constant vs. $\tilde{z}$ as the normal dielectric displacement field components are continuous for an effectively layered material as it is given here. In order to calculate the potential on the electrodes, Laplace's equation $\mathrm{div}\varepsilon_0 \mathbf{T}^{\varepsilon_r}_{\vec{n}} \mathrm{grad}\varphi = 0$ must be solved. For the given problem, i.e. $\partial/\partial x = \partial/\partial y = 0$ Laplace's equation minimises to

$$\frac{\partial}{\partial \tilde{z}} \varepsilon_0 \varepsilon_{r,zz}(\tilde{z}) \frac{\partial}{\partial \tilde{z}} \varphi = 0. \tag{2.32}$$

D_z is obtained by (indefinitely) integrating Eqn. (2.32) over $\tilde{z}$, which is, as also explained above, a constant. Solving Eqn. (2.32) further for the potential φ, Eqn. (2.33) is obtained:

$$\varphi = \int_0^1 \frac{1}{\varepsilon_0 \varepsilon_{r,zz}(\tilde{z})} D_z d\tilde{z}. \tag{2.33}$$

The capacitance density is in this case given by

$$C' = q_e/\varphi = D_z/\varphi$$

which equals the effective permittivity as the capacitor thickness is one. The effective relative permittivity, therefore, evaluates to

$$\varepsilon_{r,eff} = \left(\int_0^1 \frac{1}{\varepsilon_{r,zz}(\tilde{z})} d\tilde{z} \right)^{-1} = \left(\int_0^1 \frac{1}{\varepsilon_{r,\perp} \sin(\Theta(\tilde{z})) + \varepsilon_{r,||} \cos(\Theta(\tilde{z}))} d\tilde{z} \right)^{-1}. \tag{2.34}$$

Using this formula and the maximum available material tunability τ_{LC}, the following tuning efficiency can be defined:

$$\eta_\tau = \frac{\varepsilon_{r,eff} - \varepsilon_{r,\perp}}{\varepsilon_{r,eff}} \cdot \frac{1}{\tau_{LC}} \tag{2.35}$$

As Eqn. (2.35) depends on $\varepsilon_{r,\perp}$ and on $\Delta\varepsilon_r$, an assumption has to be made concerning the values of these two variables with regard to a valid assessment of the effective tunability in the microwave region. As will be seen in section 3.1.3, $\varepsilon_{r,\perp}$ usually takes values around 2.5. The set of curves in Fig. 2.6(b) is obtained by evaluating Eqn. (2.35) for combinations of $2 < \varepsilon_{r,\perp} < 3$ and $0.2 < \Delta\varepsilon_r < 2$. These intervals comprise all values obtained from LCs at microwave frequencies in this work. The result is again plotted versus bias voltage normalised by the threshold voltage (see Eqn. (2.31)). In order to achieve 90 % of the material's tunability, as indicated in Fig. 2.6(b), the V_b/V_{th} ratio should be seven. For 95 % V_b/V_{th} should be 16.

It should be noted that the above estimation of the necessary voltage is rather pessimistic. As stated before strong anchoring of the director at the electrodes is assumed which means that the director is fixed according to the boundary value problem. If this is not the case, and in reality it is most often not, the boundary condition has to be modeled by so-called weak anchoring. This means that the director directly at the electrodes can have angles of up to 90 °. In Eqn. (2.29) this would be reflected by additional energy terms with positive signs. The surface energy terms are not discussed in detail here as they do not offer additional insight for this works purpose. The elastic constants describing the weak anchoring usually depend on the LC and on the surface treatment used. Although not considered further here, weak anchoring can have several consequences [BC94, YW06]. Firstly, the threshold voltage is lowered because, graphically, the director bulk does not need to be distorted as much as for the strong anchoring case; the director layer at the electrodes gives way at some point. Secondly, the curve shown in Fig. 2.6(b) will have a much steeper slope and will saturate at much lower voltages. This is of course in general advantageous for devices but needs very precise design of the LC-surface interaction, which, as mentioned before, was not in the focus of this work. However, it can be assumed that the devices realised in the scope of this work feature relatively strong anchoring.

2.4.3 Response Times

In this section, general relations between LC parameters and the switching times or the tuning speed behaviour, respectively, are given. The underlying theory is reviewed shortly for that purpose. Almost all literature assumes strong anchoring for the respective derivations.

In order to obtain the neccessary relations the right side of Eqn. (2.31) (zero) is replaced by the retarding torque:

$$\frac{\partial^2\Theta}{\partial\tilde{z}^2} - \frac{V^2}{V_{th}^2}\pi^2 \sin\Theta\cos\Theta = \frac{\gamma_1}{K_{11}}\frac{\partial\Theta}{\partial t} \tag{2.36}$$

The term on the right side of Eqn. (2.36) represents the damping of the spring-mass system which is represented by Eqn. (2.31). Eqn. (2.36) is commonly known as the Erikson-Leslie equation. γ_1 is the rotational viscosity of the liquid crystal. From Eqn. (2.36), the response time t_0 is commonly derived to be

$$t_0 = \frac{\gamma_1 d^2}{K_{11}\pi^2}. \tag{2.37}$$

Eqn. (2.37) is given in almost all literature, however mostly for twist distortion (K_{11} instead of K_{22}). t_0 is defined according to

$$\Theta_m(t) = C \exp\left(\frac{t}{t_0}\right) \tag{2.38}$$

with $\Theta_m(t)$ being the angle in the middle of the bulk ($z = d/2$) and C being an arbitrary constant describing that angle. In [KW93], the characteristic constant t_0 is further refined in the rise and the decay time depending on the applied voltage:

$$t_{rise} = \frac{t_0}{\left|\frac{V}{V_{th}} - 1\right|} \tag{2.39}$$

$$t_{decay} = \frac{t_0}{\left|\frac{V_{rem}}{V_{th}} - 1\right|} \tag{2.40}$$

V_{rem} is the remaining voltage after the bias voltage is removed. For the parameter γ_1 the same holds true as for the elastic constants, it is directly available only for a limited number of LCs. The times in Eqns. (2.39) and (2.40) can also be considered as a maximum tuning speed.

From Eqns. (2.39) and (2.40), several conclusions can be made. First of all, the higher the voltage step while switching on is, the faster the tuning process will be. Secondly, the same holds true for the switching off, i.e. the lower V_{rem} the faster the response time will be. These two facts are the reason why in display applications the so called overdrive method is used [YW06]. For tuning to higher voltages a short spike is applied before switching to the actual voltage which is necessary to maintain the required bias state. For tuning to lower voltage levels, the bias is shortly removed entirely and then set to the required bias voltage.

In [YW06], it is stated that for an accurate calculation of the response times still more hydrodynamic parameters have to be included. Nevertheless, the fundamental relation of Eqns. (2.39) and (2.40) remains the same: The response times are proportional to d^2 which means that the response times can be improved dramatically by reducing d. For LC displays, it is usual to have layer thicknesses of $d \leq 5\,\mu\text{m}$ in order to gain the fast switching characteristics known from todays displays (some 10 ms or less). It was therefore one of the major aims of this work to make the technology of such thin layers available for microwave devices.

2.4.4 Pre-Orientation of Nematic LCs

Above the concept of anchoring was introduced with respect to the alignment of the LC director parallel to substrate surfaces. In fact, most devices, as well as those developed in this work, rely on special layers on the substrate surface in order to achieve a director configuration like in Fig. 2.5. These layers are often made of polyimide or polyamide films which are spin coated and subsequently cured. The layer then exerts anchoring forces on the LC director directly at the surface. An important step in processing this orientation layer is the mechanical rubbing. The rubbing process is most often done using a velvet cloth which is under applying of soft force rubbed over the substrate surface [THI+05]. The result of this rubbing is a microscopic grooving of the polyimide surface which leads to a pre-alignment of the LC molecules, i.e. the molecules are oriented parallel to each other.

On an industry scale, the rubbing is done using large velvet covered barrels. Such a rubbing machine was also developed on a smaller scale in the scope of this work in order to make this rather rough process step more reproducible. Fig. 2.7 shows a photograph of the developed rubbing machine. The velvet covered barrel rotates while the table underneath is slowly moved below the barrel. The pressure with which the barrel presses on the substrate is adjusted by moving the table vertically such that for a given substrate thickness always the same pressure is obtained.

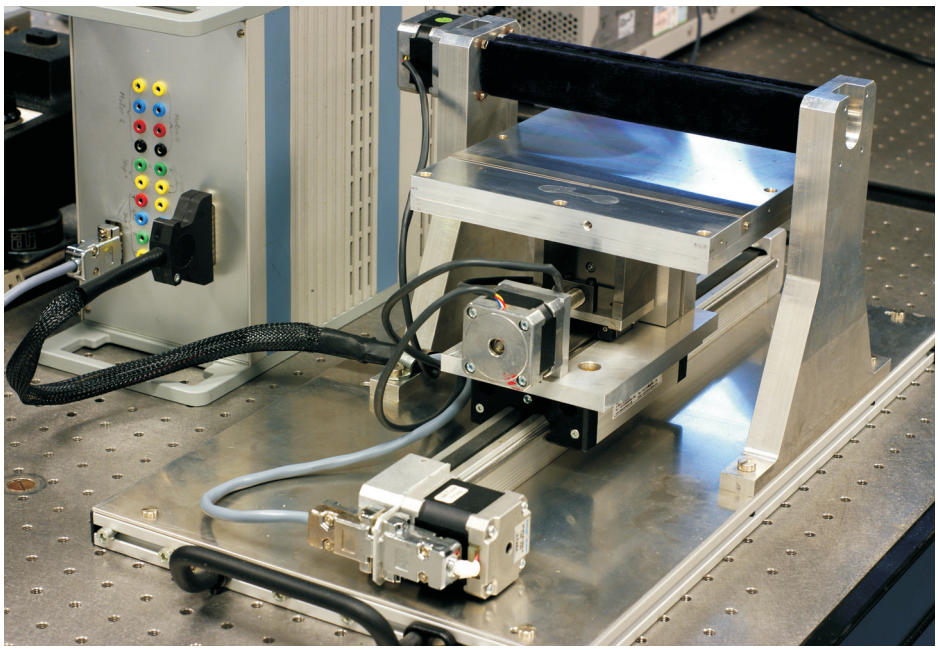

Figure 2.7: Photograph of the rubbing machine built in the scope of this work. More details can be found in Appendix C.

In terms of the pre-orientation with respect to the substrate surface, so called planar and homeotropic alignment is distinguished. Planar means that the director is in parallel to the substrate

surface, homeotropic means that it is perpendicular. Furthermore, angles in between these two extremes can be obtained which is described by a so called pre-tilt angle. As mentioned previously, it is assumed in this work that the orientation is purely planar. In this work, Nylon 6 was used as orientation film. The respective process parameters can be found in Appendix A.

2.5 Dispersion of the Dielectric Properties of Nematic LCs

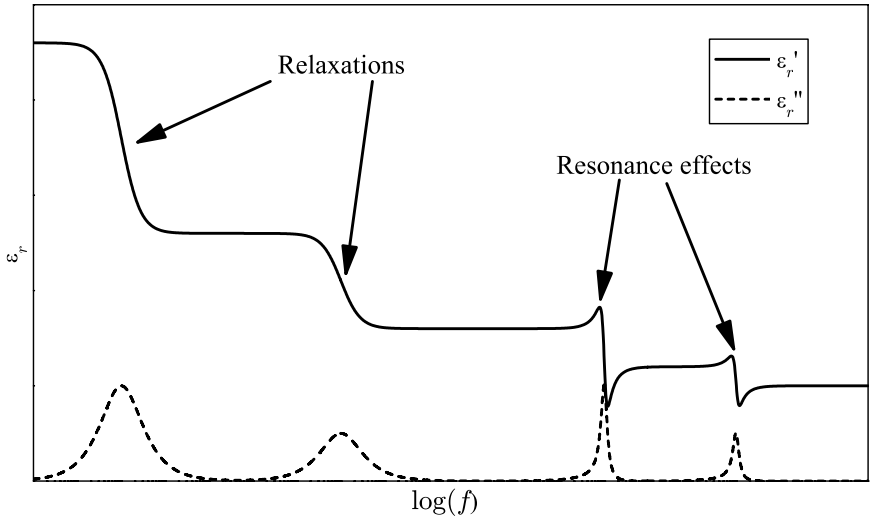

Figure 2.8: General dispersion diagram of the permittivity, after [MH97].

Like with most materials, the dielectric properties of LCs are subject to dispersion. Fig. 2.8 shows the general dispersion present in many material classes. In principle, two different processes determine the characteristic of the permittivity: Relaxations and resonance processes. Common to both process types is the fact that from a certain frequency onwards the polarisation induced by an external, alternating field cannot follow the field anymore. In case of a resonance the process is described by a linear second order ordinary differential equation according to [ST07]. These processes are usually atomic in nature and occur at frequencies above 10^{13} Hz. Therefore, they are not considered in the scope of this work.

Relaxation processes are described in the simplest case by a linear first order ordinary differential equation, i.e. the polarisation follows the electric field but is hindered by dissipation [MH97]. In the frequency domain, the dispersion of the electric susceptibility χ_e of such a process is given by [CON$^+$04]

$$\chi_e(\omega) = \frac{\Delta\chi_e}{1 + j\frac{\omega}{\omega_0}}. \tag{2.41}$$

$\Delta\chi_e$ is the difference between the electric susceptibility for $\omega \to 0$ and for $\omega \to \infty$. ω_0 is the angular frequency at which the relaxation occurs and where the value of $\Im(\chi_e)$ is maximum.

Eqn. (2.41) can be augmented with additional parameters [HW03] leading to the Havriliak-Negami equation:

$$\chi_e(\omega) = \frac{\Delta\chi_e}{(1+(j\frac{\omega}{\omega_0})^{\alpha})^{\beta}}. \tag{2.42}$$

This formula allows a better description of real relaxation processes by introducing the paramters α and β, both in the range between 0 and 1. For $\alpha = \beta = 1$, one obtains the Debye equation (Eqn. (2.41)) and for $\beta = 1$ and $0 < \alpha < 1$ the Cole-Cole relation. By adjusting α, the characteristic of the relaxation can be made broader and the parameter β influences its symmetry. Regardless which process is involved, the dielectric loss always increases strongly around the respective frequency (see Fig. 2.8). This increase is the stronger, the higher the permittivity drop across the respective ω_0 is. Eqns. (2.41) and (2.42) can be generalised in order to account for multiple processes as given in Eqn (2.43).

$$\chi_e(\omega) = \sum_i \frac{\Delta\chi_{e,i}}{(1+(j\frac{\omega}{\omega_{0,i}})^{\alpha_i})^{\beta_i}}. \tag{2.43}$$

The fact that the dielectric dispersion of LCs at frequencies up to 1 GHz is governed by relaxation processes is a well established fact [DGG+99, HW03]. In Fig. 2.9, a simplified diagram of the relaxation characteristics is shown.

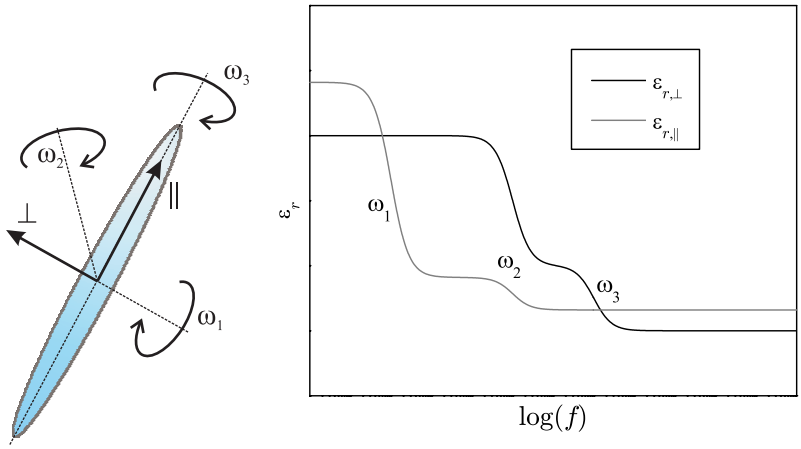

Figure 2.9: Simplified dispersion diagram of nematic LC (after [GDG+98a]). (a) The molecular rotational modes, (b) the corresponding dispersion characteristic

The angular frequencies ω_1 and ω_3 are associated with rotations around the short and the long axis of the molecule, respectively. In some LC compounds, further rotational modes around other axes can also be identified (ω_2). In general, $\omega_1 \ll \omega_2 < \omega_3$. The actual value of these frequencies is determined by molecular or dipolar interaction, respectively.

Many nematic LC molecules have a strong dipole moment in parallel to the long axis of the molecule. But as nematic LCs feature orientational order, defined by the director $\vec{n}$ with a mirror symmetry with respect to a plane on which $\vec{n}$ is perpendicular concerning all its physical properties, no net polarisation exists. On the molecular level, this can be understood by the fact that the molecules are in parallel but pointing randomly up and down. If an electric field is applied in parallel to the director, assuming that the molecules feature a permanent dipole along the molecule's long axis, those molecules oriented with their dipole in an unfavourable direction with respect to the electric field will start to align with the field by rotating by 180° around the short axis [GP93, RSGK96]. This process is described by diffusion laws and happens against the nematic potential [HW03]. The latter is also, beside the larger inertia around that axis, a reason why this process around the short axis usually relaxes at very low frequencies (several 10 kHz or less, depending on he molecule structure). It is also worth noting that the collective reorientation of the director is governed by completely different dynamics which also occur on a much longer time scale compared to ω_1.

In case the electric field is perpendicular to the molecule long axis, rotational diffusion is excited around the long axis. The excitation of this mode depends strongly on the dipole moment perpendicular to the molecule long axis. This rotational mode relaxes, as hinted previously, at much higher frequencies (up to the GHz range) as the inertia around the long axis is much smaller and no nematic potential has to be overcome. Depending on the angle the effective molecular dipole has with the molecule axis, also negative anisotropies can occur at angular frequencies $<\omega_1$. Certain compounds have a strong dipole moment perpendicular to the long axis and therefore feature such negative anisotropy at low frequencies.

The relaxation processes ω_1 to ω_3 depend, in general, strongly on temperature. The relaxation times $\tau = \omega^{-1}$ follow the Arrhenius law, but are also influenced by the order parameter. The actual values of the parallel and perpendicular permittivity depend on temperature as the order parameter depends on temperature. However, resonant atomic processes as shown in Fig. 2.8 show no or only little temperature dependence [ST07].

Chapter 3

Characterisation of LCs and LC Composite Materials

In this chapter, several approaches are presented which all aim for an enhancement of various properties of microwave devices based on LC material. On the one hand, these are investigations on porous PTFE membranes impregnated with LC which are supposed to accelerate the response time of respective devices as well as to make the handling of the tunable material LC itself more convenient. On the other hand, LC mixtures are investigated with particular focus on the relationship between chemical composition and microwave properties. Particularly, studies are carried out, which parameters in the composition of LC mixtures are important for optimising LC mixtures for microwave applications. Furthermore, LC loaded with carbon nanotubes is analysed which represents another interesting approach to the optimisation of LC for microwave devices.

3.1 LC Mixtures and Nano-Composites

In this section, the systematic evaluation of various nematic LC mixtures is presented. The aim was to identify mixtures with superior microwave properties, i.e. with high tunability and low loss. The cavity perturbation method was used for characterising the individual mixtures as this technique offers high precision and can also be used for the investigation of the temperature dependence of the dielectric properties. The underlying principle of the cavity perturbation method will therefore be reviewed briefly in the following.

3.1.1 The Cavity Perturbation Method

The cavity perturbation method belongs to the class of the resonant perturbation methods for material characterisation [CON+04, COT99]. It assumes that a resonant cavity with a complex angular resonance frequency ω_c is perturbed by a small material sample which causes the resonance frequency to shift by $\Delta\omega$ to ω_s. In this work a cavity operated in the TE_{101} mode is used. The measurement principle is shown in Fig. 3.1 with the respective mode and the dimensions of the cavity indicated. The tube in the center of the structure represents the sample and has the diameter d. The method is applicable if the conditions $d \ll a$ and $d \ll l$ are fulfilled.

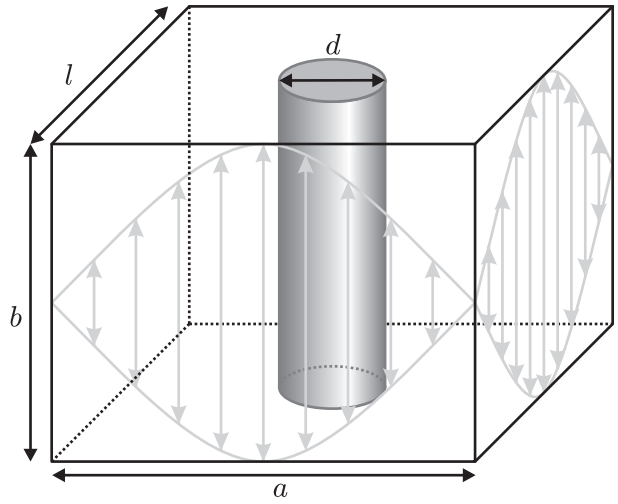

Figure 3.1: Principle of the employed perturbation of a resonant cavity.

For a nonmagnetic material the relative frequency shift is given by

$$\frac{\Delta\omega}{\omega_c} = \frac{\int_{V_s} (E_s \cdot D_c - E_c \cdot D_s) dV}{\int_{V_c} (E_c \cdot D_s - H_c \cdot B_s) dV} \tag{3.1}$$

V_s and V_c are the volumes of the sample and the cavity, respectively. E_s, D_s and B_s are the electromagnetic fields of the cavity with the perturbing sample inserted. E_c, D_c and H_c are the respective field quantities of the unperturbed cavity. All field quantities are treated as complex phasors. The only simplifying assumption made in Eqn. (3.1) is that the walls of the cavity are perfect conductors, which is for metallic cavities usually a justified assumption [Car01]. Otherwise Eqn. (3.1) holds without any restriction. The problem is that a full-wave evaluation in terms of the unknown perturbing material is necessary in order to evaluate Eqn. (3.1) which is in general neither fast nor precise due to meshing inaccuracies. Therefore, further assumptions must be made in order to simplify Eqn. (3.1) and make it analytically accessible.

The first assumption is that the electric displacement current D can be expressed in terms of E and the samples' $\varepsilon_{r,s}$. This affects only the numerator of Eqn. (3.1). The second assumption is that the influence of the sample on the electric field outside the sample is negligible and that furthermore the influence of the $D_s \neq D_c$ inside the sample is negligible. This allows to rewrite the denominator as the total energy of the unperturbed cavity, eventually leading to

$$\frac{\Delta\omega}{\omega_c} = -\frac{\Delta\varepsilon_r \int_{V_s} (E_s \cdot E_c) dV}{2\varepsilon_{r,c} \int_{V_c} (E_c \cdot E_c) dV} = -\frac{\Delta\varepsilon_r \int_{V_s} (E_s \cdot E_c) dV}{2\varepsilon_{r,c} \int_{V_c} |E_c|^2 dV} \tag{3.2}$$

with $\varepsilon_{r,c}$ being the relative permittivity of the cavity volume (usually one), and $\Delta\varepsilon_r$ the difference between the sample permittivity $\varepsilon_{r,s}$ and $\varepsilon_{r,c}$. The final assumption made is that the perturbing sample is small enough compared to the wavelength so that the electric field in the sample does not deviate from the field distribution without sample, i.e. $E_s = E_c$ in the entire volume. Then Eqn. (3.2) rewrites as

$$\frac{\Delta\omega}{\omega_c} = -\frac{\Delta\varepsilon_r \int_{V_s} |E_c|^2 dV}{2\varepsilon_{r,c} \int_{V_c} |E_c|^2 dV} = C\frac{\Delta\varepsilon_r}{2\varepsilon_{r,c}} \tag{3.3}$$

which can be interpreted such that the relative change in the permittivity is proportional to the relative change in the resonance frequency. The integrals represent the ratio between the energy in the sample volume and the energy in the entire unperturbed cavity.

The complex angular resonance frequency shift $\Delta\omega$ can be expressed as

$$\frac{\Delta\omega}{\omega_c} = \frac{\Re(\omega_s - \omega_c)}{\Re(\omega_c)} - j\left(\frac{\Im(\omega_c)}{\Re(\omega_c)} - \frac{\Im(\omega_s)}{\Re(\omega_s)}\right) = \frac{\Re(\omega_s - \omega_c)}{\Re(\omega_c)} - j\frac{1}{2}\left(\frac{1}{Q_c} - \frac{1}{Q_s}\right) \tag{3.4}$$

with Q_c and Q_s being the respective intrinsic quality factors of the resonator. This expression assumes that $\Re(\omega_c) \approx \Re(\omega_s)$ and that $\Im(\omega_{c,s}) \ll \Re(\omega_{c,s})$. The general quality factor of a resonator is given by (see [Col92, CON$^+$04, Poz04])

$$Q = \frac{\Re(\omega_0)}{2\Im(\omega_0)}. \tag{3.5}$$

Q is the so called loaded quality factor of the respective resonator which includes the influence of the coupling. At the resonance angular frequency, the transmission of a weakly coupled resonator is $|S_{21}| = 4k^2/(1+2k)^2$ with k being a coupling factor which relates the loaded quality factor Q to the unloaded, that is intrinsic, quality factor Q_0 according to $Q_0 = Q/(1+2k)$ [CON$^+$04].

The characterising parameters of a resonator can be found by fitting Eqn. (3.6) to the measured $|S_{21}|$ [SF63].

$$|S_{21}| = \frac{4k^2}{(1+2k)^2 + Q_0^2\left(\frac{\omega}{\Re\{\omega_0\}} - \frac{\Re\{\omega_0\}}{\omega}\right)^2}. \tag{3.6}$$

Eqn. (3.6) contains the three parameters k, Q_0 and $\Re(\omega_0)$ the latter two of which can be used directly in Eqn. (3.4). The function is fitted to the measurement within the 3 dB bandwidth in order to assure that dispersion of the coupling has as little influence on the curve as possible. The formula assumes symmetric coupling.

3.1.2 Measurement Setup

The application of cavity perturbation method to the characterisation of liquid crystals follows [Mül07] and [PMS+04]. Furthermore, the actual characterisation setup was enhanced in order to be able to characterise more LC samples in considerably less time while increasing the accuracy at the same time. Fig. 3.2 shows a schematic of the cavity used in this work.

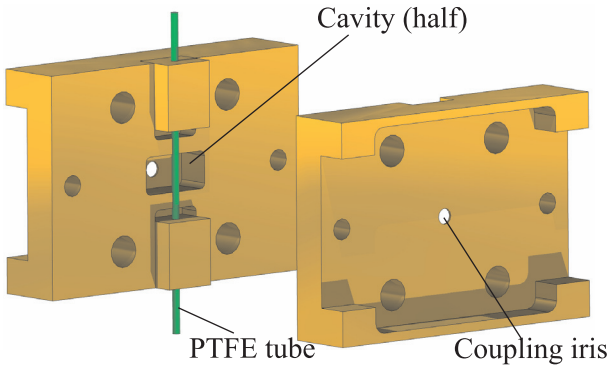

Figure 3.2: Schematic of the used resonator setup. The cavity is directly milled into a brass solid. The surfaces of the cavity are gold plated in order to enhance the quality factor of the resonator.

As indicated in Fig. 3.2, a PTFE tube[1] is used to hold the LC in the cavity. Given that the theory presented in the previous section only considers a homogeneous (and isotropic) sample, the method has to be modified in order to account for the presence of the PTFE tube. This can be done by assuming that the empty resonance, i.e. the one resulting in ω_c is measured with the empty PTFE tube inserted in the cavity. This, however, will change the energy term in the denominator in Eqn. (3.3). Under the assumption that the small volume of the PTFE tube and

[1] Zeus Inc. PTFE Tubing, AWG 30 Light Weight Wall (inside diameter nominally 380 µm, wall thickness nominally 200 µm)

also its low relative permittivity ($\varepsilon_r = 2$) do not disturb the electric field in the resonator, Eqn. (3.3) can be rewritten as follows:

$$\frac{\Delta\omega}{\omega_c} = -\frac{\Delta\varepsilon_r \int_{V_s} |E_c|^2 dV}{2\varepsilon_{r,c} \int_{V_c} |E_c|^2 dV + (\varepsilon_{r,t} - \varepsilon_{r,c}) \int_{V_t} |E_c|^2 dV} \tag{3.7}$$

V_t is the volume of the tube and $\varepsilon_{r,t}$ is the relative permittivity of the tube. It should be noted that the V_s volume only encompasses the LC volume, i.e. not the containing tube. All integrals can be solved numerically (see [Mül07]) and Eqn. (3.7) is finally solved for the sought after sample permittivity.

As the cavity perturbation method assumes isotropic samples, it has to be made sure that the LC is aligned in the tube such that the principal axes of the LC align with the electric field of the resonance mode. Fig. 3.3 illustrates how the parallel and the perpendicular permittivity ($\varepsilon_{r,||}$ and $\varepsilon_{r,\perp}$) can be measured by applying a strong magneto static field ($\approx 0.5\,\mathrm{T}$) parallel and perpendicular to the tube.

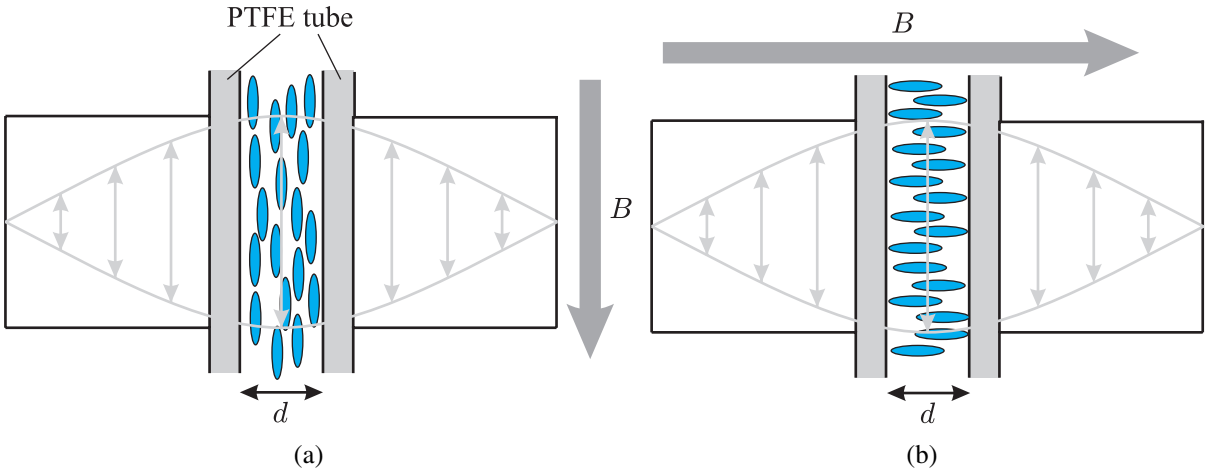

Figure 3.3: The alignment of the LC director with respect to the resonant field using a strong magnetic field: (a) Parallel, (b) perpendicular

Measurements were conducted with a cavity resonating at 30 GHz with the dimensions of $a = 7.11\,\mathrm{mm}$, $b = 3.56\,\mathrm{mm}$, $l = 6.6\,\mathrm{mm}$ and $d = 0.7\,\mathrm{mm}$. The inner diameter of the tube is $d_{LC} = 0.36\,\mathrm{mm}$. This value was determined by measuring the dimension under a microscope. Fig. 3.4(b) shows a photograph of the entire automated characterisation setup with temperature control and a remote controllable permanent magnet setup. The magnets have a specified magnetic field of 1.29 T (N40) [Neo]. Three magnet discs with a diameter of 10 cm and a thickness of 15 mm were stacked on either side of the cavity in order to increase the magnetic field. Temperature control is achieved by using a thermostat which heats/cools a synthetic oil which in

turn delivers the temperature to the resonator block. Fig. 3.4(a) depicts the resonator block with attached coaxial to WR-28 waveguide transitions and installed in the heating/cooling system outside of the magnet setup right before it is inserted into the magnet field. In Appendix C, a schematic is given showing the magnet setup in more detail.

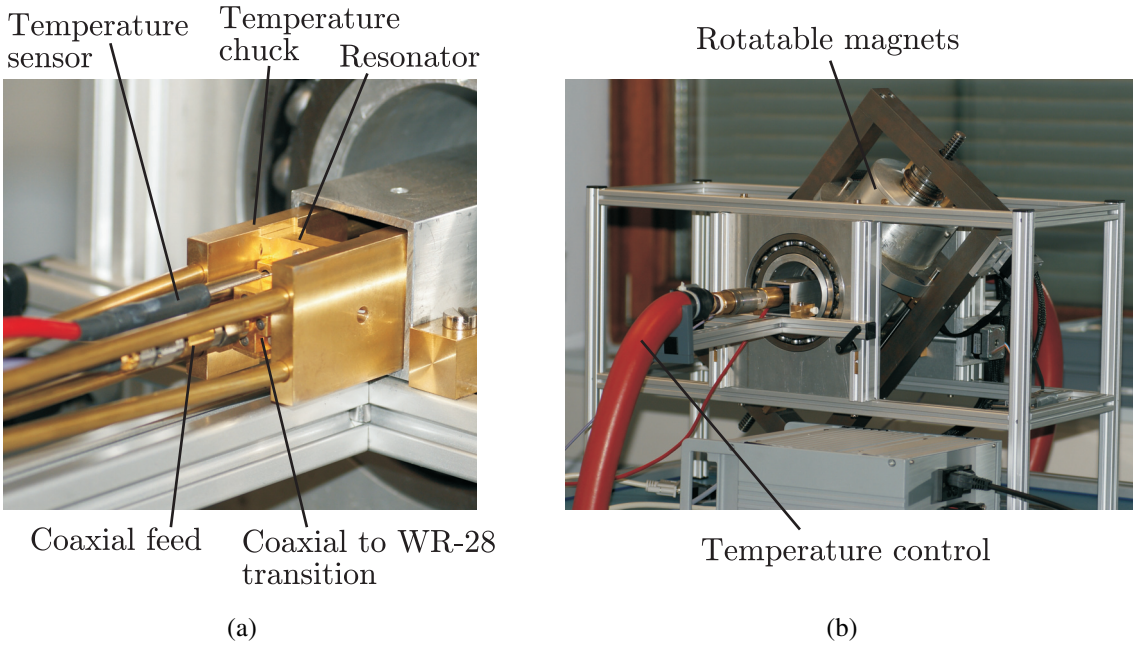

Figure 3.4: (a) The resonator including temperature chuck about to be inserted in the magnet setup. (b) The entire setup. The magnet setup allows arbitrary rotation of the magnetic field (remote controllable) and also, to some extent, control of the magnetic field strength by adjusting the distance of the magnets.

The setup allows basically two different measurement strategies: The first, which was used for most materials, heats the LC up to a defined maximum temperature and aligns the LC at this temperature. This is beneficial as the viscosity at higher temperatures is much lower and ordering by an external magnetic field is therefore more effective and faster. Once the maximum set temperature is reached, the LC is cooled down meanwhile measurements are being taken approx. every three seconds. This is done by tracking the resonance frequency and recording the S_{21} parameter in a narrow interval around the resonance frequency which enables to do the parameter fitting according to Eqn. (3.6) in order to obtain the exact resonance frequency and the quality factor of the resonance. Once one orientation is finished, the magnetic field is reoriented and the procedure is repeated. As indicated previously, the reference measurement yielding ω_c and Q_c is taken with an empty PTFE tube inserted in the cavity. This reference measurement is also performed vs. temperature as the cavity size changes with temperature and hence the resonance frequency changes. Also the conductivity of the cavity walls change which impacts on the quality factor.

For the second measurement strategy the LC is cooled down to the minimum required temperature and then heated stepwise. At each defined temperature step, the parallel and perpendicular measurement is taken in direct succession by turning the magnet field accordingly.

An estimation of the error of the cavity perturbation measurements can be found in [Mül07]. Here, the error in permittivity was found to be at most $\pm 5\,\%$ and in the loss tangent at most $\pm 20\,\%$ for typical values of LCs. These errors are, by nature, predominantly systematic as they arise particularly from the imprecisely known geometric dimensions of the cavity and the LC containing tube. The repeat accuracy is much higher if the same setup and particularly the same type of tube is used for each measurement. The latter is given for the measurements presented in this chapter. In terms of the error introduced by the hole through which the PTFE tube is inserted, in [BE60] and [LB82] it is shown that the hole in the cavity has negligible influence if the hole is small enough. The dimensions used in this work can be assumed to introduce less than 10 % additional sytematic error due to the influence of the insertion hole.

3.1.3 Microwave Anisotropy and Loss

The LC material investigated in the scope of this work can be divided into three groups: Nematic LCs with knowledge about the chemical constituents, nematic LCs without knowledge about the chemical properties but optimised externally in terms of microwave performance and lastly, nematic LCs with suspensions of carbon nano-tubes (CNTs). In this section, the investigation of nematic LC mixtures is presented with special focus on the dependency of the microwave performance on the specific chemistry. Results of specially optimised mixtures are presented then in section 3.1.4 and results of nematic LC loaded with Carbon Nanotubes are presented in section 3.1.5.

As an example measurement, the results for the commercially available LC 5CB[2] are shown in Figs. 3.5(a) and 3.5(b). Figs. 3.5(c) and 3.5(d) show the derived values tunability τ_{LC} and material efficiency η_{LC}. The fact that the permittivities and the loss tangent are governed by the order parameter is clearly visible in the figures. Additionally, the loss tangent is increasing with temperature, an issue which will be addressed in more detail later on.

In the following, only the material performance parameters, i.e. tunability τ_{LC} and material efficiency η_{LC} are shown for the individual materials unless additional information can be gathered by considering also the permittivities and loss tangents. In fact, all LCs feature a relative perpendicular permittivity $\varepsilon_{r,\perp}$ of around 2.5 (± 0.1, at room temperature) and only differ substantially in the parallel permittivity $\varepsilon_{r,||}$.

[2] Distributed under the trade name K15 from Merck KGaA, Germany

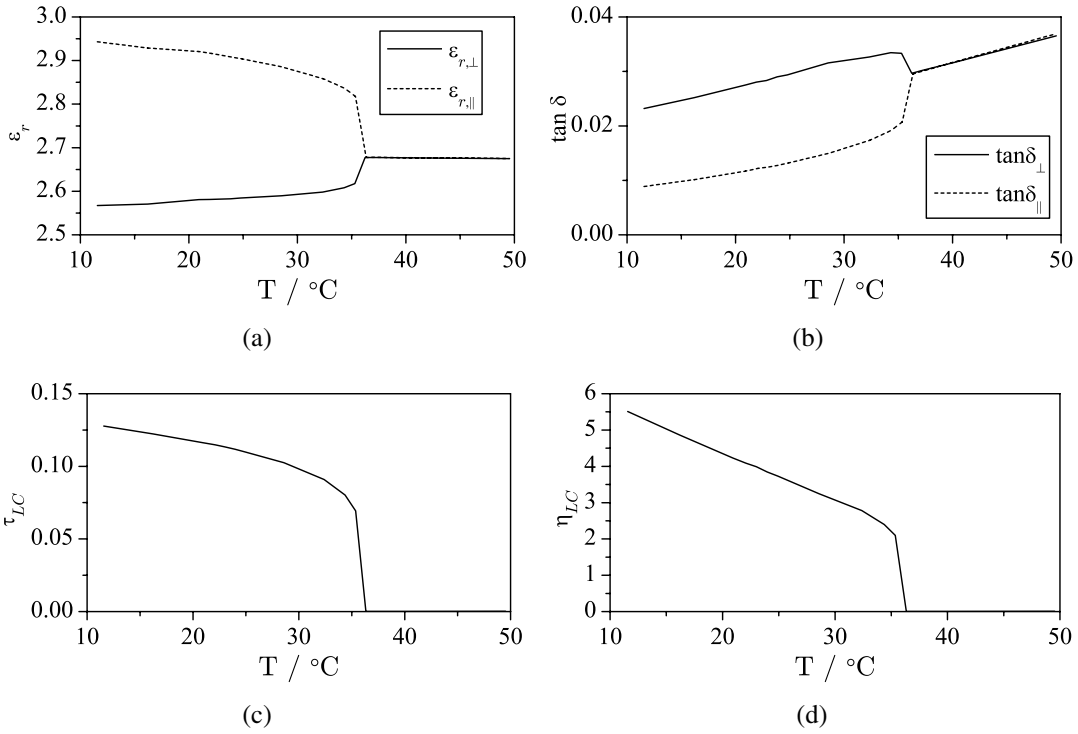

Figure 3.5: Extraction results of the LC 5CB: (a) The relative perpendicular and parallel permittivity, (b) the perpendicular and parallel loss tangent, (c) the tunability and (d) the material efficiency.

Selection of Compounds

In order to identify the chemical LC compounds which exhibit enhanced microwave performance, i.e. large anisotropy and low loss tangent, three base matrices were selected:

- 5CB, as a commercially available LC (Fig. 3.6(a))
- NCS[3] containing compounds based on p-alkyl-cyclohexyl-phenyl-thiorhodanides as a compound with high anisotropy at low frequencies [KW93] (Fig. 3.6(b))
- Tolanes[4], with high optical anisotropy but low anisotropy at low frequencies [KW93] (Fig. 3.6(c))

The symbol "A" in Figs. 3.6(b) and 3.6(c) represents alkyl groups. These base matrices consist of several molecules of the type in Figs. 3.6(b) and 3.6(c) but with different alkyl groups (see Appendix B) with varying concentrations.

Figs. 3.7(a) and 3.7(b) show the material performance parameters of all three base matrices with respect to temperature. The dielectric parameters at room temperature are given in Table. 3.1.

[3]The compound is characterised by the NCS endgroup, hence this description is used further on.

[4]The term Tolane is used here as the compound is characterised by a Diphenylacetylene (aka. Tolane) core.

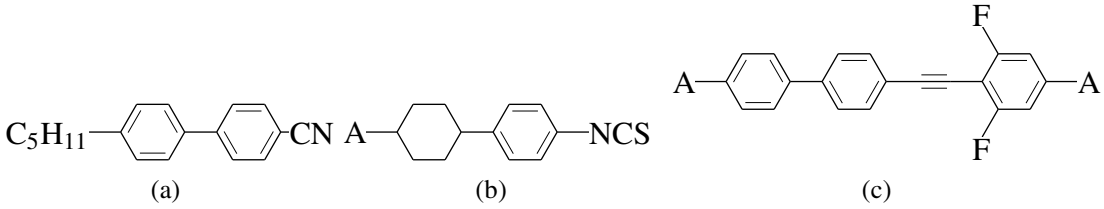

Figure 3.6: The three base matrices: (a) 5CB, (b) NCS (c) Tolane

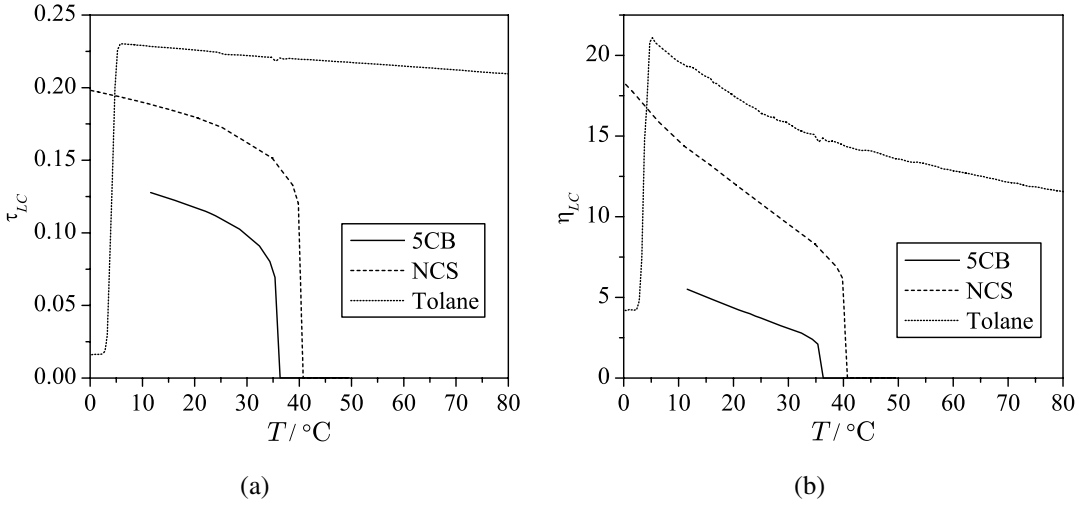

Figure 3.7: The material performance of the three base matrices: (a) The tunability and (b) the material efficiency.

Obviously, 5CB has only very limited microwave performance as was also shown in [Mül07]. Furthermore, the nematic range is very limited (only up to 36 °C, see also e.g. [Zel82]). However, due to its simplicity and the fact that it is available in arbitrary amounts, this compound is well suited for basic investigations, and will be used also later on in this work (Section 3.2). The other two mixtures show better or much better performance: The NCS-mixture has higher anisotropy and therefore higher tunability, also at low frequencies, and a wider temperature range. The Tolane mixture has the best performance, also in terms of temperature range. Nevertheless, this mixture has the two shortcomings of being limited towards low temperatures and furthermore of having low anisotropy at low frequencies (<1 kHz) which increases the necessary bias voltage

	$\varepsilon_{r,\perp}$	$\varepsilon_{r,\|\|}$	$\tan\delta_\perp$	$\tan\delta_{\|\|}$
5CB	2.58	2.91	0.0284	0.0124
NCS	2.43	2.94	0.0155	0.0096
Tolane	2.48	3.19	0.0133	0.003

Table 3.1: Dielectric parameters at room temperature for the three base matrices.

(see section 2.4.2). From that point of view, 5CB and the NCS mixture are clearly superior because they have large anisotropy at low frequencies.

In order to optimise the base matrices, several compounds were available as additives. It should be noted that the additives were chosen according to their solvability in the host material or according to whether the overall mixture builds a stable eutectic mixture. Also it is important to note that almost all of the additives do not form a nematic phase anywhere near room temperature. In fact, many additives have a melting point well above 100 °C. The mixtures are labeled according to their working names. The performance parameters of the evaluated mixtures are presented in the following, separated according to the respective base matrix. A summary, which will be referred to more often in this chapter, listing all important parameters at room temperature, is given in Table 3.2

Investigation of the dielectric anisotropy

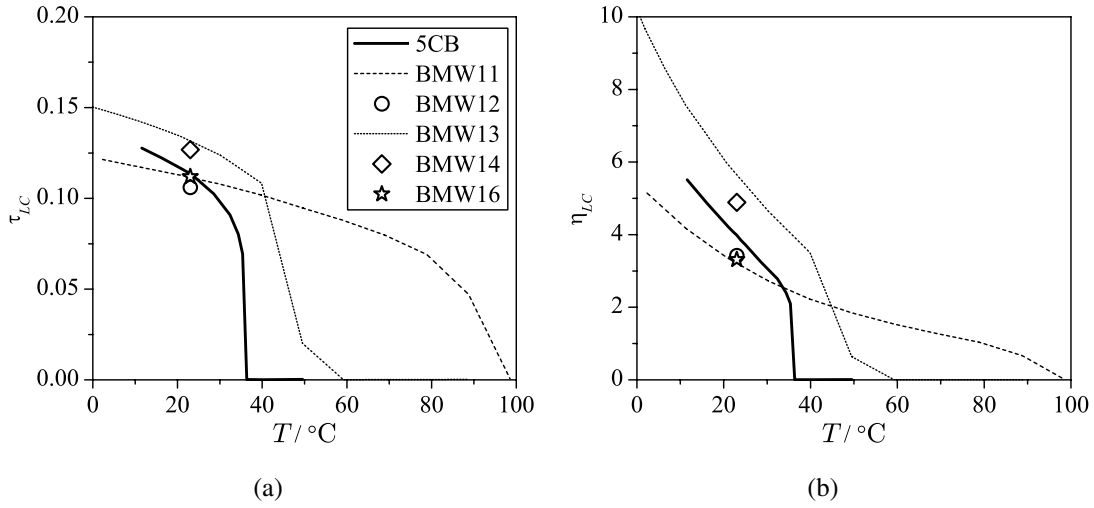

Figure 3.8: The material performance of the mixtures based on 5CB. (a) Tunability, (b) Material efficiency.

Fig. 3.8 shows the results of the evaluated mixtures based on 5CB. The aim was to obtain a LC mixture based on a very cheap and commercially available compound with enhanced properties by adding dopants. As can be seen, it is possible to improve the microwave performance, even if only limitedly. In addition, the operation temperature range can be expanded which can be understood when looking into the tables in appendix B. Only compounds with at least three rings are added which have in general a higher melting point.

In terms of performance, a clear improvement can be seen from BMW13. The compounds added to this mixture are C_9 and C_{10} which have much higher optical anisotropy than 5CB (>0.27). The compound C_{27} added to BMW14, on the other hand, features only little higher optical anisotropy (0.19) but obviously increases the anisotropy at optical frequencies as well as at 30 GHz. The

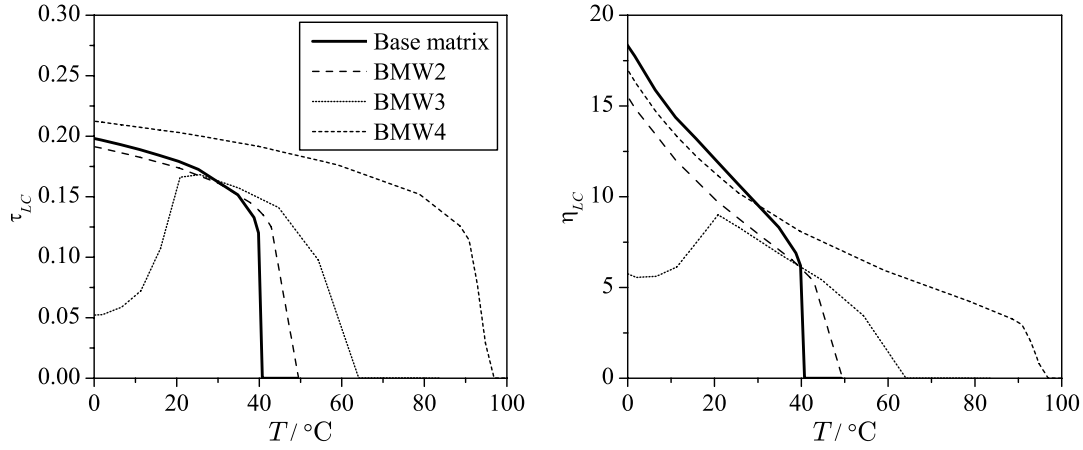

Figure 3.9: The material performance of the mixtures based on the NCS matrix. (a) Tunability, (b) Material efficiency.

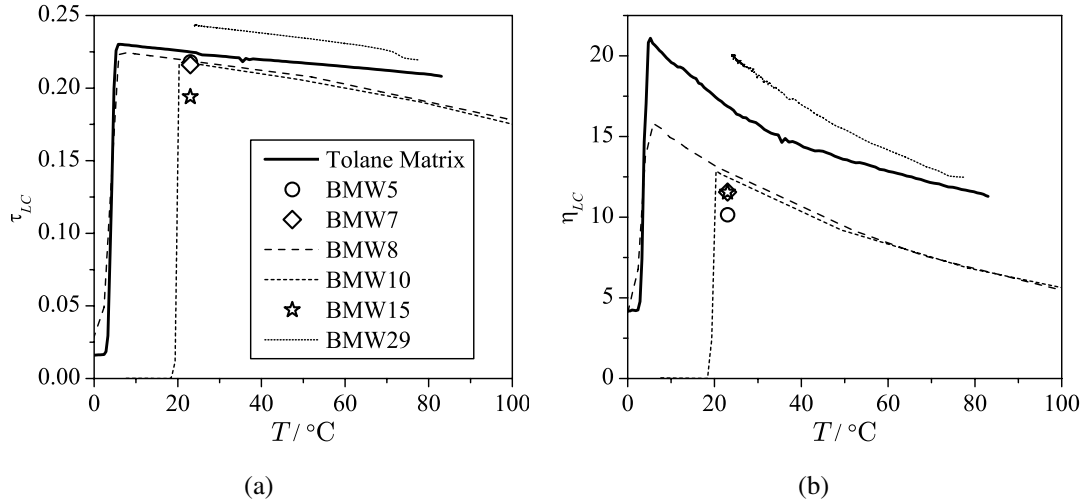

Figure 3.10: The material performance of the mixtures based on the Tolane matrix. (a) Tunability, (b) Material efficiency.

other mixtures based on 5CB, which show actually decreased performance, have partly additives with higher optical anisotropies but also with lower optical Δn compared to 5CB. Nevertheless, the overall optical anisotropy of the 5CB mixtures seems (at least in average) to indicate that an increased optical anisotropy leads to a higher GHz-anisotropy.

Looking at the NCS based mixture (Fig. 3.9), this observation is confirmed. The compounds added to mixtures BMW2 and BMW3 feature roughly the same optical anisotropy as the base mixture (around 0.17) which also does not influence the microwave anisotropy considerably.

The mixture BMW4, however, contains additives with high optical anisotropy (0.3) which also shows in the microwave anisotropy.

The Tolane base matrix, showing comparatively high performance in itself, was studied in more detail. LCs based on this matrix where already presented in [Mül07] but without focus on the chemical details or the relation between the optical anisotropy and the tunability at microwave frequencies. The optical and microwave anisotropy of the respective mixtures are listed in Table 3.3 and the chemical composition are also included in Appendix B. The reason for the high optical anisotropy is the Tolane triple bond [GDG+98b] which provides a large amount of relatively mobile charge which can contribute to the polarisation.

From Fig. 3.10, it can be seen that all mixtures, except BMW15 and BMW29, feature more or less the same tunability as the base matrix. Concerning BMW15, although the optical anisotropy is hardly diminished by the low Δn_{opt} additive C_{25}, the microwave anisotropy is strongly influenced. BMW29, on the other hand, uses exclusively quarterphenyles as additives which feature high optical anisotropy which in turn seems to influence the microwave anisotropy positively. In BMW10 a quarterphenyle additive is present, too, however, it is compensated by other low Δn_{opt} additives. The remaining mixtures BMW5, BMW7 and BMW21 use exclusively additives with much lower Δn_{opt}.

Taking the LHB mixtures into account, the influence of the quarterphenyles can be further confirmed. By looking at LHB-6 first it is again obvious that adding a low Δn_{opt} (LM2F-1) compound the optical anisotropy is diminished. This also has a slight effect on the microwave tunability as can be seen from Table 3.3[5]. LHB-13 is similar as it mainly consists of LHB-6. LHB-16 to LHB-18 use exclusively quarterphenyle additives which gives them higher optical anisotropy which is also reflected in the microwave tunability but the change is relatively small. In terms of chemical composition, LHB-16 to LHB-18 and BMW29 are very similar which is reflected in a very similar performance.

From the above made observations, it is difficult to establish an immediate dependency of the microwave tunability on the optical anisotropy, at least when comparing the 5CB and the NCS base matrices. Nevertheless, the Tolane matrix has high optical anisotropy and high microwave tunability. Furthermore, it can be seen from the NCS and the 5CB base matrices that an increase of the optical anisotropy can lead to an increased microwave tunability. For the Tolane base matrix it is rather difficult to identify these effects as the level of anisotropy is anyway rather high. It can however be concluded that the low frequency anisotropy does not influence the microwave anisotropy.

[5]The characterisation frequency for these mixtures was 38 GHz and the values are therefore directly comparable to those presented in Table 3.2.

	Base matrix	$\varepsilon_{r,\perp}$	$\varepsilon_{r,\|\|}$	τ_{LC}	$\tan\delta_\perp$	$\tan\delta_{\|\|}$	Δn (GHz)	Δn (opt.)	$\Delta\varepsilon_r$ (1 KHz)
5CB	*Base*	2.58	2.91	0.11	0.0284	0.0124	0.10	0.18	12
BMW11	5CB	2.55	2.87	0.11	0.0349	0.0103	0.10	0.17	11.3
BMW12	5CB	2.53	2.83	0.11	0.031	0.0145	0.09	0.21	10.5
BMW13	5CB	2.51	2.89	0.13	0.0234	0.0096	0.12	0.26	11.6
BMW14	5CB	2.48	2.84	0.13	0.0259	0.0098	0.11	0.26	12.9
BMW16	5CB	2.54	2.86	0.11	0.0338	0.0104	0.10	0.21	8.5
NCS	*Base*	2.43	2.94	0.17	0.0155	0.0096	0.16	0.17	7.7
BMW2	NCS	2.44	2.95	0.17	0.0185	0.0101	0.16	0.17	9.7
BMW3	NCS	2.47	2.97	0.17	0.0193	0.0098	0.15	0.17	10.8
BMW4	NCS	2.43	3.04	0.20	0.0188	0.0087	0.18	0.22	7.5
Tolane	*Base*	2.48	3.19	0.22	0.0133	0.003	0.21	0.34	-
BMW5	Tolane	2.4	3.07	0.22	0.0215	0.0049	0.20	0.3	0.2
BMW7	Tolane	2.43	3.1	0.22	0.0187	0.0044	0.20	0.32	8.4
BMW8	Tolane	2.43	3.11	0.22	0.0172	0.0042	0.20	0.33	3.9
BMW10	Tolane	2.49	3.18	0.22	0.0175	0.0043	0.21	0.33	6.25
BMW15	Tolane	2.41	2.99	0.19	0.0168	0.0057	0.18	0.32	4.6
BMW21	Tolane	2.55	3.05	0.16	0.0359	0.0113	0.15	-	-1.5
BMW29	Tolane	2.44	3.22	0.24	0.0122	0.0039	0.23	-	-

Table 3.2: Various dielectric parameters at room temperature.

	Δn (opt.)	τ_{LC}	η_{LC}	$\Delta\varepsilon_r$ (1 KHz)
LHB-6	0.32	0.21	10.3	4.8
LHB-13	0.33	0.2	16.7	4.4
LHB-16	0.37	0.23	20.8	4.0
LHB-17	0.37	0.23	20.3	1.0
LHB-18	0.4	0.22	21.0	2.6

Table 3.3: Further nematic LCs based on the Tolane matrix and their microwave properties at 38 GHz. Values at room temperature taken from [Mül07]. Only the aggregated values (τ_{LC}, η_{LC}) are available.

Investigation of the perpendicular dielectric loss

So far only the anisotropy of the investigated materials was discussed. The other important factor, the dielectric loss will be addressed in the following. Starting again from the 5CB mixtures, it can be seen from Table 3.2 that some additives add loss to $\tan\delta_\perp$ (BMW11, BMW12, BMW16) and some decrease the loss (BMW13, BMW14). Concerning the parallel loss $\tan\delta_{||}$, a dedicated discussion will be given further below as it is always considerably smaller than $\tan\delta_\perp$. Both LCs featuring a decrease in the loss tangent have additives with four rings. Why this is an important factor, will be discussed in detail further below. In case of the NCS based mixtures, the used additives increase the loss without exception. The additives consist of 3-ring structures (except for C_{18} which has a mass fraction of only 4 %).

As the Tolane base matrix has already rather low loss, the impact of the additives can yield valuable information. From Table 3.2 (and also Fig. 3.10(b)), it is obvious that the loss is increased except for BMW29. The latter mixture uses as additives only quarterphenyles which were also suspected to improve the loss in the 5CB mixture BMW13. Table 3.3 confirms that LHB-16 to LHB-18 have high η_{LC} with the tunability almost being the same as that of the base mixture. LHB-6 in turn does not contain any quarterphenyles and has approx. twice the loss of e.g. LHB-16. LHB-13, being 91 % LHB-6 with 9 % quarterphenyles has an improved η_{LC} and therefore a lower $\tan\delta_\perp$.

In order to investigate the origin of the dielectric loss, i.e. both $\tan\delta_\perp$ and $\tan\delta_{||}$, further analysis is necessary. Starting with $\tan\delta_\perp$, it is interesting to understand the impact of the dispersion of the perpendicular permittivity, especially as the relaxation frequency of the rotation around the molecule long axis can be rather high. The investigation of the lower frequency dispersion can be done using e.g. capacitive methods. For this works purpose, the capacitors which will be introduced in section 4.2 were employed.

In the scope of this work, first two nematic LCs with known pronounced relaxation effects were investigated: 5CB (see above) and the very similar LC E7. E7 is a commercial mixture which consists partly of 5CB plus terphenyle additives [LKS+98]. The microwave behaviour in terms of the aggregated performance parameters at 30 GHz is shown in Fig. 3.11. E7 has slightly higher tunability and slightly lower loss but with $\eta_{LC} \approx 5.6$ at room temperature the overall performance is only little higher than that of 5CB. The main advantage of E7 compared to 5CB is that it allows investigations over a larger temperature range.

The Havriliak-Negami formula in Eqn. (2.42) is used for performing a data fitting to the permittivity dispersion extracted from capacitive measurements. Only a single relaxation process is considered here which yields the following formula for the frequency dependent $\varepsilon_{r,\perp}$:

$$\varepsilon_{r,\perp}(\omega) = \varepsilon_{r,\perp,\infty} + \frac{\Delta\varepsilon_{r,\perp}}{(1+(j\frac{\omega}{\omega_0})^{\alpha_r})^{\beta_r}}. \tag{3.8}$$

$\varepsilon_{r,\perp,\infty}$ is the relative permittivity for $\omega \to \infty$. Figs. 3.12(a) and 3.12(b) show examples of the data fitting for various temperatures for both LCs and demonstrate the temperature dependency

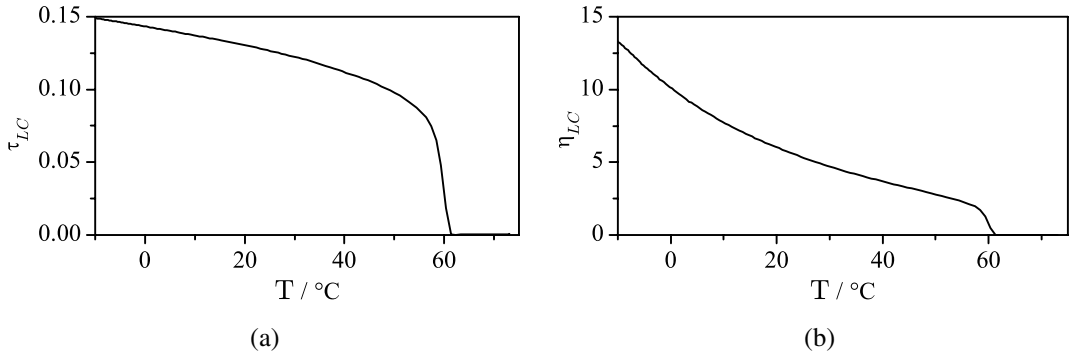

Figure 3.11: Microwave behaviour of E7 at 30 GHz. (a) The tunability, (b) the material efficiency.

of the material. The range which is fitted with the measured data goes up to 500 MHz and down to the lowest recorded frequency. The maximum frequency was chosen low enough in order to avoid influence of the series resonance of the capacitors. As can be seen from Figs. 3.12(a) and 3.12(b) data fitting is possible with excellent agreement with the measured data for both LCs. Fig. 3.12(c) depicts the characteristic of the relaxation time $\tau = 1/\omega_0$. τ is plotted versus the inverse temperature. From Fig. 3.12(c) it can be seen that in the isotropic phase the relaxation frequency follows the Arrhenius law (see [HW03]). In the nematic phase, the characteristic is superimposed by the influence of the order parameter.

With the obtained temperature dependent parameters $\varepsilon_{r,\perp,\infty}$, $\Delta\varepsilon_{r,\perp}$, α_r and β_r, the values of $\varepsilon_{r,\perp}(30\,\mathrm{GHz})$ can be calculated using Eqn. (3.8). In other words, the complex permittivity extracted at below 1 GHz is extrapolated to 30 GHz. The loss tangent $\tan\delta_\perp$ is calculated according to $\tan\delta_\perp = \varepsilon''_{r,\perp}/\varepsilon'_{r,\perp}$. Fig. 3.13(a) shows these values for 5CB and Fig. 3.13(b) for E7. For 5CB it is obvious that the extrapolated curve resembles the real loss tangent at 30 GHz very much except for an offset. Particularly, the slope of the curves is the same.

However, the extrapolated characteristic of E7 is less distinct. The reason for this is most likely that E7, unlike 5CB, is a mixture of different molecules, so more than one relaxation process may be present. Nevertheless, also with only one process as in the examples in Fig. 3.12(b) it can be shown that the slope of the extrapolated loss is very much the same as the real loss. That shows, just as for 5CB, that there is a strong relation between the relaxation processes around the molecule long axis and the loss even in the higher GHz-range.

Capacitive measurements were also conducted with the Tolane base matrix, which exhibit much lower loss compared to 5CB or E7. However, as can be seen from Fig. 3.13(c), there is hardly any temperature dependence in the range between 10 and 65 °C. In addition, there is no relaxation process identifiable down to 10 MHz. There is a slight drop of the permittivity versus frequency visible, but this can within the precision of the measurement not clearly be attributed to a LC related effect. With the given capacitive measurement facilities, the extraction of low loss materials like the Tolane base mixture is therefore more error-prone as then the metallic loss and the frequency dependency of the fringing fields of the capacitance play a larger role.

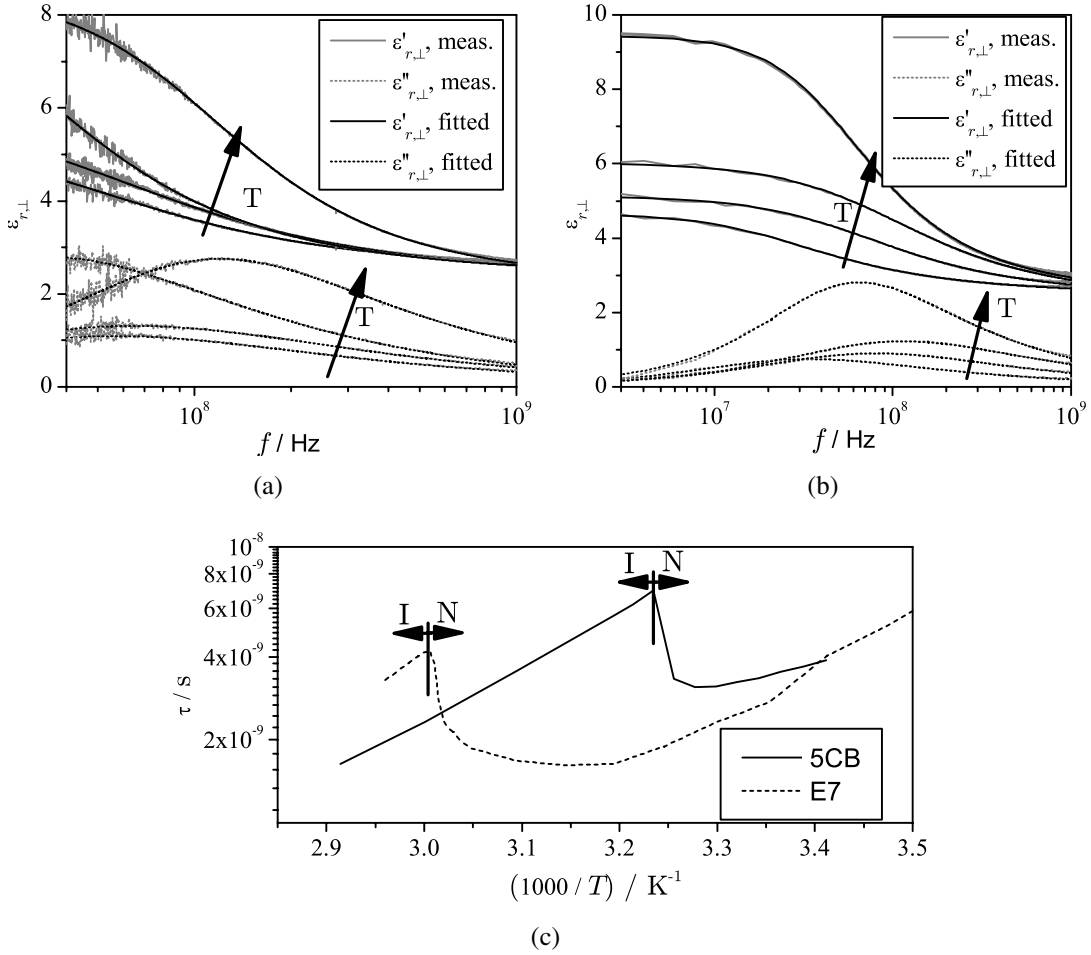

Figure 3.12: Examples for the data fitting of the complex permittivity extracted using a capacitive method. The arrows in (a) (5CB) and (b) (E7) indicate increasing temperature. Already here the temperature dependency of the relaxation process is clearly visible. 3.12(c) shows the relaxation time $\tau = 1/\omega_0$.

With the understanding obtained so far, it is interesting to revisit Tables 3.2 and 3.3 in terms of the perpendicular loss. From the findings presented above, it could be claimed, that the loss in the microwave region is influenced by the rotation around the molecule long axis; at least the temperature dependence of the lossy LCs 5CB and E7 shown above suggests that. Furthermore, the absence of a (visible and i.e. strong) relaxation process in the measurements of the Tolane base matrix seems to confirm this as this LC has considerably lower loss.

In [Jeu79], a comparison between different molecules with and without polar terminal groups is made. It can be seen there that a large $\varepsilon_{r,||}$ (at 1 KHz) produces also a larger $\varepsilon_{r,\perp}$ which is due to the projection of the permanent dipole along the molecule axis on the component perpendicular to the director. The latter argument assumes that a probing electric field is perpendicular to the director, which means that the not entirely ordered molecules will have a permanent dipole

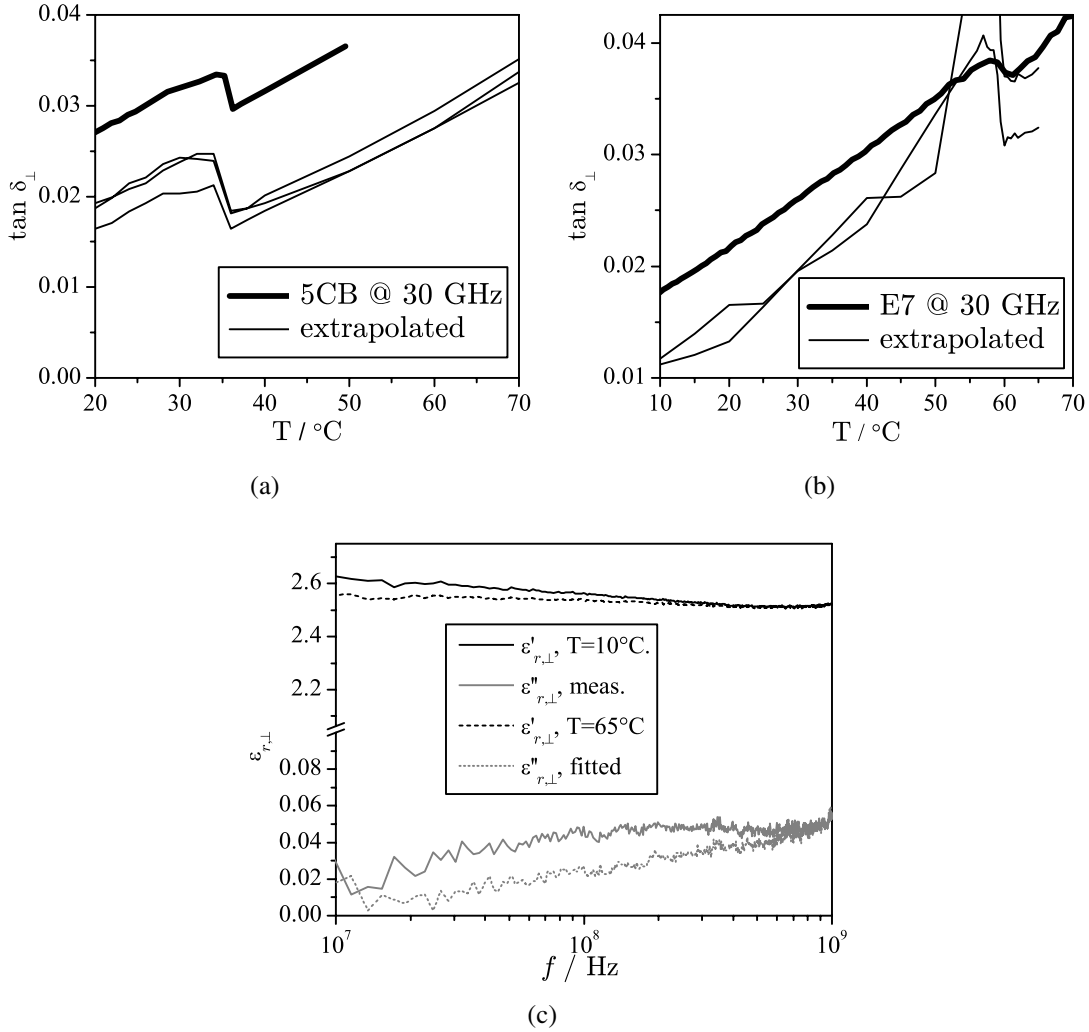

Figure 3.13: Extrapolated values for (a) 5CB and for (b) E7. The results for 5CB were obtained from three different capacitors and for E7 from two. Fig. 3.13(c) shows the measured results for the Tolane base mixture (without a fitted function).

also perpendicular to the director and hence the rotation around the long axis can be triggered. Relaxations around the long axis can, of course, also be triggered by a molecular permanent dipole perpendicular to the long axis. This permanent dipole moment is e.g. observed in LCs with strongly electronegative lateral substituents like Fluorine.

The simplest LC in the lineup above, i.e. 5CB, has a strong parallel dipole moment because of the terminal cyano (CN, also electronegative) group resulting in a 1 KHz $\varepsilon_{r,||}$ of around 20 [HW03, CDL75]. The respective $\varepsilon_{r,\perp}$ is around 6 as it can also be extrapolated from Fig. 3.12(a). As demonstrated, this leads to a strong dielectric response in terms of $\varepsilon_{r,\perp}$ in the lower GHz region. The influence of the real part of the permittivity decays rather quickly but the loss tangent is influenced also at 30 GHz. From all described so far, the assumption can be made

that the dielectric loss increases if constituent molecules have a strong permanent dipole along the long axis and/or perpendicular to the long axis. On the other hand, the loss decreases if the molecules are non-polar in either direction. Furthermore, it can be assumed that the more the relaxation around the long axis is shifted to low frequencies the lower the loss will be at microwave frequencies. In the following, all investigated LCs listed in Tables 3.2 and 3.3 are examined in terms of the validity of the so far made assumptions. The arrows in the column "Loss" indicate whether the loss is increased or decreased compared to the respective base matrix.

Mixture	Loss	Comment
5CB		CN group, i.e. large dipole moment, as described
BMW11	⇑	C_{20} has a CN terminal group plus a perpendicular dipole moment (COO, [RPP$^+$08], as has C_{22}) which increases the 1 kHz $\varepsilon_{r,\perp}$ and therefore the impact of the relaxation.
BMW12	⇑	Additives with strong perpendicular dipoles, i.e. stronger relaxation
BMW13	⇓	Quarterphenyle (C_{10}); Although it is slightly polar it can be speculated that relaxation frequency decreases due to its length.
BMW14	⇓	Decrease despite the lateral groups in C_{27}. Potentially because of the four ring structure.
BMW16	⇑	Increase because of C_{20} as in BMW11
NCS		Lower loss compared to 5CB. The NCS terminal group has a less strong influence compared to the CN group of 5CB. This can also be seen from the 1 KHz $\Delta\varepsilon_r$ (both 5CB and the NCS base mixture have no perpendicular dipole)
BMW2	⇑	The additive C_{28} has a strong dipole both along the molecule and perpendicular to it.
BMW3	⇑	For the additives C_{14} and C_{29} the same as for C_{28} holds true. The four ring additive C_{18} has only a weight percentage of 4 %.
BMW4	⇑	The increased loss most likely originates from additive C_3 with a strong perpendicular dipole.
Tolane		All molecules in this base matrix have virtually no dipole parallel to the molecules. The lateral electronegative fluorine atoms are balanced. The loss of this mixture is comparatively low.
BMW5	⇑	Both additives C_2 and C_8 have strong lateral dipoles. This is also reflected in the very low 1 kHz $\Delta\varepsilon_r$.
BMW7	⇑	C_{15} and C_{29} are both polar parallel and perpendicular to the molecule long axis.
BMW8	⇑	C_{33} has only a perpendicular dipole, C_{15} as in BMW7.
BMW10	⇑	Consists of 5CB and another polar molecule (C_{34}). The impact of the 7 % C_{10} (see BMW13) against 14 % seems not to suffice.
BMW15	⇑	C_{25} has mainly a large dipole moment parallel to the molecule due to the lateral fluorine atoms.

BMW21	⇑	This mixture uses the same additives as BMW5 but in higher weight percentages. The 1 kHz $\Delta\varepsilon_r$ is therefore negative and due to the intense excitation of rotations around the long axis the loss is very high.
BMW29	⇓	BMW29 uses only quarterphenyle structures as additives. As with BMW13 it can be speculated that the longer molecules have lower relaxation frequencies and hence their impact on the high frequency behaviour.
LHB-6	⇑	The added mixture LM2F-1 consists only of molecules with a parallel dipole moment.
LHB-13	⇑	LHB-13 is LHB-6 with 9 % of the weight replaced by a quarterphenyle structure which seems to decrease the loss considerably compared to LHB-6.
LHB-16 to LHB-18	⇓	All three mixtures have different quarterphenyle structures as additives and have very similar performance. LHB-18, having the best performance, has the highest weight percentage of these additives (30 %).

Table 3.4: Detailed analysis of the origin of $\tan\delta_\perp$ for all investigated mixtures.

The results listed in Table 3.4 confirm the assumption that polar molecules cause higher loss in the microwave region. Furthermore, molecules having four rings seem to decrease the microwave loss. Quarterphenyles particularly have positive effect on the loss. Long molecules potentially have lower relaxation frequencies as their interaction with neighboring molecules is stronger. According to the literature, the moment of inertia, which is of course higher for longer molecules, plays only a minor role. In fact, in many theoretical derivations the moment of inertia is completely neglected [CK93].

It should be noted that all the above described investigations hint that the influence of the relaxation is not the only one but rather that there is another polarisation process, or its loss mechanism, respectively, present which also contributes to the loss. This can be seen particularly from Figs. 3.13(a) and 3.13(b) in which the extrapolated loss is always lower than the real loss.

Investigation of the parallel loss

So far the parallel loss tangent $\tan\delta_{||}$ was not considered. If the origin of the parallel loss is to be explained, the relaxation processes are inadequate as they usually occur at frequencies below or well below 1 MHz [HW03] (see also section 2.5) and are, hence, at least two decades below the relaxation process around the long axis. With this larger distance to the GHz-region, the influence of a Debye-type relaxation becomes negligible compared to the process around the long axis.

What can already be seen from Table 3.2, i.e. that the parallel loss is always lower than the perpendicular loss but nevertheless correlated with it (high perpendicular loss means higher parallel

loss), will be highlighted further now. For that purpose, the ratio between the two loss tangents is defined according to

$$r_{\tan\delta,m} = \frac{\tan\delta_{\perp}}{\tan\delta_{||}}.$$

The subscript m indicates that measured quantities are considered. In Fig. 3.14 the characteristic of $r_{\tan\delta,m}$ is depicted for various LCs. The behaviour of especially 5CB and E7 suggests that the relation between $\tan\delta_{\perp}$ and $\tan\delta_{||}$ is determined by the order parameter S and therefore depends on temperature. In other words, the question must be answered whether $\tan\delta_{||}$ can be explained by the influence of $\tan\delta_{\perp}$ due to the imperfect ordering which causes the higher $\tan\delta_{\perp}$ to be seen by an electric field parallel to the director. As explained in section 2.3.2, the effective

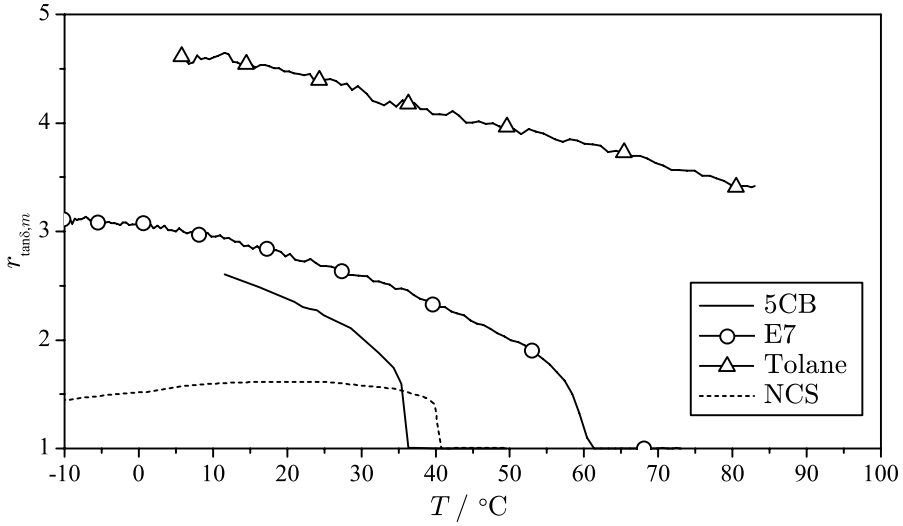

Figure 3.14: Measured values of $r_{\tan\delta,m}$ versus temperature for several LCs.

perpendicular and parallel relative permittivities can be expressed in terms of order parameter independent values ($\varepsilon_{r,\perp}^{S=1}$ and $\varepsilon_{r,||}^{S=1}$) and the order parameter S itself (Eqns. (2.18) and (2.19)). The permittivities $\varepsilon_{r,\perp}^{S=1}$ and $\varepsilon_{r,||}^{S=1}$ are assumed to be complex, i.e. with associated loss tangents $\tan\delta_{\perp}^{S=1}$ and $\tan\delta_{||}^{S=1}$. Eqns. (2.18) and (2.19) can then be rewritten as

$$\begin{aligned}\varepsilon_{r,\perp}(1-j\tan\delta_{\perp}) &= \frac{1}{3}\Big(\varepsilon_{r,\perp}^{S=1}(1-j\tan\delta_{\perp}^{S=1})(2+S) \\ &\quad +\varepsilon_{r,||}^{S=1}(1-j\tan\delta_{||}^{S=1})(1-S)\Big) \qquad (3.9)\\ \varepsilon_{r,||}(1-j\tan\delta_{||}) &= \frac{1}{3}\Big(\varepsilon_{r,\perp}^{S=1}(1-j\tan\delta_{\perp}^{S=1})(2-2S) \\ &\quad +\varepsilon_{r,||}^{S=1}(1-j\tan\delta_{||}^{S=1})(1+2S)\Big). \qquad (3.10)\end{aligned}$$

Because the influence of the perpendicular loss on the parallel loss is sought-after the order parameter independent parallel loss is assumed to be zero ($\tan\delta_{||}^{S=1} = 0$). Doing so, the ratio $r_{\tan\delta,t} = \tan\delta_{\perp}/\tan\delta_{||}$ (subscript t for theoretical) can be defined which, by separating Eqns. (3.9) and (3.10) in real and imaginary part, evaluates to

$$r_{\tan\delta,t} = \frac{\varepsilon_{r,||}(2+S)}{\varepsilon_{r,\perp}(2-2S)}. \tag{3.11}$$

The validity and the agreement with the measurements can best be evaluated with LC mixtures with known clearing points T_{NI} as the characteristic of the order parameter depends on T_{NI}. Fig. 3.15 depicts the theoretical behaviour according to Eqn. (3.11) together with three examples with known clearing points. The curves are adjusted such that T_{NI} coincides for all LCs. The values for $\varepsilon_{r,||}$ and $\varepsilon_{r,\perp}$ in Eqn. (3.11) are taken from the respective measurement and the value of S is calculated according to section 2.2.2.

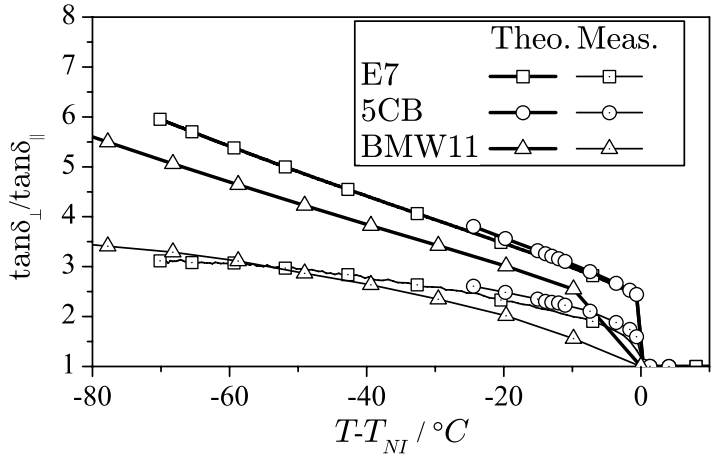

Figure 3.15: Comparison between the theoretical value of $r_{\tan\delta,t}$ and the measured $r_{\tan\delta,m}$.

From Fig. 3.15, it can be learned that approximately half of the parallel loss $\tan\delta_{||}$ is determined by the perpendicular loss as the measured curves show always approx. 50 % of the value of the theoretical curve. For the example of 5CB, it can be explicitly shown, using data from [HW03], that the parallel loss can not be explained by the relaxation around the short axis as the extrapolated loss tangent would amount to approx. $1 \cdot 10^3$ which is only a tenth of the measured loss at 30 GHz (compare also Fig. 3.5(b)). It must be therefore assumed that additional loss mechanisms are effective for $\tan\delta_{||}$ than only the projection of $\tan\delta_{\perp}$ due to the imperfect ordering. These can, for instance, be influences of other weak relaxation effects. Such relaxation effects have, due to their particular strength, experimentally been verified in [JCDL99] for exactly the same LC type as the NCS base matrix which differs from the behaviour of the other LCs rather strongly (Fig. 3.14). In the mentioned paper, it is found that the molecular structure of this specific compound features more complex relaxation processes. One process is even assumed to be around 1 GHz and the assumption that the parallel loss tangent of the perfectly ordered system (S=1) is zero is therefore definitely not valid.

Mixture	$\varepsilon_{r,\perp}$	$\varepsilon_{r,\parallel}$	τ_{LC}	$\tan\delta_{\perp}$	$\tan\delta_{\parallel}$
1	2.38	3.17	0.25	0.0063	0.0016
2	2.37	3.14	0.24	0.0054	0.0015
3	2.37	3.16	0.25	0.0059	0.0016

Table 3.5: Results of the three mixtures synthesised by Merck KGaA at room temperature.

The Tolane base matrix, not included in Fig. 3.15 as the precise clearing point is unknown, features a clearing point well above 140 °C which is one reason why the ratio is high at the investigated temperatures. An additional reason could be that the ordering in these systems is higher due to the longer molecules involved and that therefore the impact of the projected $\tan\delta_{\perp}$ is lower.

3.1.4 Optimised LC Mixtures

In the scope of this work, the opportunity was given to obtain LCs synthesised by the company Merck KGaA. The main aim of this synthesis was to influence $\tan\delta_{\perp}$ by reducing the relaxation frequencies around the long axis as much as possible. Furthermore, the polarity of the mixtures was kept as low as possible. Figs. 3.16(a) and 3.16(b) show the results of three high performance mixtures. The dielectric properties at room temperature are listed in Table 3.5. Looking at Fig.

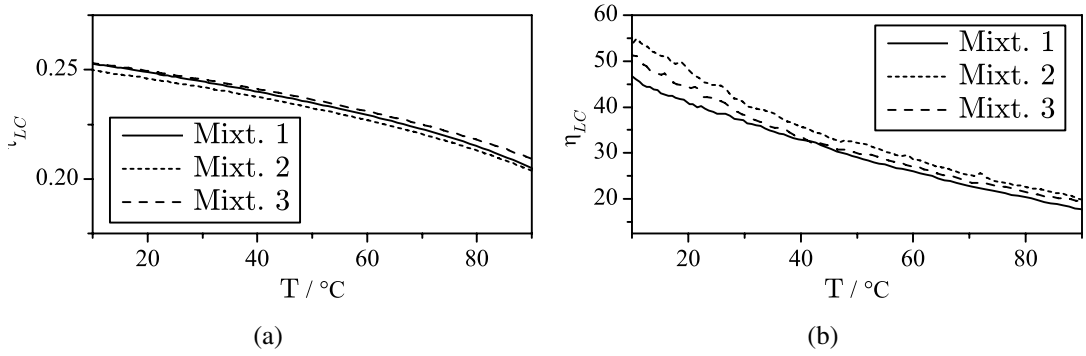

Figure 3.16: Result for three mixtures synthesised by Merck KGaA. The high performance stems from the very low loss. (a) Tunability, (b) efficiency.

3.16 and Table 3.5, it can be seen that the - compared to the other LCs investigated in this work and actually all so far reported LCs - very high microwave performance stems from the extremely low perpendicular loss tangent $\tan\delta_{\perp}$. This also confirms that the basic strategy for the optimisation of LCs has to be the mitigation of the influence of the relaxation processes.

3.1.5 Liquid Crystal Doped with Carbon Nanotubes

Carbon Nanotubes (CNTs) are nano particles which exhibit extreme shape anisotropy, i.e. with a very high length to diameter ratio [SDD98]. Usually they have diameters of 1-10 nm and lengths of several μm. Depending on the configuration of the CNTs they can be anything in between metallic and semiconducting. They exist in so called single-walled configuration (SWCNT) with diameters of usually around 1 nm or as multi-walled configuration (MWCNT) which means that nanotubes of different diameters are arranged concentrically.

Due to these conducting properties, it is, for instance, proposed to fabricate microwave absorbers using CNTs embedded in a polymer matrix [SBD$^+$06]. In [TWQL08] it is found that pure CNT bundles have virtually no dispersion in the microwave region. It is interesting to note that given the right solvent (not LC) and the right concentration, CNTs can form nematic like phases by themselves [ZK08] due to their shape anisotropy.

Recently, CNT suspensions in nematic LC (as well as other liquid crystalline phases) are subject to intensive research. It was found that nematic LC can organise the CNTs such that the CNTs align with the LC matrix, i.e. along the director [LP02, DSML04]. It was furthermore shown that reorientation of such a system is possible by electric and magnetic fields [DSM05, SLS$^+$07]. As a potential application, for instance, a magnetic sensor is proposed [DS05] which exploits the fact that the conductivity of a CNT doped LC layer between two electrodes changes as the orientation of the LC host changes. In [HHPL05] it is shown that adding a small amount of CNTs to the LC E7 increases the anisotropy at 1 kHz.

The essential idea of using CNTs as additives for nematic LCs in this work was to increase the anisotropy of the LC host also in the microwave region. In [LLMS93] results are presented which demonstrate that Δn_{MW} (at 30 GHz) can be increased by over 50 % by adding 0.2 %wt metallic micro tubules (500 nm in diameter and 10-30 um in length) to a LC host.

The host LC chosen for this work was also E7 due to its availability and large temperature range. For doping the LC only SWCNTs[6] were evaluated. The CNTs were available as purified material. The material is a mixture of metallic and semiconducting nanotubes.

The CNT material was dispersed in the LC host using ultrasonic treatment. In general, it is difficult to disperse CNTs in LC as they tend to quickly form bundles. The first experiments with CNT containing LC were conducted with only trace amounts of different CNT types (also MWCNTs) present in the LC host. Due to the extremely low concentration the fact that CNTs were contained in the LC could hardly be perceived with the naked eye, i.e. the white milky texture of the LC material was not modified. Although the great advantage of such mixtures with low concentrations is their stability, i.e. the concentration is low enough for the CNTs not to agglomerate, no change of the microwave properties could be detected using the same cavity perturbation setup as in the previous section.

[6] obtained from Carbon Nanotechnologies Inc.

In a next step, the CNT concentration was drastically enhanced to 0.005 %wt and 0.01 %wt, respectivelly. These mixtures showed deep black appearance. For the 0.01 %wt mixture CNTs were dispersed in the LC host using ultrasonic treatment for 6 hours at 300 W in the nematic phase. The 0.005 %wt mixture was prepared by diluting the 0.01 %wt mixture with pure E7 with subsequent ultrasonic treatment.

The cavity perturbation setup was again used for characterising the new mixtures. The measurement strategy chosen was to cool down the cavity and hence the LC first and then take measurements at discrete temperature points. The two orientations were taken in direct succession with a waiting period of at least two minutes before every measurement in order to guarantee stable temperature and orientation conditions. This measurement strategy was chosen as elevated temperatures accelerate the bundling process and therefore cooling down from a high temperature was considered inadequate for characterising these unstable mixtures. Once the mixture was heated beyond the clearing point T_{NI} (60 °C for E7) the mixture behaved isotropic in the entire temperature range due to intense bundling of the CNTs. This bundling can also be verified visually because larger chunks of CNTs can be seen with the naked eye.

Fig. 3.17 shows the results. In all figures, the properties of pure E7 are printed in gray. Obviously, for the 0.01 %wt mixture, both $\varepsilon_{r,\perp}$ and $\varepsilon_{r,||}$ are increased by the CNTs whereas $\varepsilon_{r,||}$ is increased far more than $\varepsilon_{r,\perp}$ (Fig. 3.17(a)) which is reflected in an increase of tunability by a factor of two. At the same time, the loss is increased (Fig. 3.17(b)). It is interesting to note that the usual behaviour of the two loss tangents $\tan\delta_\perp$ and $\tan\delta_{||}$ is reversed due to the CNTs, i.e. $\tan\delta_{||}$ is now larger than $\tan\delta_\perp$. The material efficiency remaines on the same level as the maximum loss increases by roughly the same factor as the tunability increases. However, there seems to be some kind of stabilisation effect on the efficiency vs. temperature imposed by the CNTs, i.e. the efficiency vs. temperature drops slower as that of pure E7. A reason for this could be that the CNTs are less affected by the decrease of ordering at higher temperatures. Conversly, it can also be speculated that the CNTs impose higher ordering in the nematic phase as it is suggested e.g. in [HHPL05]. Such a stabilisation effect can at any rate be observed from the permittivity characteristic in Figs. 3.17(a) and 3.17(c). The dielectric properties of the mixture after heating beyond the clearing point and cooling down in the nematic phase again are characterised by overal increased isotropic permittivity and loss.

The 0.005 %wt mixture was measured only at room temperature as this mixture was quite unstable and degraded quickly over time. However, because the diluted mixture has intermediate properties, from this single measurement (the bullets in Fig. 3.17), it can be learned that the behaviour of the mixture can be adjusted with the CNT concentration. The efficiency is slightly increased but both $\tan\delta_\perp$ and $\tan\delta_{||}$ are identical.

The encountered behaviour can be explained by employing a simple model which assumes that the CNTs are macroscopic conducting particles. In Fig. 3.18(a), the two extreme tuning states are depicted. In both cases, the CNTs in the nematic host align perfectly with the LC. Assuming that the CNTs are very thin, it is obvious that the electric field in the planar orientation (see section 2.4.4), corresponding to $\varepsilon_{r,\perp}$, is hardly disturbed by the presence of the CNTs. In case of

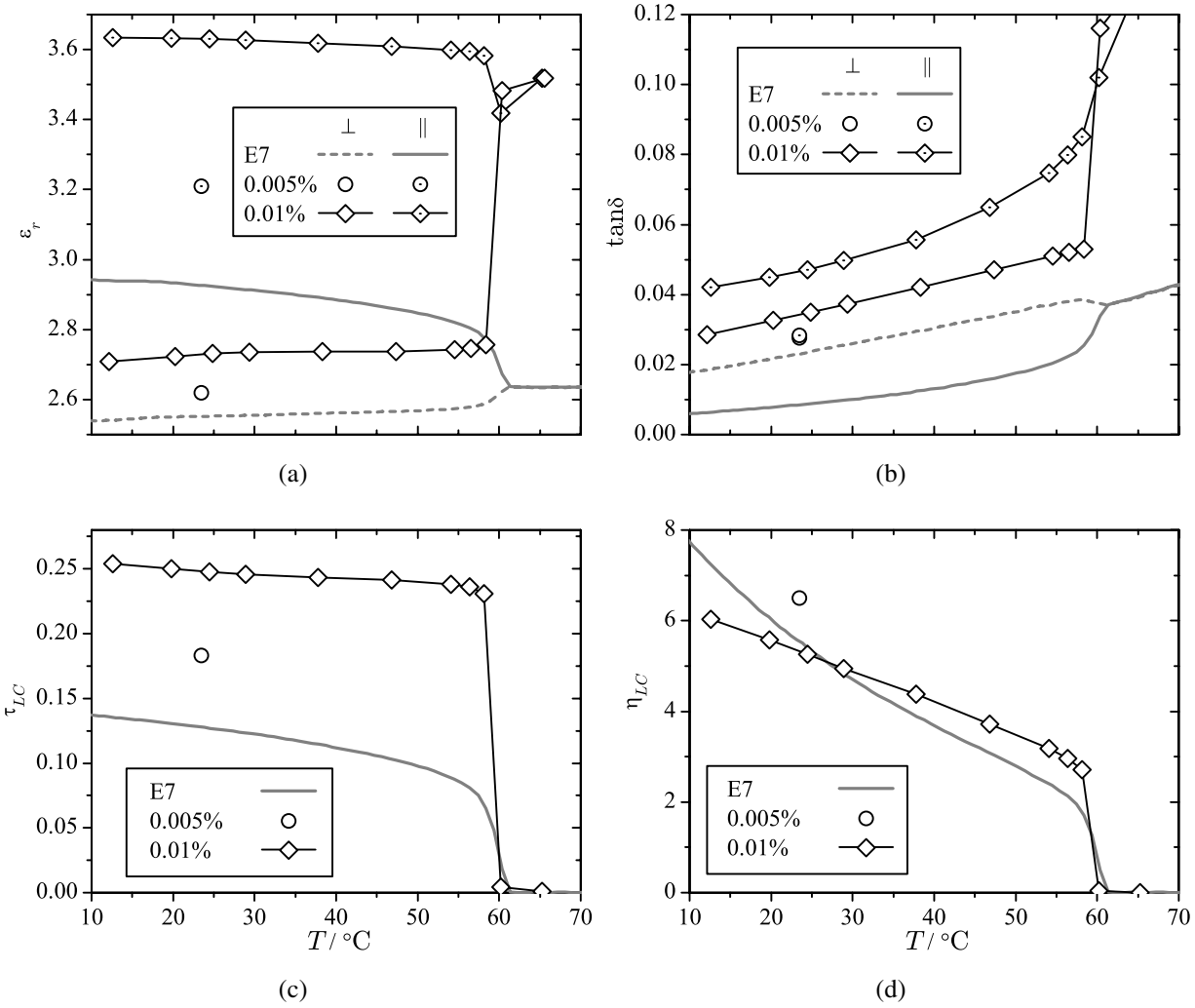

Figure 3.17: Results for E7 loaded with CNT in two different concentrations 0.01 %wt and 0.005 %wt. The properties of pure E7 are printed in grey. The markings on the 0.01 %wt curve indicate the temperatures at which the measurements were taken. (a) The permittivities, (b) the loss tangents, (c) the tunability and (d) the material efficiency.

the homeotropic alignment ($\varepsilon_{r,||}$) the CNTs have a large impact on the electric field. Fig. 3.18(b) depicts the electric field around a single CNT and it can be seen that the overall permittivity of the material will increase due to the field distortions.

The loss behaviour observed from the 0.01 %wt mixture can be qualitatively explained using this simplified model. For that purpose, it is assumed that the CNTs have finite conductivity. In case of the planar orientation (i.e. $\tan\delta_{\perp}$), there is charge induced into the CNTs but on reversing of the polarity this charge must only travel across the diameter of the CNTs. In case of homeotropic alignement ($\tan\delta_{||}$), the charge induced in the CNTs will mostly be concentrated at the tips (see Fig. 3.18(b)). This will lead, on reversing of the polarity, to a current along

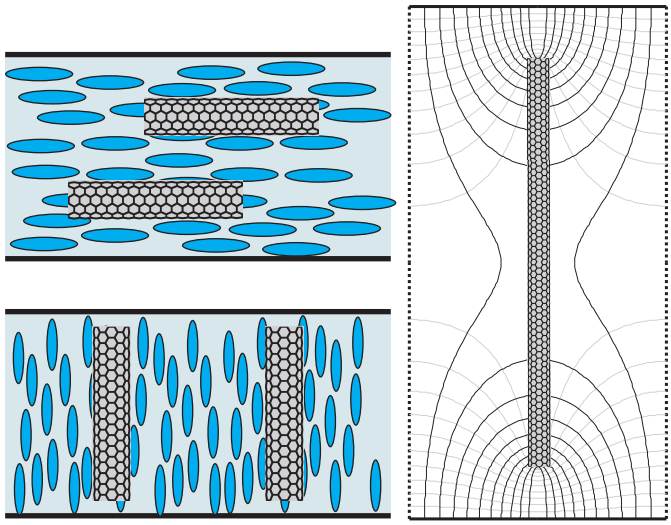

Figure 3.18: (a) The alignment of the CNTs in planar (top) and homeotropic (bottom) configuration. (b) Distortion of the electric field in the vicinity of a CNT.

the CNTs which in turn will generate loss. The fact that also the perpendicular loss $\tan\delta_\perp$ is increased can be explained by the imperfect ordering and also by the fact that the CNTs are never perfectly dispersed but always form bundles.

3.2 Porous PTFE Membranes Impregnated with LC

This section describes the evaluation of ePTFE (Expanded PTFE) membranes impregnated with nematic LC. Such layers are formed by dispersing, or embedding LC in a solid polymer matrix in order to reduce the response times due to increased anchoring of the LC inside the polymer matrix. The approach pursued in this work has the same motivation as the polymer-dispersed LC (PDLC) or the polymer stabilised LC (PSLC) technique which are well described in the literature [LKS+98, MNS98]. The polymer matrix in this work is given ab initio.

The characterisation procedures presented in this section represent also the first effort within the scope of this work which aim to realise thin layers of tunable material. Although it is possible with the presented material to realise layer thicknesses of more than 100 µm while still having fast response times, in the scope of this work only membranes with thicknesses of 30 and 60 µm were available. The major challenge in that respect was to realise the necessary thin cavities in between two substrates with adequate precision. The actual goal of using the membranes was to accelerate the tuning speed of devices based on the material when DC bias fields are applied. Another potential advantage of such membranes is that the material can be handled more easily as it represents a means of stabilising the LC layer. In addition there is the possibility

of structuring electrodes directly on such a membrane which would enable very compact tunable components.

3.2.1 Structure and Function of the Membranes

As has already been pointed out in section 2.4.3 the response times, particularly the switching-off time of nematic LCs is proportional to the LC layer thickness squared (d_{LC}^2). With that in mind, the general idea of the approach chosen in this work as well as in previous works [KFKN03, FKK+03] dealing with PDLC or PSLC can be described as follows: Due to the presence of many boundaries the initial LC alignment is no longer determined only by enclosing surfaces carrying electrodes, but by the fine-structure of the polymer matrix. This fine-structure is therefore assumed to provide additional anchoring which reduces the effective thickness experienced by the director which in turn should lead to decreased response times. The combination of nematic LCs and porous PTFE membranes for the use in microwave devices was evaluated in the above mentioned work [KFKN03] with the aim to reduce response times of microwave devices but this publication fails to highlight the particular structure of the used membranes.

Fig. 3.19 shows a Scanning Electron Microscope (SEM) photograph of the membrane type used for this work. The membrane is obviously porous which allows to impregnate the material with liquids. There is no scale given in Fig. 3.19 as the membranes can be manufactured with arbitrary porosities. The structure of ePTFE membranes is composed of so called nodes and fibrils which connect the nodes.

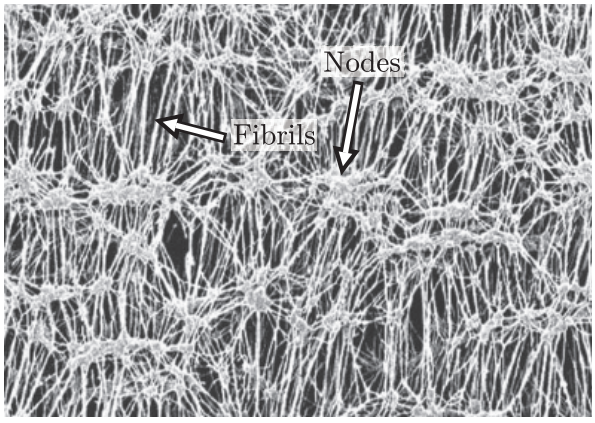

Figure 3.19: SEM image of the fine-structure of the PTFE membranes used in this work. The mesh forms a network with open pores. Image taken from [WHB+07]

The capability of PTFE to orient nematic, as well as other classes of LCs, is well investigated [CFN03, HDGG95, THI+05]. The works to be found in the literature deal with thin PTFE films obtained by rubbing a PTFE bar on a glass substrate. From these works, it can be assumed that thin PTFE fibers, as they are present in the membranes investigated in this work, also impose a certain anchoring force on the LC.

Because of the previous reason, on the downside, this will also increase the necessary tuning voltage as the overall anchoring is much stronger. With the membranes available in this work, it was possible to evaluate the influence of two different pore sizes: 0.3 and 4 µm. The pore sizes are defined according to [WHB+07]. For the given PTFE matrices the pore size can roughly be understood as the average distance between two fibrils within the matrix. Fig. 3.20 shows a simple model for the membranes used in this work. It is assumed that all fibrils are in parallel to the electrodes (Fig. 3.20(a)). This in turn will lead to an orientation of the LC in parallel to the fibrils and therefore to the electrodes.

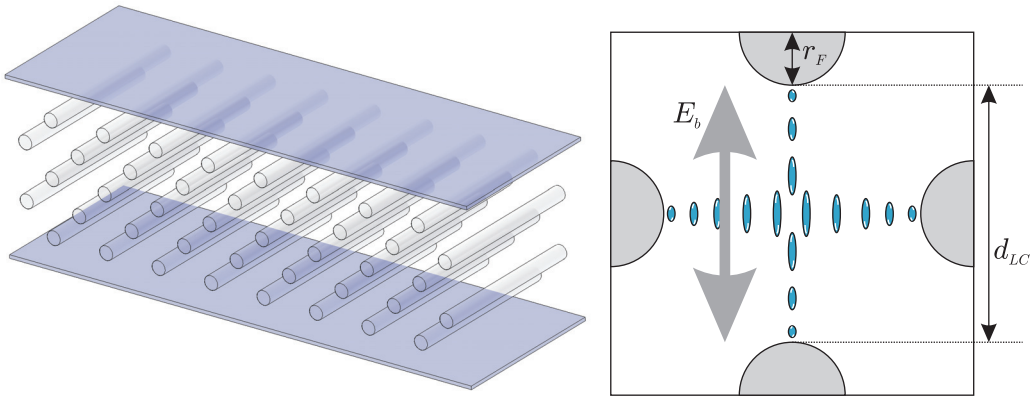

Figure 3.20: (a) A simplified model of the PTFE fibers between two electrodes. (b) Cutout of the cross section of the fiber structure. The orientation of the LC director is indicated for a vertically applied bias field E_b.

Fig. 3.20(b) shows a cross section of the fiber structure with the LC orientation indicated when a vertical bias field is applied. In the horizontal direction, the director experiences twist deformation as there is some anchoring of the director along the fibers indicated on the left and right wall of the cutout. In the vertical direction, the director experiences splay deformation as between two parallel plates. In the remaining, volume the molecules will orient accordingly.

Obviously, the fiber diameter r_F should be as small as possible in order to obtain as much volume for the tunable material as possible. Fig. 3.21 depicts the behaviour of the tuning efficiency η_τ vs. the r_F/d_{LC} ratio. The results were obtained using a 2D electrostatic field solver. The applied structure is the one shown in Fig. 3.20(b), however without considering any anisotropy i.e. it was assumed that in the entire LC filled volume either $\varepsilon_{r,\perp}$ or $\varepsilon_{r,||}$ is effective. The electrostatic field was calculated with electric boundaries at the top and bottom and magnetic boundaries left and right. The LC volume was considered in the tuned and the not tuned state using the respective permittivities ($\varepsilon_{r,\perp} = 2.5$, $\varepsilon_{r,||} = 3.2$). The actual characteristics of the curve in Fig. 3.21 changes only little as the tunability changes. In a real membrane, the effective tunability is further decreased as the nodes in between the fibrils take additional space (see Fig. 3.19). The relative permittivity of the fibrils was assumed to be two (PTFE).

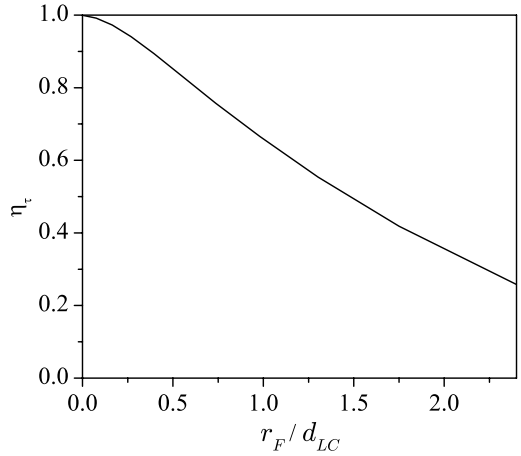

Figure 3.21: Available tunability vs. the ratio r_F/d_{LC} for typical values ($\varepsilon_{r,\perp} = 2.5$, $\varepsilon_{r,||} = 3.2$)

3.2.2 Planar Dielectric Characterisation

Although there exist various methods to characterise liquids and also LC - as seen in the previous chapter - only one characterisation topology presented itself suitable for evaluating the membranes as described above: The inverted microstrip line (IMSL) (see also [Mül07]). The possibility of fabricating electrodes directly on the membranes was not given in the scope of this work.

The concept of contacting the actual IMSL section used in [MSW+04, Mül07] could not be used here as this would require a feed substrate with a total thickness of at least 30 µm. This would in turn require a 70 µm wide strip for contacting the structure. Given that another requirement of the test setup was the possibility of simple contacting by means of a microstrip test fixture, this approach was not pursued any further. In [KFNU02] a IMSL with a thickness of 50 µm is presented, however this report does not describe how this line is contacted and what the spacers are made of. As for the aforementioned reasons, a transmission line setup with galvanic coupling was not suitable for an extraction of the permittivity. Instead, a resonator method based on a IMSL resonator strip which is excited capacitively was developed. In the next section, the theory of transmission line resonators and how they can be applied to the above described problem is therefore reviewed.

Transmission line resonators

For the extraction of the permittivity of the above described ePTFE membranes, transmission line resonators were employed. Unlike the cavity perturbation method described above the resonator is more or less fully loaded with the material under test (MUT) and not only perturbed. A simple circuit model of such a resonator including coupling is shown in Fig. 3.22.

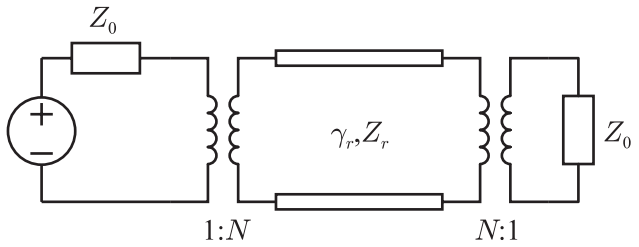

Figure 3.22: Circuit diagram of a transmission line resonator. The coupling is modeled by transformers. The resonator including transformers is embedded in a system with the characteristic impedance Z_0.

Using the transmission matrix for the transmission line resonator having the physical length l

$$\mathbf{A}_{TL} = \begin{pmatrix} \cosh(\gamma l) & Z_r \cdot \sinh(\gamma l) \\ \frac{1}{Z_r} \cdot \sinh(\gamma l) & \cosh(\gamma l) \end{pmatrix}$$

with

$$\gamma = \alpha + \frac{j\omega\sqrt{\varepsilon_{r,eff}}}{c_0} \tag{3.12}$$

with α being the attenuation constant, $\varepsilon_{r,eff}$ the effective permittivity determining the propagation speed and c_0 the speed of light and furthermore the transformer matrices

$$\mathbf{A}_{TF,fwd} = \begin{pmatrix} 1/N & 0 \\ 0 & N \end{pmatrix}, \mathbf{A}_{TF,bwd} = \begin{pmatrix} N & 0 \\ 0 & 1/N \end{pmatrix},$$

one obtains the overall transmission matrix

$$\mathbf{A}_{res} = \begin{pmatrix} \cosh(\gamma l) & \frac{Z_r}{N^2} \cdot \sinh(\gamma l) \\ \frac{N^2}{Z_r} \cdot \sinh(\gamma l) & \cosh(\gamma l) \end{pmatrix}$$

Embedding this resonator in a Z_0-System (see Fig. 3.22), i.e. multiplying

$$\mathbf{A}_{Z_0,series} = \begin{pmatrix} 1 & Z_0 \\ 0 & 1 \end{pmatrix}$$

from the left and

$$\mathbf{A}_{Z_0,shunt} = \begin{pmatrix} 1 & 0 \\ 1/Z_0 & 1 \end{pmatrix}$$

from the right, the matrix $\mathbf{A}_{sys}$ is obtained. The resonance angular frequency ω_0 can be calculated by solving the equation $\mathbf{A}_{sys,11} = 0$ for ω_0. Doing so yields:

$$\omega_0 = \frac{c_0}{2l\sqrt{\varepsilon_{r,eff}}} \left(1 + j\frac{l\alpha - \ln\left(\left|\frac{Z_r - Z_0N^2}{Z_r + Z_0N^2}\right|\right)}{\pi} \right) \tag{3.13}$$

For $Z_r = Z_0 N^2$ the imaginary part in Eqn. (3.13) takes infinite values which corresponds to the fact that then the resonator is effectively connected to the same impedance as its characteristic impedance. From Eqn. (3.13), the quality factor Q of the resonator can again be defined according to Eqn. (3.5). For $N \to \infty$ one obtaines the unloaded or intrinsic quality factor

$$Q_0 = \frac{\pi}{2l\alpha}. \tag{3.14}$$

Together with Eqn. (3.13), the unloaded quality factor Q_0 and the external quality factor Q_{ext} can be differentiated:

$$\frac{1}{Q} = \frac{1}{Q_0} + \frac{1}{Q_{ext}}$$

with Q being the loaded quality factor. The value of Q can be directly calculated from a $|S_{21}|$ measurement using the 3 dB bandwidth. Nevertheless, in order to obtain the intrinsic value α (Eqn. (3.12)) of the resonator, the unloaded quality factor must be determined as it was the case for the cavity perturbation method. This is achieved by fitting the formula in Eqn. (3.6) to the measured $|S_{21}|$.

Permittivity extraction

As the measurement setup used for the material parameter extraction of thin sheets is comprised of a multi-layer structure, it is necessary to find a suitable method to extract the complex permittivity of a certain layer of the multi-layer structure. Fig. 3.23(a) shows a schematic side view of the measurement setup and Fig. 3.23(b) the cross section, respectively. The actual resonator strip is on the lower side of the carrier substrate (in this case made of sapphire). This resonator strip is excited by feed lines on top of the same substrate. Both the feed lines and the resonator strip share the same ground plane. The resonator strip has the length l. The area below the resonator strip is filled with the material under test (MUT).

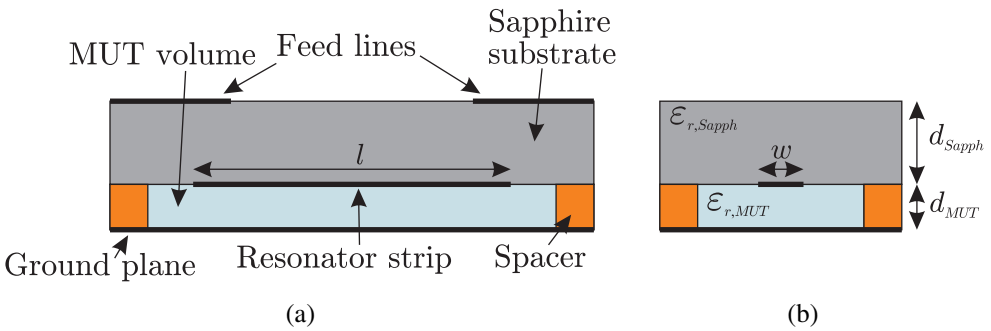

Figure 3.23: (a) Side view of the resonator. (b) Front view of the resonator (Not to scale).

Before the MUT permittivity can be extracted, the effective permittivity $\varepsilon_{r,eff}$ of the cross section (Fig. 3.23(b)) must be determined. In [CON+04], a simple method is described how the effective

permittivity $\varepsilon_{r,eff}$ determining the propagation of a TEM wave of two resonators having the lengths l_1 and l_2, can be calculated. Both resonators must have the same cross section. These two resonators will have the complex resonance frequencies $f_{r,1}$ and $f_{r,2}$. Due to the fringing fields at the tips of the resonator strips, the strips are elongated by a differential length δl. Using the two resonators, δl can be calculated according to

$$\delta l = \frac{f_{r,2} l_2 - f_{r,1} l_1}{f_{r,1} - f_{r,2}}.$$

From this the complex effective permittivity is given by

$$\varepsilon_{r,eff} = \left(\frac{c_0 (n_1 f_{r,2} - n_2 f_{r,1})}{2 f_{r,1} f_{r,2} (l_2 - l_1)} \right)^2. \tag{3.15}$$

n_1 and n_2 are the respective orders of resonance. In Eqn. (3.15), it is assumed that the imaginary part of the resonance frequencies only stem from dielectric loss. The advantage of this method is that the length increments caused by the fringing fields at the ends of the resonator strips do not have to be considered which makes this method, in principle, very accurate. In general, the two lengths should be integer multiples of each other while the resonators are evaluated at an n_1 and n_2 such that both have the approximately the same resonance frequency.

In order to be able to employ Eqn. (3.15), it must be ensured that the dielectrics of the resonators are identical. Provided that this is not the case for whatever reason, i.e. the material to be tested shows some fluctuation from specimen to specimen, the potential impact on the result of Eqn. (3.15) must be investigated. In fact, such a fluctuation was observed during the experiments which was the reason why a different approach was chosen as will be shown further below. In the following the impact of these fluctuations is shortly reviewed.

In order to assess the impact of the fluctuation, only the real part of the resonance frequencies is considered and the error $\Delta\varepsilon_{r,eff}$ is associated with the material sample loading the resonator having the length l_2. Furthermore, it is assumed that $l_2 = 2l_1$ which was considered the maximum length difference reasonable for efficient fabrication of the test setup. Then Eqn. (3.15) simplifies to

$$\varepsilon_{r,eff} = \left(\sqrt{\varepsilon_{r,eff}^{real}} - 2\sqrt{\varepsilon_{r,eff}^{real} + \Delta\varepsilon_{r,eff}} \right)^2.$$

Calculating the Taylor series expansion of this formula, one obtains

$$\varepsilon_{r,eff} \approx \varepsilon_{r,eff}^{real} + 2\Delta\varepsilon_{r,eff} + \frac{\Delta\varepsilon_{r,eff}^2}{2\varepsilon_{r,eff}^{real}}.$$

This means that the absolute uncertainty is always at least doubled. This effect is mitigated if the difference in length between the two resonators is chosen larger but the experimental setup becomes naturally much larger and unwieldy then, especially when low frequencies ($< 10\,\mathrm{GHz}$) are to be considered.

For the above given reasons, a different approach was used. The influence of the permittivity mismatch between the samples can be limited by measuring more than one sample of the same material and by then calculating the average $\varepsilon_{r,eff}$. For two resonators or two samples, respectively, this would cut the influence of $\Delta\varepsilon_{r,eff}$ in half instead of doubling it. The effective permittivity is then calculated according to

$$\varepsilon_{r,eff} = \frac{1}{2}\left(\left(\frac{c_0}{2f_{r,1}(l_1+\delta l)}\right)^2 + \left(\frac{c_0}{2f_{r,2}(l_2+\delta l)}\right)^2\right)$$

The problem remaining is the length increment δl. In the literature, several closed form expressions can be found for regular open microstrip lines (e.g. [KJK81]). For multilayer structures as the one used in this work, only numerical evaluations can be found. Hence, as will be presented below, δl should be determined using reference resonators. As the value of δl will nevertheless contribute most significantly to the extraction error, the impact of this error must be determined. Assuming that the resonance frequency measurement and δl are erroneous, the absolute error is

$$\Delta\varepsilon_{r,eff} = \left|\frac{\partial\varepsilon_{r,eff}}{\partial f_{r,1}}\right|\Delta f_{r,1} + \left|\frac{\partial\varepsilon_{r,eff}}{\partial f_{r,2}}\right|\Delta f_{r,2} + \left|\frac{\partial\varepsilon_{r,eff}}{\partial\delta l}\right|\Delta\delta l. \tag{3.16}$$

From $\varepsilon_{r,eff}$ determined from the resonance frequencies, the ε_r of the MUT-layer can be found. In [Sva92], a formula (called $fct_{\varepsilon_{r,eff}}$) based on a conformal mapping approach is given which allows to calculate $\varepsilon_{r,eff}$ as a function of $\varepsilon_{r,MUT}$, $\varepsilon_{r,Sapph}$, d_{MUT}, d_{Sapph} and w (see Fig. 3.23). This in turn allows to determine the complex $\varepsilon_{r,MUT}$ if $\varepsilon_{r,eff}$ is known. The function $fct_{\varepsilon_{r,eff}}$ can be analytically solved for $\varepsilon_{r,MUT}$ which gives the function $fct^{-1}_{\varepsilon_{r,eff}}$. It should be noted that for very thin layers $\partial fct^{-1}_{\varepsilon_{r,eff}}/\partial d_{MUT}$ and $\partial fct^{-1}_{\varepsilon_{r,eff}}/\partial\varepsilon_{r,Sapph}$ are negligible so the potential error arising from these uncertainties was not considered. The error of $\varepsilon_{r,eff}$ as calculated in Eqn. (3.16) can be accounted for by calculating the error $\Delta\varepsilon_{r,MUT}$ of $\varepsilon_{r,MUT}$:

$$\Delta\varepsilon_{r,MUT} = \left|\frac{\partial fct^{-1}_{\varepsilon_{r,eff}}}{\partial\varepsilon_{r,eff}}\right|\Delta\varepsilon_{r,eff}$$

Extraction of the loss tangent

The parameter α in Eqn. (3.14) contains the metallic loss α_m and the dielectric loss α_d with the respective Q_m and Q_d which are related to Q_0 according to

$$\frac{1}{Q_0} = \frac{1}{Q_m} + \frac{1}{Q_d} \tag{3.17}$$

while assuming that no magnetic loss is present. The problem at this point is to determine Q_m experimentally. For that purpose the attenuation constant of a TEM waveguide has to be considered [ZB00]:

$$\alpha \approx \frac{\sqrt{L'C'\varepsilon_{r,eff}}}{2}\left(\frac{R'}{L'} + \frac{G'}{C'}\right) \overset{G'=0}{=} \alpha_0\sqrt{\varepsilon_{r,eff}}. \tag{3.18}$$

Assuming that no dielectric loss is present ($G' = 0$) the attenuation is proportional to $\sqrt{\varepsilon_{r,eff}}$. α_m can be determined theoretically if the resonator could be loaded with a material having the same permittivity as the MUT but no dielectric loss, i.e. $1/Q_d = 0$. This is of course not realistic and so one usually has to resort to using air because this is the only material for which zero dielectric loss can be assumed. The resonator designed to extract α_m must have its resonance at the same frequency as the MUT resonator, i.e. $f_m = f_r$. This can be achieved if the relation

$$\sqrt{\varepsilon_{r,eff}^{Air}} \cdot l_{Air} = \sqrt{\varepsilon_{r,eff}^{MUT}} \cdot l_{MUT} \tag{3.19}$$

is ensured with l_{Air} being the length of the air resonator and l_{MUT} the length of the resonator loaded with the MUT. The major drawback of this method is of course that ε_r^{MUT} must be known in advance, at least roughly, in order to design the air resonator.

If Eqn. (3.19) is fulfilled, the quality factor of the air resonator will be, due to Eqn. (3.18), the same as the quality factor of a resonator loaded with the MUT without loss, that is Q_m. This enables to solve Eqn. (3.17) for Q_d and hence for α_d. For $\tan\delta \ll 1$, the transmission line attenuation α_d caused by dielectric loss is related to the loss tangent $\tan\delta_{eff}$ according to

$$\alpha_d = \frac{\omega}{2c_0}\sqrt{\varepsilon_{r,eff}}\tan\delta_{eff}.$$

Eventually the loss tangent can be calculated according to

$$\tan\delta = \frac{\pi c_0}{l\omega_0\sqrt{\varepsilon_{r,eff}^{MUT}}} \cdot \frac{Q_m - Q_0}{Q_m Q_0} = \frac{Q_m - Q_0}{Q_m Q_0}.$$

However, as stated previously, Eqn. (3.19) cannot be fulfilled as $\varepsilon_{r,eff}^{MUT}$ is not known beforehand. This makes the evaluation of Q_m inaccurate because the resonance frequency f_m will be in general different from the loaded resonators frequency f_r. Nonetheless, this error can be corrected if an adequate correction factor for Q_m can be derived. This is shown in the following paragraphs.

Eqn. (3.14) can be rewritten for a general transmission line resonator (see also [Poz04]):

$$Q = \frac{\pi}{2l\alpha} = \frac{\beta}{2\alpha} = \frac{\omega_0}{2c_0\alpha_0}.$$

Assuming that the quality factor Q'_m has been measured at the angular frequency f_m the quality factor can be shifted to f_r by multiplying Q'_m by f_r/f_m. This is possible because α_0 does not depend on $\varepsilon_{r,eff}$ (see Eqn. (3.18)). Nevertheless, α_0 depends on R' due to the fact that the skin effect is approximately proportional to $\sqrt{\omega}$. This makes it necessary to add the correction factor $\sqrt{f_r/f_m}$ for α_0. Finally, the quality factor of a resonator having the same permittivity as the resonator loaded with the MUT but without dielectric loss can be calculated:

$$Q_m = Q'_m\sqrt{\frac{f_r}{f_m}}$$

Hence, the loss tangent is

$$\tan\delta_{eff} = \frac{1}{Q_0}\left(1 - \frac{Q_0}{Q'_m}\sqrt{\frac{f_m}{f_r}}\right). \tag{3.20}$$

The smaller the correction factor is, the smaller the difference between the resonance frequency of the MUT resonator and the reference resonator is. This is why a reference resonator was designed according to Eqn. (3.19) with $\varepsilon_{r,eff}$ around 2.5. It should be noted that the above modeling does not consider the current distribution change in the cross section of the conductor with changing $\varepsilon_{r,MUT}$.

The loss tangent determined in Eqn. (3.20) is also a quantity which is effective for the cross section of the resonator. Like $\varepsilon_{r,eff}$, $\tan\delta_{eff}$ must be corrected according to the multilayer structure in Fig. 3.23(b). The complex permittivity of the material under test is therefore calculated as

$$\underline{\varepsilon}_{r,MUT} = fct^{-1}_{\varepsilon_{r,eff}}(\varepsilon_{r,eff}(1 - j\tan\delta_{eff})) = \varepsilon_{r,MUT}(1 - j\tan\delta_{MUT})$$

This equation is only valid for $\tan\delta_{eff} \ll 1$, as only then the field distribution, which is implicitly contained in $fct_{\varepsilon_{r,eff}}$, is determined by the real part of the permittivity.

In order to calculate the error, it is assumed that only Q_0 and Q'_m are erroneous quantities. The resonance frequencies in Eqn. (3.20) are also inaccurate due to the error caused by δl (see Eqn. (3.16)). It was however found that that effect is negligible compared to the error in the quality factors.

The error of the effective loss tangent is given by

$$\Delta\tan\delta_{eff} = \left|\frac{\partial\tan\delta_{eff}}{\partial Q_0}\right|\Delta Q_0 + \left|\frac{\partial\varepsilon_{r,eff}}{\partial Q'_m}\right|\Delta Q'_m.$$

Finally, the error of the material's loss tangent yields analogous to the permittivity

$$\Delta\tan\delta_{MUT} = \left|\frac{\partial fct^{-1}_{\varepsilon_{r,eff}}}{\partial\tan\delta_{eff}}\right|\Delta\tan\delta_{eff}.$$

3.2.3 Measurement Setup and Results

For the purpose of characterising layers with thicknesses of 30 and 60 µm, the choice of materials for the cover substrate is limited. While i.e. in [Mül07] so called soft substrates (ceramic or PTFE composites) were used exclusively, it was found that such substrates are not suitable for the given task due to rough surfaces and overall slack rigidness. As a replacement material not suffering from these mechanical disadvantages, sapphire was evaluated. From the microwave point of view, sapphire offers very good performance. Literature values are $\varepsilon_r = 10$ [Oxb07] (sapphire is actually slightly anisotropic but $\varepsilon_r = 10$ was assumed for this work and the loss tangent is usually given smaller than $1 \cdot 10^{-4}$).

The material was evaluated at three frequencies: 5 GHz, 10 GHz and 20 GHz, however only 5 and 10 GHz were considered, as for higher frequencies no additional knowledge could be gained and the extraction errors became too high. Fig. 3.24 shows the layout of the 10 GHz sapphire substrate carrying two resonators designed for the MUT and two reference resonators (the longer ones) for extracting the metallic loss of the microstrip line. For the 5 GHz setup, the layout is scaled accordingly. The fabrication of the respective wafers (550 µm thickness, 2 µm gold electrodes) was done in an external laboratory. The resonators are capacitively coupled to

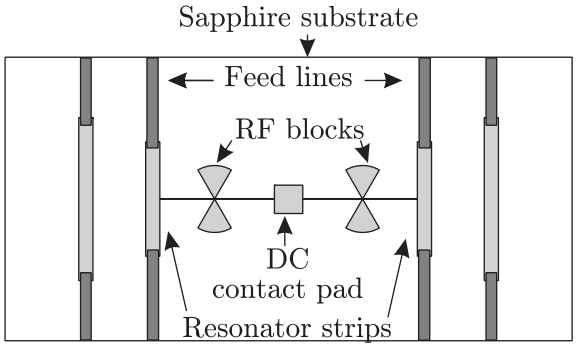

Figure 3.24: Layout of the 10 GHz setup. The electrodes printed in dark gray are on the top side of the sapphire substrate, the light gray ones on the bottom side forming the actual resonator strips.

the feed lines, as described before. The overlap between the feed electrode and the resonator strip was designed to have a transmission at resonance frequency of no more than -10 dB. This design was done using the 2.5D planar fullwave solver SONNET assuming a dielectric loss of the MUT of $3 \cdot 10^{-2}$. The feed lines were designed to have a characteristic impedance of 50 Ω.

The bias feed lines are 50 µm wide and are connected to the center of the resonators. This ensures that at resonance frequency a negligible amount of power leaks from the resonator into the bias feed. Furthermore, it was confirmed by 3D fullwave simulations that within the 3 dB frequency range around the resonance the influence on the quality factor is negligible if radial stubs, representing a RF short at the respective positions, are used as depicted in Fig. 3.24. Fig. 3.25 shows the setup of the measurement fixture (10 GHz). The ground plane is a single piece of brass onto which all other parts of the setup are fixed. The spacers are made of either 30 or 60 µm thick brass sheets, depending on the material under test. The specific shape of the brass sheets was achieved by etching. The measurement setups for the other frequencies are scaled accordingly. Fig. 3.26 shows a photograph of the measurement setup installed in a microstrip test fixture.

Dielectric Properties

The LC used for impregnating the ePTFE membranes is 5CB, representing a standard material (see also section 3.1.3). Although the microwave performance of this material is not very high, it sufficiently serves the purpose of the evaluations presented in the following. The measurements were performed using an Anritsu 37397C Vector Network Analyser (VNA).

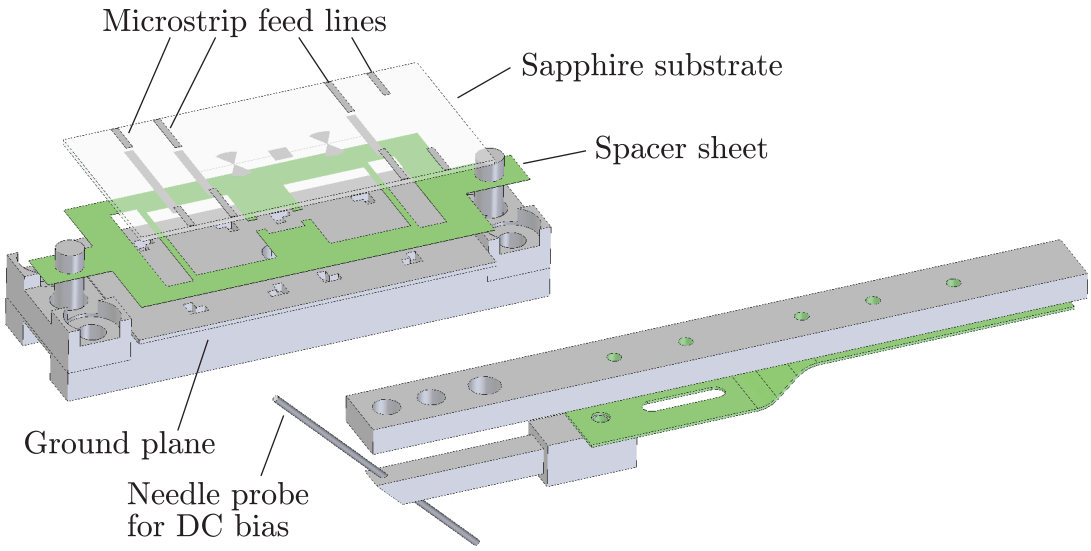

Figure 3.25: Exploded view of the 10 GHz measurement setup. The needle probe is brought in contact with the DC bias contact pad from below through a hole in the ground plane. The ground plane is made of brass which was plated with gold for better conductivity.

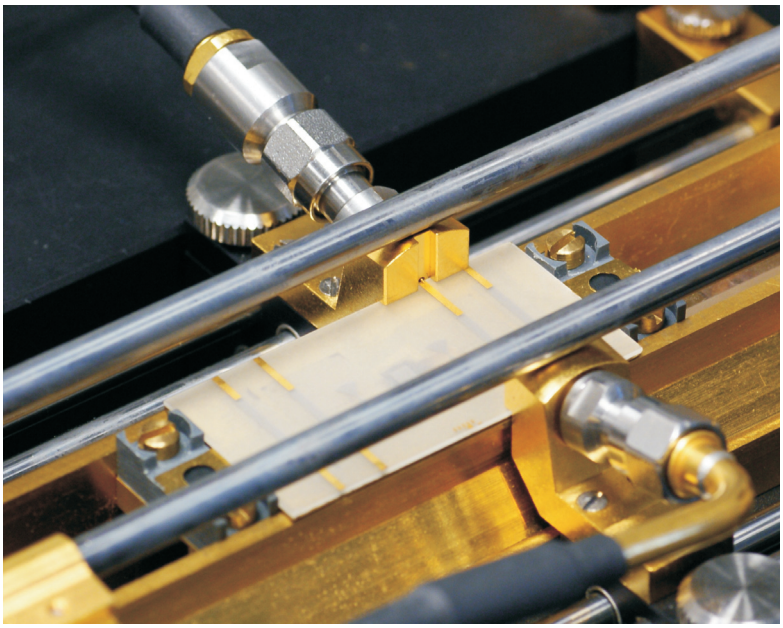

Figure 3.26: The 10 GHz setup installed in a microstrip test fixture.

For comparison, the pure material 5CB (i.e. without ePTFE matrix) was evaluated first by using the 5 GHz resonator and the 60 µm spacer sheet. As can be seen, the results deviate from the values shown in Fig. 3.5. This can be explained by the fact that the permittivities are larger at 5 GHz (compare [Mül07]) and that the extraction error is relatively large for the given measurement setup.

For this measurement, a polyimide film was applied to the surface of the groundplane and the sapphire substrate in order to ensure proper orientation of the LC. Furthermore, several ePTFE membranes impregnated with 5CB were evaluated. The results of two membranes are representatively set forth in the following. The two samples feature 30 and 60 µm thickness. Fig. 3.27 shows the results for the permittivity and the loss tangent.

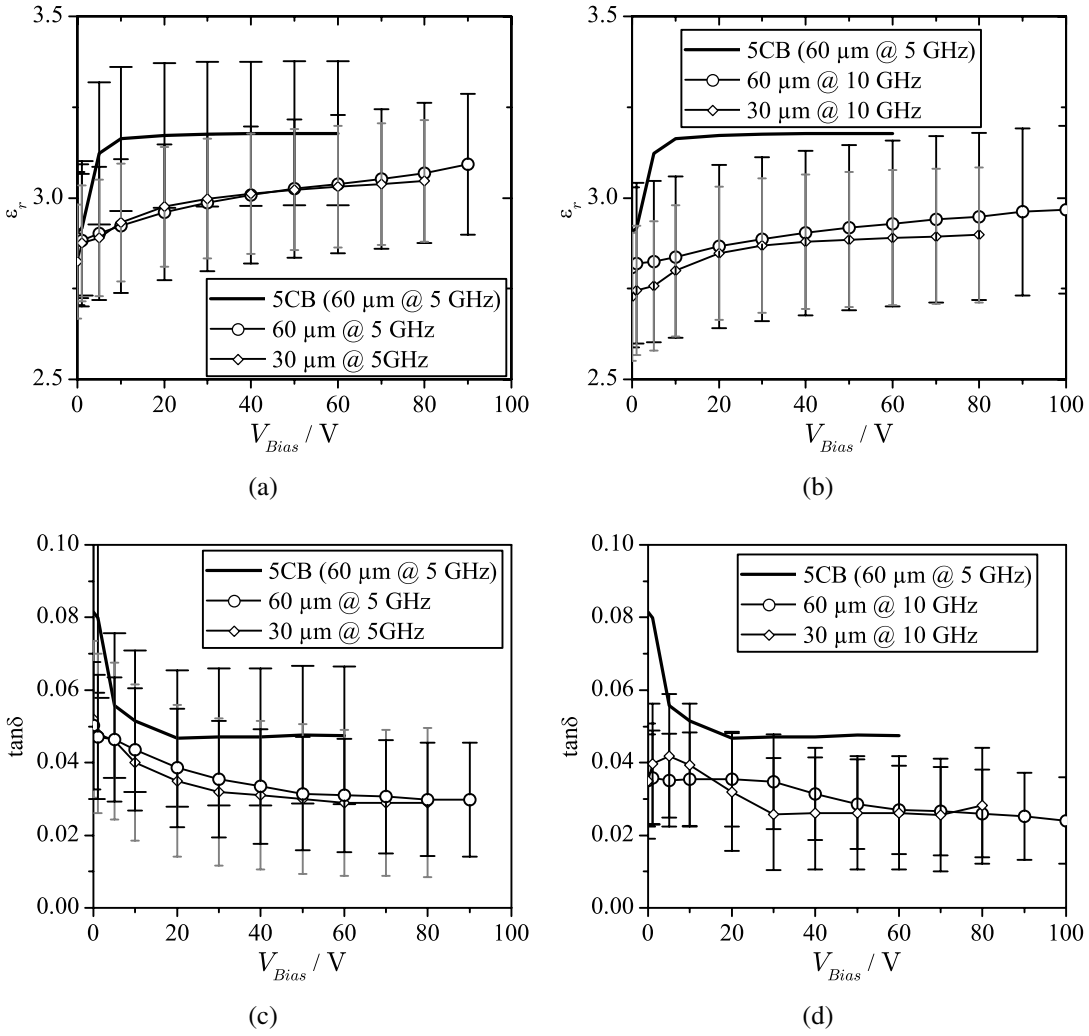

Figure 3.27: Extracted values of 5CB (at 5 GHz) and the two samples (at 5 GHz and 10 GHz). (a) and (b): ε_r for both sheets as obtained by the 5 GHz and 10 GHz setup. (c) and (d): $\tan\delta$ for both sheets as obtained by the 5 GHz and 10 GHz setup. For the error the following uncertainties were assumed: For $\Delta f_{r,1}$ and $\Delta f_{r,2}$ $\pm 2\,\%$, for $\Delta\delta l$ $\pm 25\,\%$ and for ΔQ_0 and $\Delta Q'_m$ $\pm 5\,\%$.

As can be seen, the permittivity of pure 5CB saturates at a voltage of about 20 V and a maximum tunability of τ_{LC}=0.09 can be calculated. The loss tangent decreases with increasing bias voltage. The permittivity of the sheets is somewhat lower which can be expected as the membranes are filled with LC and therefore represent a mixture of a material with lower permittivity (PTFE,

$\varepsilon_r \approx 2$) and higher permittivity (LC, $\varepsilon_r \approx 2.8$, depending on frequency). Although the error bars in Figs. 3.27(a) and 3.27(b) imply that a interpretation in terms of absolute values is not permissible, it should be noted that the error indicated in these two figures is the maximum error to be expected, i.e. it includes the systematic error, caused by $\Delta\delta l$, and the random measurement uncertainty $\Delta f_{r,1,2}$. Only taking the measurement uncertainty into account, the effective error is much smaller which allows to deduce that the permittivity of the 30 µm sheet saturates while the permittivity of the 60 µm sheet does not saturate even at 100 V. This effect is particularly pronounced in Fig. 3.27(b). This can be explained by the higher field strength in the thin sheet. The effective tunability of the sheets does not exceed 0.06 and is, consequently, considerably lower compared to the pure LC material.

The loss tangent reflects the behaviour of the permittivity. For the membranes a lower loss tangent is found which can be attributed to the low loss of the PTFE part in the composite. It should be noted that the assumed error of the $\tan\delta$-extraction does not permit precise evaluation of the impact of the ePTFE membrane on the overall loss tangent. Nevertheless, the experiments seem to confirm the expectation of a lower loss tangent.

Response Times

The response times were measured for each sample for all evaluated frequencies by using the VNA in the same configuration as for the scattering parameter measurements. To this end, the internal calibration of the VNA was turned off in order to improve the recording speed. As actual measure, the complex S_{21} parameter was chosen which was recorded every 3 ms at the resonance frequency of the resonator without bias (continuous wave (CW) measurement). Fig. 3.28 shows

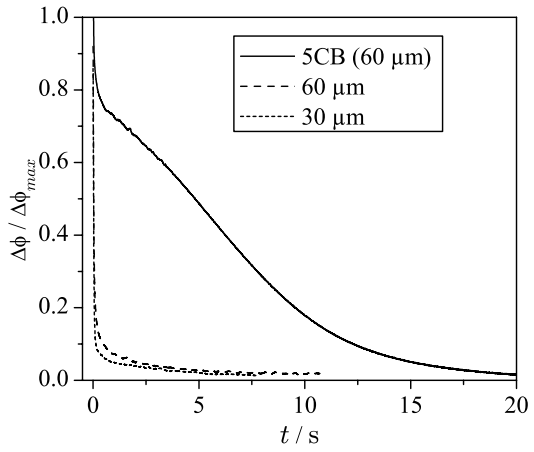

Figure 3.28: Representative recorded tuning processes of pure 5CB (60 µm) and the two membranes.

the results. Plotted is the relative change of the transmission phase ($\angle(S_{21})/\max(\angle(S_{21}))$) vs. time. The transmission phase was chosen as this parameter offered higher contrast and resolution.

5CB	60 µm sheet	30 µm sheet
>10 s	100-400 ms	450-700 ms

Table 3.6: Switch-off times for the different sheets. The response times varied from sample to sample which is why ranges are given.

As stated previously, one of the main goals of the presented evaluations was to demonstrate that the response times can be improved under DC bias conditions by using ePTFE membranes. From Fig. 3.28, it is obvious that both ePTFE samples have dramatically improved response times compared to pure 5CB. The particularly long response time of 5CB can be explained by charging effects caused by free ions in the LC [HLTB03]. Apart from the tuning acceleration of the additional anchoring by the PTFE fibrils this effect is obviously also lessened by the use of the membranes. Table 3.6 lists the switch-off times measured for different samples. The 30 µm membrane appears to be somewhat slower which can be attributed to the increased ionisation effect due to a higher effective field strength.

Switching on was for all membranes and pure 5CB equally fast (<3 ms, the resolution of the measurement system) which allows the assumption that the anchoring of the fibrils is not very strong. This can be understood with Eqns. (2.37) and (2.39) the latter of which also depends on the voltage drop across the LC volume. If the fibrils did impose strong anchoring, V_{th} would remain the same (it is a material property assuming strong anchoring) but the actual voltage drop across the LC volume, i.e. from fibril to fibril inside a pore, is less which would raise the effective threshold voltage considerably. From the dielectric measurement, it can be seen that there is no distinct threshold effect visible which also corroborates that the $\left|\frac{V}{V_{th}} - 1\right|$ term in Eqn. (2.39) must be large even though the effective voltage drop from fibril to fibril is small. In the scope of this work, membranes with a pore size of 0.03 µm were also evaluated. These membranes showed no tunability at all, even at 100 V bias voltage. This can be explained by the fact that the effective voltage drop from fibril to fibril is much smaller (less than a hundredth compared to the larger pores) which is why the effective threshold cannot be exceeded.

3.3 Conclusion

This chapter explores different LC materials and material composites with LC as functional component for microwave applications. In order to reduce the response time of LC based microwave devices, the use of ePTFE membranes impregnated with LC is investigated. As could be shown, it is indeed possible to enhance the response times from several seconds down to 100 ms. In terms of microwave performance, i.e. tunability and loss, the material still has to be optimised which can be done by using a LC with higher performance.

In terms of the dependency between the microwave performance and the chemical composition of the material it can be learned that compounds with higher optical anisotropy have in general

also higher microwave tunability. The microwave anisotropy, expressed by the birefringence property Δn is for all mixtures considerably lower than that at optical frequencies. The reason for that is most likely that in between the microwave range and optics further relaxation or resonance processes exist.

In terms of dielectric loss, specifically the perpendicular loss, a rather obvious relationship between loss and the molecular properties can be observed: If the molecules have a strong permanent dipolar moment, the microwave loss is higher. This is the case for dipolar moments along the molecule's long axis but even more for molecules with perpendicular dipole moments. The associated loss mechanism is the relaxation around the molecule long axis. The parallel loss could, at least partly, be explained by the projection of the higher perpendicular loss on the molecule's long axis. LC mixtures which have been synthesized with particular focus on the reduction of the relaxation around the molecule long axis show exceptionally low dielectric loss. By adding CNTs to a LC host it could furthermore be shown that by introducing these conductive and highly anisotropic particles the tunability of the LC can be improved by a factor of two.

Chapter 4

Devices with Fast Response Times

In section 3.2, the attempt was made to reduce the effective layer thickness in order to reduce the response times by using porous PTFE membranes. Yet, although this approach significantly reduces the switching times, there are some downsides. For instance, if the material is to be used as a dielectric in an IMSL configuration and if the metallic loss is to be kept low, the layer thickness has to be at least 100 µm or more. Specifically this issue will be addressed in detail in this chapter. A relatively thick layer in turn increases the necessary bias voltage considerably because the effective voltage drop within a pore of a PTFE membrane is the lower, the thicker the material layer is.

If fast response times combined with reasonable bias voltages are required, there is virtually no way around realising very thin LC layers with thicknesses down to a few microns and without an additional PTFE matrix. As was explained in section 3.2, soft substrates are in general not suitable for fabricating thin LC layers due to their insufficient mechanical properties in terms of stiffness and flatness. Sapphire could be used, particularly because of the excellent microwave performance but, nevertheless, the immense hardness (Vickers hardness $H_V = 2300$ [Kyo]) makes it rather unwieldy and costly if the material itself has to be mechanically processed (e.g. by dicing, drilling, etc). Also the high permittivity can be disadvantageous in terms of tuning performance as it draws the electric field from the tunable LC layer into the enclosing substrate. Therefore, a material representing a better compromise concerning microwave performance and mechanical qualities had to be found.

A far better choice as a substrate material is fused silica or fused quartz, respectively. This material consists of highly pure SiO_2 in amorphous (i.e. non-crystalline) form. This material is most often used as a substrate for photomasks in the semiconductor industry and therefore well specified from the near infrared down to the far ultraviolet wavelength range. For the microwave region however, vendors do not specify the performance. In the literature a relative permittivity of 3.8 and a loss tangent of $\approx 10^{-4}$ is given. The material used for this work's applications (Schott Lithosil Q1) was characterised using a cylindrical split cavity resonator at 16 GHz which confirmed the literature values.

4.1 Inverted Microstrip Line Phase Shifters with Thin Layers

As a first step towards reducing the thickness of the LC layer, a tunable transmission line phase shifter in inverted microstrip line (IMSL) topology was developed. This topology was also used in section 3.2.3, however as a resonator. In order to design a broadband phase shifter, this approach is of course not suitable which is why an alternative device topology had to be found. The aim was furthermore to decrease the response times when using DC bias voltages.

4.1.1 Device Design and Implementation

The targeted thickness was 20 µm which even thinner than that required for the ePTFE membranes. The solution to the problem of realising a means of contacting the thin IMSL chosen in this work was to design a coplanar waveguide to inverted microstrip line transition. As operating frequency for the device 20 GHz was defined. Fig. 4.1(a) shows a schematic of the transition from CPW to IMSL. The broad band characteristic of this transition is realised by the capacitive coupling of the CPW ground to the IMSL ground. Spherical spacers made of plastics with a nominal diameter of 20 µm were used to ensure a defined gap between the two substrates. The real thickness of 23 µm was determined using a white light interferometer. A cross section through the IMSL section is shown in Fig. 4.1(b). The CPW feed section is a 50 Ω line and can be contacted with CPW probes having a pitch of 150 µm or larger.

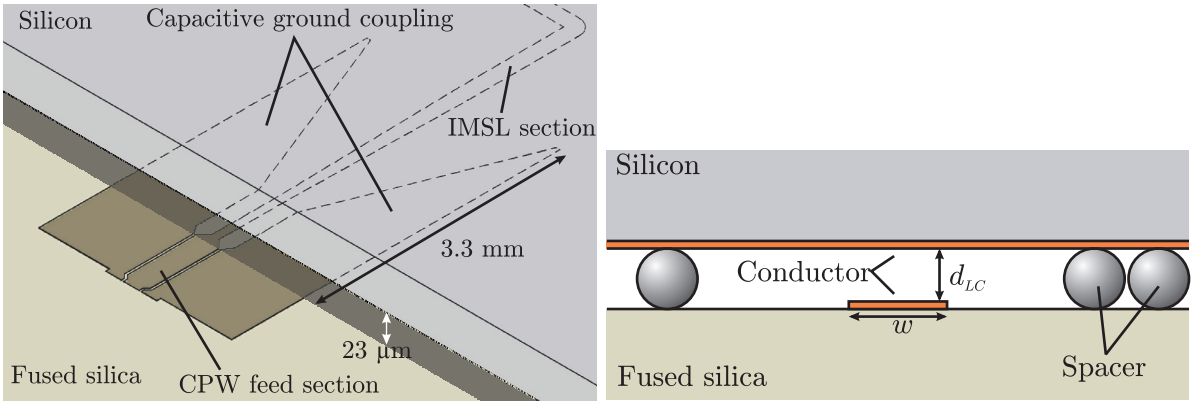

(a) (b)

Figure 4.1: Functional principle of the tunable IMSL phase shifter. (a) Schematic of the feed section. The CPW feed line is located on the lower fused silica substrate. At the edge of the silicon substrate, the coupling structure from the CPW ground to the microstrip ground on the silicon substrate is located. A cross section of the IMSL phase shifter section is shown in (b).

As the upper substrate only carries the ground plane and the electric field does not penetrate the substrate, it was possible to use silicon. This material also offers excellent surface quality and mechanical stiffness, both properties which are very important for realising thin LC layers. The

substrate was cut to the correct size using a dicing saw, which allows to reach the high precision necessary to realise the CPW to IMSL transition as depicted in Fig. 4.1(a) on both sides of the substrate. The lower substrate, which is penetrated by the electric field, is made of fused silica, which offers, as mentioned previously, beside the excellent mechanical properties, very good microwave performance.

The electrodes on the fused silica substrate were patterned according to the process steps listed in Table A.1 in Appendix A. For applying the spacers to the surface, a special technique was developed. As the spherical spacers are comparatively large, i.e. they could impair the microwave performance if the are in too great numbers in areas penetrated by the electric field, the aim was to restrict them to certain spots only. For that purpose the spacers were dispersed in photo resist (PR, SU-8 2007) which was further diluted by a thinner in order to allow for very thin PR layers. After spin coating the mixture on the patterned fused silica substrate and subsequent curing, a thin PR layer ($\approx 1\,\mu$m) is formed with the spherical spacers sticking to it. Using an additional mask, the areas where the PR and spacers remain on the substrate, could be defined.

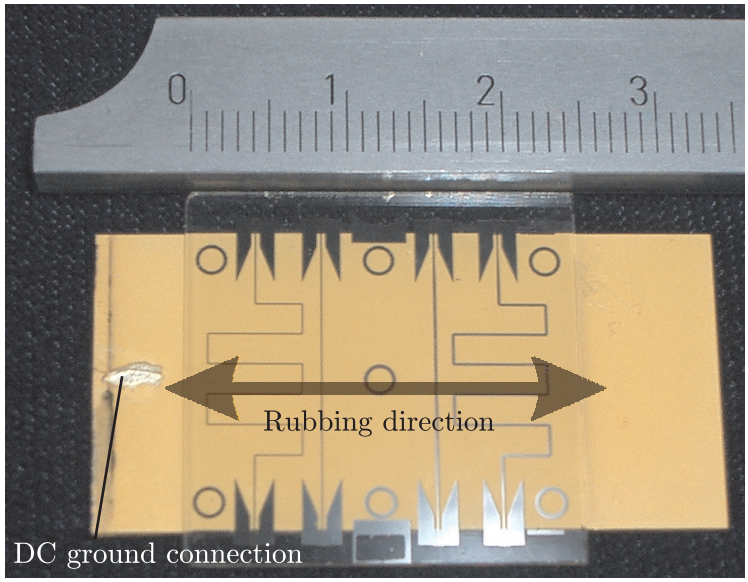

Figure 4.2: Photo of the realized device (bottom side). Four different phase shifters were realized on one substrate. The presented results were obtained with the two right most phase shifter (20 Ω transmission lines). The spacer areas are located within the circles on the fused silica substrate. The arrow indicates the rubbing direction. Ruler scale is in centimeter.

Fig. 4.2 shows a photograph of the fabricated structure. The view shows the bottom side of the device. Four phase shifter devices were fabricated in parallel: Two short sections and two meandered sections with each pair consisting of a transmission line with low impedance (20 Ω, $w = 200\,\mu$m) and one with slightly higher impedance (35 Ω, $w = 100\,\mu$m). The design was optimised for the 20 Ω line. The second line was put on the mask in case the manufacturing tolerances especially of the LC layer thickness are too large. The ground plane on the silicon substrate is connected to DC ground by carrying the ground potential via a thin copper wire to

the backside of the silicon substrate where it can easily be contacted on-wafer by an additional bias probe. Both substrates are treated with rubbed polyimide layers for orientation. The rubbing direction is indicated in Fig. 4.2. The orientation layer was realised using Nylon 6 (see Appendix A).

Characterisation results

The characterisation of the device was done using an Alessi REL-4300 probe station with 150 µm CPW probes and an Anritsu 37397C VNA. During the measurement, the silicon plate was placed under applying of slight pressure on top of the fused silica substrate (with the spacers glued to it, as described above). Fig. 4.3 shows the measurement results. The measurements are compared with the simulation (Fullwave, Sonnet). The agreement is in general fairly good although the input matching is not as good as simulated but nevertheless still acceptable. The transmission loss is one dB higher than simulated which can be attributed to the higher metallic loss due to the surface roughness of the gold electrodes.

The input matching of the short phase shifter is also acceptable but differs from the simulation more than in case of the long phase shifter. In both cases, the frequency of good input matching is shifted to lower frequencies. For both phase shifters, the insertion loss reduces by 2 dB when applying a bias voltage of max. 40 V. In Fig. 4.3(c), the efficiency of both phase shifters is shown. This phase shifter efficiency η_{PS} is defined as (see [Mül07])

$$\eta_{PS} = \frac{(\arg(S_{21}(V_b = V_{max})) - \arg(S_{21}(V_b = 0))) * 180}{\pi \cdot 20\log(\min(|S_{21}|))} \cdot \frac{^\circ}{\mathrm{dB}} \tag{4.1}$$

i.e. as the differential phase shift in degree divided by the maximum insertion loss in dB. In both cases, the efficiency is not very high which can be attributed to the high metallic loss which comes with thin LC layers[1]. The efficiency of the short phase shifter is slightly less compared to the long phase shifter as here the impact of the not tunable feed section has more influence. For both phase shifters, the efficiency is improving versus frequency as the metallic loss increases only with $\sqrt{\omega}$.

Fig. 4.3(d) depicts a typical switching process which takes place when the bias voltage is removed. The response time is about 3.5 s which represents an improvement compared to [Mül07] and to the results shown in section 3.2.3 for the 60 µm LC layer. The response time could be further accelerated by using low frequency AC bias voltages. The use of such AC bias voltages will be addressed in more detail in section 4.2. The results of the phase shifter with the 30 Ω transmission lines are not shown because their performance was greatly degraded by poor input matching.

While the device and the technology developed for it are a good start for further development to reduce the LC layer thickness even further, it is obvious that the overall transmission line loss is rather high. On the one hand, this originates from the lossy LC used in the device. On the other

[1] or with thin microstrip substrates in general

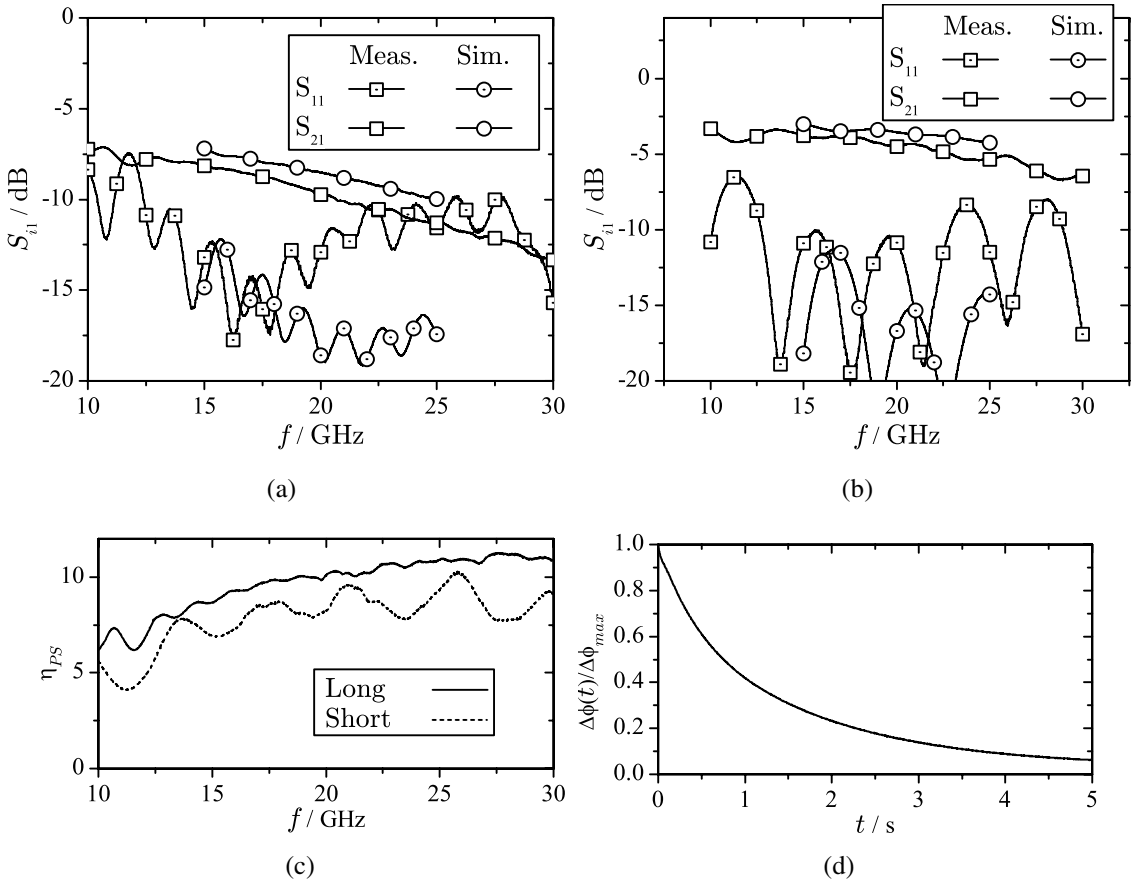

Figure 4.3: Results of the phase shifters shown in Fig. 4.2. (a) Recorded scattering parameters of the longer 20 Ω phase shifter and (b) the results of the short 20 Ω section. (c) The phase shifter efficiency for both sections. (d) The response time t_{decay} of the devices. Shown is the differential phase shift $\Delta\phi$ vs. time normalised by the maximum available phase shift.

hand the performance is dominated by the metallic loss due to the small gap between conductor and groundplane. In [KFNU02], this is investigated by means of simple full-wave simulation. Due to the high impact of the metallic loss the distributed element approach was not pursued further but the technology was used for realising tunable capacitors. Before this is presented in the next section, the asymptotic characteristic of the metallic loss in a transmission line structure is given which will show why transmission lines are asymptotically unsuitable. On this basis, it will be shown later on in this chapter why a tunable capacitor is the better choice for realising devices with thin LC layers with which it will eventually be demonstrated that fast response times are possible also for microwave devices.

4.1.2 Metallic Loss in Striplines

The general dependency of metallic loss of a Metal-Insulator-Metal (MIM) type transmission line on its physical dimensions can be examined easily using a structure as shown in Fig. 4.4. This structure is insofar general, as the canonical domain of a conformal mapping of an arbitrary

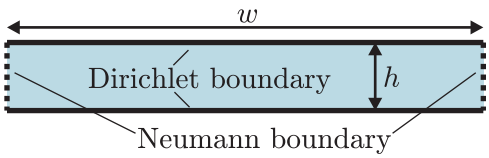

Figure 4.4: Simple model of a Metal-Insulator-Metal waveguide.

TEM waveguide problem looks like the structure shown in Fig. 4.4. The top and bottom sides of the calculation domain in Fig. 4.4 are electrodes (Dirichlet boundaries), the left and right side walls are Neumann boundaries. The problem is simplified such that the calculation domain is uniformly filled with an arbitrary material. The actual material properties do not play a role in the following considerations.

As given in e.g. [Whe64], the inductance per unit length for a problem as in Fig. 4.4 is given by

$$L' = \mu \frac{h}{w} \tag{4.2}$$

and the capacitance per unit length by

$$C' = \varepsilon \frac{w}{h}. \tag{4.3}$$

The impedance of such a transmission line is then given by

$$Z_{MIM} = \sqrt{\frac{\mu}{\varepsilon}} \cdot \frac{h}{w} \tag{4.4}$$

For a TEM transmission line for high frequencies and low loss, the following relation for the attenuation constant can be assumed [ZB00]:

$$\alpha \approx \frac{\sqrt{L'C'}}{2} \left(\frac{R'}{L'} + \frac{G'}{C'} \right). \tag{4.5}$$

As G' is associated with the dielectric loss and only metallic loss is to be considered here, $G' = 0$ can be assumed. For the simple structure in Fig. 4.4 R' can be assumed to be

$$R' = \frac{R'_0}{w}. \tag{4.6}$$

R'_0 is a general resistance per unit length of the transmission line describing effects like metal conductivity, conductor thickness and skin effect. Eqn. (4.6) does explicitly not include e.g.

effects like current crowding at conductor edges as there are no such edges for the considered structure. It should be noted that if the structure of Fig. 4.4 is to be considered as the canonical domain of a conformal mapping operation, edge effects can be included by assuming a more complex description of R'_0, i.e. $R'_0(w)$ has to be considered.

Substituting Eqns. (4.2), (4.3) and (4.6) in Eqn. (4.5) the following formula for the attenuation can be obtained:

$$\alpha \approx \sqrt{\frac{\varepsilon}{4\mu}} \left(\frac{R'_0}{h} \right). \tag{4.7}$$

From this, it can be easily seen that, in terms of geometry parameters, only the thickness h of a MIM structure plays a role in terms of metallic loss. This insight is more or less directly applicable to microstrip topologies or parallel stripline topologies. However, Eqn. (4.7) only describes the asymptotic behaviour for large w/h ratios of real MIM topologies. This can be understood if one considers the current crowding at the edges of a stripline. The wider such a strip line becomes, the smaller the influence of the edge effects becomes and the resistance per unit length can be described by Eqn. (4.6).

In Eqn. (4.7), it is implicitly assumed that the characteristic impedance of the transmission line can be chosen arbitrarily. If this is not the case and Z_{MIM} is fixed, Eqn. (4.7) is reformulated as

$$\alpha \approx \frac{R'_0}{2 Z_{MIM} w}. \tag{4.8}$$

Although this is only a simple mathematical reformulation in order to express the losses in terms of the characteristic impedance, Eqn. 4.8 shows that low impedances mean high metallic losses which can only be avoided by using a broad conductor which in turn means a large h due to the fixed w/h ratio.

The above reasoning shows why simple transmission line structures are not suitable to build LC based tunable devices: While low layer thicknesses h are necessary for fast response times, the metallic losses increase due to Eqn. (4.7) in a most unfavourable way. Taking the examples presented in [Mül07] which feature a rather high phase shifter efficiency, it is obvious that these transmission lines, if they had a LC layer thickness of 20 µm like the one presented in section 4.1 instead of ~ 250 µm, would exhibit an approximately 10 times higher attenuation only due to metallic loss. The input matching of a low impedance transmission line poses additional problems. The only benefit of transmission lines with low impedance (and hence thin dielectric) would be the slightly increased tuning efficiency due to the higher w/h aspect ratio due to which more electric field is concentrated in the tunable material.

4.2 Tunable Parallel Plate Capacitors

Beside the fact of increased metallic loss, the thin layers in section 4.1 also did not quite meet the expectations in terms of response time. In order to overcome these limitations, a parallel plate

capacitor can be used. This device combines the advantages of being able to realize very thin layers (down to a few µm) while at the same time the metallic loss does (almost) not depend on the layer thickness as will be shown below. For the realisation of such thin layers, the technology introduced in the previous section can be used with some enhancements in terms of applying the spacers. Furthermore, a substrate material like silicon cannot not be used anymore as no large groundplane is necessary but rather on both sides substrates with good microwave properties are necessary.

A further advantage of going towards very thin layers is the significantly reduced amount of liquid crystal necessary for filling a device. The fact that very little material is necessary has in particular significance for research efforts as they have been conducted in the scope of this work. While standard materials (5CB, E7) are available in arbitrary amounts, optimised laboratory grade materials are only available in some 100 mg or very often even less. This problem is furthermore severe because no good commercial materials are known at this time. If a cavity height of 5 µm is assumed and a footprint size of 1 cm^2, one obtains a volume of $0.5 \cdot 10^{-3}$ cm^3. As most nematic liquid crystalline materials have a density around 1 g/cm^3 [SBR+83], devices fabricated according to the scheme presented here only require some micrograms. This will of course also be an advantage once such a scheme for RF devices is commercialized. The market prices for display liquid crystals range below 15 $/gram [HH08] and it can be conjectured that the material cost for LC will only play a minor role.

4.2.1 Fundamental Design

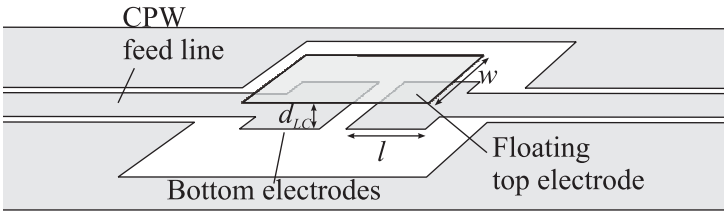

Figure 4.5: The structure of a single series capacitor

Fig. 4.5 shows the structure of the parallel plate capacitor developed in the scope of this work. The capacitor consists mainly of two patches which are fed by a coplanar waveguide (CPW) line. The actual parallel plate capacitor is formed by using a floating electrode above the two patches. This approach was chosen in order to avoid the necessity for interconnects through the LC layer and to keep the overall manufacturing effort low. Particularly, interconnects through the LC layer need more advanced fabrication technology, the means for which were not available in the scope of this work.

The basic schematic shown in Fig. 4.5 also enables the adjusting of the stray capacitance to ground. However, if the ground electrode is moved away from the center electrode, the lowered

stray capacitance is bought at the expense of a low series inductance. The patterning of the necessary conductors on the fused silica substrate can be done by standard lithography processes. The detailed process steps are given in Appendix A. For the capacitors as well for the devices presented in the following sections, Nylon 6 was used as orientation layer.

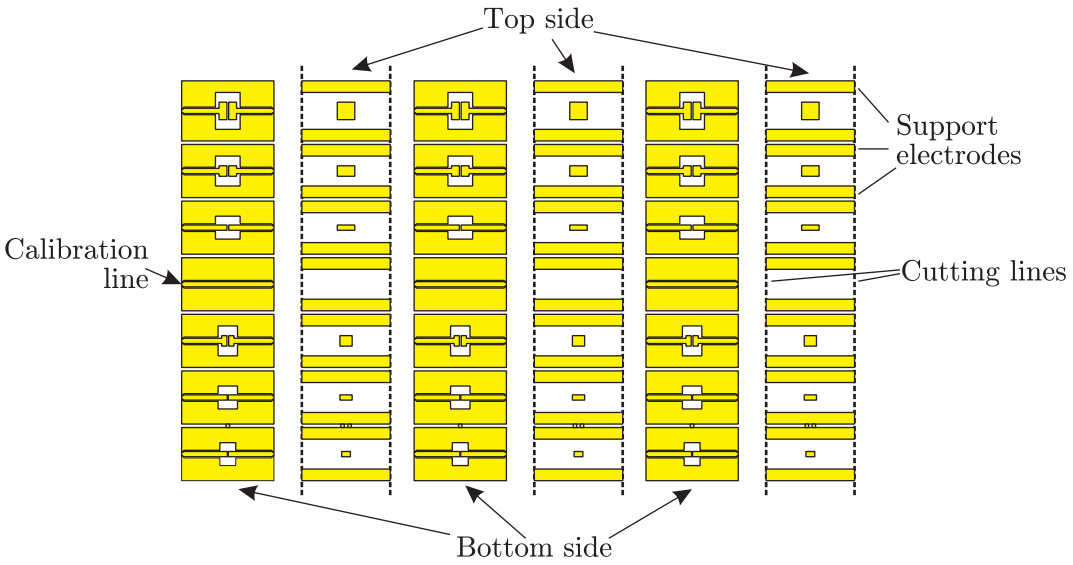

Figure 4.6: Mask layout used for fabricating three sets of capacitors in one lithography step.

In order to verify the principle and evaluate the technological feasibility, a set of capacitors was realised. Fig. 4.6 shows the mask used for the fabrication of the devices. Always three sets of capacitors were fabricated in one lithographic step in order to obtain enough working devices. The dashed lines in Fig. 4.6 represent the cut lines for the dicing process. In every set, a straight transmission (calibration) line is included having the same dimensions as the feed lines of the capacitors. This line is used for deembedding the individual devices and it is designed to have a characteristic impedance of 50 Ω.

As a broadband evaluation of the individual devices was aimed for, particularly for the material characterisation, a TRL calibration is not suitable as then the frequency range would be limited particularly towards low frequencies. Although the frequency range could by extended to low frequencies by using a multi-TRL calibration, the required through line standard would be unwieldily long and would therefore take much substrate space and extra fabrication effort. As a simpler method, a standard short-open-load-through (SOLT) calibration was chosen which however required that the calibration plane is directly located at the feed line of the device. With the available accuracy due to dicing this could be achieved. A schematic of the transition from a regular CPW line to the sandwiched CPW line is shown in Fig. 4.7(a). The top substrate is cut along the dashed lines indicated in Fig. 4.6 such that the CPW probes (150 µm pitch) can be placed within a distance of 120 µm from the edge of the top substrate and therefore from the feed line. As the SOLT-calibration plane is located at the tips of the CPW probes this short distance is electrically negligible. Therefore, as will be explained in more detail below, it is possible to deembed the individual capacitors by measuring the straight transmission line.

In Fig. 4.7(b), a cross sectional view through the feed and the capacitor section is shown. Fig. 4.7(c) shows a photograph of a realised set of capacitors. The cavity in between the two substrates is filled with liquid crystal by capillary attraction after the substrates have been glued, i.e. the cavity is not sealed.

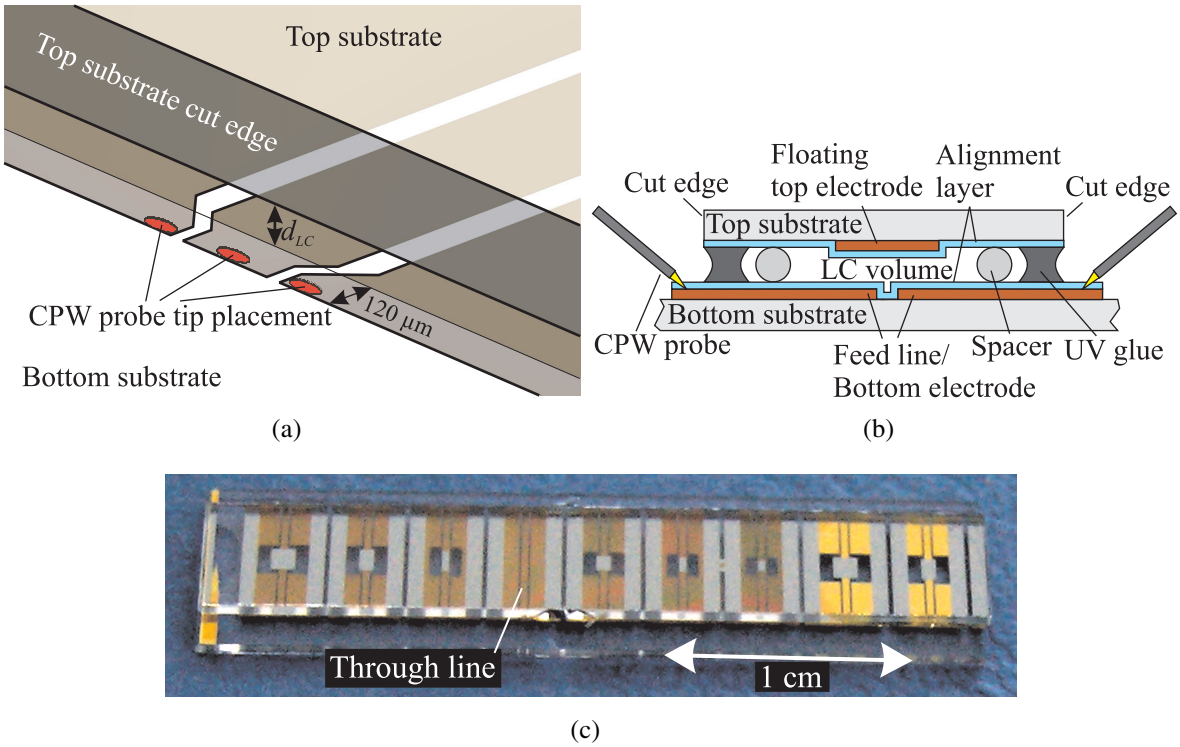

Figure 4.7: The realised parallel plate capacitors. (a) Schematic of the transition from the CPW probes to the sandwiched CPW line (the vertical distance d_{LC} between the two substrates is not to scale). (b) Cross sectional view on the structure. (c) Photograph of a realised structure. The substrates have a thickness of 700 µm.

The actual parallel plate capacitor is evaluated by removing the influence of the feed lines which are identical to the straight transmission line, which is part of each set of capacitors. For that purpose, the scattering parameters of a generic TEM waveguide are considered:

$$\begin{aligned} S_{11} = S_{22} &= \frac{(Z_l^2 - Z_0^2)(1 - \mathrm{e}^{-2\gamma l})}{(Z_l + Z_0)^2 - (Z_l - Z_0)^2 \mathrm{e}^{-2\gamma l}} \\ S_{21} = S_{12} &= \frac{4 Z_l Z_0 \mathrm{e}^{-2\gamma l}}{(Z_l + Z_0)^2 - (Z_l - Z_0)^2 \mathrm{e}^{-2\gamma l}} \end{aligned} \tag{4.9}$$

Z_0 is the reference impedance. The characteristic impedance Z_l can be determined by evaluating the measured $|S_{11}|$ at $\gamma l = j\beta l = j\pi/2$ which corresponds to the maximum value of $|S_{11}|$. This assumes that the transmission loss is small enough which is given for the present transmission line:

The insertion loss is 0.4 dB at most at the first maximum of $|S_{11}|$. The real valued characteristic impedance is then given by

$$Z_l = Z_0 \frac{\sqrt{1-S_{11}^2}}{1-S_{11}}$$

for S_{11} being real valued with $-1 < S_{11} < 1$. With the accordingly calculated Z_l, Eqn. 4.9 can be solved for γl which then represents the phase delay and the insertion loss of the transmission line. With l_c being the length of the measured calibration line and l_f the length of the feed line of a capacitor, the electrical length of one feed line is

$$\gamma l_f = \gamma l \frac{l_f}{l_c}.$$

With the obtained parameters Z_l and γl_f it is possible to determine the ABCD-parameters $\mathbf{A}_{feed}$ of the feed lines. The inverse matrix $\mathbf{A}_{feed}^{-1}$ is obtained by using $-\gamma l_f$ instead of γl_f. The capacitor, represented by the ABCD-matrix $\mathbf{A}_C$ can then be deembedded according to

$$\mathbf{A}_C = \mathbf{A}_{feed}^{-1} \mathbf{A}_{meas} \mathbf{A}_{feed}^{-1}.$$

$\mathbf{A}_{meas}$ is the ABCD-matrix of the respective measurement with the SOLT calibration plane directly at the edge of the upper substrate (see Fig. 4.7(a)). Fig. 4.8 shows a typical measurement of the through line. As can be seen, the input matching is very good, suggesting that the transmission line has a characteristic impedance very close to 50 Ω. In fact, the evaluated impedance of all structures realised in the scope of this work is around 52 Ω.

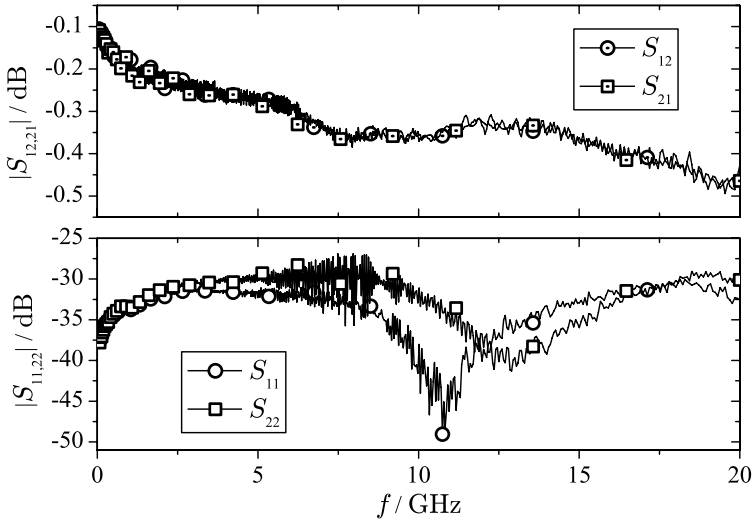

Figure 4.8: Typical measurement results of the transmission line used for deembedding the capacitors.

The capacitance value itself can by determined by converting $\mathbf{A}_C$ to the Y-matrix representation. Then, the series capacitance C_s is given by

$$C_s = -\frac{\Im(Y_{21})}{\omega} \tag{4.10}$$

with Y_{21} being the respective entry of the Y-matrix representation. The quality factor is calculated accordingly:

$$Q = \frac{\Im(Y_{21})}{\Re(Y_{21})} \tag{4.11}$$

Before presenting results of realised capacitors in the following sections, important properties of tunable parallel plate capacitors are reviewed. These are the asymptotic behaviour of the metallic loss, the frequency dependency of the tunability and the quality factor. In the next section, an estimate of the tuning efficiency is derived, i.e. it will be shown at what percentage the tunability of the material is exploited in the device.

4.2.2 Tuning Efficiency Calculation Using Conformal Mapping

In [Mül07] it was shown that with an inverted microstrip line for reasonable line impedances at most 70 % tuning efficiency can be obtained. In the aforementioned work, a conformal mapping method was employed in order to determine the geometric tuning efficiency $\eta_{\tau,geom}$ in terms of geometric parameters of the cross section of a transmission line. This conformal mapping approach was extended further in this work in order to evaluate the influence of the more complex geometries of the capacitors presented above on $\eta_{\tau,geom}$. It is worth mentioning that the evaluations performed in this chapter could have also been done using 3D field solvers. However, using these tools usually comes with high meshing effort, specially due to the high aspect ratios.

The Schwarz-Christoffel Formula

In section 3.2.2, a conformal mapping approach was already used for extracting the permittivity of a tunable layer from the effective permittivity of a dielectric multilayer structure. To some extend, the same formulas [Sva92] can also be used to asses the tuning efficiency of the capacitor structures presented previously. However, one is limited to one specific geometry which does not entirely reflect the geometric structure of the capacitors. Therefore, a simple tool was needed to efficiently evaluate the tuning efficiency of the tunable capacitors.

The problem of computing the field distribution or the potential of a (2D) structure with more or less arbitrary boundaries can be elegantly solved if the conformal mapping function from the actual physical problem domain into a so called canonical domain is known, the latter of which allows greatly simplified solution of e.g. Laplace's equation. The physical domain can also extend to infinity. Laplace's equation can be solved in either domain as it is invariant under conformal transformation [SL03].

The Schwarz-Christoffel mapping, establishing a conformal map from the upper complex half plane w to the interior of a polygon in the complex z plane, is commonly used to solve Laplace's

equation for more complex electrode structures. The function $f(z)$ for this mapping is given by Eqn. (4.12) [SL03, BSMM95]. The geometrical meaning of Eqn. (4.12) is depicted in Fig. 4.9.

$$z = f(w) = C_1 \int_0^w \frac{dt}{\prod_{i=1}^{N} (t - w_i)^{1-\frac{\xi_i}{\pi}}} + C_2. \tag{4.12}$$

The integration path can be arbitrarily chosen as the integrand is analytic. Solving the integral numerically is in general difficult specially due to the singularities present in the equation [Ban08]. It should be noted that in [Whe64] or [Sva92], for that matter, methods are shown how to simplify the problem to make it analytically manageable.

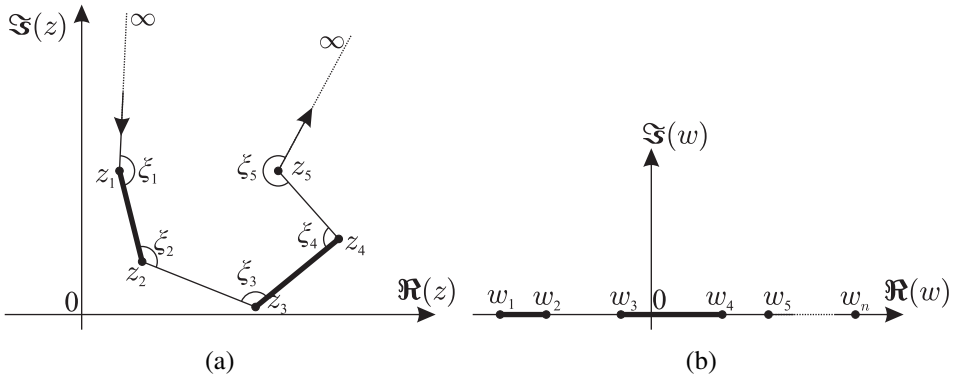

Figure 4.9: The principle of the Schwarz-Christoffel transformation. The function maps points from the (b) upper complex half plane (the canonical domain) onto the (a) interior of a polygon (the physical domain)

The actual problem when using the Schwarz-Christoffel mapping is to find the so called prevertices w_i in Eqn. (4.12) which determine the actual mapping function [DT02]. Furthermore, the constants C_1 and C_2 have to be found. This is called the Schwarz-Christoffel parameter problem. For simple polygons, this problem can be solved analytically as done in [Whe64]. If the polygon becomes more complex, the parameter problem has to be solved numerically which results in a system of nonlinear equations relating the unknown w_i to the polygon corners z_i (Fig. 4.9(a)).

With the parameter problem solved, a second conformal mapping step is necessary to map the upper complex half plane, which is still infinite, to a confined structure, that is to an ideal parallel plate capacitor with two electrical boundaries (the plates, Dirichlet boundaries, see the bold printed lines in Fig. 4.9) and two Neumann boundaries (the side walls). This mapping can be directly derived from Eqn. (4.12) with the polygon assumed to be a rectangle. The respective corners z_i of the rectangle and therefore the extend of the ideal parallel plate capacitor are then directly determined from Eqn. (4.12). Generally, the respective mapping results in elliptical integrals which can be solved easily [KO89]. For instance, conformal mapping approaches for coplanar waveguides (e.g. [Poz04]) usually incorporate such elliptical integrals as for such electrode configurations only the upper half plane needs to be considered with the electrodes located

directly on the real axis. The ideal parallel plate capacitor domain will furthermore be called canonical domain.

All solutions to the above mentioned problems, i.e. solving the parameter problem and computing the actual map are contained in a powerful MATLAB toolbox which is freely available[2] [Dri02, Dri05]. Furthermore, the toolbox implements the numerical inversion (see [Tre79]) of the mapping in Eqn. (4.12). It supports infinite (physical) vertices and therefore allows to map infinite physical domains to finite canonical domains. An example how the toolbox is used for a similar application can e.g. be found in [GBC+01].

Application to Parallel Plate Capacitors with Tunable Dielectric - Quasi-static Evaluation

The tunable capacitors as introduced in section 4.2.1 are evaluated in terms of the geometric tuning efficiency in the following. This tuning efficiency is defined as the ratio between the effectively available tunability of the capacitor τ_C and the tunability of the material τ_{LC}, i.e.

$$\eta_{\tau,geom} = \frac{\tau_C}{\tau_{LC}}. \tag{4.13}$$

This efficiency depends mainly on the electrode geometry and on the permittivities of the materials involved. Although a more complex treatment is necessary for anisotropic materials, the dielectric is considered as isotropic for each tuning state. In terms of the director, this means that for the perpendicular alignment (no bias) the director is always fully perpendicular to the electric field and fully parallel for the parallel alignment. Because of this, the evaluation will always be slightly optimistic. For the perpendicular case, i.e. with the director oriented parallel to the substrate surfaces, the effective permittivity will be in reality higher as the electric field has partly parallel components which makes the isotropically calculated permittivity too low. For the parallel case this effect is negligible as the director can be assumed to be in parallel to the bias field and therefore in parallel to the RF field.

The evaluated structure is shown in Fig. 4.10(a) with the respective cross section in Fig. 4.10(b). The model also accounts for the thickness of the electrodes. The cross sections shown in Figs. 4.10(b) and 4.10(c) are used to evaluate the tuning efficiency. For that purpose, the respective cross section has to be transformed into the canonical domain, i.e. into the ideal parallel plate domain. In order to do that, an adequate polygon representing the physical domain has to be found. For the cross section in Fig. 4.10(b) the polygon shown in Fig. 4.11 is used. The evaluation of the cross section in Fig. 4.10(c) is done using the simple model from [Sva92] (see also section 3.2.2). The polygon edges printed in bold are transformed into the electrical boundaries of the ideal parallel plate capacitor. The polygon in Fig. 4.11 contains an electrical wall (Edges $\overline{12}$ and $\overline{910}$) which allows to limit the calculation to only half of the structure. The model also allows to consider a finite extent of the lower electrode (Edges $\overline{23}$ and $\overline{89}$). The vertex coordinates and polygon angles in the complex plane are listed in Table 4.1 with the origin located at vertex 1.

[2] As a matter of fact this toolbox is highly popular, judging from how often it is referred to.

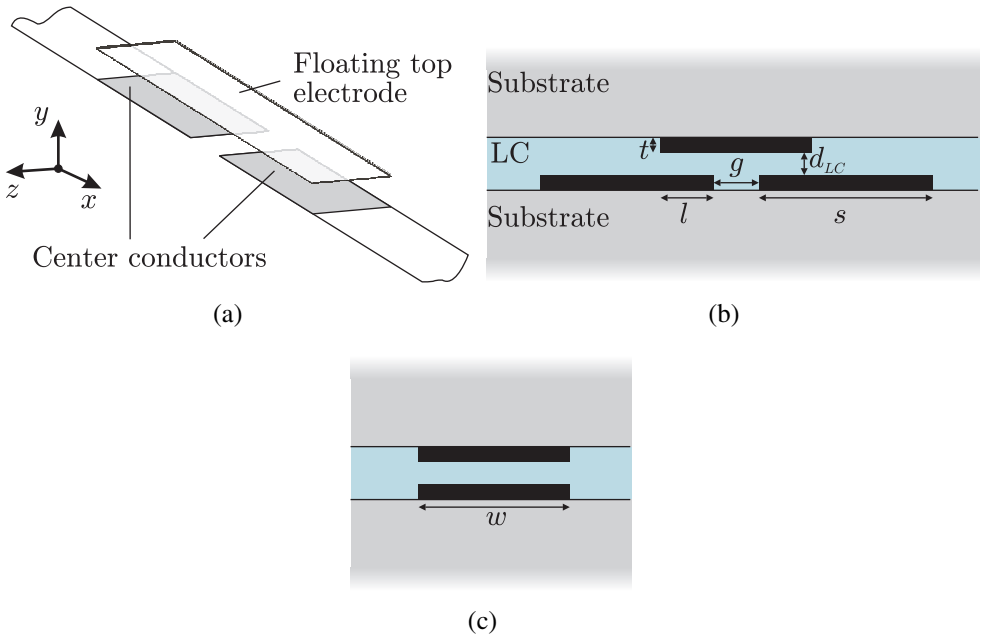

Figure 4.10: (a) The considered capacitor structure with floating electrode. (b) Two dimensional cross section along the structure with the corresponding dimensions. (c) Two dimensional cross section across the structure.

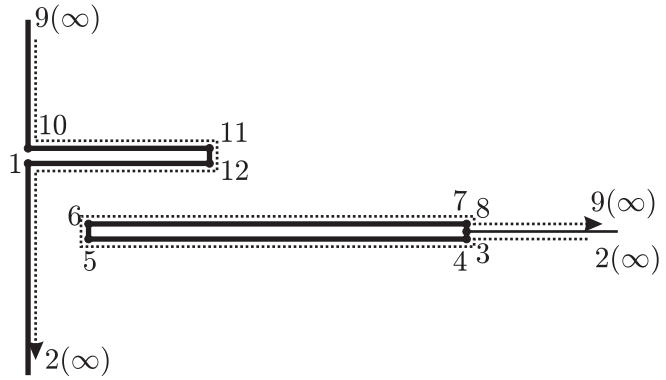

Figure 4.11: The polygon in the physical domain. The dashed lines indicate the orientation of the polygon.

The Matlab toolbox mentioned above allows to calculate the conformal map from a rectangle to the polygon as shown in Fig. 4.11 using only the vertex information listed in Table 4.1. The corners, and therefore the width and height, of the canonical domain are a result of the solution of the parameter problem. The remaining problem is how to treat the different permittivities of the involved layers because the conformal mapping approach either assumes that there is uniform material [Whe64] or that the mapped material boundaries can be further simplified which allows then to section the ideal parallel plate capacitor into series and parallel capacitances according to the corresponding permittivities [Whe65, Sva92].

Vertex	Pos. z_i	Angle ξ_i
1	0	$1/2\pi$
2	∞	$-1/2\pi$
3	$g/2+s-j\cdot(d_{LC}+t/2)$	$1/2\pi$
4	$g/2+s-j\cdot(d_{LC}+t)$	$3/2\pi$
5	$g/2-j\cdot(d_{LC}+t)$	$3/2\pi$
6	$g/2-j\cdot d_{LC}$	$3/2\pi$
7	$g/2+s-j\cdot d_{LC}$	$3/2\pi$
8	$g/2+s-j\cdot(d_{LC}+t/2)$	$1/2\pi$
9	∞	$-1/2\pi$
10	$j\cdot t$	$1/2\pi$
11	$g/2+l+j\cdot t$	$3/2\pi$
12	$g/2+l$	$3/2\pi$

Table 4.1: Vertices of the polygon in Fig. 4.11.

The approach for a simple tuning efficiency estimation chosen in this work follows a hybrid scheme which uses the conformal mapping as described above using the Matlab toolbox. In a second step, Laplace's equation is solved on a Finite Integration (FIT) grid [Wei05] in the canonical domain including the accordingly mapped material regions. A FIT electro static solver can be implemented rather straight forwardly, specially if two boundaries are electric and two are Neumann type boundaries. The mesh used in this work is equidistant but as the problem is only two dimensional a high mesh density is affordable (500x500 mesh cells). The outlined approach actually follows e.g. [WL97, CC93, ZM95]. Further applications of this hybrid scheme can be found in [SWJC88, CWC90, KS95, KLV08].

Prior to the presentation of the analysis of the impact of the structural parameters, an example is shown, how the material boundaries according to Fig. 4.10(b) map into the canonical domain. Fig. 4.12 shows a comparison of the physical and canonical domains. In the physical domain, the electric flux lines and the equipotential lines are shown, however without influence of the material, i.e. they are obtained by direct mapping of vertical (electrical flux) and horizontal (equipotential) lines in the canonical domain to the physical domain. Conversely, the material borders in the canonical domain are found by mapping the dashed lines in Fig. 4.12(a) into the canonical domain. Once the material boundaries in the canonical domain are known, a electrostatic field solver can be applied.

Results of the Quasi-static Evaluation

The tunability in the following evaluations is assumed to be $\tau_{LC} = 25\,\%$ with $\varepsilon_{r,\perp} = 2.5$, which represents usual values for LC in the microwave region. The results were found to vary only very little as τ_{LC} changes. For the permittivity of the enclosing substrates, the values of 1, as an optimum value, and 3.8, being the permittivity of fused silica, are selected. The impact of a

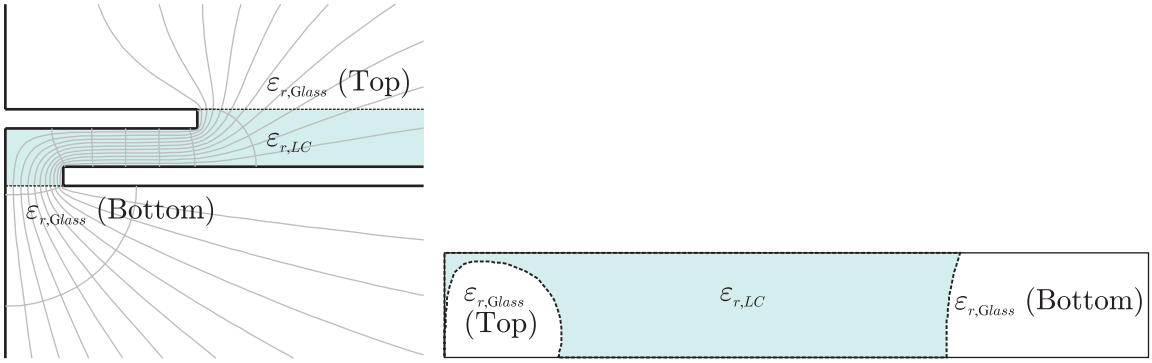

Figure 4.12: (a) The physical domain of the cross section along the tunable capacitor with material boundaries. Also sketched are the electric flux lines and the equipotential lines (without influence of the material). (b) The canonical parallel plate capacitor. Indicated are the individual regions corresponding to the material regions in the physical domain.

high permittivity substrate (ε_r =10) is also analysed. The crucial parameters which determine the tuning efficiency are obviously the ratios g/d_{LC} and l/d_{LC} (see Fig. 4.10(b)). Fig. 4.13 shows the results of the conformal mapping approach according to Fig. 4.12.

Obviously, the permittivity of the enclosing substrates should be as low as possible. Achieving a high efficiency is easy without any substrate ($\varepsilon_r = 1$), but already with a material like fused silica, which has a not too high permittivity, large l/d_{LC} aspect ratios are necessary. The reason why the tuning efficiency is rather strongly deteriorated for high enclosing permittivities is that the portion of the field going through the not tunable substrate becomes rather large and therefore the capacitance made up by these fringing fields, which is parallel to the actual, tunable capacitance, becomes large. As can be seen from Fig. 4.13, increasing the g-dimension does not improve things significantly. The latter argument is actually important as this means that the capacitor can be kept small, i.e. no trade-off is necessary between high tuning efficiency and the series inductance which strongly depends on the overall length $(2l + g)$.

Fig. 4.14(a) shows the influence of the aspect ratio w/d_{LC} (see Fig. 4.10(c)). Obviously, the influence of the fringing fields is not as strong as for the other cross section in Fig. 4.10(b). The evaluation again considers different permittivities of the containing substrates. Finally, the tuning efficiency of the overall structure in Fig. 4.10(a) must be determined. This can be done by multiplying the efficiencies in the xy-plane (η_τ^{xy}, Fig. 4.10(b)) and the efficiency in the yz-plane (η_τ^{yz}, Fig. 4.10(c)). Assuming that $w = l$, the efficiency can be computed according to Fig. 4.14(b). It should be noted that a tunable capacitor with a simple step, as shown in Fig. 4.15(a), will have higher tuning efficiency because the actual tuning capacitance value will be twice as large as the fringing capacitance in parallel to it.

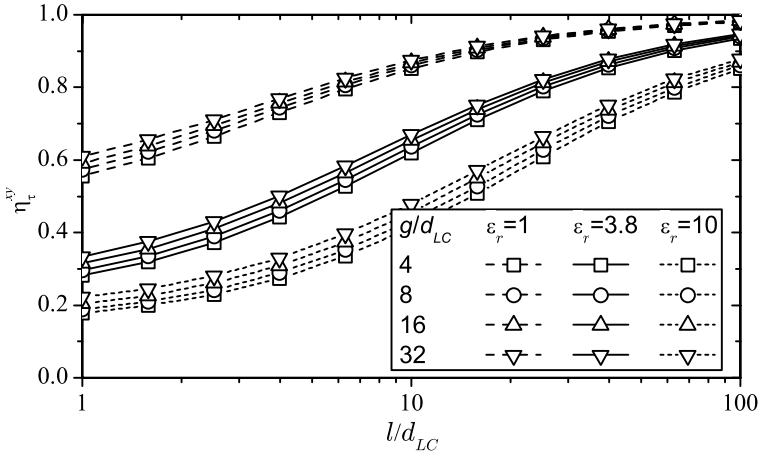

Figure 4.13: The calculated tuning efficiency of the two dimensional structure in Fig. 4.10(b) as a function of the l/d_{LC} ratio for different permittivities of the containing substrates and different g/d_{LC} ratios.

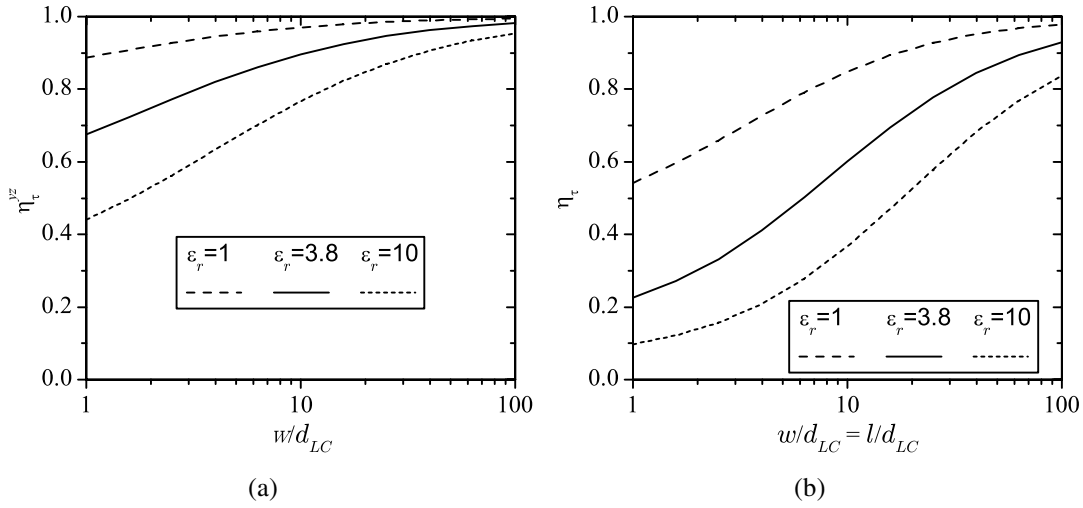

Figure 4.14: (a) Tuning efficiency along the *yz*-plane. (b) Overall efficiency of the entire structure.

4.2.3 Metallic Loss and Series Inductance of a Parallel Plate Capacitor

In order to determine the asymptotic behaviour of the metallic loss of a parallel plate capacitor in terms of the geometric dimensions, the current distribution on the electrodes must be known. The current distribution of a parallel plate capacitor as introduced in section 4.2.1 is therefore considered now. The derivations are made for a series capacitor embedded in a transmission line. More precisely, the capacitor is assumed to be fed by striplines and be made up by an overlap of these two striplines as shown in Fig. 4.15(a). The actual topology of the transmission line, i.e. whether it is a microstrip, strip or CPW line does not matter for the following considerations.

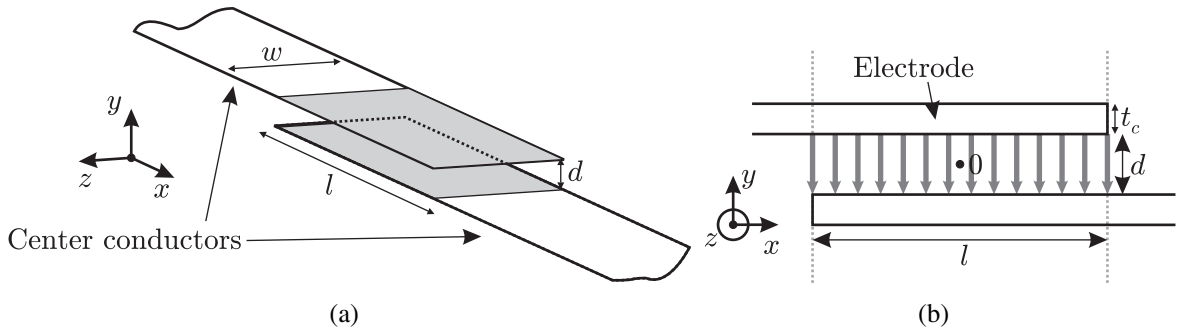

Figure 4.15: (a) The physical structure of a stripline fed parallel plate capacitor along with the coordinate system. (b) Cross section of the parallel plate capacitor. The vertical arrows indicate the electric field. The origin of the coordinate system is assumed to be in the center of the structure as indicated by the dot.

Fig. 4.15(a) shows the schematic of the considered structure along with the used coordinate system and the geometric dimensions. It represents half of the structure presented in section 4.2.1. In Fig. 4.15(b), a cross section of the same structure is depicted with the electric field indicated. The origin of the coordinate system is placed in the center of the structure (Fig. 4.15(b)). Although the electrodes have the thickness t_c in the figure, the actual value of the thickness is not considered and the electrodes are considered to be infinitely thin but to have two sides. The electric field, as well as the magnetic field, is assumed to be constrained to the capacitors area $l \cdot w$ which makes the model that of an ideal parallel plate capacitor. Taken for granted that the ratios l/d and w/d are large (e.g. > 10), this assumption can be considered to be a sufficiently precise model. As all fields are constrained to the gap, the material distribution of the real structure is irrelevant, however the gap is assumed to be filled with the relative permittivity ε_r.

For the treatment presented in this section, the conductivity of the electrodes is infinite. This means that only surface currents are present on the top and the bottom sides of the electrodes. As long as for a real capacitor the electrodes are considerably thicker than the skin depth, this is a valid simplification. As indicated above, the electrodes are also assumed to be thin enough in order to be able to neglect the influence of the electrode ends at $x = -l/2$ and $x = l/2$. The structure is assumed to be much shorter than a wavelength and the electric field in the gap is therefore describable by a potential. Ampere's Law

$$\nabla \times H = J + j\omega D \tag{4.14}$$

and Faraday's law

$$\nabla \times E = -j\omega B \tag{4.15}$$

are then decoupled. For the structure in Fig. 4.15 this allows to calculate the magnetic field inside the gap ($-l/2 < x < l/2$ and $-d/2 < y < d/2$) according to Eqn. (4.14):

$$\frac{\partial H_z}{\partial x} = j\omega D_y. \tag{4.16}$$

Accordingly, one obtains the following expression for H_z in the gap:

$$H_z(x) = j\omega\varepsilon_0\varepsilon_r E_y \cdot x + C. \tag{4.17}$$

Here, the constant C can be determined to be zero if the magnetic fields at $x = -l/2$ and $x = l/2$ have the same value but opposite sign. For an in y-direction symmetric transmission line like a CPW this is given, as will be seen below. In case of a microstrip line which has different magnetic field strengths below and above the signal electrode, C must be calculated such that $H_z(x)$ takes the respective values at $x = -l/2$ and $x = l/2$.

The current flow in x-direction on the electrode sides facing the gap can be calculated using Ampere's law in its integral form:

$$I(x) = H_z \cdot w = j\omega\varepsilon_0\varepsilon_r E_y wx = j\omega\varepsilon_0\varepsilon_r w\frac{V_c}{d} \cdot x. \tag{4.18}$$

This result is obtained by choosing the integration path according to Fig. 4.16(a). Eqn. (4.18) takes its simple form due to the absence of fields outside the capacitor area. The direction of the current on the other electrode is opposite. V_c is the voltage across the capacitor.

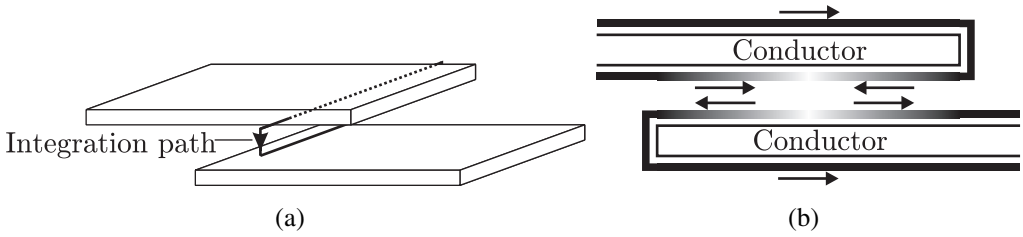

Figure 4.16: (a) Integration path used for the calculation of the current on the electrode sides facing the gap. (b) Current along the electrode. The shade of the bar surrounding the electrodes indicates the current magnitude.

Subsituting $x = l/2$ in Eqn. (4.18), half the current flow through an ideal parallel plate capacitor is obtained. As Eqn. (4.18) only gives half the current flow on the electrode sides facing the gap, the other half must be flowing on the sides not facing the gap which can be immediately understood from Fig. 4.16(b). Naturally, this means that the current flow through the capacitor is only determined by the actual capacitance value. Assuming that a certain capacitance value is to be realised, the dimensions w and l of course depend on the thickness d, i.e. as d is reduced the overlap area $w \cdot l$ has to be reduced accordingly. Considering the derived current distribution but a finite conductivity, which can be described by a sheet resistance $R_\square$, it can be immediately seen that the series resistance R_s of the capacitor will not change if the w/l ratio does not change. If it is possible to reduce l relatively more than w, the metallic loss can be reduced. In general, however, it is desirable to maintain $w \approx l$ as then the tuning efficiency is maximised (compare section 4.2.2). It can therefore be concluded that a thin LC layer (d_{LC}) does not increase the metallic loss of a capacitor as it is the case for transmission lines.

In order to verify the derivations presented before, a structure with representative dimension was examined using the EM simulation tool CST Microwave Studio. Figs. 4.17(a)-(c) show the results. The simulated structure corresponds to the one shown in Fig. 4.15(a) with the center electrode being embedded in a 50 Ω coplanar waveguide. The vertical gap between the overlapping center electrodes is $d = 10\,\mu\text{m}$. From Fig. 4.17, several properties can be identified as predicted above. First of all, from Fig. 4.17(a) it can be seen that the current on the outsides of the electrodes (i.e. the sides not facing the 10 µm gap) travels across the structure as it would over a straight electrode. In other words, in terms of current flow the capacitor behaves like a piece of transmission line. Fig. 4.17(c) shows the current flow on the insides of the electrodes, i.e. the sides facing the gap. Obviously, the current flow is predominantly in x-direction which corresponds to the derivations above. It is worth noting that the surface currents on the electrode sides facing the gap are bent in z-direction to the center of the structure as the l dimension becomes smaller as then the assumption that all fields are concentrated in the gap is more and more violated. From the theoretical derivation as well as from the results in Fig. 4.17, it can be deduced that the overall metallic loss depends on the current density of the transmission line that the capacitor is embedded in or, more general, on the current density on the strips.

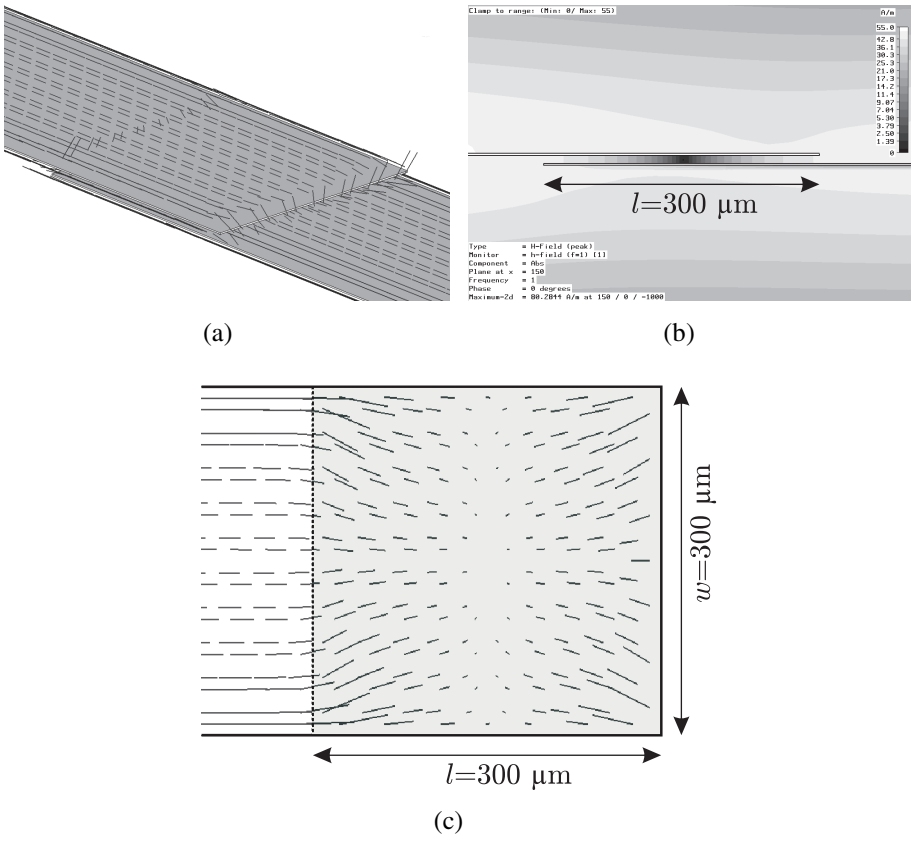

Figure 4.17: (a) Streamlines of the current flowing through the capacitor. (b) Cross section of the capacitor. The gray scale in the cross section indicates the strength of the magnetic field. (c) Surface current at the inside of either electrode

The series inductance of a capacitor as in Fig. 4.17(a) is consequently determined by the current distribution on the feeding strips. More precisely, because the capacitor behaves in terms of current flow like a continuous piece of transmission line, the self-inductance of the capacitor is determined by the transmission line type the capacitor is embedded in. The current on the electrode sides facing the gap, which is at most as large as the current flowing on the feeding strip line, does not contribute to the series inductance because the magnetic flux inside the gap associated with the current on the electrode sides facing the gap is negligible.

4.2.4 Frequency Dependency of Tunability and Quality Factor

In this section a model of a capacitor is described which allows to describe the characteristics of a capacitive device using a tunable dielectric. Fig. 4.18 shows the equivalent circuit. The loss of the actual capacitor C is represented by the parallel resistor R_P. The inductance of the conductors is represented by the inductance L.

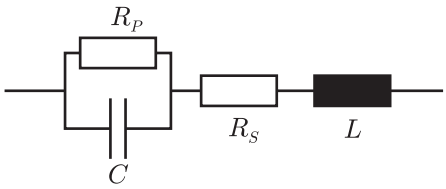

Figure 4.18: A general model of a capacitor. The parallel resistor R_P represents the loss in the dielectric and the inductor L the inductance of the conductors. The conductor loss is represented by R_S.

The capacitor is assumed to have a tunability of τ_{C0} with $C = C_0/(1-\tau_{C0})$. If the conductor loss is neglected ($R_S = 0$) and the capacitor is assumed to have an intrinsic quality factor of Q_0 determined by the dielectric, then $R_P = Q_0/(\omega C)$. If Q_0 is large, the series resonance of the circuit with the not tuned capacitor C_0 is $\omega_r = 1/\sqrt{LC_0}$. The inductance can be expressed in terms of the series resonance ω_r and the capacitance C_0:

$$L = \frac{1}{C_0 \omega_r^2}$$

The admittance Y of the circuit in Fig. 4.18 in terms of a tunability τ is then given by

$$Y(\tau) = \frac{\omega_r^2 \omega C_0 (1 + jQ_0)}{\omega_r^2 Q_0 (1-\tau) + \omega^2 (j - Q_0)} \tag{4.19}$$

Using Eqn. (4.19) the effective tunability τ_C of the circuit is calculated according to Eqn. (4.20).

$$\tau_C = \frac{Y(\tau = \tau_{C0}) - Y(\tau = 0)}{Y(\tau = \tau_{C0})} \tag{4.20}$$

The complete evaluation of Eqn. (4.20) is not shown here as the result is a lengthy expression which does not provide much insight except for one thing: It is independent of C_0.

Fig. 4.19(a) shows τ_C for different quality factors Q_0 with a constant tunability of 0.25 vs. ω/ω_r. Constant tunability and varying quality factors are considered because the tunability of liquid crystals does not vary too much from compound to compound but the loss does so quite much. As can be seen from the figure, the tunability increases as the frequency reaches the series resonance. The more pronounced this effect is, the higher the intrinsic quality factor is. The effective quality factor normalised by the intrinsic Q_0 of the circuit in Fig. 4.18 is given by

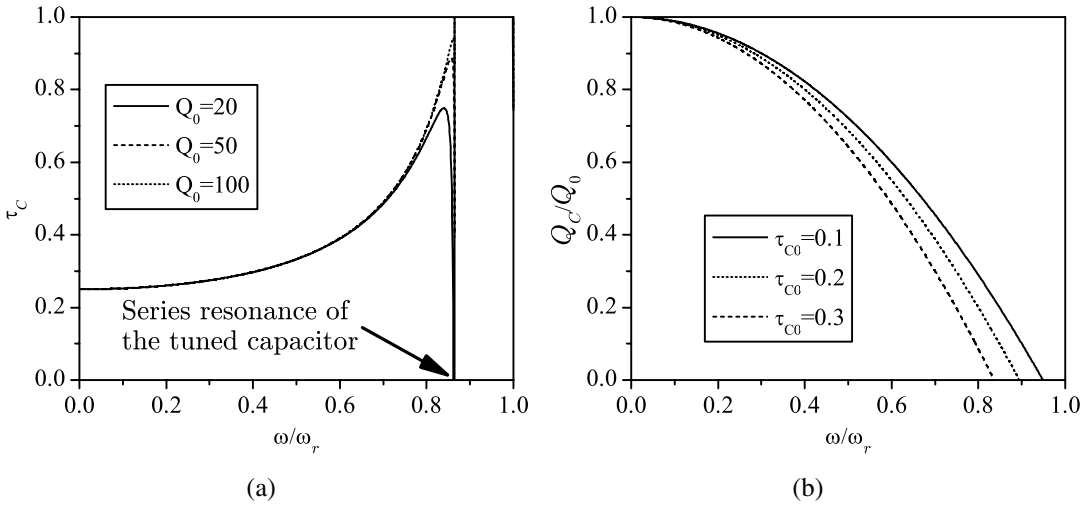

Figure 4.19: Impact of the series inductance on the tunability and the quality factor. (a) The tunability for different intrinsic quality factors and for $\tau_{C0} = 0.25$. The arrow indicates the series resonance of the tuned capacitor which is always lowest. (b) The normalised quality factor of the entire capacitor for different tunabilities.

$$\frac{Q_C}{Q_0} = 1 - \frac{Q_0^2 + 1}{Q_0(1-\tau_{C0}) \cdot \frac{\omega^2}{\omega_r^2}}.$$

Q_C does not depend on C_0, either. For $Q_0 \gg 1$ the impact of Q_0 becomes negligible and only the influence of τ_{C0} plays a role. Fig. 4.19(b) shows that influence for different τ_{C0}.

Interesting is the efficiency of the device in terms of tunability and loss, specially when it comes to the application of tunable capacitors in a circuit. The efficiency can be defined, similar to [HZL+07], as

$$\eta_C = \tau_C Q_C. \tag{4.21}$$

The normalised efficiency of the varactor $\eta_C/(\tau_{C0}Q_0)$ is shown in Fig. 4.20. Obviously, at least for the given example, η_C decreases monotonously which means that the increase in tunability caused by the series inductance does not compensate the decrease of Q_C. It can be shown analytically that $\eta_C/(\tau_{C0}Q_0)$ is always less than one.

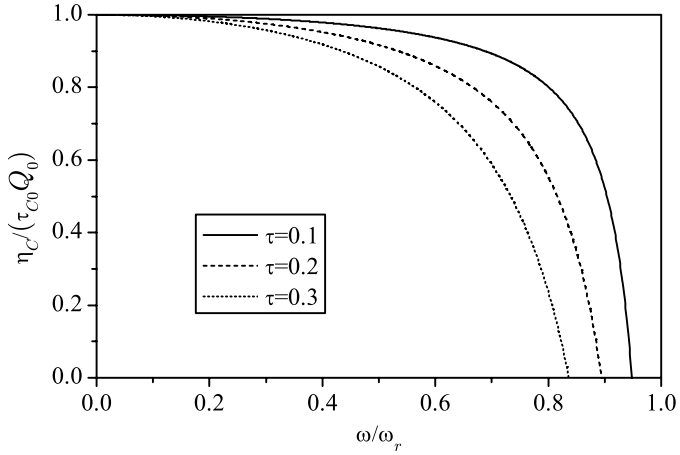

Figure 4.20: The normalised varactor efficiency $\eta_C/(\tau_{C0}Q_0)$ vs. the normalised frequency ω/ω_r. The zero crossing is related to the zero crossing of Q_C.

Using the above found relations and expanding Eqn. (4.21), normalised by $\tau_{C0}Q_0$, in a taylor series one obtains

$$\frac{\eta_C}{\tau_{C0}Q_0} = 1 + \frac{\tau_{C0}(1-Q_0^2)-2}{Q_0^2\omega_r^2(1-\tau_{C0})}\omega^2 + \frac{\tau_{C0}(3-Q_0^2)-4}{Q_0^2\omega_r^4(1-\tau_{C0})}\omega^4 + \mathcal{O}(\omega^6).$$

It can easily be seen that the ω^2 and the ω^4 terms are always negative for $Q_0 \gg 1$. This confirms that η_C is constantly decreasing as frequency is increasing.

As a design rule, the series resonance should be pushed as high as possible because for a usual tunability of 0.2 to 0.3, 10 to 15 % of the efficiency η_C is already lost when the device is operated at half the series resonance frequency of the tuned device.

4.2.5 Measurement Results

Performance Characterisation vs. Frequency

The measurement results presented in the following were obtained using the methodology outlined in section 4.2.1. In Fig. 4.21(a), a typical set of (deembedded) scattering parameters of a capacitor is shown. The device is symmetric which is reflected by the congruence of both amplitude and phase of all scattering parameters. In general, for the presented devices, the difference in amplitude for both reflection and transmission was less then 0.05 dB and the for the extraction more crucial difference between the S_{21} and the S_{12} phase was less than 0.3 °. The difference of the reflection phases was in general smaller than 5 °.

Fig. 4.21(b) shows the extracted parameters of the example capacitor both empty and filled with the LC 5CB. The quality factor of the empty capacitor is very high as expected and is in the example limited towards 10 GHz by the series resonance. Upon filling the capacitor with the rather

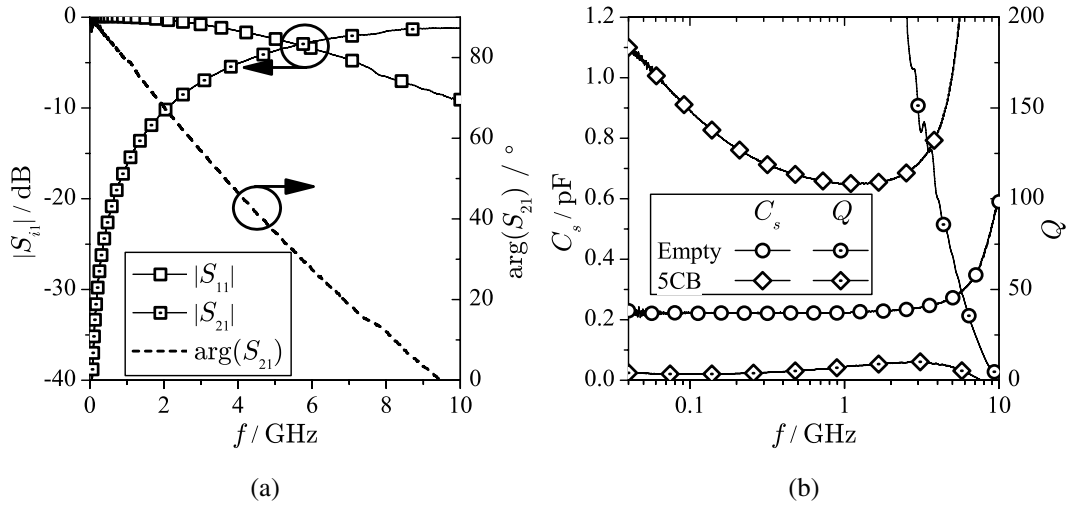

Figure 4.21: (a) Example of the measured scattering parameters of an empty parallel plate capacitor. Forward and backward direction of the measurement results are identical with respect to both amplitude and phase. (b) Examples of the empty capacitor and the same capacitor filled with 5CB.

lossy LC 5CB the quality factor declines as expected. As the capacitors were also to be used for characterisation purposes (see section 3.1.3), the behaviour of the individual devices was evaluated in terms of frequency, temperature and bias voltage. The temperature dependence of the device is of course dominated by the LC material and was already discussed in section 3.1.3. In order to improve the quality of the deembedding, the calibration line of each capacitor set was measured at the same temperatures and bias voltages as the capacitors. In the following paragraphs, some examples of the electrical characteristic of realised capacitors will be discussed. The LC material used is 5CB and the Tolane base matrix.

The results are shown in Fig. 4.22 for 5CB and in Fig. 4.23 for the Tolane base matrix. The characteristics of the Tolane filled capacitor are quite straight forward, i.e. they feature comparatively high quality factor and tunability. The tunability increases as the frequency increases towards the series resonance. The quality factor decreases accordingly.

Fig. 4.23(b) depicts the behaviour of tunability and quality factor versus bias voltage. The threshold voltage evaluates to $\approx 8\,\mathrm{V}$ and is therefore quite high. As the fabricated capacitors represent effectively two capacitors in series, the effective threshold voltage is $\approx 4\,\mathrm{V}$. The high threshold can be explained by the fact that the molecules in the base matrix are very non-polar and have therefore low anisotropy near DC. Due to the high threshold voltage, the maximum tunability is not quite reached at the maximum applied bias voltage of 40 V.

Compared to the Tolane filled capacitor, the 5CB filled capacitor shows of course inferior performance. In fact, at the frequency of 350 MHz the tunability becomes negative. At this point the second cross over frequency is located where $\varepsilon_{r,\perp}$ becomes larger than $\varepsilon_{r,||}$ (see Fig. 2.9(a) on page 23). As relaxations are also located at these frequencies, the quality factors are accordingly

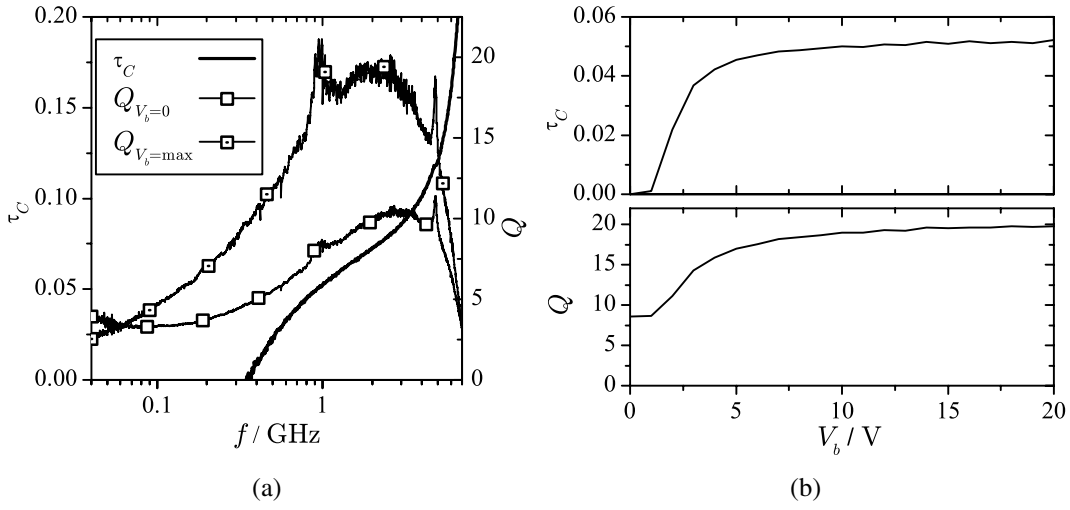

Figure 4.22: (a) Tunability and maximum and minimum quality factor of a capacitor with $d_{LC} \approx 6\,\mu m$, $w = 600\,\mu m$ and $l = 300\,\mu m$ filled with 5CB. The gap between the bottom pads is 100 µm. (b) Tunability and quality factor as a function of the bias voltage at 1 GHz. All values are measured at room temperature.

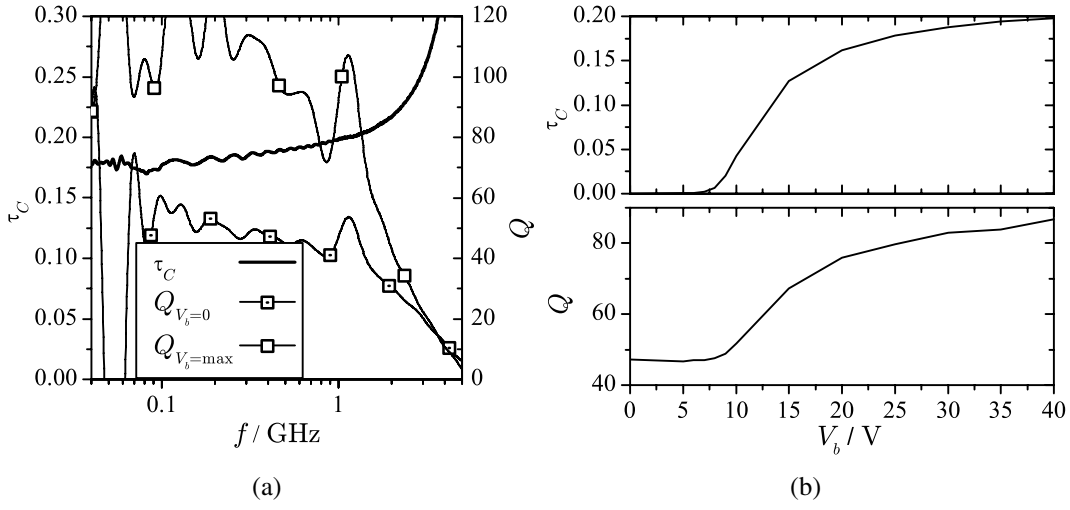

Figure 4.23: (a) Tunability and maximum and minimum quality factor of a capacitor with $d_{LC} \approx 5\,\mu m$, $w = 600\,\mu m$ and $l = 450\,\mu m$ filled with the tolane base matrix. The gap between the bottom pads is 100 µm. (b) Tunability and quality factor as a function of the bias voltage at 1 GHz. All values are measured at room temperature.

low. Again for frequencies > 1 GHz, the series resonance has more and more influence. From the tunability and quality factor (Fig. 4.22(b)) at 1 GHz, it can be seen that the threshold voltage is below 1 V and the saturation is reached above 10 V. It can be deduced from both examples that the anchoring has good quality as the threshold behaviour is quite pronounced.

Analysis of the transient behaviour

As the main goal of the development of the thin layer technology was the reduction of the response time, special attention was given to the tuning speed behaviour. Particularly, the response to the removing of the bias voltage (t_{decay}) was of major interest, since the response to an application of a bias voltage (t_{rise}) can be more or less arbitrarily reduced by using the so called overdrive technique [Chi99]. This technique is of course not applicable for reducing t_{decay} since no lower voltage than 0 V can be applied.

In the context of the tuning speed behaviour, an additional parameter was introduced in the measurements, namely the bias voltage frequency f_{V_b}. While the focus so far was on using DC voltages in order to keep microwave devices based on LC as simple as possible, for the capacitors AC bias voltages having frequencies of 1 kHz or less were used in order to mimic display technology more consistently since there commonly AC bias voltages are used [HLTB03]. The waveform of this bias voltage is rectangular with a duty cycle of 50 % and a constant component of zero.

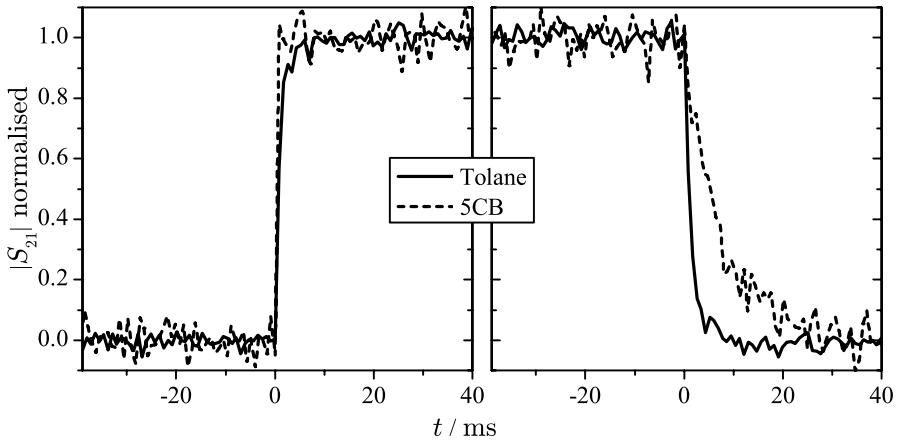

Figure 4.24: Recorded transient behaviour of two capacitors: One filled with 5CB with $d_{LC} \approx 5\,\mu$m, the other filled with the tolane base matrix with $d_{LC} \approx 1\,\mu$m. The results were obtained at room temperature with a bias frequency of $f_{V_b} = 1\,$kHz. The 5CB filled capacitor is biased with 20 V, the tolane filled capacitor with 40 V.

Fig. 4.24 depicts the switching characteristic of two capacitors having a LC layer thickness of 5 µm and 1 µm, respectively. The plots show the transmission amplitude normalised by the maximum tuning contrast. The thin capacitor is filled with the Tolane base matrix, the other one with 5CB. Due to the extremely low d_{LC}, the response time t_{decay} of the Tolane filled LC is as low as 4 ms. The measure used for t_{rise} is the time it takes for $|S_{21}|$ to climb from 10 % to 90 % of the maximum tuning contrast (compare section 2.4.3). t_{decay} is accordinly the time it takes the $|S_{21}|$ to drop from 90 % to 10 % after the bias voltage is removed. It should be noted that a device with a thickness of 1 µm is rather difficult to reproduce and could be achieved only for one set of capacitors. Although the thickness of the 5CB filled capacitor is much larger, this device has

comparable switching behaviour concerning t_{decay} because of the much lower viscosity of 5CB. Concerning t_{rise}, the 5CB filled capacitor is faster which can be attributed to the much higher V_b/V_{th} ratio (see Eqn. (2.39)). t_{rise} of the tolane filled capacitor could be further decreased by increasing the bias voltage. The curve of the 5CB filled device features more noise due to the much lower tuning contrast, i.e. anistropy, of 5CB.

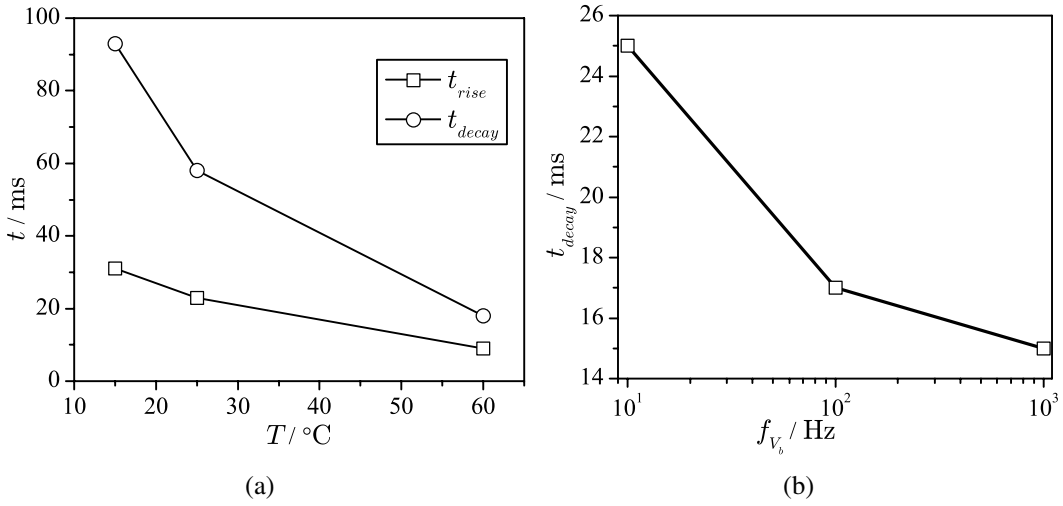

Figure 4.25: (a) Both response times (on and off) of a capacitor with $d_{LC} \approx 4\,\mu m$ versus temperature. (b) Response time of the switching off process for a 5CB filled capacitor with $d_{LC} \approx 6\,\mu m$ versus the bias frequency.

In Fig. 4.25, two more general aspects of the tuning speed behaviour are presented. In Fig. 4.25(a), the rise and decay times of a tolane filled capacitor are plotted versus temperature. As can be seen, both times decrease significantly with increasing temperature. This is in general attributed to the decreasing of the viscosity as temperature increases.

The decay time for a 5CB filled device also shows dependency on the bias voltage frequency f_{V_b}, as shown in Fig. 4.25(b). As the frequency increases, t_{decay} decreases. This behaviour can be explained by an ionisation effect [HLTB03] which is very slow and therefore more pronounced at low f_{V_b} [HLTB03]. In fact, for DC bias t_{decay} depends on how long the voltage had been applied, i.e. the more ionisation occurs, the slower the process relaxes. This is the reason why t_{decay} of the phase shifter presented in section 4.1 was only slightly but not significantly faster compared to the devices in [Mül07]. For the Tolane filled devices, such behaviour could not be observed. The testing of the DC conductivity of the devices yielded that the resistance of the 5CB devices ranges in the MΩ range, while the resistance of Tolane filled devices was several GΩ and therefore to large to be measurable with the given source meter. It can therefore be speculated that LCs with high resistivity cause less problems with ionisation effects and can therefore be driven with low f_{V_b} or for experimental purposes also with DC voltages.

4.3 Phase Shifters Based on Periodically Loaded Lines

As a simple capacitor alone is not much use for anything, it has to be employed in a circuit. In this section, it will be demonstrated how the parallel plate capacitor concept presented in the previous section can be used to build a tunable phase shifter with fast response times. For that purpose, the theory and application of periodic structures is reviewed and presented first and the design constraints for such a device are outlined. Finally, the results of realised loaded line structures are discussed.

4.3.1 Theory of Tunable Periodically Loaded Transmission Lines

In order to efficiently design phase shifters based on periodically loaded transmission lines with tunable capacitors, at first certain requirements have to be identified. For simple tunable phase shifters as e.g. presented in [Mül07], this is rather straight forward: The tunable transmission line should have a certain impedance and the tunability of the material should be exploited as much as possible. Such a tunable transmission line was, in principle, also used in section 4.1 in this work.

Considering the cross section of such an IMSL and also referring to section 4.1.2, these two requirements are contradictory. For the specific problem of designing tunable phase shifters based on LC, it is required that the ratio of electrode width to substrate height, the latter being the LC layer thickness, is as high as possible. This in turn requires wide electrodes which lowers the line impedance. Together with the additional requirement of having LC layer thicknesses of less or even much less than 100 µm in order to obtain fast response times, it is very difficult, if not impossible, to achieve high tuning efficiency, low response times, acceptable line impedances and low metallic loss at the same time.

As shown in section 4.2.3, the impact of the metallic loss on the performance of parallel plate capacitors is much lower compared to transmission lines when it comes to thin LC layers. As the Q-factor of a parallel plate capacitor can be kept constant independent of the dielectric thickness, phase shifters can be realized using the periodically loaded line approach with capacitors as tunable shunt elements. In the following, the theory of such structures will be reviewed and adapted to the specific problem of this work. Particularly, it will be addressed how such structures can beneficially be implemented using liquid crystal as tunable dielectric. The derivation follows [Poz04] insofar as fixed, i.e. not tunable periodic structures are concerned and is enhanced in order to be able to treat the specific challenges of tunable phase shifters.

The approach chosen here assumes that the periodic structure is composed of pieces of not tunable transmission lines and shunt tunable capacitors. Fig. 4.26 shows the periodic structure with the important variables associated with it. A real device is composed of N unit cells like those shown in Fig. 4.26. As in [Poz04], at first number of unit elements is assumed to be infinite ($N \rightarrow \infty$). Although the structure to be realised later will use tunable capacitors as shunt elements, the derivation presented below will be done using a general shunt impedance Z_x. This approach

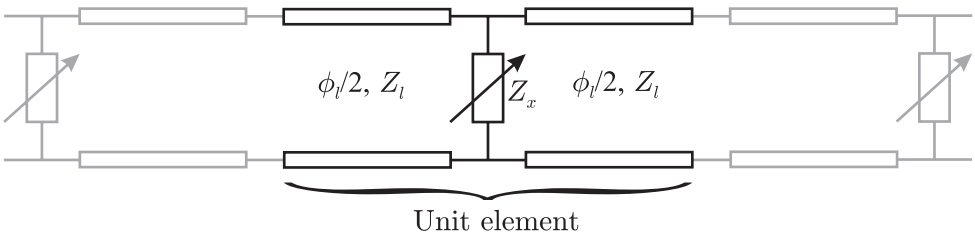

Figure 4.26: Periodically loaded line with tunable shunt elements

has the advantage that the derivation is frequency independent. The not tunable transmission line pieces are characterised by their electrical length ϕ_l and the characteristic impedance Z_l. In accordance with [Poz04], the transmission line used for the derivation of the theory has the normalised characteristic impedance 1 Ω. Z_x is normalised according to

$$z_x = \frac{Z_x}{Z_l}. \tag{4.22}$$

Concerning the specific requirements, the most obvious one can be stated immediately: The effective characteristic impedance Z_b of the periodic structure should have a certain value Z_0 (e.g. 50 Ω). Next, given that the structure is supposed to work as a tunable phase shifter, the structure should have a certain differential phase shift $\Delta\phi_b$ at a design frequency f_d. Furthermore, the real structure will have a finite number of elements. In order to minimise the fabrication effort or increase the fabrication yield of the periodic structure, the number of elements N should be kept as low as possible while $\Delta\phi_b$ should be achieved at f_d at the same time.

While the requirements listed so far are rather obvious, another important requirement is that the real periodic structure should have the same or less physical length as a normal tunable transmission line. The term "normal tunable transmission line" means a transmission line having the same tunable dielectric as it is used for the shunt tunable elements (i.e. capacitors in the realisation). In order to simplify things, it is assumed that the normal tunable transmission line has a tuning efficiency of 100 %, i.e. the available tunability τ_{LC} of the material is fully used. Additionally, it is assumed that the shunt capacitors of the periodic structure have 100 % tuning efficiency, too. The shunt element of the periodic structure is furthermore assumed to have negligible size. In the next section, it will be shown how all four requirements can be fulfilled at the same time.

4.3.2 Implementation of the Design Constraints

In the following derivations, loss in both the transmission line pieces and the shunt elements is neglected. The derivation is presented in a reduced form owing to the rather bulky mathematical expressions. It will, nevertheless, be shown step by step while it will be outlined which quantity is obtained at each step. The order how the derivation is conducted is important due to the non-linear nature of the equations involved. It should be noted that the expressions presented

in i.e. [Reb03] are simpler than here. The reason for this is that the author models the short line elements in between the loads with inductors and capacitors rather than with transmission line models. The method presented in this work, however, allows a direct calculation of the transmission line parameter which in turn can be used directly in a simulation and allows also direct calculation of the transmission line loss.

The ABCD-matrix of half a transmission line piece $\mathbf{A}_{TL}$ is

$$\mathbf{A}_{TL} = \begin{pmatrix} \cosh(\gamma l/2) & \sinh(\gamma l/2) \\ \sinh(\gamma l/2) & \cosh(\gamma l/2) \end{pmatrix} \tag{4.23}$$

with γ being the complex propagation constant and l the physical length. For a lossless transmission line, the $\mathbf{A}_{TL}$ matrix and the matrix of the shunt element $\mathbf{A}_S$ can be expressed as

$$\mathbf{A}_{TL} = \begin{pmatrix} f_{\cos} & j \cdot f_{\sin} \\ j \cdot f_{\sin} & f_{\cos} \end{pmatrix}, \mathbf{A}_S = \begin{pmatrix} 1 & 0 \\ 1/z_x & 1 \end{pmatrix} \tag{4.24}$$

with $f_{\sin} = \sin(\phi_l/2)$ and $f_{\cos} = \cos(\phi_l/2)$. ϕ_l is the electrical length of the transmission line segments.

The ABCD-matrix of a unit element as shown in Fig. 4.26 is then given by

$$\mathbf{A}_{UE} = \mathbf{A}_{TL} \cdot \mathbf{A}_S \cdot \mathbf{A}_{TL} \tag{4.25}$$

According to [Poz04], the electric length ϕ_b of such a unit element is given by

$$\phi_b = \ln\left(\frac{\mathbf{A}_{UE,11} + \mathbf{A}_{UE,22} + \sqrt{(\mathbf{A}_{UE,11} + \mathbf{A}_{UE,22})^2 - 4}}{2}\right) \tag{4.26}$$

As pointed out before, the entire derivation is based upon the assumption that the considered structure has infinite length. However, for the following derivations, it will be assumed that the unit elements behave essentially like a piece of a regular transmission line which can be interconnected arbitrarily and can therefore have finite length. Doing so, i.e. implying that the artificial line consists of N unit elements, the above mentioned requirement that the structure should have a certain differential phase shift $\Delta\phi_b$ can be expressed as

$$\frac{\partial \phi_b}{\partial z_x} \Delta z_x N = \frac{\partial \phi_b}{\partial z_x} z_x \tau_{z_x} N = -j\Delta\phi_b. \tag{4.27}$$

τ_{z_x} is the tunability according to

$$\tau_{z_x} = 1 - \frac{z_{x,min}}{z_{x,max}}$$

which corresponds to the material tunability τ_{LC} if z_x is an ideal capacitor with 100 % tuning efficiency. It should be noted that Eqn. (4.27) holds a certain inaccuracy as z_x does not linearly depend on the tuning quantitiy, i.e. the capacitance value. This could be tackled by writing

Eqn. (4.27) in terms of $z_x = 1/(jb)$ (compare also [Poz04]) and calculating the derivative in terms of b. This however would tremendously complicate the mathematical expressions derived furter below and this approach was therefore not used. The before mentioned inaccuracy will be resolved later by choosing z_x such that it represents an intermediate tuning state.

From Eqn. (4.27) one can obtain

$$z_x^{\pm} = \frac{j\Delta\phi_b\left(2f_{\cos}^2 - 1\right) \pm \sqrt{4\tau_{z_x}^2 N^2 f_{\cos}^4 - 4\tau_{z_x}^2 N^2 f_{\cos}^2 - \Delta\phi_b^2}}{4\Delta\phi_b f_{\cos} f_{\sin}}. \tag{4.28}$$

As indicated, Eqn. (4.28) has two solutions. In order to choose the correct solution, one has to remember that the periodic structure is to use tunable capacitors as load elements which results in z_x being purely negative and imaginary by design. As $4\tau_{z_x}^2 N^2 f_{\cos}^4 < 4\tau_{z_x}^2 N^2 f_{\cos}^2$ is always given, the entire expression in Eqn. (4.28) is obviously always imaginary. Concerning the sign of z_x, it is assumed that $\phi_l < \pi$ which makes the denominator of Eqn. (4.28) always positive. For determining which sign to use for computing Eqn. (4.28), first the use of the positive sign is considered. For the extreme case of $\tau_{z_x}^2 N^2 = 0$ one obtains

$$z_x^{+}(\tau_{z_x} = 0, N = 0) = \frac{j\left(2f_{\cos}\right)}{4f_{\sin}} \tag{4.29}$$

which is always positive imaginary. It can also be seen from Eqn. (4.28) that any $\tau_{z_x} > 0$ and $N > 0$ will increase the value of z_x^{+}. In the same manner it can be shown that using the negative sign the result of Eqn. (4.28) is always negative imaginary. Again considering the extreme case, one obtains

$$z_x^{-}(\tau_{z_x} = 0, N = 0) = \frac{j\left(2f_{\cos}^2 - 2\right)}{4f_{\cos} f_{\sin}} \tag{4.30}$$

which evaluates always to imaginary values < 0. Any $\tau_{z_x} > 0$ and $N > 0$ will decrease this imaginary value accordingly.

The next requirement to be considered is the impedance of the entire structure. According to [Poz04], the line impedance Z_b is given by

$$Z_b = \frac{\mathbf{A}_{UE,12} Z_l}{\sqrt{\mathbf{A}_{UE,11}^2 - 1}}. \tag{4.31}$$

The above obtained z_x is substituted in Eqn. (4.31) which yields the following equation:

$$Z_b = Z_l \frac{\sqrt{4\tau_{z_x}^2 N^2 f_{\cos}^2 + \Delta\phi_b^2 - 4\tau_{z_x}^2 N^2 f_{\cos}^4} - \Delta\phi_b}{2f_{\sin} f_{\cos} \tau_{z_x} N}. \tag{4.32}$$

Eqn. (4.32) is consequently solved for ϕ_l. At this point, the problem of multiple solutions arises again. Solving $Z_b = Z_0$ for ϕ_l, one obtains the solution

$$\phi_l^{\pm} = \pm 2 \arctan\left(\frac{\Delta\phi_b Z_0 Z_l}{\tau_{z_x} N (Z_0^2 - Z_l^2)\zeta_0^2}\right) \tag{4.33}$$

with ζ_0 being the roots of the polynomial $p(\zeta)$ with

$$p(\zeta) = \tau_{z_x}^2 N^2 (Z_l^2 - Z_0^2)^2 (\zeta^4 - \zeta^2) + Z_l^2 Z_0^2 \Delta\phi_b^2.$$

Substituting $\zeta^2 = \zeta'$, ζ'_0 can be given by

$$\zeta'^{\pm}_0 = \frac{1}{2} \pm \frac{\sqrt{\tau_{z_x}^2 N^2 (Z_l^2 - Z_0^2)^2 - 4 Z_l^2 Z_0^2 \Delta\phi_b^2}}{2\tau_{z_x} N (Z_l^2 - Z_0^2)} \tag{4.34}$$

Regardless which solution of Eqn. (4.34) is the physically meaningful, the argument of the root expression must never be negative for the electrical length given in Eqn. (4.33) to be real valued. Therefore, a condition for the minimum number of unit elements N can directly be derived from the root expression in Eqn. (4.34):

$$N_{min} = 2 \frac{Z_l Z_0 \Delta\phi_b}{\tau_{z_x} (Z_l^2 - Z_0^2)} \tag{4.35}$$

N_{min} does not directly determine the cutoff frequency of the periodic structure as will be shown further below. Eqn. (4.35) is naturally not integer valued so the minimum necessary number of unit elements will be the next larger integer. Further on, for the sake of analysis, N, as well as N_{min}, will be treated as real valued variables.

For the moment it shall be assumed that positive electrical lengths are sought for which implies that ϕ_l^+ is the right choice of sign. The electrical length is therefore, taking the other undefined sign into account,

$$\phi_l^{\pm} = 2 \arctan \left(\frac{N_{min}}{N} \cdot \frac{1}{1 \pm \sqrt{1 - \frac{N_{min}^2}{N^2}}} \right). \tag{4.36}$$

It can easily be shown that $\pi/2 < \phi_l^- < \pi$ and that $0 < \phi_l^+ < \pi/2$ for any $N \geq N_{min}$. As the structure should be as short as possible, ϕ_l^- can be ruled out.

From ϕ_l, the physical length of the artificial structure can be determined. This is straightforwardly possible if the load z_x is assumed to have no physical dimension. Then the physical length l_l is given by

$$l_l = \frac{\phi_l}{\beta_l} = \phi_l \frac{c_0}{\omega \sqrt{\varepsilon_{r,l}}} \tag{4.37}$$

with β_l being the propagation constant of the transmission line segments and $\varepsilon_{r,l}$ the effective permittivity of the transmission line segments. The differential phase shift of an ideal transmission line phase shifter (see above) having the same physical length as the periodic structure (Eqn. (4.37)) is given by

$$\Delta\phi_{TEM} = N l_l \frac{\omega}{c_0} \left(\sqrt{\frac{\varepsilon_{r,\perp}}{1 - \tau_{z_x}}} - \sqrt{\varepsilon_{r,\perp}} \right) = N \phi_l \frac{\Delta n}{\varepsilon_{r,l}} \tag{4.38}$$

with Δn being the anisotropy of the refractive index at GHz frequencies. τ_{z_x} is assumed to be the tunability for both the load z_x and the dielectric of the ideal transmission line. From Eqn. (4.38) the final condition can be derived:

$$\Delta\phi_{TEM} = \Delta\phi_b \tag{4.39}$$

This equation is solved for Z_l, the last missing parameter, yielding

$$Z_l^{\pm} = \frac{Z_0\Delta\phi_b(1+g_{\tan}^2)}{2g_{\tan}\tau N}\left(1 \pm \sqrt{1+\frac{4g_{\tan}^2\tau_{z_x}^2N^2}{\Delta\phi_b^2(1+g_{\tan}^2)^2}}\right) \tag{4.40}$$

with

$$g_{\tan} = \tan\left(\frac{\Delta\phi_b\sqrt{\varepsilon_{r,l}}}{2N\Delta n}\right).$$

The correct solution of Eqn. (4.40) can be found by calculating

$$\lim_{N\to\infty}(Z_l) = \frac{\Delta nZ_0}{\tau_{z_x}\sqrt{\varepsilon_{r,l}}}\left(1 \pm \sqrt{1+\frac{\tau_{z_x}^2\varepsilon_{r,l}}{\Delta n^2}}\right). \tag{4.41}$$

It can immediately be seen from Eqn. (4.41) that the positive sign must be chosen as otherwise Z_l becomes negative. The line impedance of the not tunable transmission line pieces for the other extreme case $N = N_{min}$ can be determined by substituting N_{min} in Eqn. (4.39) and solving for Z_l again:

$$Z_l^{N=N_{min}} = \frac{\Delta nZ_0\pi}{2\tau_{z_x}\sqrt{\varepsilon_{r,l}}}\left(1+\sqrt{1+\frac{4\tau_{z_x}^2\varepsilon_{r,l}}{\Delta n^2\pi^2}}\right). \tag{4.42}$$

From Eqn. (4.42) it can be seen that $Z_l^{N=N_{min}}$ is always larger than $Z_l^{N\to\infty}$. In fact, in between these two extremes, Z_l is a monotonous function in terms of N which offers some degree of freedom for the design. This is exemplified in Fig. 4.27[3]. The figure depicts the behaviour of the characteristic impedance Z_l of the not tunable line segments in terms of the used number of unit elements for two different effective carrier substrate permittivities. All curves start at the Z_l as calculated in Eqn. (4.42) and the respective N_{min} (Eqn. (4.35)) and converge to the Z_l for $N \to \infty$ as given in Eqn. (4.41). The targeted characteristic impedance of the entire structure Z_0 is $50\,\Omega$ and the targeted differential phase shift is $\Delta\phi_b = \pi/2$.

The same methodology as used for the consideration of the behaviour of Z_l can now be extended to the other parameters of the artificial line as derived above. ϕ_l in Eqn. (4.36) is obtained by substituting the found solution of Z_l and z_x is consequently found by substituting ϕ_l in Eqn.

[3] $\varepsilon_{r,l} = 10$ is potentially interesting if carrier substrates such as sapphire or high resistivity silicon [SDPN+05, KBC+06] are used.

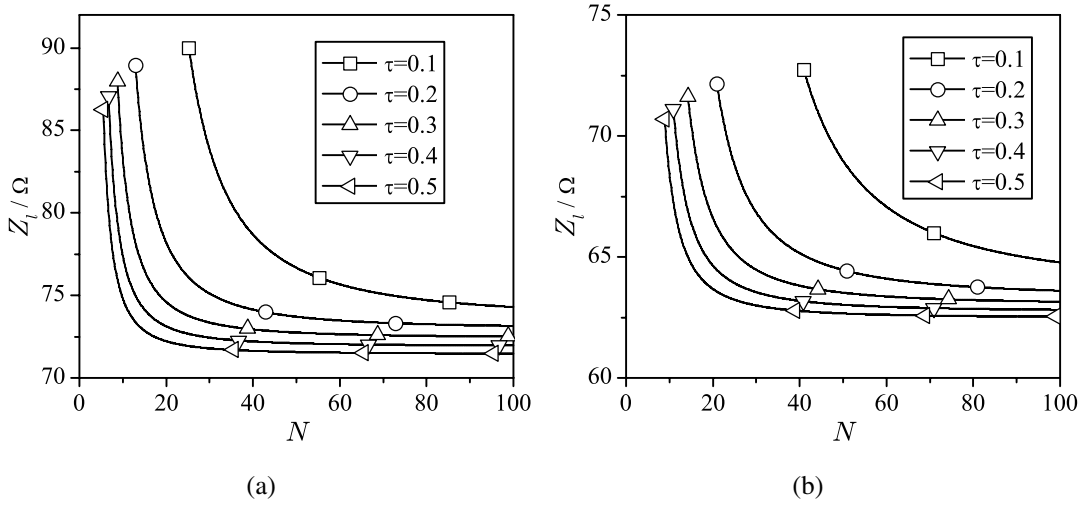

Figure 4.27: Influence of the tunability on the characteristic impedance Z_l of the not tunable line segments and the minimum number of necessary unit elements under the conditions applied in this work. (a) for $\varepsilon_{r,l} = 3.8$ (Fused silica), (b) for $\varepsilon_{r,l} = 10$.

(4.28). The values for $N = N_{min}$ and $N \to \infty$ can be calculated in the same way as for Z_l. It should, however, be mentioned that, if the condition in Eqn. (4.39) is dropped, Z_l can be chosen arbitrarily. Thus, as will be demonstrated further down, Z_l should always be chosen as large as the chosen technology approach permits in order to minimise the overall physical length.

If the condition in Eqn. (4.39) is kept, the total electrical length $N\phi_l$ is, by design, a constant regardless which number of unit cells N is chosen. $N\phi_l$ becomes smaller as the tunability becomes larger. The behaviour of $Z_x = Z_l z_x$ (Eqn. (4.22)), i.e. the effective load impedance, is depicted in Fig. 4.28 for different carrier substrate permittivities. From Fig. 4.27 and Fig. 4.28 it can be concluded that a larger number of unit cells is in general beneficial as it lowers both the characteristic impedance of the not tunable line segments and the load impedance Z_x. The latter is important because this allows to use smaller capacitance values. Nevertheless, as can be seen from Fig. 4.28, Z_x slightly increases before it decreases with increasing N. Choosing a high $\varepsilon_{r,l}$ does not make sense as the load impedance does not become considerably smaller. Although the necessary Z_l is lower for higher $\varepsilon_{r,l}$, this comes for realisations at the price of larger distances between signal and ground electrodes which increases the series inductance of the load capacitors. The potential benefit of being able to realise physically shorter lines with higher $\varepsilon_{r,l}$ is marginal as can be seen when the above presented equations are evaluated accordingly.

Finally, the impact on the loaded line parameters will be analysed if Z_l is chosen freely. The following analysis is done for $N = N_{min}$ (depending on Z_l) and again for a varying tunabilities. As can be seen from Fig. 4.29(a), the tunability only has influence on the total length, i.e. the larger the tunability the shorter the structure can be. Furthermore, the length of the structure can be greatly reduced if a large Z_l is chosen. The result shown in Fig. 4.29(b) agrees with Eqn. (4.28), that is the load impedance does not depend on the tunability for $N = N_{min}$. Otherwise,

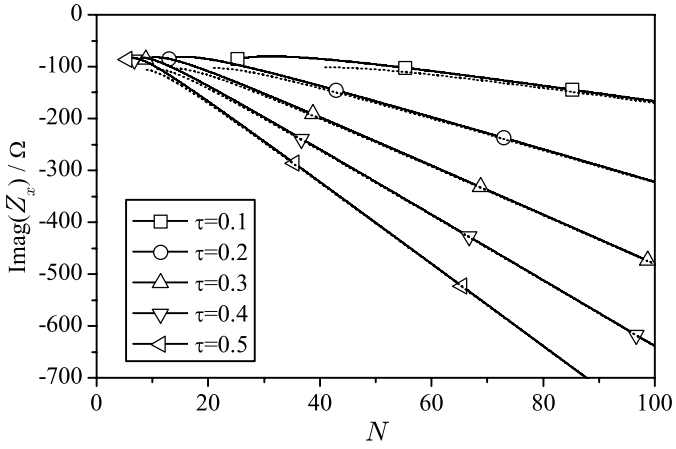

Figure 4.28: The imaginary part of the load impedance Z_x vs. the number of unit cells for different tunabilities. The solid lines represent the behaviour for $\varepsilon_{r,l} = 3.8$, the dashed ones that for $\varepsilon_{r,l} = 10$.

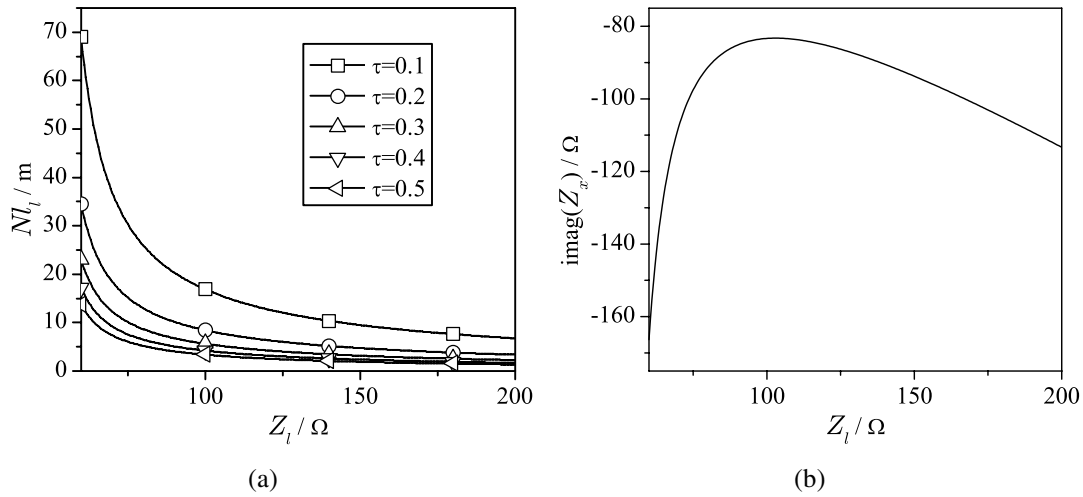

Figure 4.29: Impact of Z_l on the (a) total length of the structure and (b) on the load impedance. For the calculation of the total length, $c_0/\omega = 1\,\mathrm{m}$ is used.

the graph shows that, up to some point, the higher Z_l and therefore shorter structure comes at the price of a smaller Z_x and therefore larger load capacitance. This can again, at least partly, be compensated by increasing N as was demonstrated in Fig. 4.28.

Next, the cutoff frequency ω_C is considered. In [Poz04], a relation is given which must be satisfied for operation in the passband. This relation is nevertheless not suitable for direct calculation of the cutoff frequency. Instead, the cutoff frequency can be calculated by finding the zero crossing of the argument of the square root in Eqn. (4.31). Doing so leads to a transcendental equation which eludes analytical solving. This problem can, at least partly, be sidestepped by

Taylor expanding the expression $\mathbf{A}^2_{UE,11} - 1$ in terms of ω around the design angular frequency ω_d:

$$\mathbf{A}^2_{UE,11} - 1 = c_0 + c_1(\omega - \omega_d) + c_2(\omega - \omega_d)^2 + \cdots \tag{4.43}$$

Because for $N = N_{min}$ ω_C is lowest, only this case is considered in the following.

The actual frequency dependency is introduced by setting the load impedance

$$z'_x = z_x \frac{\omega_d}{\omega} \tag{4.44}$$

and the electrical length

$$\phi'_l = \pi/2 \frac{\omega}{\omega_d}. \tag{4.45}$$

z'_x (with z_x as calculated in Eqn. (4.28)), ϕ'_l and N_{min} (Eqn. (4.35)) are substituted in Eqn. (4.43). The constant term of the taylor expansion is given by

$$c_0 = \frac{\sqrt{2} Z_l^4 Z_b^2}{(Z_l^2 + Z_b^2)^2}$$

which is obviously always positive. The linear term of the taylor expansion is for realistic parameters always negative and the values become negligibly small from the cubic term on. The cutoff frequency can thus be calculated by solving $\mathbf{A}^2_{UE,11} - 1 = 0$ with the respective taylor series which only needs to be considered up to the square term. For realistic parameters, it can be shown that the cutoff frequency is always higher than the design frequency. Furthermore, it can be shown that ω_C depends more or less only on the impedance Z_l. Of course, the cutoff frequency also shifts if the load capacitor is tuned. Depending on the actual tunability τ_{z_x} and the direction of the tuning, i.e. wether the z_x in Eqn. (4.28) represents the tuned or untuned state, the cutoff frequency can then shift below the design frequency. If the tuning direction is chosen such that the load capacitor becomes smaller, $\omega_C(\tau_{z_x})$ will always be higher than ω_C calculated from $\mathbf{A}^2_{UE,11} - 1 = 0$. It is important to note that the direction of tunability also affects the obtainable phase shift. If z_x represents the untuned capacitor, the obtainable phase shift is always larger than the given $\Delta\phi_b$. On the other hand, it will be smaller than $\Delta\phi_b$ if z_x represents the tuned state. In both cases, the deviation from the design $\Delta\phi_b$ is owed to the dispersive characteristic of the periodic structure near ω_C.

Fig. 4.30 shows the influence of Z_l on ω_C. The plot is normalised with respect to the design frequency. This is possible as the cutoff frequency only depends on Z_l. As can be seen, ω_C comes closer to the design frequency, the higher the impedance Z_l is. The behaviour of a periodically loaded line versus frequency will be discussed in the next section.

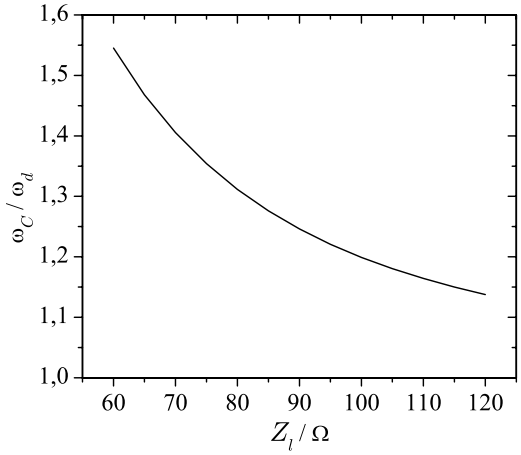

Figure 4.30: The ratio of the cutoff frequency ω_C and the design frequency ω_d vs. the characteristic impedance of the not tunable line segments.

4.3.3 Dispersion Relations

Input matching

The general behaviour of the effective impedance Z_b vs. frequency is analysed next. Although Z_b is fixed by design according to Eqn. (4.32), the value is only obtained for the design frequency. Fig. 4.31(a) shows the behaviour of Z_b vs. frequency for $N = N_{min}$ normalised with respect to the design frequency. Again, only Z_l is the parameter which influences the characteristics. In the figure, actually both effects, the shift of the cutoff frequency and the dispersion of Z_b, are visible.

Fig. 4.31(b) shows how the dispersion of Z_b impacts on the input reflection of a periodic structure embedded in a $50\,\Omega$ system. The dispersion of Z_b increases, the higher Z_l is chosen. The number of ripples increases for low Z_l due to the increase of the electrical length. It is however possible to lessen the Z_b dispersion by increasing N as then ω_C shifts to higher frequencies.

Dispersion of the Differential Phase Shift and Group Delay

So far, it was tacitly assumed that Z_x represents the untuned load. This is, however, not necessarily the best solution. Depending on how Z_x or the corresponding capacitance C_x is chosen within a tunable interval ΔC_x, the cutoff frequency will be shifted to or away from the design frequency as the load impedance is tuned. Furthermore, this will determine the frequency response of the group delay and the differential phase shift. With

$$\Delta C_x = C_\perp \left(\frac{\tau_{z_x}}{1 - \tau_{z_x}} \right)$$

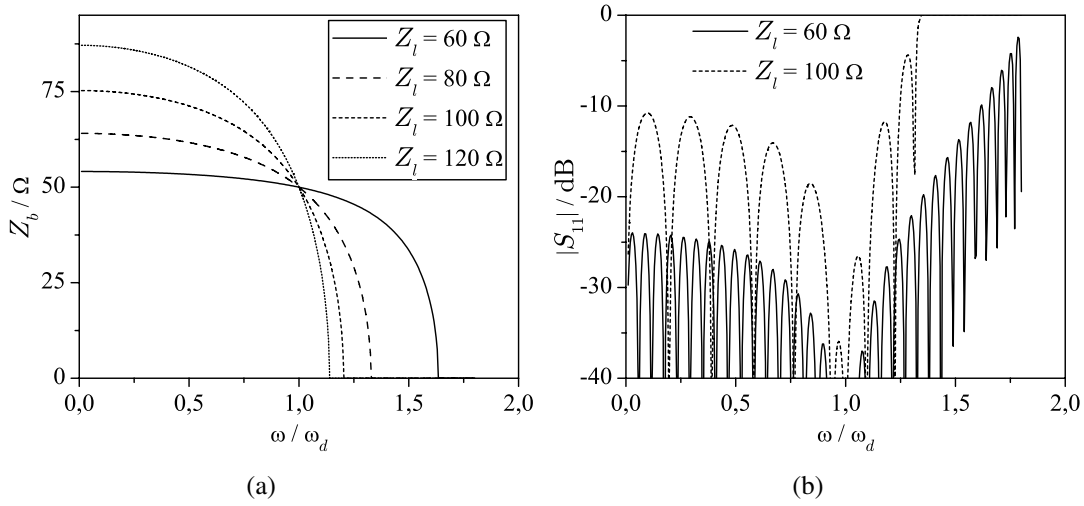

Figure 4.31: (a) The effective impedance of the periodic structure according to Eqn. (4.32) vs. frequency. (b) Impact on the input reflection of such a structure for $N = N_{min}$. The assumed tunability is $\tau_{z_x} = 0.25$. The frequency is normalised with respect to the design frequency ω_d.

the tunable interval can be determined. $C_\perp$ corresponds to the lower tuning state, i.e where the LC is oriented perpendicular to the field. $C_\perp$ is calculated according to

$$C_\perp = C_x + x \cdot \Delta C_x \implies C_\perp = C_x \frac{1-\tau_{z_x}}{1+\tau_{z_x}(x-1)} = \frac{1}{j\omega_d Z_x} \frac{1-\tau_{z_x}}{1+\tau_{z_x}(x-1)}.$$

The variable x determines the distance between $C_\perp$ and C_x or, in other words, where C_x is located in the interval ΔC_x, i.e. $0 < x < 1$.

For minimum N and the other design parameters chosen as in the examples above, the choice of x impacts on the differential phase shift $\Delta\phi$ as shown in Fig. 4.32(a) for $N = N_{min}$ and for $N = N_{min} + 5$. By increasing N, the dispersion issue can obviously be mitigated. Furthermore, for $x = 0.5$, $\Delta\phi \approx \Delta\phi_d$. It can be shown that this holds true regardless of how other parameters of the structure chosen. The maximum group delay, which corresponds to the maximum value of the load capacitor, is shown in Fig. 4.32(b). From the group delay point of view, the minimum number of elements is not advisable. The higher the element count is, the less dispersive the structure will be. For $x = 0.5$, the group delay dispersion can be considered as a compromise.

Concluding the above presented derivations, the characteristic impedance Z_l should be chosen as high as possible in order to obtain short structures. Nevertheless, this must be balanced with the tolerable dispersion and with the technological constraints as a high Z_l means either thick substrates in case of microstrip lines or broad gaps in case of CPW lines. Apart from the increased series inductance of the load elements in both cases, another downside of a high Z_l is the need for narrow signal strips, especially if the CPW gap or the microwave substrate thickness should not be too large. Narrow signal strips however will inevitably cause increased metallic loss in the not tunable segments of the artificial structure. The impact of loss in the structure is addressed in the next section.

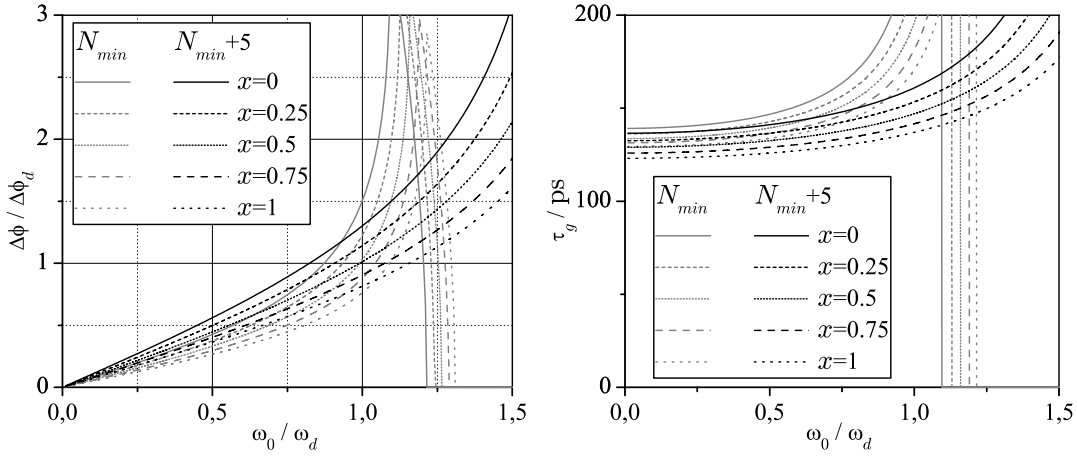

Figure 4.32: (a) The differential phase shift in terms of the frequency and the location ratio x both for minimum N and for $N = N_{min} + 5$. (b) The same for the maximum group delay. In both cases the tunability is 0.25 and the carrier substrate is assumed to be glass.

4.3.4 Incorporation of Loss

The results and analytical expressions can be used to asses how the mostly metallic loss in the not tunable transmission line segments and the mostly dielectric loss in the load capacitors influence the overall loss of the structure. Based on that the important phase shifter efficiency η_{PS} can be determined. Effects like the influence of the series resonance of the load capacitors as described in section 4.2.4 are neglected in this analysis.

Loss is introduced in the load impedance according to

$$Z_{x,loss} = \frac{jQ_C Z_x}{1 + jQ_C}. \tag{4.46}$$

Q_C is the effective quality factor of the load capacitor as used in section 4.2.4. The electric length $\phi_{l,loss}$ incorporating the loss of a unit element is given according to

$$\phi_{l,loss} = \phi_l(\frac{\alpha}{\beta} + j) \tag{4.47}$$

with α being the loss per unit length and β the propagation constant. $\phi_{l,loss}$ is substituted for γl in (4.23) and $Z_{x,loss}/Z_l$ for z_x in Eqn. (4.24). The resulting Eqn. (4.26) is evaluated again which results in $\phi_{b,loss}$. The expression for $\phi_{b,loss}$ is not printed here as the terms are rather large and unwieldy.

In the previous section, the performance of a tunable loaded line phase shifter was exemplified by means of some typical values for N, Z_l and τ_{z_x} which were considered at an arbitrary but

fixed frequency. This is also possible if the relations for α and β are taken from [LL92] for transmission lines with mostly metallic loss and negligible dielectric loss:

$$\alpha = \beta_0 \tan\delta_R;\ \beta = \beta_0(1+\tan\delta_R^2/8)$$

$\tan\delta_R$ is defined as $R'/(\omega L')$ with $\tan\delta_R < 0.1$. In analogy to the usual quality factor definition of a capacitor the quality factor $Q_R = 1/\tan\delta_R$ is defined. Thus Eqn. (4.47) can be rewritten as

$$\phi_{l,loss} = \phi_l\left(\frac{1/Q_R}{2(1+1/Q_R^2/8)} + j\right) \tag{4.48}$$

The efficiency of the loaded line phase shifter device η_{PS} can be defined according to Eqn. (4.1) as

$$\eta_{PS} = \Delta\phi_b \frac{180^\circ}{\pi\Re(\phi_{l,loss})N \cdot 8.686\,\mathrm{dB}}$$

Setting $\tau_{z_x} = 0.25$, $\varepsilon_{r,l} = 3.8$ and choosing N to be the smallest possible integer, the impact of both the transmission line quality factor Q_R and the loss in the load capacitor quality factor Q_C can be analysed.

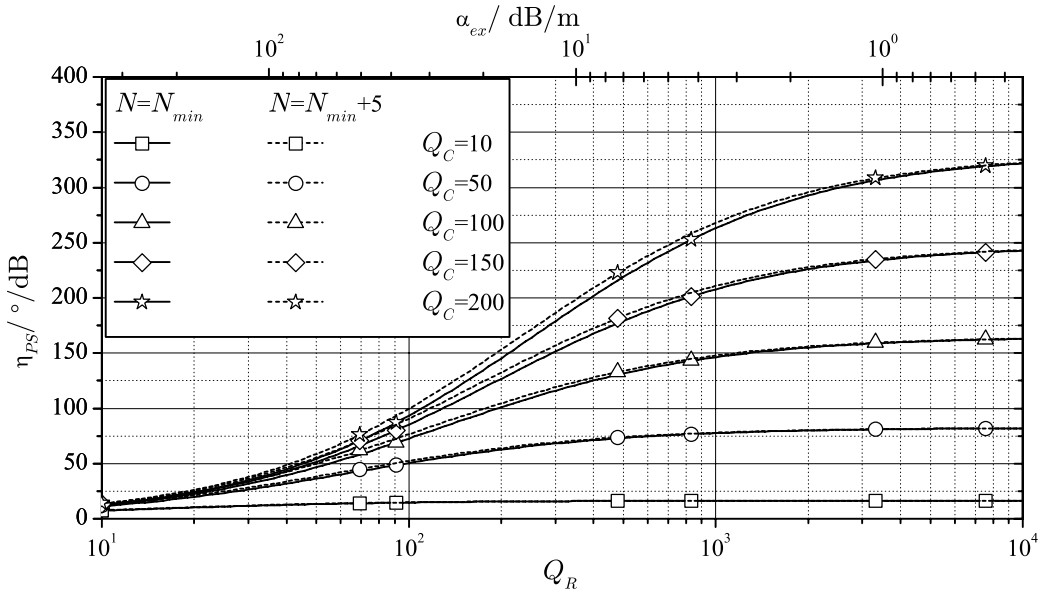

Figure 4.33: The obtainable phase shifter efficiency η_{PS} in terms of the transmission line quality factor Q_R and the capacitor quality factor Q_C. The solid lines show the achievable η_{PS} for minimum N, the dashed lines the result for the structure with five elements more than necessary. The tunability in this example is $\tau_{z_x} = 0.25$. The top x-axis exemplifies the real loss α_{ex} of a transmission line having a propagation constant of $800\,\mathrm{m}^{-1}$ which e.g. would correspond to a frequency of 20 GHz and an $\varepsilon_{r,l}$ of 3.8.

Fig. 4.33 shows the result of the analysis. The bottom x-axis represents the transmission line quality factor Q_R. The efficiency increases with decreasing transmission line and capacitor loss.

It can furthermore be observed that increasing the number of unit cells can also improve the efficiency. Although not explicitly shown here, it can immediatly be understood that the curves in Fig. 4.33 would shift to higher values if the tunability is increased. Interestingly η_{PS} converges for $Q_R \to \infty$, i.e. no loss on the transmission line pieces, to the value $\tau_{z_x} Q_C \cdot 6.6$, which corresponds to the maximum possible efficiency for a phase shifter based on a regular TEM transmission line as defined in [Mül07].

As explained in the previous section, the physical length of the structure can be reduced by increasing Z_l, which is in terms of realisability the most critical parameter. In Fig. 4.34, the impact of increasing Z_l above the minimum value given by the design criteria outlined in the previous section is shown. For the example shown in Fig. 4.33, $Z_l^{N=N_{min}} = 78\,\Omega$ which is used for comparison in Fig. 4.34. Obviously, η_{PS} can be increased considerably by increasing Z_l. However, as stated before (see Fig. 4.29(b)), the load capacitors must have larger capacitance values.

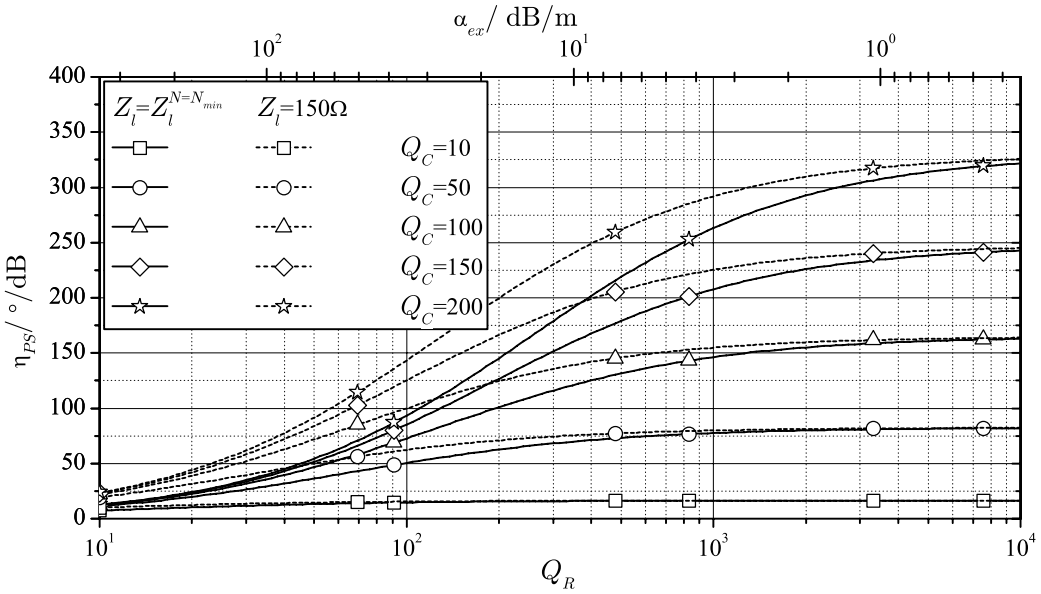

Figure 4.34: The obtainable η_{PS} under the same conditions as in Fig. 4.33 but with higher Z_l. The dashed line shows the result for increased Z_l with five more unit elements than necessary. $Z_l^{N=N_{min}} = 78\,\Omega$.

Phase Shifter Efficiency vs. Frequency

The above developed and presented relations yield the performance at the design frequency without taking in account the effects of the cutoff frequency. For that matter, the values in Fig. 4.33 show the maximum possible performance when dispersion is not taken in account. Furthermore, no assumption is made how Z_x or C_x are chosen with respect to the tuning range.

Above it was shown that C_x is best located in the middle of the tuning range ΔC_x. In the following, this is defined as a design constraint also for the evaluation of how η_{PS} behaves vs. frequency.

ω is incorporated in Eqns. (4.46) and (4.48) in the same manner as in Eqns. (4.44) and (4.45):

$$Z_{x,loss}(\omega) = \frac{jQ_C Z_x \omega_d}{\omega(1+jQ_C)}. \tag{4.49}$$

$$\phi_{l,loss}(\omega) = \phi_l\left(\frac{1/(Q_R\sqrt{\omega/\omega_d})}{2(1+1/(Q_R^2(\omega/\omega_d)/8)} + j\right)\cdot\frac{\omega}{\omega_d}. \tag{4.50}$$

Using Eqns. (4.49) and (4.50) the efficiency can be calculated according to

$$\eta_{PS}(\omega) = \frac{180^\circ}{N\cdot 8.686\,\mathrm{dB}}\cdot\frac{\left|\Im(\phi_{l,loss}^{C_x=C_\perp+\Delta C_x}(\omega)) - \Im(\phi_{l,loss}^{C_x=C_\perp}(\omega))\right|}{\pi\max\left(\Re(\phi_{l,loss}^{C_x=C_\perp+\Delta C_x}(\omega)), \Re(\phi_{l,loss}^{C_x=C_\perp}(\omega))\right)}.$$

Fig. 4.35 shows two representative examples of the behaviour of $\eta_{PS}(\omega)$. As the frequency

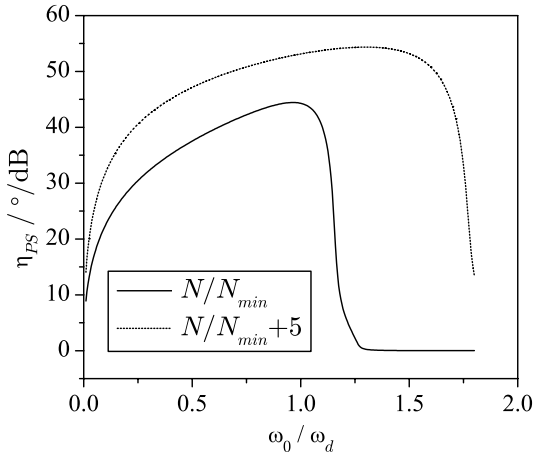

Figure 4.35: The phase shifter efficiency vs. frequency for two examples. The tunability is again 0.25, the load capacitor quality factor 50 and the transmission line quality factor 100.

approaches ω_C, the differential phase shift increases (see Fig. 4.32(a)). At the same time, the loss of the structure increases more. Thus, the overall efficiency is diminished near ω_C. As N is increased, this effect of course shifts to higher frequencies. As predicted in Fig. 4.33, the increase of N also increases η_{PS} as the overall loss is decreased.

In principle, an artificial structure using pieces of transmission lines suffers the same dispersion in η_{PS} like a regular TEM tunable phase shifter as presented in [Mül07]. As the loss per electrical length increases with decreasing frequency, the phase shifter efficiency will always be lower at low frequencies. This can also be seen from Fig. 4.35.

4.3.5 Realisation of Tunable Loaded Line Phase Shifters

Structure of the Devices

A realisation of a tunable loaded line phase shifter was designed according to the design rules presented in the previous sections. The targeted differential phase shift $\Delta\phi_b$ was $\pi/2$ in order to keep the complexity of the prototype low. More phase shift is of course possible as length and hence complexity of the structure increases linearly with $\Delta\phi_b$. Nevertheless, the yield of structures manufactured at laboratory scale becomes then an issue. Details about the fabrication process are given in Appendix A in Tables A.1 and A.2.

Fused silica ($\varepsilon_{r,l} = 3.8$, $\tan\delta = 1 \cdot 10^{-4}$) was selected again as substrate material due to the superior electrical and mechanical properties. The thickness of the substrate for the loaded line structures is 300 µm. The remaining underlying design parameters are listed in Table 4.2. The effective impedance is $Z_b = 50\,\Omega$. For the structure to be realised the parameters listed in Table

$\varepsilon_{r,l}$	$\tan\delta$	d_{LC}	$\varepsilon_{r,\perp}$	τ
3.8	$1 \cdot 10^{-4}$	4 µm	2.5	0.25

Table 4.2: Design parameters of the loaded line structure to be realised.

4.3 were obtained for a design frequency of 20 GHz.

N	Z_l	C_x	l_l
$N_{min} = 8$	103 Ω	100 fF	1.94 mm
10	93 Ω	108 fF	1.55 mm
10	100 Ω	122 fF	1.15 mm

Table 4.3: Resulting parameters of the loaded line structure with a design frequency of 20 GHz.

In the table, three different cases are listed. The structure represented by the values in the first row is the result if the structure is to have the same physical length as an ideal TEM phase shifter. As mentioned in the previous section, it is assumed that the load capacitors have zero dimension. Thus, in reality the structure is 10 to 20 % longer. In the second row, two elements are added to the minimum number of elements which, if the same physical length is to be retained, lowers the necessary Z_l and increases the load capacitor only slightly. If the structure is to be significantly shorter than the ideal TEM phase shifter, the values listed in the third row must be used. This comes, however, at the expense of having to realise a larger load capacitance. The parameters in the third row are the ones used for realising the actual structure presented in this section.

The transmission line topology is a coplanar waveguide (CPW) because this ensures simple realisation. Particularly, shunt elements, i.e. the load capacitors, can be realised without much technological effort. The drawback is of course the significantly higher metallic loss of CPW

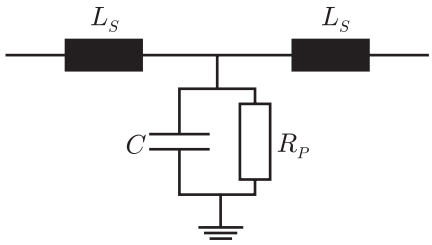

Figure 4.36: Equivalent circuit of the load varactor.

lines compared to for instance microstrip lines. The usage of a microstrip line would, however, require vias through the substrate which is particularly for substrates with high mechanical rigidity (i.e. glass) requiring much more elaborate and expensive processing.

In order to realise a line impedance of above 100 Ω, the gap width g_c of the CPW line has to be large. This, however, poses the problem that the load capacitor has to span this gap which induces a larger series inductance, the larger the gap is. Hence, the gap should be chosen as small as possible, which implies that the center conductor width w_c should be accordingly narrow. A good compromise was found to be a conductor width of 60 µm and a gap width of 195 µm for a CPW with fused silica as substrate and superstrate which has thus an effective permittivity of 3.8. The latter was already implicitly used in Table 4.3 for the calculation of the physical length of the transmission line segments.

Other parameters for the structure are the thickness of the gold electrodes ($\approx 1\,\mu$m) and the spherical spacers to be used (5 µm). As it was observed in the course of this work, the spherical spacers tend to dent the gold electrodes slightly which leads to a decrease of the layer thickness. Therefore the effective layer thickness d_{LC} for the design was assumed to be 4 µm.

First, an individual load capacitor was designed using the Sonnet EM suite. Fig. 4.37(a) shows the dimensions of a single capacitor and Fig. 4.37(b) the from the simulation extracted results. The respective extraction was done using the equivalent circuit shown in Fig. 4.36. The dimensions of the used capacitor are $w_{V,l} = 590\,\mu$m and $w_{V,p} = 148\,\mu$m. With the given aspect ratio of approx. 40, a geometric tuning efficiency of about 85 % can be found from Fig. 4.14(b)

Assumed were a permittivity of 2.9 ($\Delta C_x/2$) with a loss tangent of 0.015 (which corresponds to the highest value for the LCs intended to be used with this structure) and a LC layer thickness d_{LC} of 4 µm. The ITO strips are 10 µm wide. The ITO on the top layer, connecting the floating electrode, is used for applying the bias voltage. The ITO strip on the bottom side, connecting the center conductor and the ground conductors assures that the center conductor is kept on ground potential for the DC or low frequency bias voltage. It was found that ITO having a sheet resistance of several 10 kΩ/□ (thickness <30 nm) has virtually no impact on the the microwave performance of the capacitor.

The series inductance L in Fig. 4.36 amounts to less than 30 pH for frequencies <30 GHz which corresponds to approx. 40 µm of the employed transmission line. Due to the small influence, the series inductance was ignored in the design.

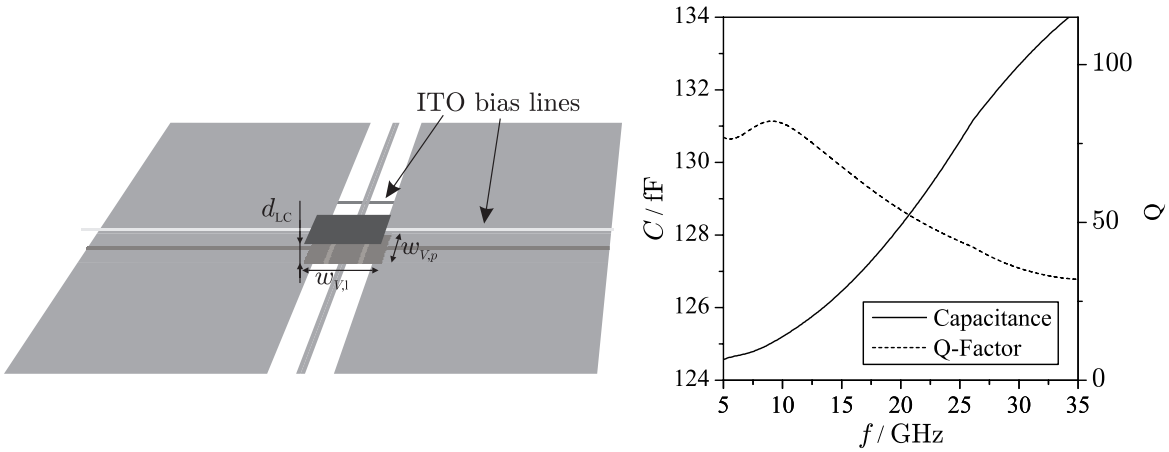

(a) (b)

Figure 4.37: (a) Schematic of a unit element of the loaded line structure. The dark gray printed patch is the floating electrode which is biased by the top layer ITO bias line. (b) Simulation results of the single capacitor as obtained from the Sonnet simulation software.

Fig. 4.38(a) depicts the actual layout of a fabricated device. Three periodic structures are fabricated in parallel on one substrate in order to increase the probability to have at least one working device. It should be mentioned that, although the smallest feature size is with 10 µm rather large, the requirements for the processing are still high because even a small defect can make an entire periodic structure unusable. Fig. 4.38(b) shows a detailed view on the feed line with two unit elements. The feed line has a length of 1 mm and its purpose is to make contacting the structure by coplanar probe tips more convenient than for the single capacitor presented in section 4.2. Fig. 4.39 shows a set of photographs of a fabricated device.

Measurement Results

Two structures were fabricated and filled with the Tolane base matrix and with a high performance mixture (Mixture 1) presented in section 3.1.4. The structure filled with the Tolane base matrix is later again used for the large signal evaluation presented in Chapter 5. The LC is applied to the structures by placing a small droplet on an overlap between the bottom and the top substrate. By capillary attraction the LC then disperses in the air gap within a few seconds. Only less than about 2 μl LC are necessary to fill the fabricated devices.

Fig. 4.40(a) shows the measured scattering parameters of one of the three structures on the device filled with the Tolane Base Matrix. Obviously, the design frequency, i.e. the frequency with the lowest reflection, is shifted to lower frequencies which indicates that the capacitors feature a higher capacitance. This is also reflected by the fact that the cutoff frequency is lower and the ripple density increases towards cutoff frequency as the capacitors are operated closer to their series resonance. Two of the three structures on this substrate were operational (called

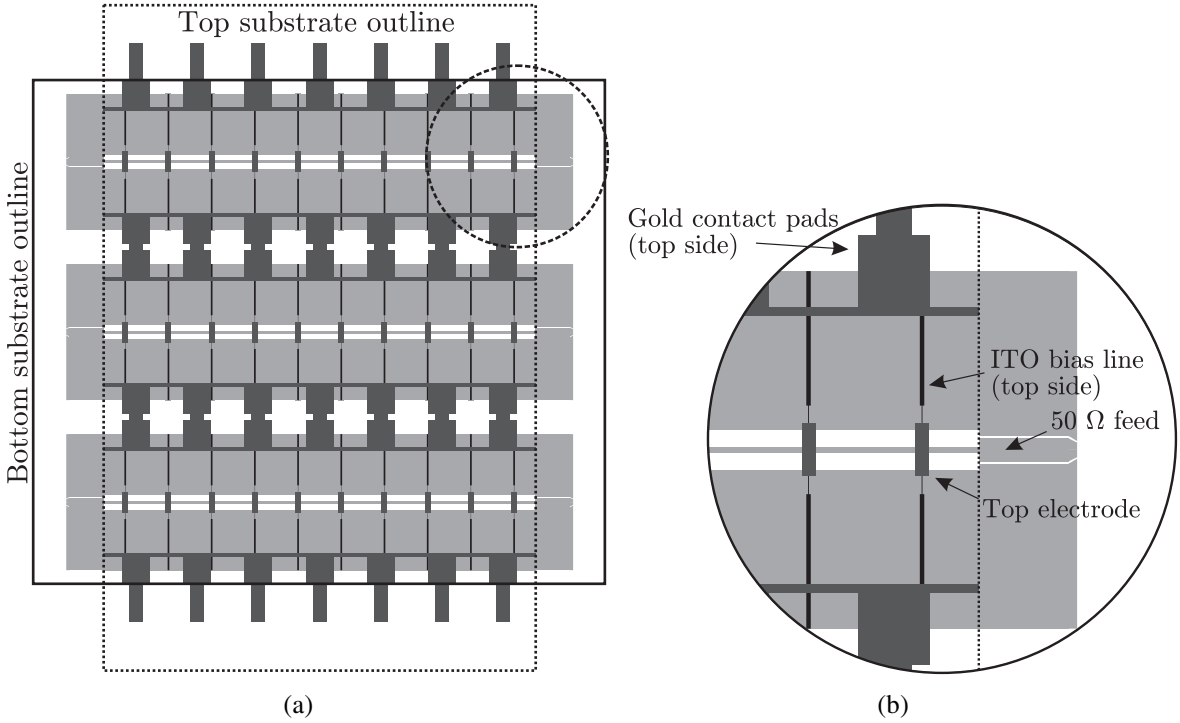

Figure 4.38: (a) Overall structure of three periodically loaded lines fabricated on one substrate. The light gray areas are gold electrodes on the bottom substrate, the dark gray areas are gold electrodes on the top substrate. The black lines are ITO bias lines, also on the top substrate. The entire length of the structure is 14.9 mm. (b) Detailed schematic of the 1 mm long 50 Ω feed line with two unit elements.

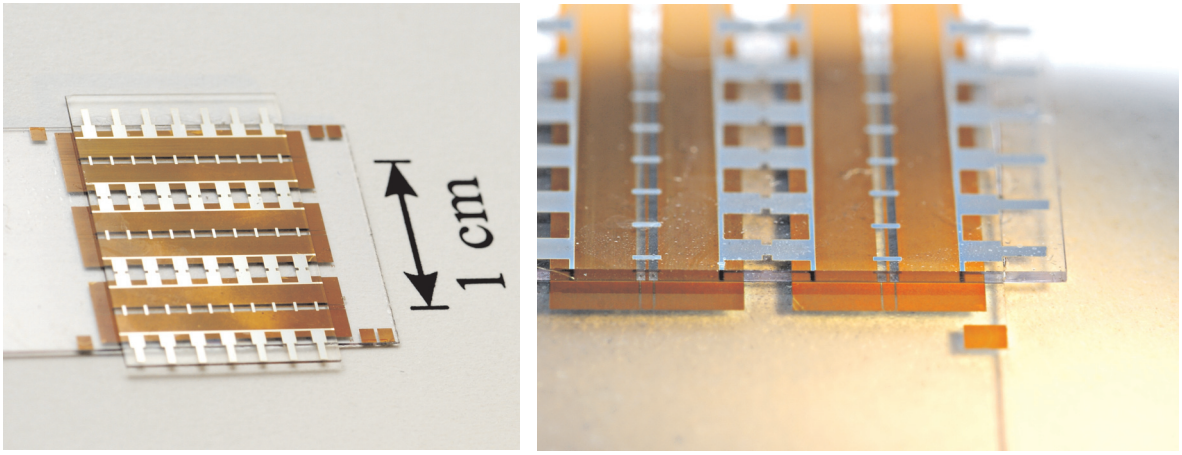

Figure 4.39: Photographs of a realised device with three loaded line structures in parallel. (a) Top view of the device. The light electrodes are located on the upper substrate. The pads on the upper substrate protruding the lower substrates can be accessed from the side in order to apply the bias voltage. (b) Detailed view on the feed section of the device.

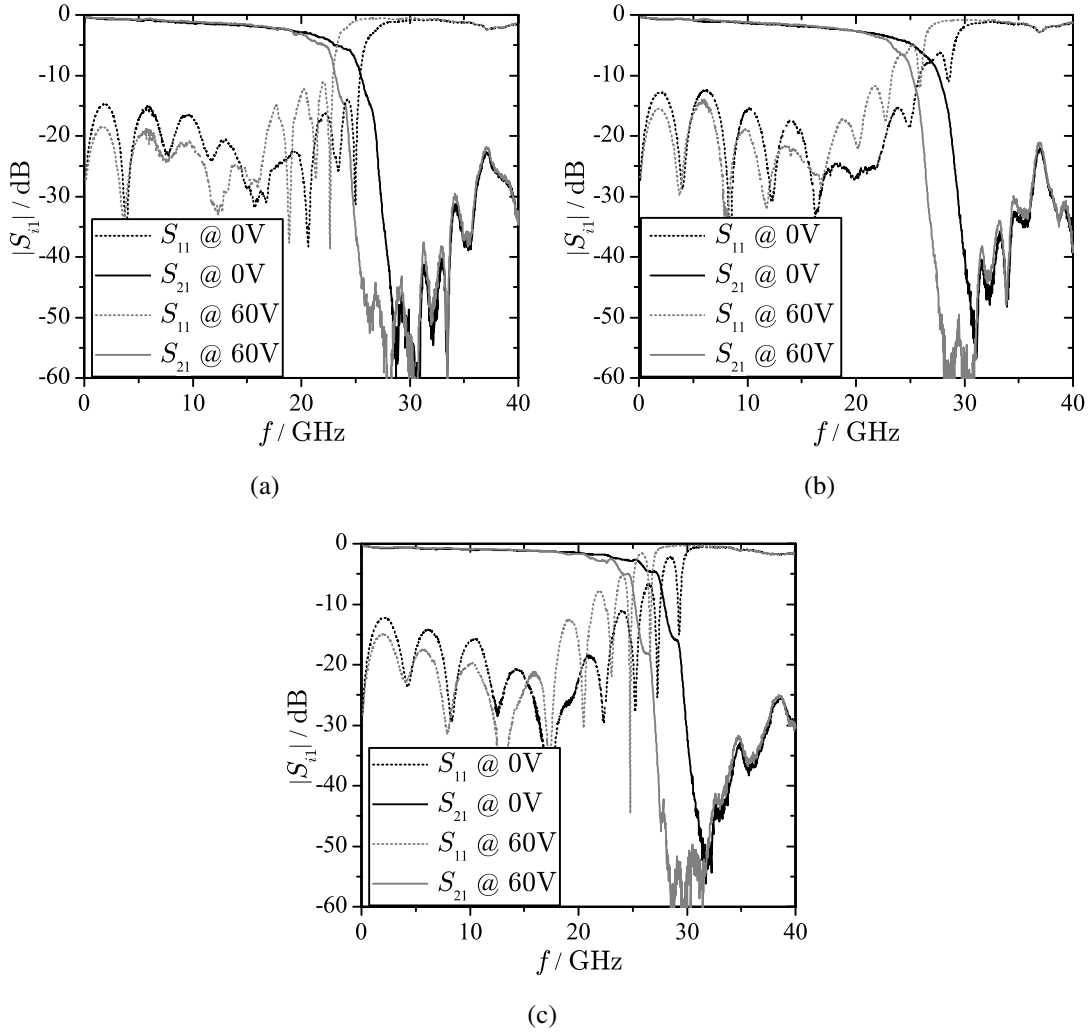

Figure 4.40: Measured scattering parameters of (a) line A (filled with the Tolane base matrix), (b) line B (same substrate) and (c) line C filled with the high performance mixture (different substrate). The maximum applied voltage is 60 V. V_{th} is 8 V for all three devices.

lines A and B in the following). The scattering parameters of the second loaded line (line B) are shown in Fig. 4.40(b). The scattering parameters of a line on the second substrate (filled with a high performance mixture as presented in section 3.1.4) are shown in Fig. 4.40(c). On this substrate only one device was operational (called line C in the following).

Fig. 4.41(a) shows the differential phase shift of the three devices and Fig. 4.41(b) the phase shifter efficiency. As stated above, line A deviates a little more from the design due to the slightly decreased LC layer thickness. The shift of the cutoff frequency to lower frequencies is also visible in the phase shifter efficiency. The slightly higher differential phase shift originates from the increased capacitance values. While lines A and B are filled with the Tolane base matrix and have correspondingly very similar performance, line C is, as stated previously, filled

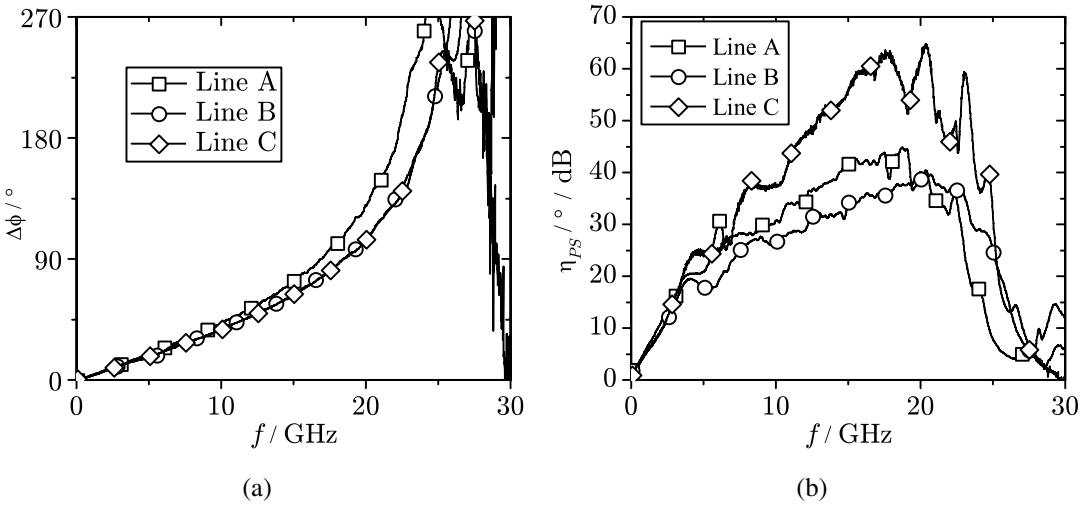

Figure 4.41: (a) Differential phase shift of the three tunable phase shifters. (b) Phase shifter efficiency of the same three lines.

with a LC mixture having very low dielectric loss. This is reflected in the efficiency, which is accordingly high.

Parameter fitting

In order to evaluate how well the realised structures agree with the design parameters, the measured scattering parameters can be fitted with a circuit model. In order to avoid ambiguities of the involved circuit parameters, the model needs to be as simple as possible. Fortunately, the realised structure contains only three parameters which are affected significantly by fabrication tolerances: The loss of the transmission line segments (conductor thickness, roughness of the plated conductor), the capacitance of the load capacitors and the quality factor of the load capacitors. All other parameters can with more or less high accuracy be determined a priori or are anyway given by design.

Fig. 4.42 shows the model for the unit element which is applied in the circuit simulation. The values for L_S and L are determined by data fitting the model of the capacitor with the simulated data shown in Fig. 4.37(b). Doing so one obtains $L_S \approx 25\,\text{pH}$ and $L \approx 13\,\text{pH}$. The values cannot be expected to be very accurate but they provide a reasonable starting point for the following analysis. The data fitting of the important parameters is anyway not too sensitive on L_S and L. Z_L and l_l are determined by design (see Table 4.3). The circuit simulation was performed using AWR Microwave Office. Ten of the unit elements shown in Fig. 4.42 are cascaded and the 1 mm $50\,\Omega$ feed lines are added to the left and the right of the periodic structure.

Firstly, the value of C_x in the not tuned state is determined. This is done by fitting the phase of S_{21} of the circuit model and the measurement. This least squares optimisation is performed

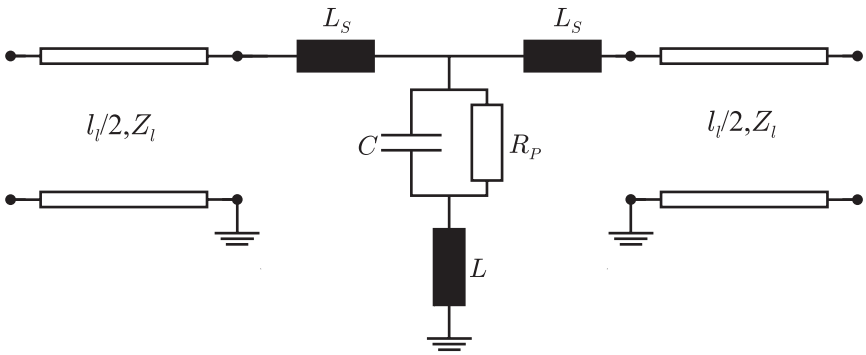

Figure 4.42: Unit element model for the circuit simulation.

Line	TL loss / dB/m	C_x /fF	Q_x
A	36	150	33
B	42	127	33
C	35	125	61

Table 4.4: Parameters obtained from the data fitting of the measured phase shifters.

from zero frequency up to the cutoff frequency. With the found value of C_x, the absolute value of S_{21} of the model is adjusted such that the difference of $|S_{21}|$ between model and measurement is minimised. As the model was kept simple, i.e. the transmission line loss is modeled with the typical $\sqrt{\omega}$ proportionality, the optimisation of $|S_{21}|$ was done from 10 GHz upwards since only for higher frequencies the loss is governed by the skin effect. Fig. 4.43 shows the result of the parameter fitting for the scattering parameters and the transmission phase of the three lines at zero bias. The important parameters obtained from the data fitting are listed in Table 4.4.

Using the parameters listed in Table 4.4, the analysis can be carried still further. Assuming that the obtained C_x values are correct, the effective tunability of the varactors can be estimated. If τ_{C_x} is estimated to be 0.2 for all three lines, the resulting differential phase shift fits very well (see Fig. 4.44(a)). An increase of 50 % of the varactor quality factor Q_x is assumed when the varactor is biased. Based on the parameters in Table 4.4, an estimate of the phase shifter efficiency can be obtained. Fig. 4.44(b) shows the results which show good agreement with the measurements.

It should be noted that the values in Table 4.4 have a certain error which is, however, difficult to quantify as the error of the underlying parameters is unknown. Particularly, the C_x value depends on the choice of L (see Fig. 4.42). In that respect, the tunability can also be slightly higher if a higher L is permitted which would lower C_x. Effects like inhomogeneities within a line structure are also not considered as well as higher current densities inside the capacitors at higher frequencies and the influence of the skin effect on the varactor quality factor. Nevertheless, the aim of the presented modeling is to show the trends of the individual parameters, in particular that of C_x. The model shows that the realised structure is very close to the design.

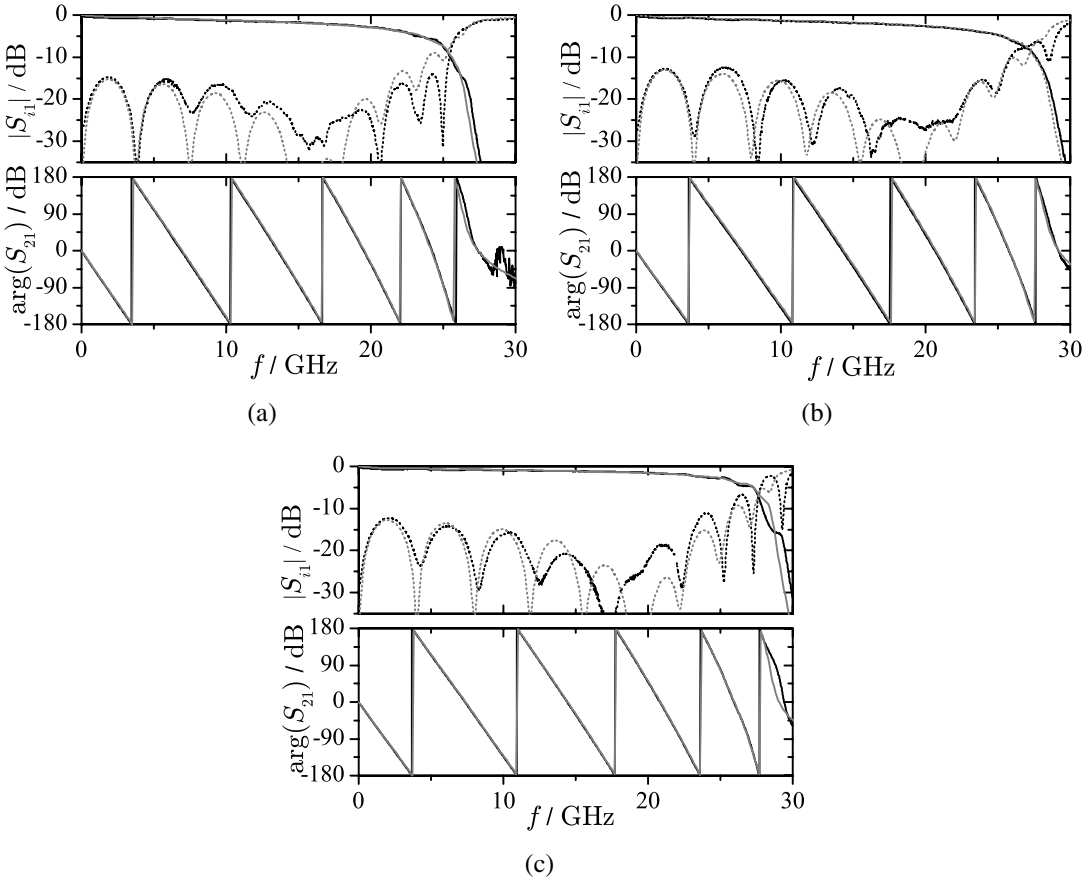

Figure 4.43: Comparison between the measured and the fitted model scattering parameters for (a) line A, (b) line B and (c) line C. The black lines represent the measurement, the gray ones the model. Both measurement and model are evaluated at zero bias.

Response Times

The response times are the fundamental advantage of the structure presented in this section. Therefore, the response times for steering the phase shifter from 10 % to 90 % of the available differential phase shift and vice versa were measured. Table 4.5 lists the results.

The difference between line A and B can be explained by the obviously thinner LC layer. The response times of line A and B roughly agree with Eqn. (2.37): As the capacitance is roughly proportional to d_{LC}^{-1} and the tuning speed t_0 is proportional to d_{LC}^2 (see section 2.4.3) $t_{0,A}/t_{0,B} \approx C_{x,B}^2/C_{x,A}^2$ with A and B indicating the corresponding line. The $C_{x,B}^2/C_{x,A}^2$ ratio is 0.72, $t_{rise,A}/\tau_{rise,B}$ is 0.76 and $t_{decay,A}/\tau_{decay,B}$ is 0.8. Hence, both for the rise and the decay time the proportionality between the tuning speed and the square of the LC layer thickness is confirmed which in turn confirms that the alignment layer has acceptable quality. The response time of line C is much slower due to the used LC which has higher viscosity.

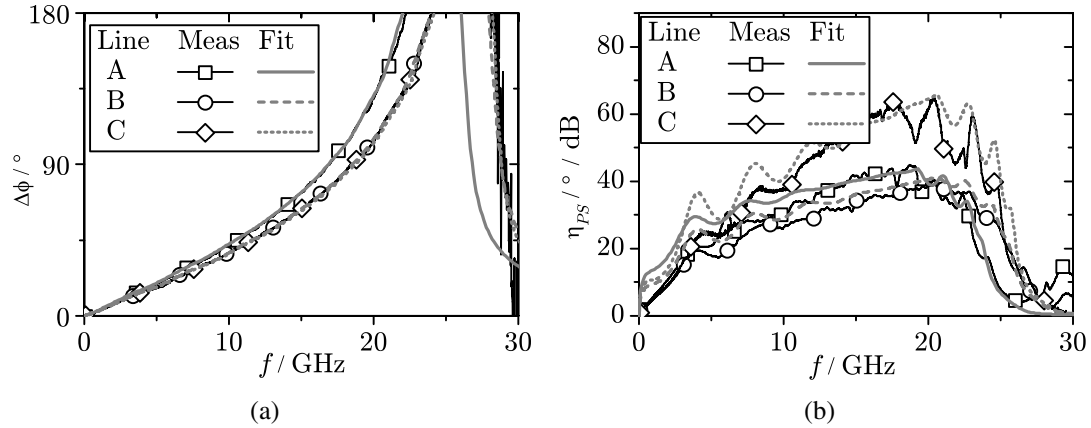

Figure 4.44: Comparison of the evaluations of the fitted parameters with the measurements for (a) the differential phase shift and (b) the phase shifter efficiency.

	A	B	C
t_{rise} / ms	19	25	110
t_{decay} / ms	75	94	340

Table 4.5: Response times

4.4 Conclusion

This chapter shows the development of devices with thin LC layers having a thickness of only a few microns. The main purpose of such thin layers is, as it is for displays, to accelerate the tuning speed of LC-based microwave devices.

In a first step, a simple transmission line phase shifter with a LC layer thickness of 23 µm is realised in order to explore the more advanced display-like fabrication style. This fabrication scheme is then enhanced further and used to demonstrate the feasibility of tunable parallel plate capacitors with fast response times. In fact, depending on the thickness of the LC layer and on the LC material itself, the response times can be as low as a few ms. It is also shown that parallel plate capacitors, as proposed in this work, do not have the unfavourable metallic loss dependency on the LC layer thickness as simple transmission line phase shifters have.

The applicability of such tunable capacitors is then demonstrated in a more complex circuit, namely a periodically loaded transmission line realising a phase shifter. The tunable capacitors are used as the periodical loads and hence the phase shift of the entire device can be controlled. A phase shifter performance of up to 60 °/dB insertion loss is obtained with a LC layer thickness of only 4 µm. Due to the use of a more viscous high performance LC, the response times of max. 340 ms are somewhat slower than those obtained from individual parallel plate capacitors. Nevertheless, they are still acceptable and one to two orders of magnitudes faster than those obtained in other works dealing with LC-based RF devices. As a further technological enhance-

ment, resistive electrodes made of Indium-Tin-Oxide (ITO) are used. With such electrodes, it is possible to have biasing circuitry which is inherently decoupled from the RF electrodes.

Chapter 5

RF Power Handling Capability of Liquid Crystal Devices

In terms of power handling capability, two effects have to be investigated: The heating of the device due to the elevated power levels and the nonlinear response of the device. Depending on the considered devices or circuits, these two issues can be treated separately or have to be treated as coupled effects. In the simplest case, high RF power just heats the device due to whatever loss mechanism in the device and it has to be determined up to which power level the heating is tolerable or how the heating affects the overall device performance. On the other hand, mechanisms inside the device have to be identified which cause nonlinear signal distortion. In amplifier devices, such distortions are caused e.g. by effects like compression and saturation. Both effects, thermal heating and nonlinearity, can also be coupled. This phenomenon is called thermal intermodulation distortion [WGS06]. It occurs when the signal applied to the device has an envelope which the thermal effect can follow. This effect is e.g. well known from thin-film resistors.

In this chapter, the response of LC based devices to signals having larger amplitude is investigated. Large amplitude in this context means signals exceeding power levels of -10 dBm as they are commonly used for small signal characterisation. More precisely, power levels of up to 30 dBm will be used to probe the power handling capability of LC devices. The presentation here is done using the periodically loaded line structure filled with the Tolane base matrix as presented in section 4.3.5. This device can be considered representative for all microwave LC devices as it is possible to demonstrate all fundamental effects with this still rather simple topology. The used devices for the large signal evaluations did not feature ITO for biasing so the bias voltage had to be applied via the center electrode using external bias tees.

In this chapter, two different approaches are used in order to characterise the large signal behaviour of the device. Firstly, the excitation of the device with a single tone and how this leads to self actuation of the LC is discussed. The results are compared with theoretical results ob-

tained using the Continuum Theory of LCs. Secondly, the intermodulation properties of the device are investigated from which the important benchmark figure IP3 can be obtained.

5.1 Self Actuation

In order to verify that self actuation is present and measurable, a single tone measurement setup was implemented. The information whether the LC, or more precisely, the director is actuated by the RF signal, can be most conveniently gathered from the phase shift the effect causes in investigated phase shifter device. Fig. 5.1 shows the complete setup schematically. Port 1 of

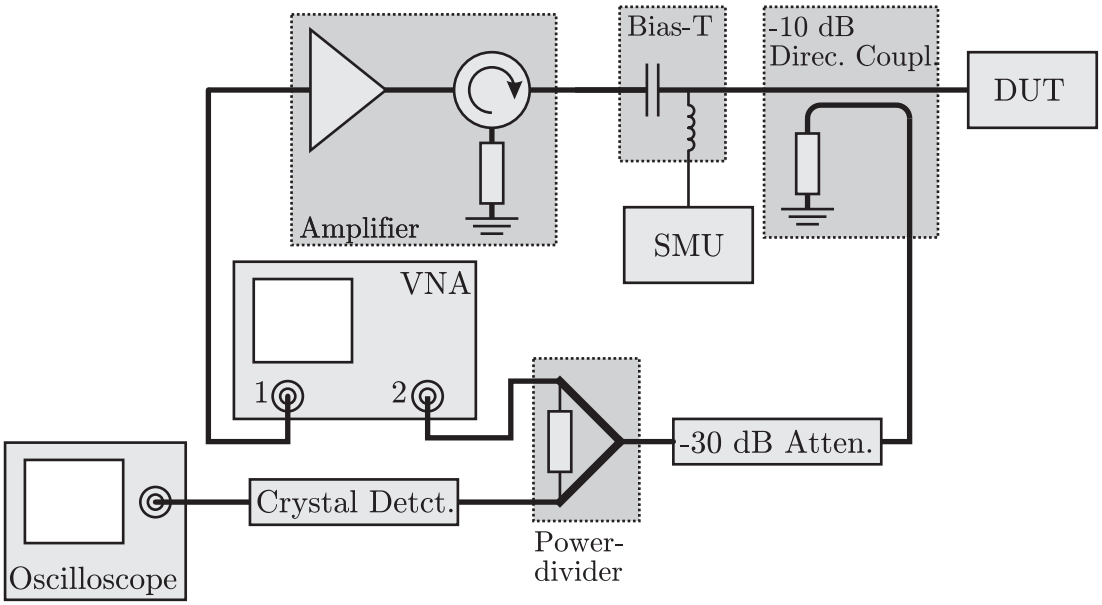

Figure 5.1: Measurement setup for determining the self actuation.

the vector network analyser (VNA) is directly fed to the input of an amplifier (Hughes 8000H traveling wave tube amplifier, TWTA) with a maximum output power of 40 dBm from 4 to 8 GHz. The VNA (Anritsu 37397C) is in continuous wave (CW) mode at a frequency of 6 GHz. This frequency has been chosen on the one hand to be able to use the available amplifier and on the other hand because the insertion loss is at most 1 dB at this frequency and therefore the influence of self-heating of the device is reduced. Nevertheless, it will be seen later that self-heating is present. A bias-tee is necessary in order to investigate the influence of tuning on the nonlinear behaviour of the LC. The DC bias voltage used for these high power measurements is provided by a Keithley 2612 source measurement unit. The utilisation of a DC voltage is feasible as the LC used in these experiments features a very low conductivity so the detrimental influence of ionisation effects is negligible in the scope of the conducted experiments. The DC current is only 10 nA even with the saturation voltage of 60 V applied .

The DUT is measured in reflection configuration. This method has been chosen in order to amplify effects caused by the LC in two ways: First of all, the wave propagation along the structure has to travel twice the distance. Second of all, because a standing wave forms on the transmission line, the voltage at the maximum is doubled. This is important because it will cause the threshold voltage of the LC to be exceeded sooner at lower input power levels, albeit only for some parts of the structure. Of course this effect is not desirable in an application but it is advantageous for investigating the response of the LC to the RF signal.

The reflected signal is taken from a -10 dB directional coupler which also eliminates the need for a second DC-blocking device for protection of the network analyser input port. In order to decrease the power level incident to the network analyser another 30 dB attenuation is included. The reflection type measurement is possible because the output circulators of the amplifiers do not exhibit increased non-linear behaviour even at high VSWR conditions.

The attenuated signal is eventually measured at port 2 of the VNA. Like for the small signal characterisation, the DUT is contacted using a CPW probe. Part of the reflected signal is coupled to a crystal detector (HP 8472A) for power level measurement vs. time. The purpose of that is to obtain a precise time base for the power sweep.

The essential measurement strategy chosen here was to sweep the power coming from Port 1 from low values to high values. Furthermore, the bias voltage was varied. The transmission vs. input power ($S_{21,0}(P_{in})$) was recorded at 6 GHz as a reference with nothing connected to the CPW probes. By placing the probe tips on the substrate surface during these measurements, it was assured that electrostatic actuation of the tip itself does not influences the reference measurement. Together with the measurements taken with DUT ($S_{21,DUT}(P_{in},V_b)$), the influence of the DUT can be calculated according to Eqn. (5.1).

$$R(P_{in},V_b) = \frac{S_{21,DUT}(P_{in},V_b)}{S_{21,0}(P_{in})} \tag{5.1}$$

P_{in} is the power fed to the DUT and V_b is the bias voltage. Normalisation of $S_{21,DUT}(P_{in},V_b)$ for each power level is necessary as the power amplifier used here shows both compression effects (AM-AM conversion) and AM-PM effects, i.e. the transmission phase depends on the input power level applied to the amplifier. Fig. 5.2 shows this behaviour for the considered power levels. The input power axis represents the power incident at the input port of the DUT. The values shown in Fig. 5.2 are normalised with respect to the $S_{21}(P_{in})$-parameter at very low power levels ($S_{21}(P_{in} \rightarrow 0)$).

The voltage drop vs. time at the crystal detector (V_{CD}) as recorded by the oscilloscope, corresponding to the incident power, is shown in Fig. 5.3. Each individual power level is applied for 11.5 ms. This time span was chosen such that it is in the same range as the response time (t_{rise}) but short enough to prevent any major influence of thermal effects. Thermal effects within the measurement setup itself, i.e. individual components heating up and changing their behaviour, were minimised by performing the power sweeps as depicted in Fig. 5.3 only once every minute. Self heating in the DUT during a power sweep was observed nevertheless, but the effect is distinguishable from the self actuation effect as will be shown further below.

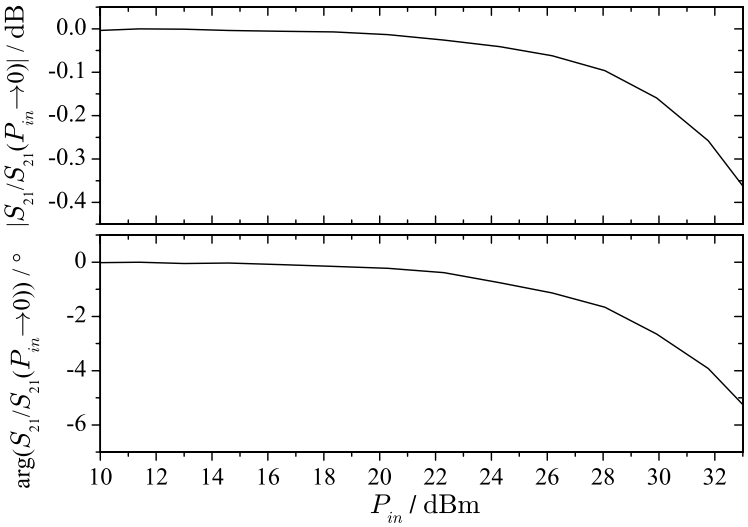

Figure 5.2: The behaviour of the measurement system vs. excitation power

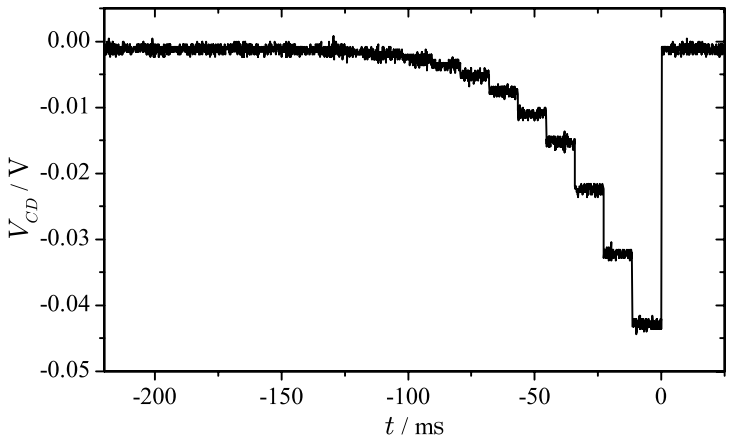

Figure 5.3: The voltage V_{CD} vs. time as measured by the crystal detector

Fig. 5.4 shows the results for both the absolute value and the argument of Eqn. (5.1). From Fig. 5.4, it can already be seen that self actuation effects are present which stem from the deformation of the director at $V_b = 0\,\mathrm{V}$. At high power levels (33 dBm), the transmission phase (Fig. 5.4(b)) decreases, i.e. the DUT becomes electrically longer. At the same time, the insertion loss (Fig. 5.4(a)) decreases suddenly. This can be explained by the fact that the effective loss tangent of the director decreases when it is turned towards parallel alignment with the field which in turn supports the assumption that self actuation is the cause of the effect visible in Fig. 5.4. With increasing bias voltage, these self actuation effects are increasingly diminished. As the bias voltage reaches saturation, the effects on the transmission phase vanish more or less completely. The impact on the insertion loss visible for the biased case, i.e. a slight increase, can be explained by an increased temperature caused by self heating which in turn increases the loss tangent of the liquid crystal. Evaluating the impact at maximum input power level ($\approx 33\,\mathrm{dBm}$), one obtains

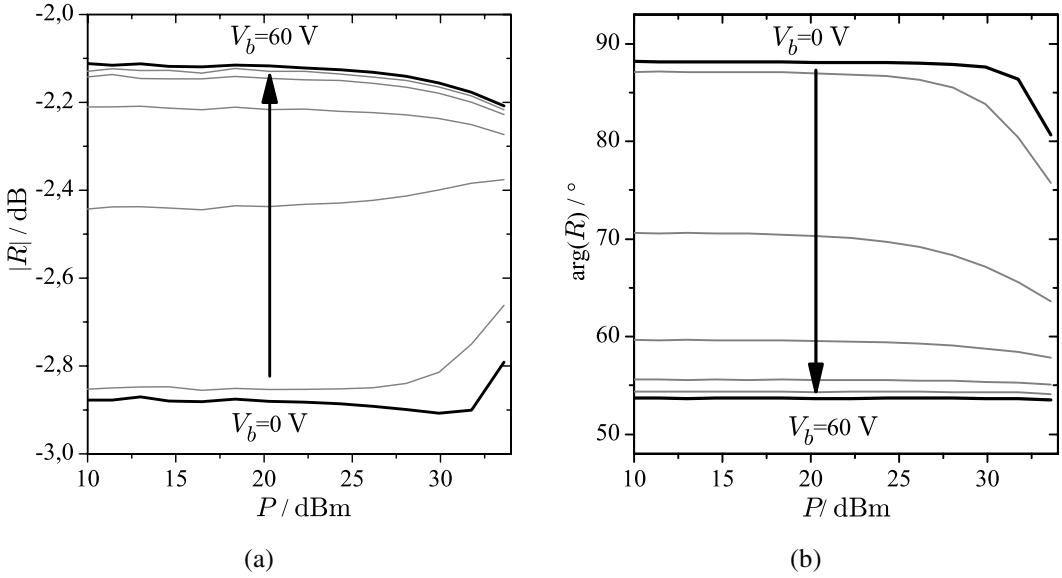

Figure 5.4: Measurement results of the self actuation experiment, calculated according to Eqn. (5.1). The bias voltage is swept from 0 V to 60 V in steps of 10 V. (a) The absolute value of $R(P_{in}, V_B)$ in dB, (b) the measured phase of $R(P_{in}, V_B)$.

the plots shown in Fig. 5.5, which highlight and explain the influence of the self actuation in more detail.

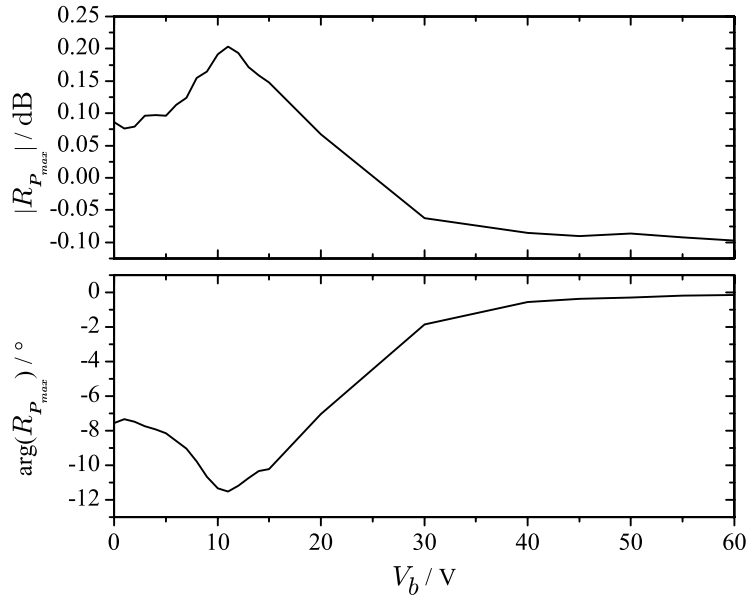

Figure 5.5: Influence of the self-actuation vs. bias voltage

The quantity plotted here is the the influence of the self actuation R normalised with respect to the (nonexistent) influence at low power levels:

$$R_{P_{max}}(V_b) = \frac{R(P_{max}, V_b)}{R(P \to 0, V_b)} \tag{5.2}$$

As can be seen from Fig. 5.5, there is a certain amount of self actuation present at zero bias condition as described above. As the bias voltage is increased, the self actuation first increases up to a voltage of about 10 V, i.e. the phase shift increases and the insertion loss decreases. This behaviour can be explained by the effective lowering of the threshold voltage for the high frequency field. If the bulk is already prebiased, the torque of the high frequency field adds to the torque caused by the bias field. Graphically, the deforming of the director becomes easier for the high frequency field if a bias field is present.

Above approx. 10 V, the influence of the self-actuation obviously decreases. This decrease at bias voltages slightly above the effective threshold for the given LC/device (see also Fig. 4.23(b)) can be explained using Fig. 2.6(b). From this figure, it is apparent that the second derivative of the depicted function with respect to the bias voltage is always positive, i.e. the slope is decreasing with increasing voltage. This means that the same holds true for the effective phase shift which is proportional to $\sqrt{\varepsilon_r(V_b)} - \sqrt{\varepsilon_{r,\perp}}$. Knowing that, it can be deduced that a fixed differential increase of the overall voltage, in this case caused by the high frequency voltage, from any bias state with $V_b > V_{th}$ will have a lower relative impact on the overall phase shift the higher the bias voltage is.

Once the bias voltage reaches saturation, the impact of the self actuation is reduced to zero. This can be seen immediately when looking at the argument of $R_{P_{max}}(V_b)$ in Fig. 5.5 which approaches zero for high bias voltages. The absolute value, however, is below zero for high bias voltages which can be attributed to heating effects which are certainly present at the employed power level.

As the investigations presented in this section are to some extent dependent on time, i.e. on how long power is applied to the DUT, an investigation aiming to separate the influence of self-actuation and thermal effects was also conducted. The results of this analysis are presented in the next section.

5.2 Influence of Thermal Effects

When higher power levels are transmitted through the device, the resulting heating of the device will have impact on the device performance. The actual impact of the absorbed power depends on the specific loss of the device and also on the capability of the device to dissipate the absorbed power. Using glass substrates is certainly not an ideal solution, however, as explained in the previous chapters, glass is still the substrate with the overall best performance for LC microwave devices. Therefore, it is necessary to study on time scale of at least several seconds how devices built using this technology behave under high-power conditions.

Like self-actuation, as presented in the previous section, thermal effects are governed by a specific time constant. It is therefore necessary to record the S_{21} parameter versus time (with DUT applied) of the setup shown in Fig. 5.1. For that purpose, the power is switched on at $t = 0$ and then S_{21} is recorded continuously for several seconds.

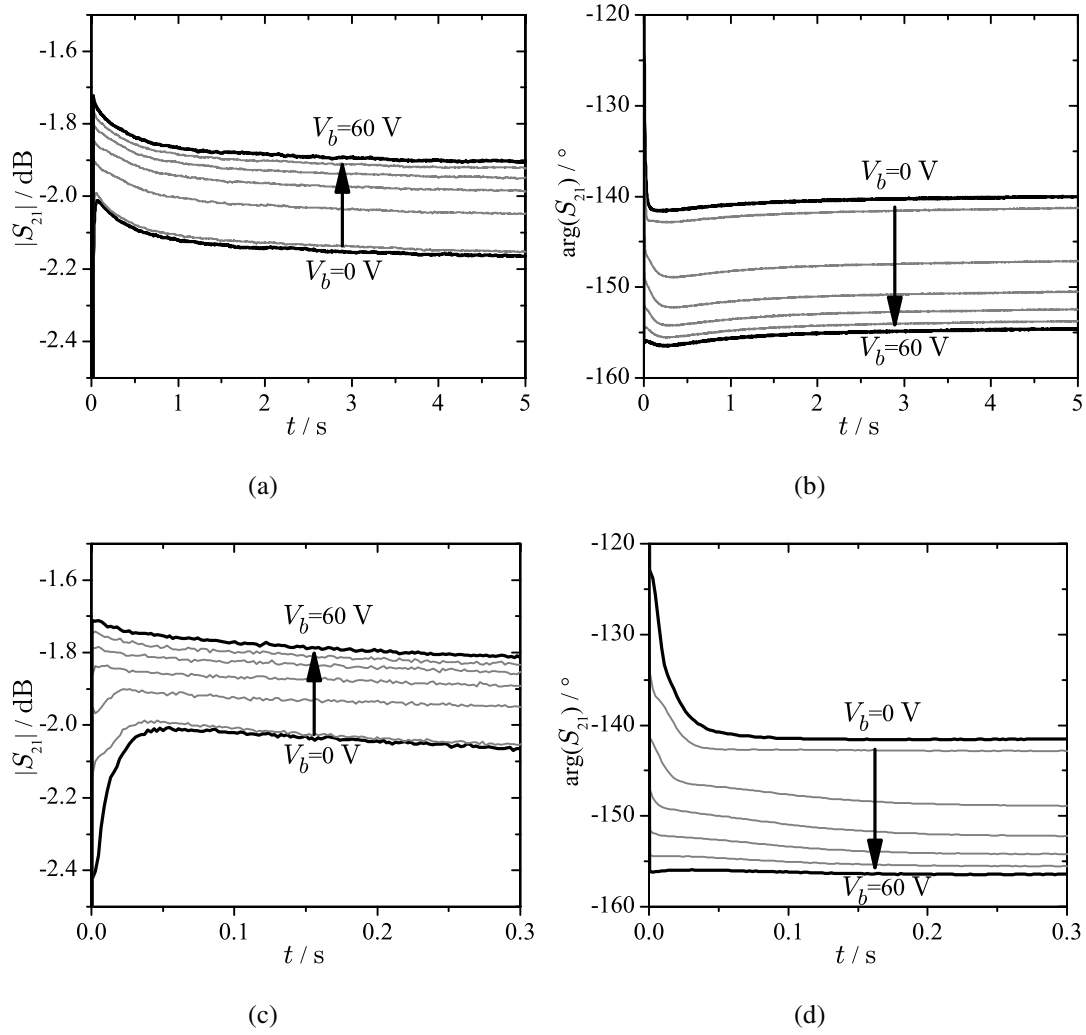

Figure 5.6: Measurement at room temperature for identifying power induced thermal effects in the liquid crystal. The black lines represent the bias states at 0 V and at 60 V. The gray lines are the bias states in between in 10 V steps. The characteristic of S_{21} were recorded for 5 s. (a) The magnitude of the measured S_{21} parameter. (b) The argument of S_{21}. (c) and (d) show a detailed view of the recorded process directly after the power is switched on.

Figure 5.6 presents the measured absolute value and argument of S_{21}. The measurements were taken at room temperature with an input power level of 33 dBm applied to the DUT. The set of curves shown in Fig. 5.6 were created by applying bias voltages from 0 to 60 V in steps of 10 V. As shown in section 3.1, the change of the loss tangent with temperature is almost linear for temperatures well below the clearing point. Therefore, a visible indication should exist in the

magnitude of S_{21}, i.e. the insertion losses should increase. This effect is clearly visible in Fig. 5.6(a). Here the insertion loss increases within a time of several seconds. The argument of S_{21} (Fig. 5.6(b)) shows that the phase shift is decreasing as the temperature increases. This can be expected as for times > 0.5 s the director is more or less in the $\varepsilon_{r,||}$ configuration which means that the effective permittivity decreases with increasing temperature due to the decreasing order.

It is interesting to focus on the behaviour of the DUT, or the LC, respectively, directly after the power is switched on. This detailed view is depicted in Figs. 5.6(c) and 5.6(d). With the help of these two figures, it is possible to distinguish the self actuation and the thermal effect. As can be seen from Fig. 5.6(c), in case of no bias, there is an immediate drop of the insertion loss directly after the power is switched on. This corresponds to an increase of the phase shift (Fig. 5.6(d)) which in turn is explained by the self actuation. This effect is, as can of course be expected from the findings in the previous section, diminished as the bias voltage increases. From this, it can be concluded, that the time constant of the self actuation is in the range of some tens of ms while the time constant of the thermal effect is in the order of seconds which makes the two processes clearly distinguishable.

5.3 Interpretation and Modeling

Looking at the results presented in the previous sections, a theory explaining the results can be developed. This theory is essentially based on Eqns. (2.28) and (2.29), which predict self-actuation of the LC director for any applied electric field, including microwave fields. It should be pointed out here that self-actuation is a very well known phenomenon also for RF-MEMS [Reb03].

However, specific to LCs, compared to RF-MEMS, is that a threshold voltage exists. This threshold voltage also exists for high frequency signals although it will assume a different value due to the fact that $\Delta\varepsilon_r$ takes different values at microwave frequencies. For most LCs, $\Delta\varepsilon_r$ has rather large values (≈ 10) at low frequencies and, as seen in section 3.1, low values at high frequencies. Consequently, the threshold voltage will be lower at microwave frequencies.

In order to predict the effect of a signal having a certain power level, the voltage being effective for the LC layer must be determined. For a regular TEM transmission line this is simple since the voltage level is linked to the power level through the line impedance. For any other circuit, the voltage must be calculated. For the loaded line topology as employed here, circuit theory has to be applied. According to the loaded line approach presented in section 4.3.1 and in [Poz04], the impedance of the artificial structure is only known at the terminals of the unit elements. Therefore, the voltage drop across the load impedance, i.e. the capacitors, has to be calculated or at least be estimated. For that purpose, the circuit depicted in Fig. 5.7 is considered.

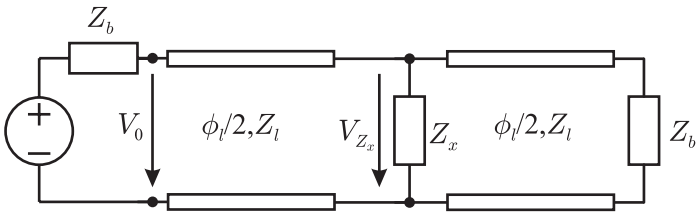

Figure 5.7: Unit element of the loaded line structure.

The unit element shown is the same as in Fig. 4.26. V_{Z_x} can be calculated by employing simple circuit analysis.

$$\left|\frac{V_{Z_x}}{V_0}\right| = \left|\frac{2Z_xZ_l}{f_{\cos}\cdot(2Z_xZ_l + Z_bZ_l) + jf_{\sin}\cdot(2Z_xZ_b + Z_l^2)}\right| \tag{5.3}$$

Z_b is calculated according to Eqn. (4.31). Although Eqn. (5.3) cannot be simplified such that general insight can be obtained, Eqn. (5.3) can nevertheless be evaluated for the parameters of the structure (Z_l, Z_x, etc.) presented in section 4.3.5. Fig. 5.8 shows the calculated results with respect to the frequency normalised by the cutoff frequency of the structure. As a matter of fact,

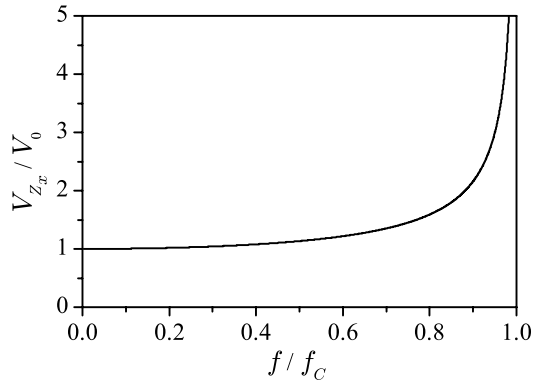

Figure 5.8: The ratio $|V_{Z_x}/V_0|$ plotted versus frequency. f_C is the cutoff frequency of the structure.

if other parameters are chosen, the behaviour remains almost the same. The information to be obtained from this analysis is that the absolute value of the effective voltage drop across the load impedance can be approximately calculated according to

$$V_{Z_x} = \sqrt{P_0 Z_b} \tag{5.4}$$

for frequencies much smaller than the cutoff frequency. Eqn. (5.4) can be employed for this works experiments as they are presented in this chapter as the probing frequency of 6 GHz is much smaller than the measured cutoff at approx. 25 GHz. For frequencies approaching the cutoff frequency, however, the voltage drop increases and hence the self actuation effects can be predicted to increase.

In order to have an estimate of the power level from which self actuation can be expected, two parameters must be known: $\Delta\varepsilon_r$ and K_{11} (compare Eqn. (2.30)). While $\Delta\varepsilon_r$ is known (at

microwave frequencies, see section 3.1 for the Tolane base matrix), the K_{11} parameter was not accessible in the scope of this work. Despite that, it can be assumed, based on the measurements presented in section 3.1.3, that there are no pronounced relaxation processes present towards low frequencies for the LC used for these experiments. This means $\Delta\varepsilon_r$ is unaltered towards low frequencies, which in turn means that the measured threshold of approx. 8 V for low frequencies can also be expected to be valid for microwave frequencies. Therefore, the threshold power level P_{th} for the given device is approximately

$$P_{th} = \frac{1}{4} \cdot \frac{V_{th}^2}{Z_b} \approx 25\,\mathrm{dBm}. \tag{5.5}$$

The factor 1/4 is introduced to reflect the fact that the measurements are done in reflection configuration, which effectively doubles the voltage across the capacitors.

Eqn. (2.36) can be used to explain and, to some extent, model the measured results presented before. The problem is to find a solution for sinusoidal excitation. Literature commonly only addresses step functions for $V(t)$ and the operation mode which is employed here is not considered at all. Eqn. (2.36) can be discretised which enables a numerical solution for an arbitrary excitation:

$$\frac{\Delta^2\Theta}{\Delta z^2} - \frac{V^2}{V_{th}^2}\pi^2 \sin\Theta\cos\Theta = \frac{\gamma_1}{K_{11}}\frac{\Delta\Theta}{\Delta t} \tag{5.6}$$

This equation can be solved for $\Delta\Theta$ which yields the following equation:

$$\Delta\Theta = \frac{\Delta t}{c_r} \cdot \left(\frac{\Delta^2\Theta}{\Delta z^2} - \frac{V^2(t)}{V_{th}^2}\pi^2 \sin\Theta\cos\Theta \right) \tag{5.7}$$

c_r is γ_1/K_{11}. The two parameters γ_1 and K_{11} are combined as the analysis presented here is only qualitative; the quantities of the two parameters were anyway not accessible in the scope of this work. From that point of view, c_r serves only as a scaling factor for the time axis and can be set one. Together with Eqn. (5.7), the following update rule for the director distribution Θ can be established:

$$\Theta(t + \Delta t) = \Theta(t) + \Delta\Theta \tag{5.8}$$

In the subsequent derivations, it will be assumed that the DC threshold and the RF threshold are equal. It should be noted that this is in general not the case, i.e. the RF threshold is larger than the DC threshold due to a lower $\Delta\varepsilon_r$. However, for the LC used here, the effective threshold voltage for both DC and RF fields are almost identical so for it is valid to use the same voltages in a simulation. In fact, this greatly simplifies the simulation as Eqn. (5.7) does not need to be expanded in order to account for a dispersive $\Delta\varepsilon_r$.

First, the excitation with a monochromatic signal is considered. The frequency is chosen high enough such that the director cannot follow it but also low enough in order to obtain an economic timestep Δt. In the example presented here, a value of $f_0 = 1 \cdot 10^6\,\mathrm{Hz}$ was sufficient.

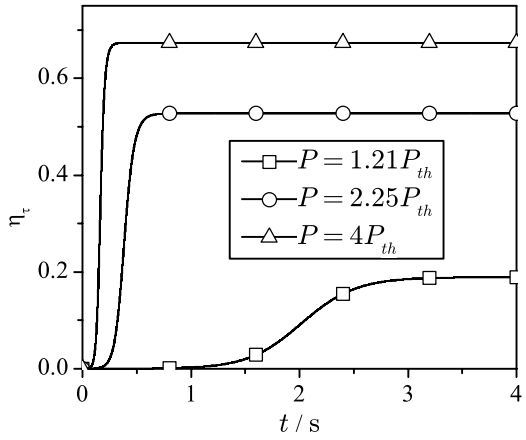

Figure 5.9: Self actuation versus time. Shown is the η_τ-parameter representing the effective utilisation of the ansitropy. The process was simulated for three different power levels.

In Fig. 5.9 the self actuation of a bulk of LC is depicted. The parameter η_τ is the same as defined in Eqn. (2.35). The values of the permittivities in the example are $\varepsilon_{r,\perp} = 2.5$ and $\Delta\varepsilon_r = 1$. The process speed depends on the applied power level as can be expected from Eqn. (2.39), i.e. the higher the power level and therefore the effective voltage, the faster the director reaches equilibrium state. Below the threshold power level, no actuation occurs.

Having such a means of evaluating the influence of an RF signal on the director, it is possible to corroborate the interpretations given above by simulation. Particularly, the behaviour shown in Fig. 5.5 can be explained.

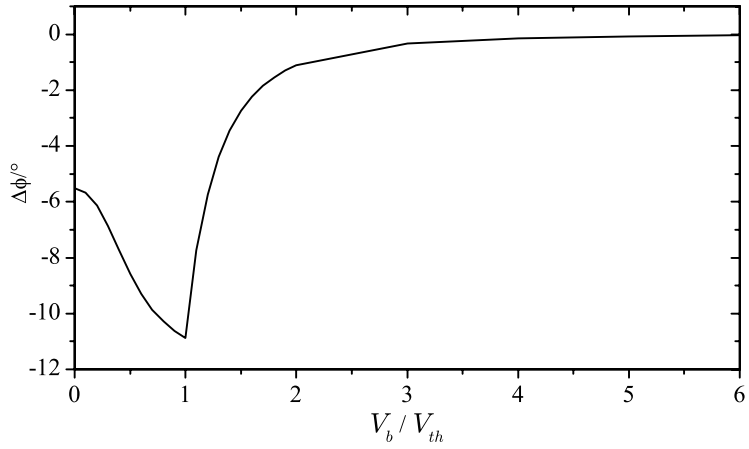

Figure 5.10: Differential phase shift of a phase shifter. The RF power is kept constant while the bias voltage is changed

Fig. 5.10 shows the result of a simulation which assumes $\varepsilon_{r,\perp} = 2.5$ and $\Delta\varepsilon_r = 1$ to be used for a tunable phase shifter. As hinted above, these values are assumed to be constant versus

frequency (i.e. $\Delta\varepsilon_r$ is constant vs. frequency). Furthermore, the electrical length of a tunable phase shifter, the differential phase shift of which is determined by $\varepsilon_{r,\perp}$ and $\Delta\varepsilon_r$, is assumed to be π. The simulation was carried out such that it reflects the conditions of the measurement presented in Section 5.1 and Fig. 5.5, i.e. the bias voltage was applied for several seconds before the RF power was applied in order to ensure equilibrium state. The simulation starts with a director configuration according to the bias voltage and the RF power is then applied from the beginning of the simulation. The director configuration without RF power and only bias voltage is calculated according to section 2.4.2. The simulation then runs a specified time (0.5 s in this example) and the director state is sampled at the end of the simulation.

The resulting values shown in Fig. 5.10, of course, do not represent the real experiment as the simulation assumes that the LC in the entire phase shifter is actuated and not only the parts near the standing wave maximum. Nonetheless, the qualitative agreement between the simulation in Fig. 5.10 and the measured results in Fig. 5.5 is incontrovertible. The only remarkable difference is that in the measurement the apex around the threshold is not as pronounced as in the simulation. Potential reasons for that can be a slightly different $\Delta\varepsilon_r$ for low and RF frequencies for the real LC material or the fact that the assumption $K_{11} = K_{33}$ used in the simulation is in reality not valid.

5.4 Investigation of Two-Tone Intermodulation

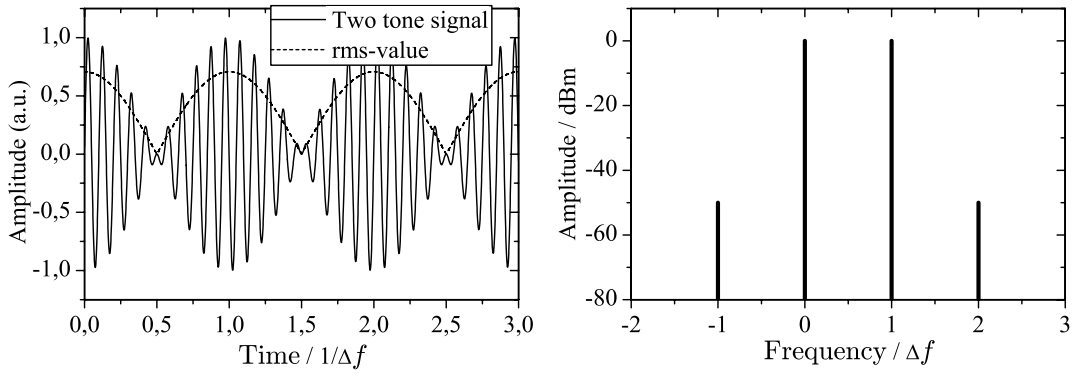

Figure 5.11: (a) Time domain signal of two combined tones having the distance Δf. The x-coordinate is normalised by $1/\Delta f$. The rms-value represents the effective value of the voltage seen by a system which is too slow to follow the high frequency signal. (b) The qualitative spectrum of the two tone signal. The x-axis is normalised by Δf.

The signal used for probing devices with respect to their two-tone intermodulation response is depicted in Fig. 5.11(a). One tone has a frequency of f_0, the other $f_0 + \Delta f$. In time domain, the signal features a beat with a repetition frequency of Δf. The distance Δf of these two tones is

arbitrary and they are assumed to have equal amplitude. The rms-value indicated in Fig. 5.11(a) shows the effective voltage as it would be seen by a device, the response of which is too slow to follow the RF signal. This concept is important with respect to LC as it can be expected that the director is not able to follow the high frequency at f_0 but that it can follow the slower beat signal Δf. This reasoning is also employed for RF-MEMS [Reb03], the response of which is determined by a mechanical spring-mass system.

The spectrum of the signal may look like depicted in Fig. 5.11(b). If the system has non-linearities, for instance if the cubic term of the Taylor Expansion of its transfer characteristics does not vanish, so called intermodulation products will be generated. They are also indicated in the figure and occur at the frequencies $f_0 - \Delta f$ and $f_0 + 2\Delta f$. Intermodulation products are in general undesirable as they cannot be removed by filtering as it is possible for harmonic distortion products. Intermodulation products lead to a broadening of the respective frequency band and thereby cause inter-channel interference. Furthermore, it can cause inter.symbol interference.

5.4.1 Definition of the Third Order Intercept Point

A measure very often used to specify the strength of two-tone intermodulation of a device or component is the third order intercept point (IP3). The definition of the IP3 is shown in Fig. 5.12.

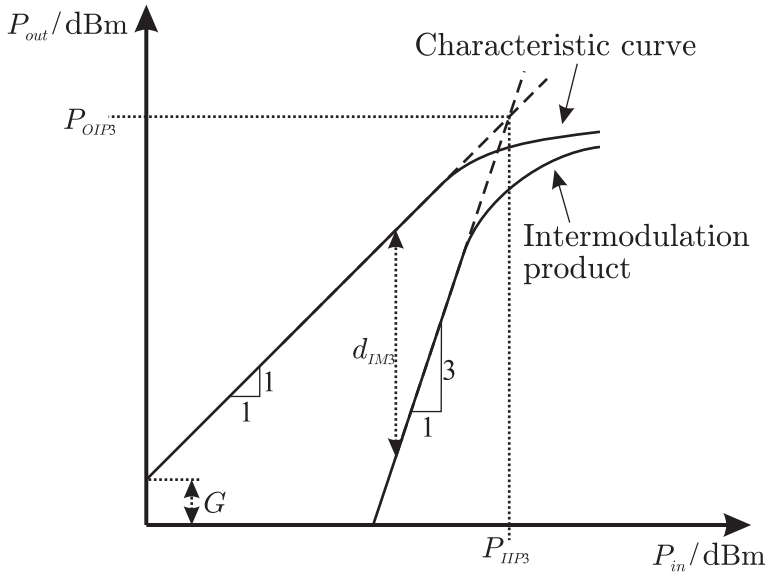

Figure 5.12: Definition of the third order intercept point.

Shown here is the response of a system or device to a two-tone signal with each of the tone having the power P_0 at the output of the DUT.

The axes in the graph shown in Fig. 5.12 are logarithmically scaled (e.g. dBm). The investigated system has a gain G as indicated in the figure. The intermodulation products have a power of P_3 and have a slope of three as indicated in the figure. The offset between the main tone power and the intermodulation tone power is called the intermodulation free range d_{IM3}.

Many systems exhibit effects like saturation as it is also hinted in Fig. 5.12. However, even if the system or device does not feature such compression, the characteristic curve of the main tone will deviate from a straight line as the intermodulation products begin to take a considerable part of the overall power. The latter is the reason why the measure IP3 is not directly accessible by measurements but needs to be calculated by an extrapolation as shown in Fig. 5.12. As shown in the figure, there are two definitions for the IP3: the input IP3 (P_{IIP3}) and the output IP3 (P_{OIP3}). Both values differ by the gain G. The interpolation can be expressed by a simple formula which can be used to calculate the output IP3 [ZB98, PC03]:

$$P_{OIP3} = P_0 + \frac{1}{2} d_{IM3}. \tag{5.9}$$

This formula is strictly speaking only valid at power levels at which no compression is effective and d_{IM3} is large enough. The input IP3 is then accordingly

$$P_{IIP3} = P_{OIP3} - G. \tag{5.10}$$

The IP3 value is commonly used to describe the nonlinear behaviour of a device or system and is therefore a very important benchmark number. The above described definitions can be further extended to higher (odd) order intermodulation products. The influence of even terms of the Taylor expansion of the transfer function of a given system or device is not considered in this work as these only generate frequencies at multiples of the working frequency and can in the majority of applications just be removed by adequate filters.

5.4.2 Prediction of Two-Tone Intermodulation

The possibility to solve the Erikson-Leslie problem for arbitrary excitations enables also the use of a two-tone signal as input for Eqn. (5.7). Accordingly, the excitation $V(t)$ is

$$V(t) = V_0(\sin(2\pi f_0 t) + \sin(2\pi(f_0 + \Delta f)t)). \tag{5.11}$$

For the simulation of the effects of such a signal on the LC or the device, c_r is again set one. The total duration of the simulation was set such that 4 beat periods were simulated in order to ensure steady state. The tone spacing Δf was varied between 0.1 Hz and 1000 Hz. Fig. 5.13 shows examples for different tone spacings.

Plotted is the response of the director quantified by the parameter $\eta_\tau(t)$ (see Eqn. (2.35)). The time axis is normalised with respect to the duration of one beat period. As can be seen, the lower the beat frequency is, the more the director is able to follow the beat signal. If the beat frequency is high enough (1 kHz for this simulation) the director will assume a state according

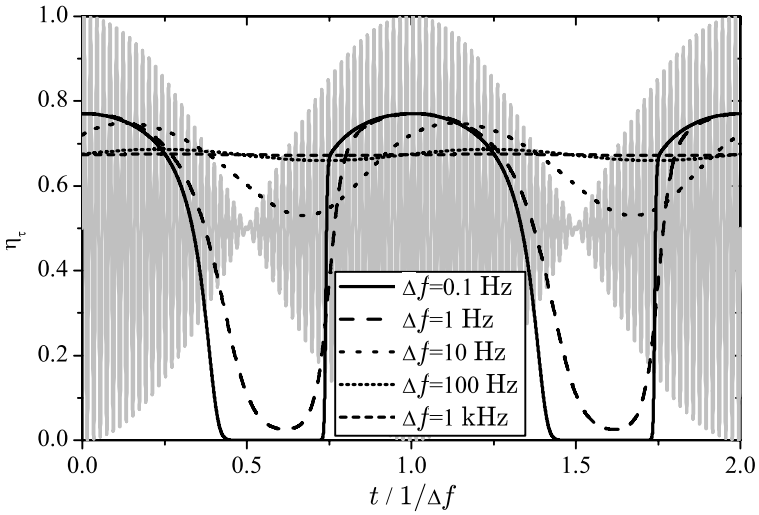

Figure 5.13: Response of the director to a beat signal. The amplitude of the beat signal is four times the threshold in this example. Five individual simulations were performed with the tone spacings indicated in the legend. The beat signal shown in gray is printed only in order to indicate the envelope of the signal and does not show the actual excitation signal for each individual simulation.

to the average effective voltage of the signal, i.e. a straight line as shown in Fig. 5.13 will be obtained.

The functions $\eta_\tau(t)$ shown in Fig. 5.13 can now be used to calculate, at least qualitatively, the influence of the director distortion on a two tone signal traveling over a tunable phase shifter device. From the calculations above, the parameter $\varepsilon_{r,eff}(t)$ (see Eqn. (2.34)) can be determined. The differential phase shift $\Delta\phi$ is calculated according to Eqn. (5.12)

$$\Delta\phi(t) = \sqrt{\varepsilon_{r,eff}(t)} - \sqrt{\varepsilon_{r,\perp}}. \tag{5.12}$$

For Eqn. (5.12), it is again assumed that the electrical length of the phase shifter is π. The distortion of the signal while traveling over the phase shifter can be calculated as in Eqn. (5.13).

$$V(t) = V_0 \cdot \left[\sin[2\pi f_0 t + \Delta\phi(t)] + \sin[(f_0 + \Delta f)\cdot(2\pi t + \frac{\Delta\phi(t)}{f_0})]\right] \tag{5.13}$$

The value of V_0 can be arbitrarily chosen as the presented analysis is qualitative. For Eqn. 5.13 to be valid, it must be assumed that the actuation of the LC only affects the transmission phase but not the transmission amplitude. As seen before, this assumption can be made for the loaded line structures as used here since these feature only little fluctuation in amplitude.

In order to assess the influence of the distortion given by Eqn. (5.13) in terms of quantities like the IP3, the signal $V(t)$ must be transformed into the frequency domain by using the Fourier

transform. Since Eqn. (5.13) is computed numerically at discrete points in time, the discrete Fourier transform must be used. In this work, this was done by employing the Fast Fourier Transform (FFT) algorithm. Nevertheless, care must be taken to to choose the sampling rate for the signal at f_0 high enough. Furthermore, several beat periods should be simulated in order to obtain higher frequency resolution.

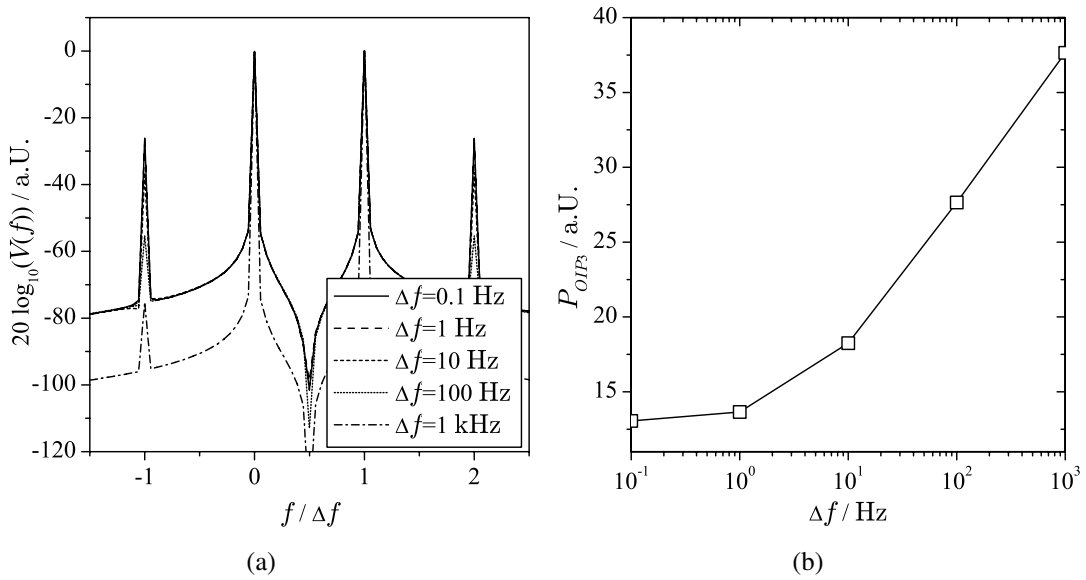

Figure 5.14: (a) The spectrum obtained from the Fourier transform of the signal described in Eqn. (5.13). (b) The IP3 value derived from that spectrum vs. tone distance.

Fig. 5.14(a) depicts the result of the Fourier Transform of the signal $V(t)$ (Eqn. (5.13)) using the distortion function shown in Fig. 5.13 for determining $\Delta\phi(t)$ in Eqn. (5.12). The result in Fig. 5.14(a) is normalised such that the power level of the main tone is zero. The result is described on a logarithmic scale which is proportional to the power of the signal but given in arbitrary units as the analysis is only qualitative. If real power levels should be considered, a more detailed modeling of the phase shifter including the physical LC parameters K_{11}, K_{33} and γ_1 would be necessary which, as mentioned previously, was not possible since the corresponding parameters were not available. For the analysis presented here, the insight to be gained from such a more detailed modeling would anyway have been negligible. Fig. 5.14(b) shows the IP3 calculated from the spectra in Fig. 5.14(b). As the distortion of the director is much stronger for small tone distances, the IP3 is low as expected and it increases with increasing tone distance. As the tone distance gets smaller the IP3 will saturate as the distortion waveform $\varepsilon_{r,eff}(t)$ does not change in shape.

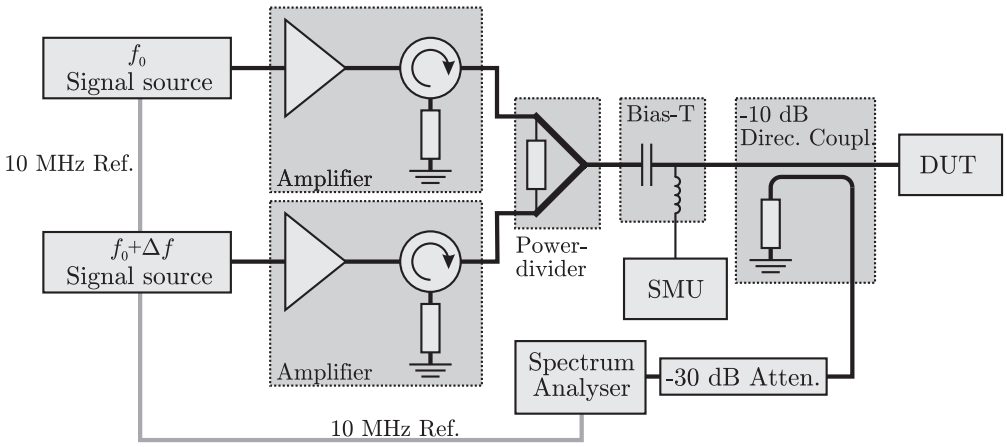

Figure 5.15: Schematic of the measurement setup used for this work. Both signal sources and the spectrum analyzer are tied to the same 10 MHz reference signal.

5.4.3 Intermodulation Measurement Setup

Fig. 5.15 shows the setup employed for the IP3 measurements. The two tones are generated each by an Anritsu MG3692A source. The frequency offset Δf is variable. The sources used here feature high spectral purity and high frequency stability which enables tone distances Δf down to 10 Hz. The two signals are amplified now by two Hughes 8000H traveling wave tube amplifiers. Although it would greatly simplify things if only a single signal generator could be used for the generation of the two tones and hence only one amplifier, this would be disadvantageous as the measurement system's resolution would be diminished by the nonlinear properties of the amplifier.

The two amplified signals are combined using a Wilkinson power divider (used as a combiner). Another commonly used approach for combining signals for intermodulation measurements is using a hybrid coupler [HCC08] with the two tones incident to the 0° and the 90° or 180° port. The combined signal is available at the input port and at the isolated port at which it is usually terminated with a $50\,\Omega$ load capable of sinking high power levels. With both methods, half of the total power is lost. In case of the Wilkinson divider, this power is dissipated in the $100\,\Omega$ resistor (a $50\,\Omega$ environment assumed) between the two output ports.

The device under test (DUT) is again measured in reflection. The high attenuation before the input port of the spectrum analyser also ensures that the receiver of the spectrum analyser (Agilent N9020A) operates linearly and does not reduce the system resolution by producing additional intermodulation. The relative frequency accuracy is ensured by tying the two signal generators and the spectrum analyser to the same 10 MHz reference signal. By doing so, the relative frequency deviation of the two signal generators is below the resolution of the spectrum analyser.

5.4.4 Measurement Strategy

The measurements with the setup as shown in Fig. 5.15 were performed depending on input power P_0, tone distance Δf, bias voltage and temperature. The power level incident to the DUT was calibrated before each measurement run. The maximum power level per tone was 22 dBm (approx. 160 mW). The spectrum of a single tone at $f_0 = 6$ GHz is shown in Fig. 5.16. As

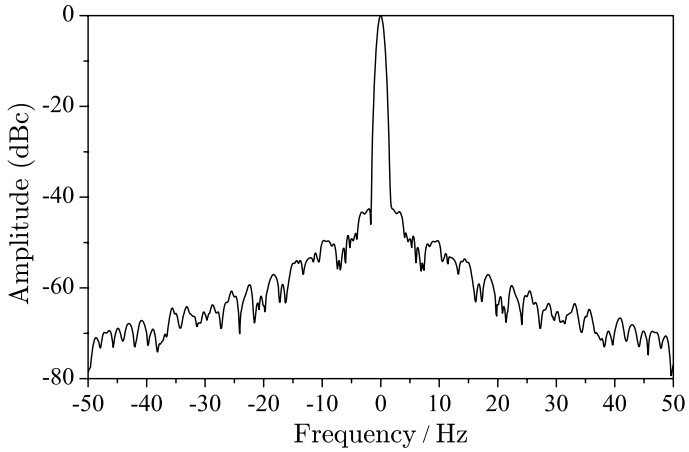

Figure 5.16: Single tone generated by the sources recorded over a bandwidth of 100 Hz around 6 GHz

can be seen, the signal has the necessary high spectral purity. For distances greater 10 kHz, the noise floor drops down to -120 dBc. The used spectrum analyser allows to conduct frequency sweeps with a minimum resolution bandwidth of 1 Hz. By choosing this resolution bandwidth, the spectrum analyser offers the lowest noise floor. A drawback of such an ultra-fine frequency resolution is the longer duration of a frequency sweep. For the given spectrum analyser, a single sweep with a bandwidth of 100 Hz and a resolution bandwidth of 1 Hz takes approx. 1.8 s. Broader sweeps take accordingly longer. In order to keep the time with power applied to the DUT as short as possible and reduce also thermal stress as much as possible, each of the four expected tones was measured individually within a bandwidth of 100 Hz which ensures maximum resolution (i.e. lowest possible noise floor) for the respective tone. Power was only applied during a frequency sweep. The tones are subsequently denoted by n_T with $n_T = 1$ being the intermodulation product at $f_0 - \Delta f$, $n_T = 2$ the fundamental tone at f_0, and so on. In order to increase resolution, averaging is performed on a measurement to measurement basis. Fig. 5.17 shows the measurement procedure for a given temperature and bias voltage. Averaging is performed in the outermost loop. After each measurement step a waiting period of 1 min was implemented in order to ensure that the device is always operated at the same temperature.

Using the N samples available for each power and tone distance combination, an error of the respective measurement is defined. The absolute error is calculated as given in Eqn. (5.14).

$$\Delta P_{out}(P_0, \Delta f, n_T) = \sqrt{\frac{1}{N}\sum_{i=1}^{N} P_{out}^{i}(P_0, \Delta f, n_T) - \overline{P_{out}(P_0, \Delta f, n_T)}} \tag{5.14}$$

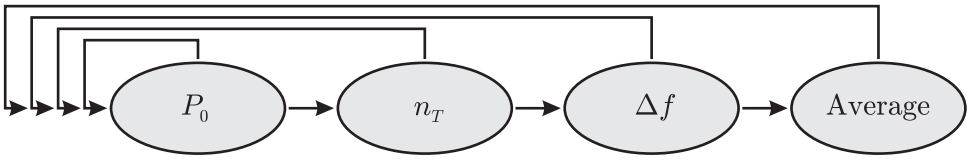

Figure 5.17: The measurement strategy for the IP3 characterisation.

$P^i_{out}(P_0, \Delta f, n_T)$ is the ith sample taken for the input power P_0, the tone distance Δf and the tone n_T. $\overline{P_{out}(P_0, \Delta f, n_T)}$ is accordingly the average of that measurement. For the IP3 characterisation five samples were measured for each input power level, tone distance and tone. Each measurement run shown in Fig. 5.17 was performed with and without bias voltage. It should be mentioned here that it became apparent that the fundamental tones ($n_T = 2, 3$) have negligible error compared to the more noisy intermodulation products. With this assumption the absolute error of the IP3 is given by

$$\Delta P_{OIP3} = \frac{\partial P_{OIP3}}{\partial d_{IM3}} \cdot \Delta P_{out}(P_0, \Delta f, n_T) = \frac{1}{2} \Delta P_{out}(P_0, \Delta f, n_T) \tag{5.15}$$

Measurement Results Without DUT

Before the actual LC device was measured, the characterisation setup as shown in Fig. 5.15 was calibrated without the DUT applied. This was again done by placing the CPW probe tip on the substrate without contacting the actual phase shifter device.

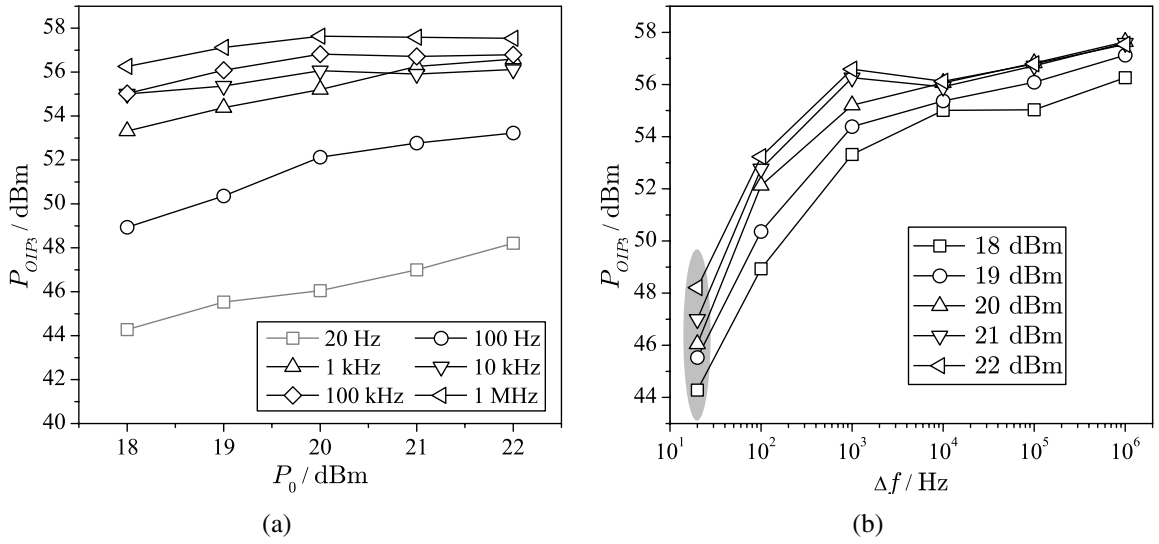

Figure 5.18: (a) The IP3 versus the input power P_0 (b) shows the same results but transposed. The grayed parts in the graphs represent measurements in which the intermodulation products are eclipsed by the noise floor

Fig. 5.11 shows the results of the system without DUT. The IP3 is calculated according to Eqn. (5.9). In Fig. 5.18(a), the IP3 is plotted versus the input power P_0. The bottom most line in this figure is the IP3 of two tones with a spacing of 20 Hz for which no intermodulation products are distinguishable from the noise shoulders of the tones (see also Fig. 5.16). All other values in this figure are computed with intermodulation products at least 10 dB above the noise floor.

Although all measurements are taken with intermodulation free ranges larger than 60 dB which should assure that Eqn. (5.9) is valid, the IP3 values show some dependency of the power at least for smaller tone distances. When looking at the intermodulation products, it can be seen that they do not follow the input power with the theoretical slope. Whether this is due to the combination of parts in the entire setup or an inaccuracy of the spectrum analyser can not be explained conclusively. Nevertheless, the overall resolution of the system is high enough.

From Fig. 5.18(b), it can be seen that intermodulation and hence the IP3 also depends on the tone distance. While for the smallest tone distance the values cannot be interpreted due to the noise floor, it can nevertheless be deduced that there is passive intermodulation, most likely thermal, in the system for $\Delta f < 10\,\text{kHz}$. The results as shown in 5.18 will be taken as reference for the following measurements with a DUT applied.

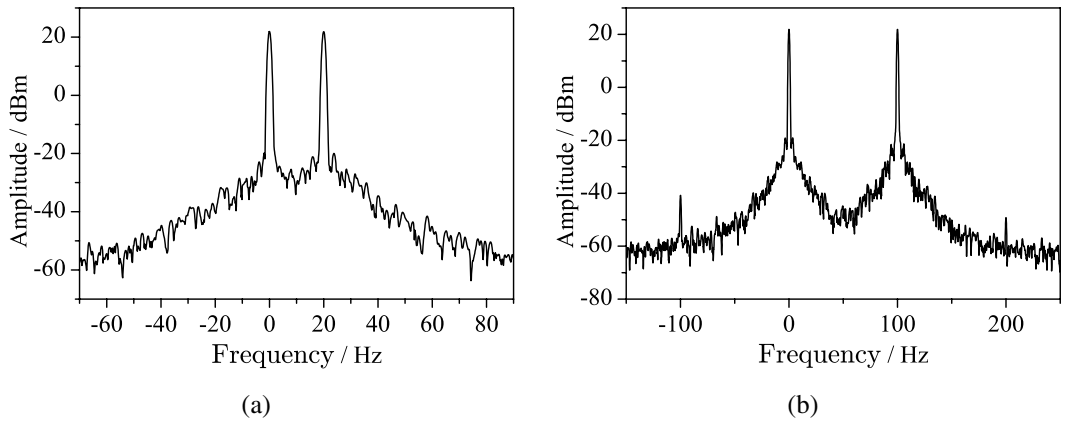

Figure 5.19: Two spectra recorded without DUT at an maximum input power of 22 dBm with (a) $\Delta f = 20\,\text{Hz}$ and (b) $\Delta f = 100\,\text{Hz}$. The spectra are stitched together using the individual spectra recorded around each tone.

Fig. 5.19 shows exemplified two recorded spectra at $\Delta f = 20\,\text{Hz}$ and $\Delta f = 100\,\text{Hz}$. With 20 Hz tone distance, there is no intermodulation product visible. The spectrum in Fig. 5.19(b) shows that there is an imbalance in the intermodulation products. This imbalance varies with power and tone distance. According to [Gol08], such unequal side products can arise when there is mixed AM-AM and AM-PM conversion in the system. In such cases, as in this work, too, the higher intermodulation product is always used for calculating the IP3 value giving such a worst-case value.

Measurement results with DUT

The DUT was characterised first at room temperature (RT, 23 °C) without bias voltage using the same parameters P_0 and $Deltaf$ as for the measurement system calibration described in the previous section. Furthermore, a complete measurement cycle at 50 °C was performed. The obtained results are directly compared to the properties of the bare measurement system. Fig. 5.20

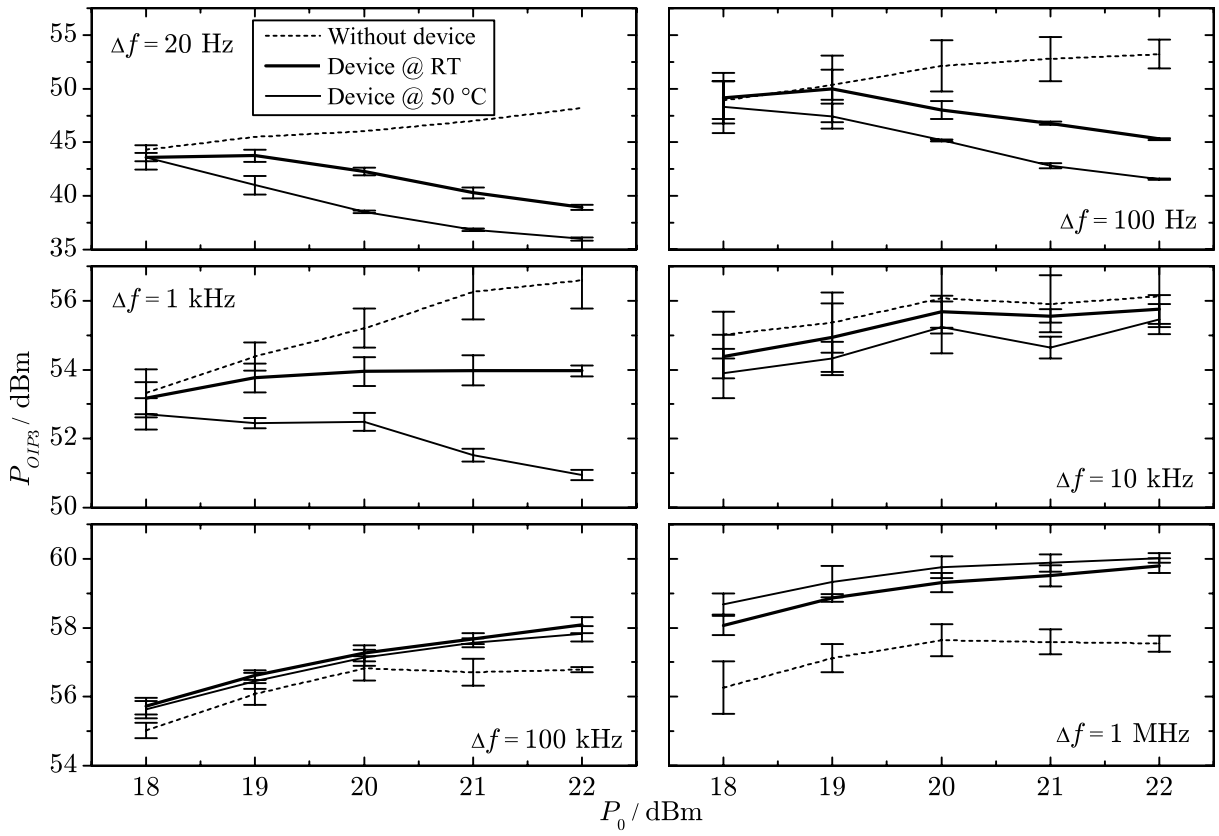

Figure 5.20: IP3 values at room temperature and at 50 °C without bias. The dashed lines represent the results of the bare measurement system. The solid thick line is the room temperature measurement, the thin line the measurement at 50 °C. The graphs show the results for different tone spacings Δf as indicated.

shows the results of the RT and the 50 °C measurement and compares it to the bare measurement setup. The output IP3 is used here. The results in Fig. 5.20 are differentiated according to the tone distance used. In order to demonstrate the unambiguity of the results further, Fig. 5.21 shows the spectrum for 20 dBm input power and $\Delta f = 20$ Hz. From this figure, it is obvious why no error is given for the bare system at $\Delta f = 20$ Hz: There are no visible intermodulation products above the noise floor so the IP3 value represents a lower limit.

Several things can be observed from Fig. 5.20. At room temperature, specially for $\Delta f \leq 1$ kHz, from a certain power level (≈ 19 dBm) the IP3 value starts to deviate significantly from the bare measurement system. This effect is much more pronounced for the 50 °C measurements. At

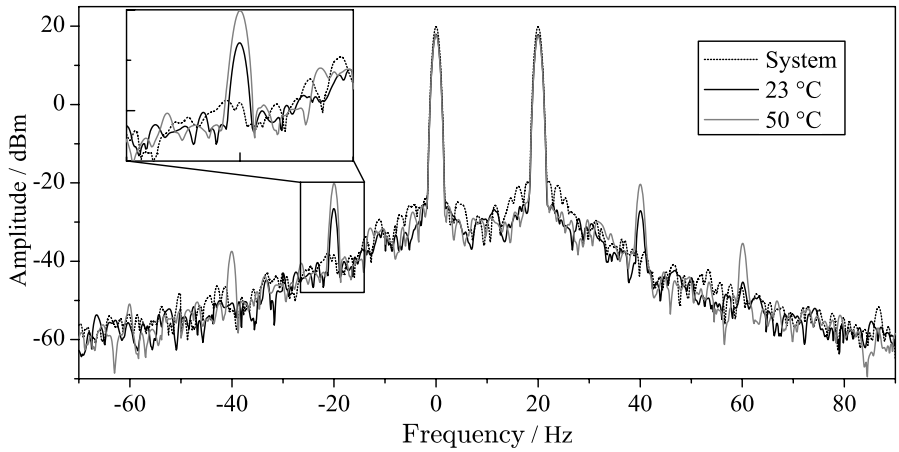

Figure 5.21: Recorded spectrum of the pure measurement system, with DUT at room temperature and 50 °C.

higher tone distances, the effect is diminished and actually not visible at all within the measurement error. For $\Delta f = 1\,\mathrm{MHz}$, the IP3 value for the device is seemingly higher which could be explained by a slight reduction of the intermodulation generation by the loss in the DUT.

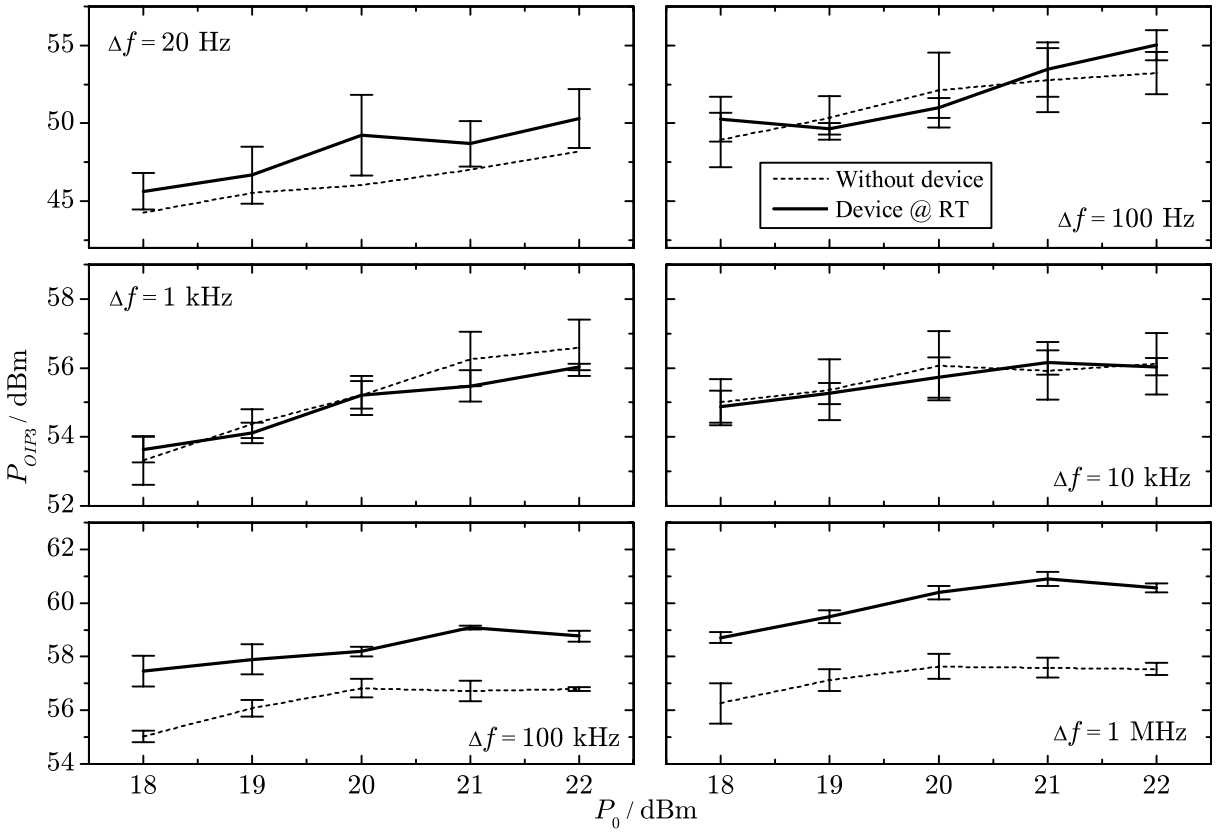

Figure 5.22: Results of the IP3 measurement with an applied bias voltage of 60 V

If a bias voltage is applied, the results change significantly. The results shown in Fig. 5.22 illustrate the effect. A voltage of 60 V is applied. As can be seen the input power and tone distance effects vanish completely. Elevated temperatures change the behaviour with bias voltage applied only little. Intermediate bias voltages will diminish the effect seen at zero bias voltage accordingly.

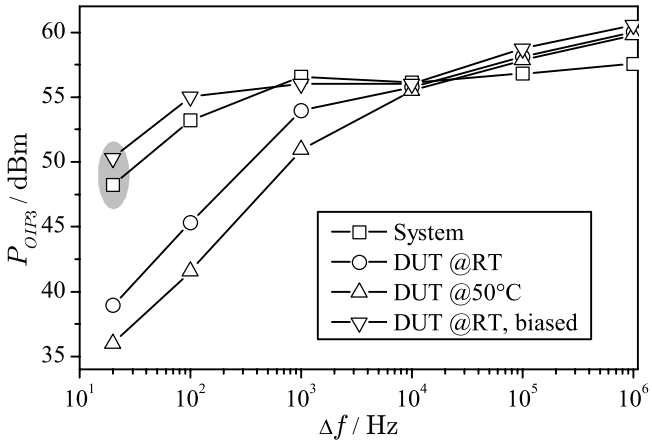

Figure 5.23: The output IP3 vs. the tone distance for the maximum applied input power (22 dBm). For the encircled measurement points for $\Delta f = 20$ Hz the intermodulation products were obscured by the noise floor. It can be assumed that these points are at the level of the neighboring tone distance $\Delta f = 100$ Hz. For clarity, the error is not given here.

Fig. 5.23 shows the compiled results at maximum input power (22 dBm). The figure shows clearly that the IP3 drops at small tone distances when the device is not biased. This drop is even more pronounced at high temperatures but has up to 1 kHz roughly the same slope as the measurement at room temperature, i.e. approx. 9 dB per decade. This value is close to the slope which can be read from Fig. 5.14(b) (approx. 10 dB per decade) for $\Delta f > 10$ Hz. Therefore, the measurement and the modeling introduced previously agree well.

5.5 Conclusion

This chapter explores the behaviour of LC based tunable RF devices under large signal conditions. More specifically, the so called self actuation is investigated as well as the intermodulation behaviour. It was shown that self actuation occurs only above a certain power level. This distinguishes LC devices from MEMS devices because self actuation of MEMS occurs for all power levels. Due to self actuation, some intermodulation can occur however only for very small tone distances[1]. For large tone distances, the IP3 is above 55 dBm.

[1] It should be noted that the specific behaviour vs. Δf depends on the actual LC material.

Finally, some comments on the choice of the LC material for the presented investigations: Standard LCs with known parameters, for which also quantitative simulation would be possible, do not really qualify for this kind of investigation as they usually show inferiour performance, particularly high loss, and most often also a limited temperature range. For both reasons, it is difficult to separate thermal effects and effects caused by the LC itself. If the LC exhibits high loss, excessive heating will occur and thermal effects will dominate the behaviour of the device also at lower power levels. If this is coupled with a low clearing point, the LC is prone to slip into the isotropic phase and back to the nematic phase according to the beat frequency and will thereby worsen both the intermodulation behaviour (at least for small Δf) and/or the entire device performance. The results shown in [Mül07] most likely originated from such a phase change effect. Specially when looking at the power level (40 dBm) and the LC (5CB, $T_{NI} = 36\,^{\circ}\mathrm{C}$) used and furthermore the large insertion loss (≈ 5 dB) caused by the LC, the addressed problems are quite likely to occur. Although such a study may of course be interesting for the sake of analysis, it nevertheless reflects that LCs with high loss are inadequate also from the power handling capability point of view and LCs like the one used in this chapter's investigations with low loss and large temperature range must be used.

Chapter 6

Conclusion and Outlook

This work focuses on the use of Nematic Liquid Crystals for reconfigurable microwave devices. In this respect, it covers all important aspects necessary for the understanding and realisation of such devices. Particularly, these aspects include material development for optimum performance of the tunable material, device technology for optimum exploitation of the material properties and finally, the power handling capability of LC microwave devices.

In terms of the LC material, most works rely on commercially available LCs. These materials, however, do not offer high microwave performance. Specially tailored LCs had been shown to exhibit very high performance, but no relationship between the chemical composition and the microwave performance had been given so far. At this point, this work offers new insights by systematically investigating the microwave performance of various LC mixtures. From these investigations, several correlations between the microwave performance and the molecular structure of the LC can be identified. First of all, the structure of the molecules should be as long as possible, i.e. contain at least four phenyl rings in order to keep the relaxation frequencies of the LC mixture low. Secondly, the polarity of the molecules should be as small as possible because polarity increases the strength of the dielectric relaxation. Nematic LCs, which have been specially tailored for very small relaxation frequencies and low polarity in fact show material efficiencies of over 40 which is an exceptional value for passively tunable materials. In terms of the anisotropy, there seems to be a correlation between the optical anisotropy and the microwave anisotropy, i.e. most mixtures with higher optical anisotropy also feature higher microwave anisotropy. Furthermore, it was shown in this work, that tunability can be increased by a factor of two if a LC host is loaded with carbon nanotubes.

Concerning device technology, the emphasis of this work is the reduction of the response times, which up to now was a major shortcoming of concepts trying to use LC at microwave frequencies. Two approaches are discussed in that respect: Porous PTFE membranes impregnated with LC and the realisation of very thin LC layers. While the first approach offers a significant reduction of the response times, which is however bought at the expense of the tuning performance, the second approach offers even more response time reduction while only very little sacrifice has

to be made concerning the RF performance of the devices. This approach is based on parallel plate capacitors which have several advantages compared to TEM waveguides which had been used in other works. First of all, the metallic loss does not increase as the LC layer thickness decreases as it is the case for TEM waveguides. Without this problem, the response time is only determined by the layer thickness, which in turn is governed by the technical feasibility. In the conducted experiments, response times of below 10 ms could be achieved LC layer thicknesses of 4 µm could be reliably fabricated. A tunable phase shifter with a phase shifter efficiency of up to 60 °/dB was realised, demonstrating the usability of the fabrication scheme at 20 GHz. Using the parallel plate capacitor scheme, it is furthermore possible to obtain devices with a tuning efficiency of over 90 %, i.e. the available tunability of the material is exploited at a significantly higher degree compared to transmission line solutions in other works (approx. 70 %). As the used approach is very close to that of LC displays in terms of the manufacturing technique, a cost effective fabrication is feasible. An additional advantage is that both display technology and the design and production of LC material is very mature. This should, in contrast to a technology like MEMS, reduce reliability issues very much.

Due to the fact that potential devices and components should also be usable in the transmit path of a communication system, they have to be able to cope with power levels exceeding those of the usual small-signal operation in the receive path. The material is therefore required to behave highly linear. It is shown in this work that LC based devices can fulfil this requirement very well. Two operation modes are distinguished for the characterisation of the power handling capabilities: Single-tone and two-tone operation. The single-tone characterisation is used to identify so called self actuation, a problem also known from MEMS, as self actuation is predicted by LC theory. It could be demonstrated that this effect is measurable, but that it only occurs from a certain power level. This is a further advantage compared to MEMS because there self actuation occurs at all power levels. Using a two-tone test setup, the intermodulation properties were investigated. It was shown that the IP3 value is very high (above 55 dBm) for tone distances >10kHz. Only for smaller tone distances, the IP3 value drops to 35 dBm which could be explained also by the self actuation effect.

In terms of material, the investigations presented in this work should be further extended. Particularly the exact dependence between the optical and microwave anisotropy should be investigated as this can give valuable information how to increase the tunability of the material. In terms of the dielectric loss, investigations such as recording a broad spectrum from very low frequencies up to GHz frequencies in order to map all relaxation processes with high accuracy, should be carried out.

Given the very low quantity of LC material necessary, even large devices (e.g. an antenna array with integrated tunable phase shifters) can be efficiently fabricated cost-efficiently. From that point of view, the proposed fabrication scheme offers the opportunity to directly use display fabrication facilities for manufacturing such antenna arrays. What is more, the respective devices and systems would benefit from additional technological options like thin film transistors or interconnnects through the LC layer, both things which could not be implemented in the scope of this work due to technological limitations.

With the use of LC within a transmit system in mind, it should be investigated how the increased intermodulation at low tone distances affects data transmission. This can be done both theoretically using the models developed in this work as well as experimentally by doing detailed system analysis of LC based devices, e.g. by investigating the impact on the bit error rate for various modulation schemes.

Finally, it could be demonstrated that LCs can also be used in tunable filters or matching networks. Using e.g. the periodically loaded line approach, it is possible to also extend the frequency range of LC based devices up to 100 GHz.

Nomenclature

α	Attenuation constant
α_p	Scalar molecular polarisability
α_r	Exponent of the Havrilak-Negami relation (Broadness)
$\mathbf{T}^{\alpha_p}$	Polarisability tensor
β_r	Exponent of the Havrilak-Negami relation (Symmetry)
χ_e	Electric susceptibility
χ_m	Magnetic susceptibility
$\mathbf{T}^{\chi_e}$	Electric susceptibility tensor
$\mathbf{T}^{\chi_m}$	Magnetic susceptibility tensor
$\vec{n}$	LC director
ε_0	Vaccum permittivity ($8.854187817 \cdot 10^{-12}$ F/m)
ε_r	Relative permittivity
$\mathbf{T}^{\varepsilon_r}$	Relative permittivity tensor
$\mathbf{T}^{\varepsilon_r}_{\vec{n}}$	Relative permittivity tensor of the nematic director
η_τ	Tuning efficiency of a device
η_C	Efficiency of a tunable capacitor (analogous to η_{LC})
η_{LC}	Efficiency of the liquid crystal material (tunability/maximum loss)
η_{PS}	Phase shifter efficiency (°/dB)
γ	Complex transmission line propagation coefficient
κ	Magnetic polarisability
$\mathbf{T}^{\kappa}$	Magnetic polarisability tensor
$\mathbf{T}^{K}$	Internal field factor tensor
ω	Angular frequency
$\tan\delta$	Dielectric loss tangent
τ	Relative tunability
θ	Angle between a single LC molecule and the director or analogously the angle between the director and the $z$axis of a Cartesian coordinate system
φ	Electric potential
B	Magnetic flux density
D	Electric displacement field
d_{LC}	Thickness of a LC layer

E	Electric field
f	Frequency
H	Magnetic field strength
I	Current
J	Current density
K	Molecular field factor
k_B	$1.3806504 \cdot 10^{-23}$ J/K
K_{ii}	Elastic constant of the nematic director with $i \in (1,2,3)$
n	Index of refraction
P	Macroscopic polarisation
p	Microscopic polarisation
Q	Quality factor of a resonator or a capacitor
S	Order parameter of nematic liquid crystals
S_{ij}	Scattering parameter from port j to i
T	Temperature ($^{\circ}C$ or Kelvin, depending on context)
t	Time
t_{rise}, t_{decay}	Rise and decay time of the LC response
T_{NI}	Temperature of the nematic-isotropic transition
V	Voltage or volume, depending on context
V_{th}	Threshold voltage
Y	Admittance
Y_{ij}	Admittance in the Y-Matrix two-port representation
Z	Impedance
CNT	Carbon Nanotube
CPW	Coplanar Waveguide
CW	Continuous Wave
DUT	Device Under Test
ePTFE	Expanded Polytetrafluoroethylene
GEO	Geosynchronous Earth Orbit
IMSL	Inverted Microstrip Line
IP3	Third order intercept point
ITO	Indium-Tin-Oxide
LC	Liquid Crystal
LEO	Low Earth Orbit
MEMS	Micro-Electro-Mechanical Systems
MIM	Metal-Insulator-Metal
MMIC	Monolithic Microwave Integrated Circuit
MUT	Material Under Test
NLC	Nematic Liquid Crystal
PR	Photoresist
PTFE	Polytetrafluoroethylene
RF	Radio Frequency
SMU	Source-Measurement-Unit

TEM	Transverse Electro-Magnetic
VNA	Vector Network Analyser

Appendix A

Fabrication process description

In the following, the process steps for fabricating the presented devices are described as they have been developed and used in the scope of this work.

No.	Schematic	Description
1	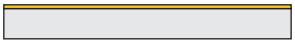	Evaporation deposition of a chrome/gold seed layer. Chrome: $\approx 30\,\text{nm}$, Gold: $\approx 70\,\text{nm}$
2		Applying of positive photo resist (PR) and patterning. The PR (AZ4533, Microchemicals) is spincoated at 4000 rpm for 30 s. The layer is exposed with UV light for 20 s and subsequently developed using a positive PR developer (AZ400K, Microchemicals) for 30-40 s.
3		Gold plating. Depending on the application, usually 1-2 µm gold is plated. The plating bath used is Puramet 402 (10 g/l). The plating current is 1 mA.
4		PR stripping with hot acetone soak
5		Etching of the chrome and gold seed layer. For etchants see Table A.3.
6	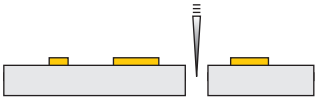	Dicing with an accuracy of $\pm 20\,\mu\text{m}$
7		Coating with orientation layer based on Nylon 6 (see Table A.5) at 6000 rpm for 30 s with subsequent curing (see Table A.4) and rubbing (see page 156 for the respective parameters)

8	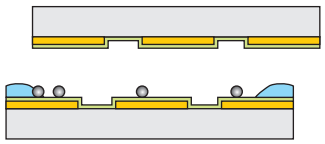	Applying of the spherical spacers (Sekisui Chemical LCD spacers made of glass) and UV curable glue (Ablestik A4086T) and subsequent aligning. The spherical spacers are dissolved in Ethanol (1 scalpel tip in 10 ml) which is spincoated at 1000 rpm for 5 s. The UV glue droplets are applied manually. Both layers are aligned using a mask aligner.
9	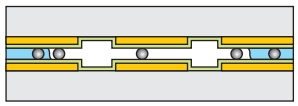	Curing of the glue by UV exposure with subsequent thermal curing on a hotplate at 120 °C for 30 min.

Table A.1: Processes steps for fabricating parallel plate capacitor based devices.

No.	Schematic	Description
1		See step 1 in Table A.1
2		Patterning of the Indium Tin Oxide (ITO) mask (AZ1518, Microchemicals). The PR is spincoated at 4000 rpm for 30 s with subsequent UV exposure (20 s) and developing in AZ400K for 20-30 s.
3	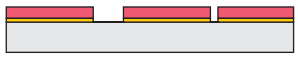	Etching of the seed layer
4		E-beam evaporation of ITO (30 nm)
5		Lift-off of the ITO. The substrate is subsequently baked at 300 °C for 20 min to oxidise the ITO which increases the conductivity and makes it chemically more inert.
6		Patterning of the gold electrodes (AZ1518, same parameters as in step 2)
7		Deposition of Chrome/Gold as in step 1
8		Lift-off of the layer deposited in the previous step
9		Spincoating of AZ4533 and patterning using the same mask as in step 6. Otherwise the parameters from step 2 in Table A.1 are used.
10		See step 3 in Table A.1
11		See step 4 in Table A.1

12	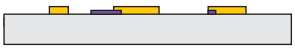	See step 5 in Table A.1
13	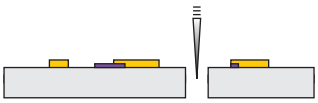	See step 6 in Table A.1
14		See step 7 in Table A.1
15	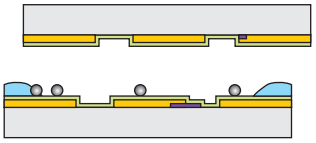	See step 8 in Table A.1
16	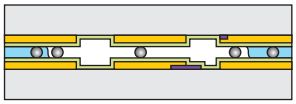	See step 9 in Table A.1

Table A.2: Processes steps for fabricating parallel plate capacitor based devices with resistive Indium Tin Oxide (ITO) electrodes.

Substance	Chem. notation	Amount
Gold etchant		
Iodine extra pure	I_2	5 g
Potassium iodide	KI	20 g
Deionised water	H_20	200 ml
Chrome etchant		
Ammonium cerium (IV) nitrate	$(NH)_4[Ce(NO_3)_6]$	41.15 g
Nitric acid	HNO_3	22.5 ml
Deionised water	H_20	250 ml

Table A.3: Substances used for the chrome and gold etchants. Taken from [Sch07].

Time	Temperature
Hotplate	
2 min	90 °C
Oven	
30 min	Ramp up to 90 °C
60 min	90 °C
30 min	Ramp up to 180 °C
60 min	180 °C

Table A.4: Curing process of the Nylon 6 orientation layer.

Substance	Chem. notation	Amount
Nylon 6	$[NH\text{-}(CH_2)_5\text{-}CO]_n$	1.5 g
Trichlorethanol	$C_2H_3Cl_3O$	100 g

Table A.5: Substances used for the orientation layer.

Appendix B

Chemical Compounds

In the following, the chemical details about the investigated mixtures are given. Table B.1 lists all chemical compounds contained in any mixture or base matrix. The base matrices are listed in Table B.2 and all mixtures based on the matrices are listed in Table B.3.

No.	Δn_{opt}	Formula	No.	Δn_{opt}	Formula
1	0.18	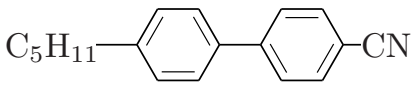	2	0.17	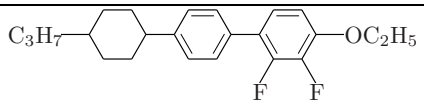
3	0.17	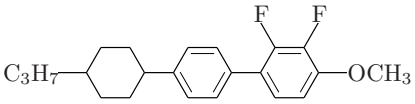	4		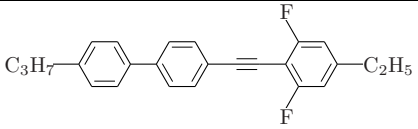
5		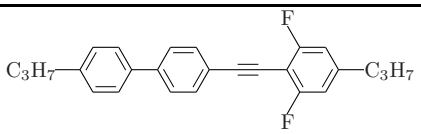	6		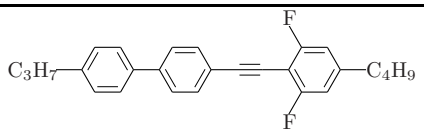
7	0,3	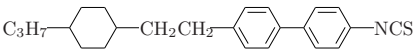	8	0,28	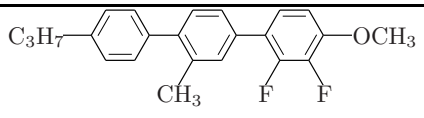
9	0,29	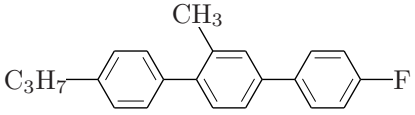	10	0,385	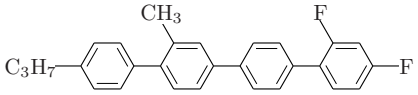
11	0,45	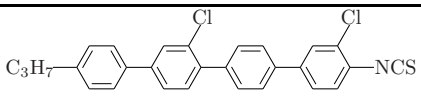	12	0,45	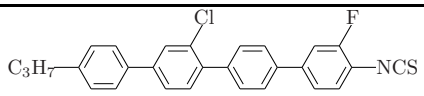
13	0,45	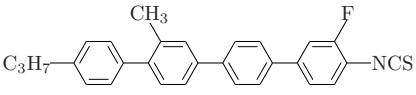	14	0,165	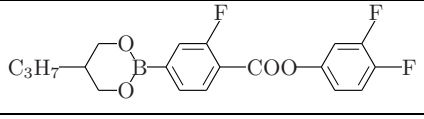

15	0,12	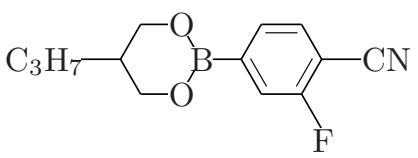	16		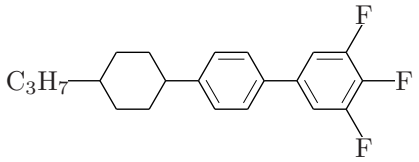
17	0,17	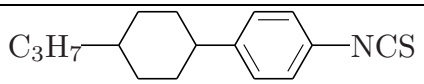	18	0,16	
19		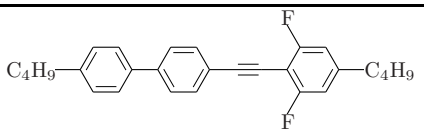	20	0,3	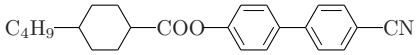
21	0,44	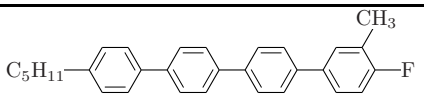	22	0,07	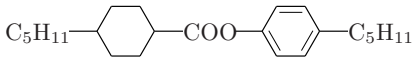
23	0,3	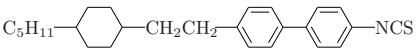	24	0,44	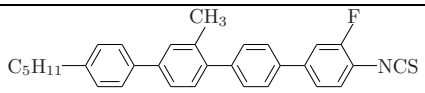
25	0,15	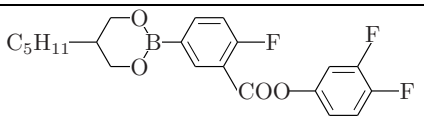	26	0,21	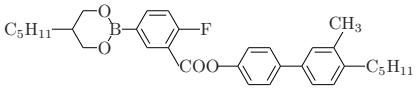
27	0,19	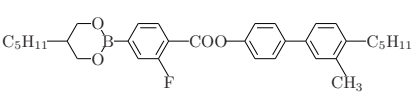	28	0,17	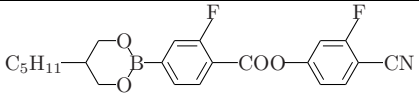
29	0,17	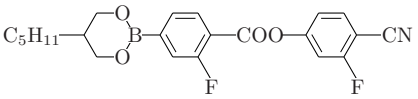	30		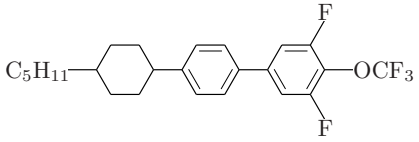
31		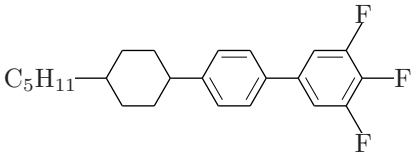	32	0,17	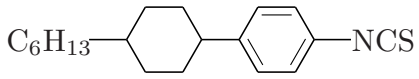
33	0,28	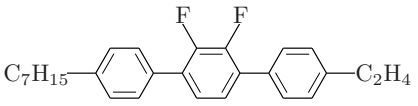	34	0,12	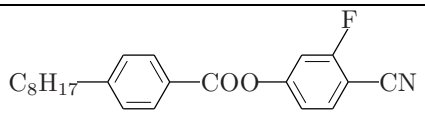
35	0,17	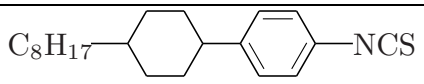			

Table B.1: The chemical compounds used in this work. Along with the number of the compound, the optical Δn_{opt} is given.

Mixture	Composition							
M_{NCS}	C_{32}	45%	C_{17}	38%	C_{35}	17%	-	-
M_{Tol}	C_{19}	42%	C_6	33%	C_4	25%	-	-
M_{Tol2}	C_5	35%	C_4	25%	C_6	25%	C_{19}	15%
LM2F-1	C_{31}	46%	C_{30}	37%	C_{16}	17%	-	-

Table B.2: The base matrices plus an additional mixture used in another mixture (LM2F-1, see Table B.3). 5CB consists of only a single molecule and is therefore not listed.

Mixture	Composition							
BMW11	5CB	63.7%	C_{20}	31.3%	C_{22}	10%	-	-
BMW12	5CB	85%	C_8	10%	C_2	5%	-	-
BMW13	5CB	80%	C_{10}	13%	C_9	7%	-	-
BMW14	5CB	80%	C_{27}	20%	-	-	-	-
BMW16	5CB	65.5%	C_{20}	26%	C_{26}	8.5%	-	-
BMW10	M_{Tol}	79%	C_{10}	7%	C_{34}	7%	5CB	7%
BMW15	M_{Tol}	80%	C_{25}	20%	-	-	-	-
BMW5	M_{Tol}	85%	C_2	10%	C_8	5%	-	-
BMW7	M_{Tol}	88%	C_{15}	7%	C_{29}	5%	-	-
BMW8	M_{Tol}	85%	C_{33}	10%	C_{15}	5%	-	-
BMW21	M_{Tol}	46%	C_8	24%	C_2	30%	-	-
BMW29	M_{Tol2}	85%	C_{12}	6%	C_{24}	5%	C_{21}	4%
LHB-6	M_{Tol}	85%	LM2F-1	15%	-	-	-	-
LHB-13	LHB-6	91%	C_{10}	9%	-	-	-	-
LHB-16	M_{Tol}	84%	C_{12}	9%	C_{24}	7%	-	-
LHB-17	M_{Tol}	84%	C_{24}	7%	C_{12}	7%	C_{10}	3%
LHB-18	M_{Tol}	70%	C_{24}	13.6%	C_{12}	9.6%	C_{11}	2.4%
	C_{10}	2.4%	C_{13}	2%	-	-	-	-
BMW2	M_{NCS}	90%	C_{28}	10%	-	-	-	-
BMW3	M_{NCS}	80%	C_{29}	12%	C_{18}	4%	C_{14}	4%
BMW4	M_{NCS}	61%	C_{23}	13%	C_7	13%	C_3	13%

Table B.3: The investigated mixtures grouped according to the base matrix.

Appendix C

Mechanical Setups

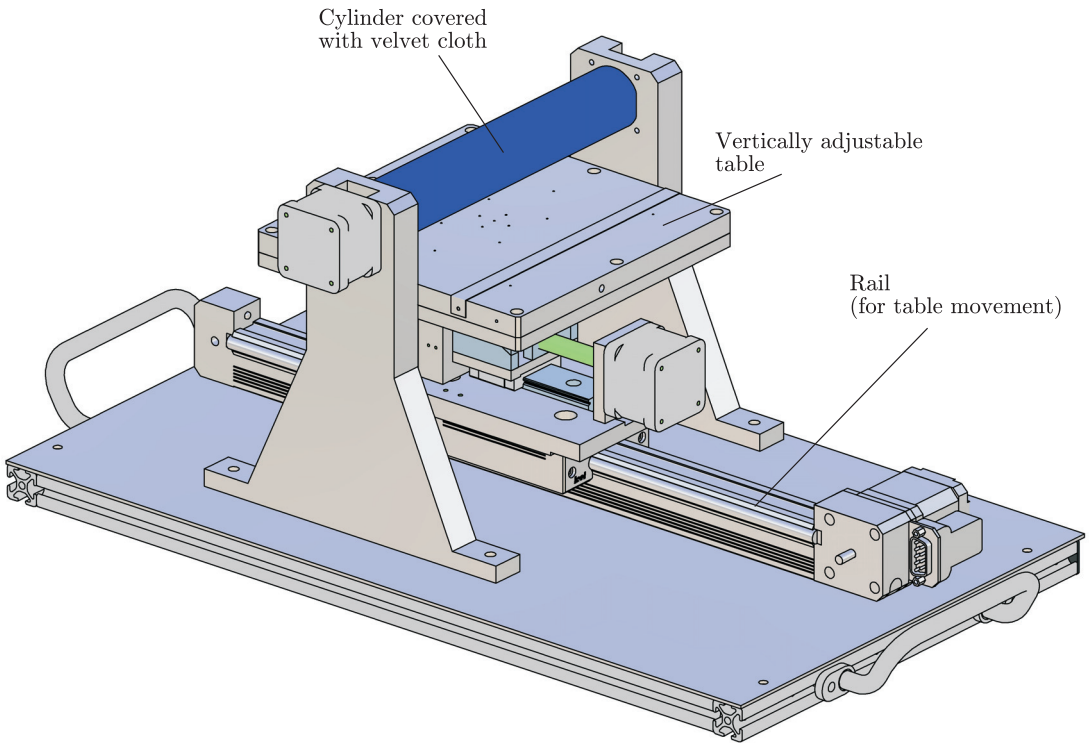

Figure C.1: Schematic of the built rubbing machine. Substrates with sizes of up to 10×10 cm can be processed. The cylinder has a diameter of 35 mm. Typically, the cylinder rotates with 40 rpm while the table is moved with a speed of 1 mm/s. The outer dimensions of the machine are 59 cm×29 cm×31 cm (Length×Width×Height).

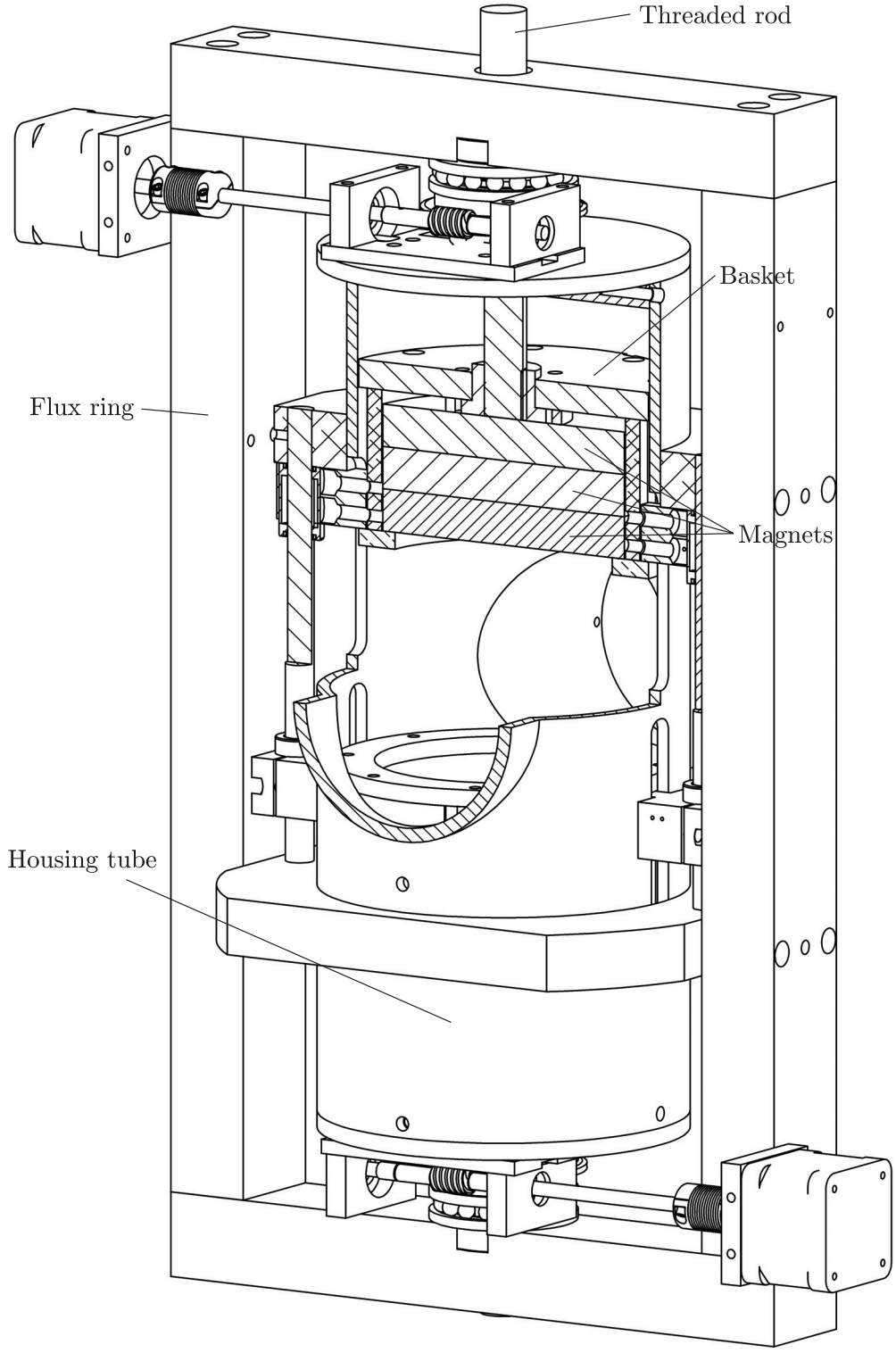

Figure C.2: The rotatable magnets in detail. In the cut open part, the three magnets within the movable basket can be seen.

Bibliography

[APE09] ABDALLA, M.A.Y. ; PHANG, K. ; ELEFTHERIADES, G.V.: A Planar Electronically Steerable Patch Array Using Tunable PRI/NRI Phase Shifters. In: *Microwave Theory and Techniques, IEEE Transactions on* 57 (2009), March, Nr. 3, pages 531–541

[ATDR03] ABBASPOUR-TAMIJANI, A. ; DUSSOPT, L. ; REBEIZ, G.M.: Miniature and tunable filters using MEMS capacitors. In: *Microwave Theory and Techniques, IEEE Transactions on* 51 (2003), July, Nr. 7, pages 1878–1885

[ATH+02] ACIKEL, B. ; TAYLOR, T.R. ; HANSEN, P.J. ; SPECK, J.S. ; YORK, R.A.: A new high performance phase shifter using $Ba_xSr_{1-x}TiO_3$ thin films. In: *Microwave and Wireless Components Letters, IEEE* 12 (2002), July, Nr. 7, pages 237–239

[Ban08] BANJAI, L.: Revisiting the Crowding Phenomenon in Schwarz–Christoffel Mapping. In: *SIAM Journal on Scientific Computing* 30 (2008), Nr. 2, 618-636

[BC94] BLINOV, L. M. ; CHIGRINOV, V. G. ; LAM, L. (Ed.) ; LANGEVIN, D. (Ed.): *Electrooptic Effects in Liquid Crystal Materials*. Springer Verlag, 1994

[BE60] BUSSEY, H.E. ; ESTIN, A.J.: Errors in Dielectric Measurements Due to a Sample Insertion Hole in a Cavity. In: *Microwave Theory and Techniques, IRE Transactions on* 8 (1960), November, Nr. 6, pages 650–653

[BR00] BARKER, N.S. ; REBEIZ, G.M.: Optimization of distributed MEMS transmission-line phase shifters-U-band and W-band designs. In: *IEEE Transactions on Microwave Theory and Techniques* 48 (2000), Nr. 11, 1957–1966

[BSMM95] BRONSTEIN ; SEMENDJAJEW ; MOSIOL ; MUEHLIG: *Taschenbuch der Mathematik*. 2. Harry Deutsch, 1995

[Car01] CARTER, R. G.: Accuracy of Microwave Cavity Perturbation Measurements. In: *IEEE Transactions on Microwave Theory and Techniques* 49 (2001), May, Nr. 5, pages 918–923

[CC93] CHANG, C.N. ; CHENG, J.F.: Hybrid quasistatic analysis of multilayer microstrip lines. In: *Microwaves, Antennas and Propagation, IEE Proceedings H* 140 (1993), April, Nr. 2, pages 79–83

[CDL75] CUMMINS, P. G. ; DUNMUR, D. A. ; LAIDLER, D. A.: The Dielectric Properties of Nematic 44' n-pentylcyanobiphenyl. In: *Molecular Crystals and Liquid Crystals* 30 (1975), pages 109 – 123

[CFN03] CAMPANELLI, E. ; FAETTI, S. ; NOBILI, M.: Azimuthal anchoring energy at the interface between a nematic liquid crystal and a PTFE substrate. In: *European Physical Journal E* 11 (2003), June, pages 199–209

[CH97] COLLINGS, P. ; HIRD, M.: *Introduction to Liquid Crystals ; Chemistry and Physics*. Taylor & Francis, 1997

[Chi99] CHIGRINOV, V.G.: *Liquid Crystal Devices ; Physics and Applications*. Artech House, 1999

[CK93] COFFEY, W. T. ; KALMYKOV, Yu. P.: On the calculation of the dielectric relaxation times of a nematic liquid crystal from the non-inertial Langevin equation. In: *Liquid Crystals* 14 (1993), Nr. 4, 1227–1236

[CKPZ90] COATS, R. ; KLEIN, J. ; PRITCHETT, S.D. ; ZIMMERMANN, D.: A low loss monolithic five-bit PIN diode phase shifter. In: *Microwave Symposium Digest, 1990., IEEE MTT-S International*, 1990, pages 915–918 vol.2

[Col92] COLLIN, Robert E.: *Foundations For Microwave Engineering*. 2nd. McGraw-Hill, 1992

[CON+04] CHEN, L. F. ; ONG, C. K. ; NEO, C.P. ; VARADAN, V. V. ; VARADAN, V. K.: *Microwave Electronics - Measurement and Materials Characterisation*. 1. Wiley, 2004

[COT99] CHEN, L. ; ONG, C. K. ; TAN, B. T. G.: Amendment of Cavity Perturbation Method for Permittivity Measurement of Extremely Low-Loss Dielectrics. In: *IEEE Trans. on Instrumentation and Measurements* 48 (1999), December, Nr. 6, pages 1031–1037

[CTPP03] CHEN, Chao-Yuan ; TSAI, Tsong-Ru ; PAN, Ci-Ling ; PAN, Ru-Pin: Room temperature terahertz phase shifter based on magnetically controlled birefringence in liquid crystals. In: *Applied Physics Letters* 83 (2003), Nr. 22, 4497-4499

[CWC90] CHANG, Chia-Nan ; WONG, Yu-Ching ; CHEN, Chun H.: Full-wave analysis of coplanar waveguides by variational conformal mapping technique. In: *Microwave Theory and Techniques, IEEE Transactions on* 38 (1990), September, Nr. 9, pages 1339–1344

[DGG+99] DEMUS, D. (Ed.) ; GOODBY, J. (Ed.) ; GRAY, G. W. (Ed.) ; SPIESS, H.-W. (Ed.) ; VILL, V. (Ed.): *Physical Properties of Liquid Crystals*. Wiley-VCH, 1999

[DKS+08] DUBOIS, Frédéric ; KRASINSKI, Freddy ; SPLINGART, Bertrand ; TENTILLIER, Nicolas ; LEGRAND, Christian ; SPADLO, Anna ; DABROWSKI, Roman: Large Microwave Birefringence Liquid-Crystal Characterization for Phase-Shifter Applications. In: *Jpn. J. Appl. Phys* 47 (2008), pages 3564–3567

[DLJH93] DOLFI, D. ; LABEYRIE, M. ; JOFFRE, P. ; HUIGNARD, J. P.: Liquid crystal microwave phase shifter. In: *Electronics Letters* 29 (1993), May, Nr. 10, pages 926–928

[Dri02] DRISCOLL, Tobin A.: Schwarz-Christoffel Toolbox Users Guide / Department of Mathematical Sciences, Ewing Hall, University of Delaware, Newark, DE 19716. 2002. – Technical report

[Dri05] DRISCOLL, Tobin A.: Algorithm 843: Improvements to the Schwarz-Christoffel Toolbox for MATLAB. In: *ACM Transactions on Mathematical Software* 31 (2005), Nr. 2, pages 239–251

[DS05] DIERKING, Ingo ; SAN, S. E.: Magnetically steered liquid crystal-nanotube switch. In: *Applied Physics Letters* 87 (2005), Nr. 23, 233507

[DSM05] DIERKING, I. ; SCALIA, G. ; MORALES, P.: Liquid crystal–carbon nanotube dispersions. In: *Journal of Applied Physics* 97 (2005), Nr. 4, 044309

[DSML04] DIERKING, I. ; SCALIA, G. ; MORALES, P. ; LECLERE, D.: Aligning and Reorienting Carbon Nanotubes with Nematic Liquid Crystals. In: *Advanced Materials* 16 (2004), Nr. 11, 865–869

[DT02] DRISCOLL, Tobin A. ; TREFETHEN, Lloyd N.: *Schwarz-Christoffel Mapping*. Cambridge University Press, 2002

[FKK+03] FUJIKAKE, H. ; KUKI, T. ; KAMODA, H. ; SATO, F. ; NOMOTO, Toshihiro: Voltage-variable microwave delay line using ferroelectric liquid crystal with aligned submicron polymer fibers. In: *Applied physics letters* 83 (2003), September, Nr. 9, pages 1815–1817

[FKN+01] FUJIKAKE, Hideo ; KUKI, Takao ; NOMOTO, Toshihiro ; TSUCHIYA, Yuzuru ; UTSUMI, Yozo: Thick polymer-stabilized liquid crystal films for microwave phase control. In: *Journal of Applied Physics* 89 (2001), pages 5295–5298

[FWS+09] FEGER, Reinhard ; WAGNER, Christoph ; SCHUSTER, Stefan ; SCHEIBLHOFER, Stefan ; JAEGER, Herbert ; STELZER, Andreas: A 77-GHz FMCW MIMO Radar Based on an SiGe Single-Chip Transceiver. In: *IEEE Transactions on Microwave Theory and Techniques* 57 (2009), pages 1020–1035

[GBC+01] GOANO, M. ; BERTAZZI, F. ; CARAVELLI, P. ; GHIONE, G. ; DRISCOLL, T.A.: A general conformal-mapping approach to the optimum electrode design of coplanar waveguides with arbitrary cross section. In: *Microwave Theory and Techniques, IEEE Transactions on* 49 (2001), Sep, Nr. 9, pages 1573–1580

[GDG+98a] GOODBY, J. (Ed.) ; DEMUS, D. (Ed.) ; GRAY, G.W. (Ed.) ; SPIESS, H.-W. (Ed.) ; VILL., V. (Ed.): *Handbook of Liquid Crystals*. Bd. 1. Wiley-VCH, 1998

[GDG+98b] GOODBY, J. (Ed.) ; DEMUS, D. (Ed.) ; GRAY, G.W. (Ed.) ; SPIESS, H.-W. (Ed.) ; VILL., V. (Ed.): *Handbook of Liquid Crystals*. Bd. 2A. Wiley-VCH, 1998

[Gie03] GIESSELMANN, F.: *Materialien zur Vorlesung*. Inst. für Phys. Chemie, Universität Stuttgart, (2002/2003)

[Gol08] GOLIO, Mike (Ed.): *The RF and Microwave Handbook*. 2nd. CRC Press, 2008

[GP93] GENNES, P. G. ; PROST, J. ; BIRMAN, J. (Ed.): *The Physics of Liquid Crystals*. Oxford University Press, 1993

[HCC08] HENRIE, J. ; CHRISTIANSON, A. ; CHAPPELL, W.J.: Prediction of Passive Intermodulation From Coaxial Connectors in Microwave Networks. In: *IEEE Transactions on Microwave Theory and Techniques* 56 (2008), Nr. 1, pages 209–216

[HDGG95] HUBERT, Pascal ; DREYFUS, Hanna ; GUILLON, Daniel ; GALERNE, Yves: Anchoring Orientation of Nematic and Smectic A Liquid Crystals on PTFE Treated Plates. In: *J. Phys. II France* 5 (1995), September, Nr. 9, 1371-1383

[HH08] HESTER, R. E. (Ed.) ; HARRISON, Roy M. (Ed.): *Electronic Waste Management*. RSC Publishing, 2008

[HHPL05] HUANG, Chi-Yen ; HU, Chao-Yuan ; PAN, Hung-Chih ; LO, Kuang-Yao: Electrooptical Responses of Carbon Nanotube-Doped Liquid Crystal Devices. In: *Japanese Journal of Applied Physics* 44 (2005), pages 8077–8081

[HLTB03] HECKMEIER, Michael ; LUESSEM, Georg ; TARUMI, Kazuaki ; BECKER, Werner: Liquid Crystals for Active Matrix Displays / Merck KGaA. 2003. – Technical report

[HR05] HANCOCK, T.M. ; REBEIZ, G.M.: A 12-GHz SiGe phase shifter with integrated LNA. In: *Microwave Theory and Techniques, IEEE Transactions on* 53 (2005), March, Nr. 3, pages 977–983

[HW03] HAASE, W. ; WRÓBEL, S.: *Relaxation Phenomena*. Springer, 2003

[HZL+07] HU, W. ; ZHANG, D. ; LANCASTER, M. J. ; BUTTON, T. W. ; SU, B.: Investigation of Ferroelectric Thick-Film Varactors for Microwave Phase Shifters. In: *Microwave Theory and Techniques, IEEE Transactions on* 55 (2007), Feb., Nr. 2, pages 418–424

[Ins07] INSTEC, Inc.: *Liquid Crystal Measurement Instruments 2007*. Brochure, 2007

[Jac65] JACKSON, John D.: *Classical Electrodynamics*. John Wiley & Sons, Inc., 1965

[JCDL99] JADZYN, Jan ; CZECHOWSKI, Grzegorz ; DOUALI, Redouane ; LEGRAND, Christian: On the molecular interpretation of the dielectric relaxation of nematic liquid crystals. In: *Liquid Crystals* 26 (1999), Nr. 11, 1591–1597

[Jeu79] JEU, W. H.: *Physical properties of liquid crystalline materials*. Gordon and Breach, 1979

[KBC+06] KRUPKA, J. ; BREEZE, J. ; CENTENO, A. ; ALFORD, N. ; CLAUSSEN, T. ; JENSEN, L.: Measurements of Permittivity, Dielectric Loss Tangent, and Resistivity of Float-Zone Silicon at Microwave Frequencies. In: *Microwave Theory and Techniques, IEEE Transactions on* 54 (2006), Nov., Nr. 11, pages 3995–4001

[KFKN03] KUKI, T. ; FUJIKAKE, H. ; KAMODA, H. ; NOMOTO, T.: Microwave Variable Delay Line Using a Membrane Impregnated with Liquid Crystal. In: *IEEE MTT-S International Microwave Symposium Digest* 1 (2003), August, pages 363–366

[KFN03] KUKI, T. ; FUJIKAKE, H. ; NOMOTO, T.: Microwave Variable Delay Line Using Dual-Frequency Swichting-Mode Liquid Crystal. In: *IEEE Transactions on Microwave Theory and Techniques* 50 (2003), November, pages 2604–2609

[KFNU02] KUKI, Takao ; FUJIKAKE, Hideo ; NOMOTO, Toshihiro ; UTSUMI, Yozo: Design of a microwave variable delay line using liquid crystal, and a study of its insertion loss. In: *Electronics and Communications in Japan (Part II: Electronics)* 85 (2002), January, pages 36–42

[Kho07] KHOO, Iam-Choon ; SALEH, Bahaa E. A. (Ed.): *Liquid Crystals*. Wiley-Interscience, 2007

[KJK81] KIRSCHNING, M. ; JANSEN, R. H. ; KOSTER, N. H. L.: Accurate Model for open end effect of microstrip lines. In: *Electronics Letters* 17 (1981), pages 123–125

[KKFN04] KAMODA, H. ; KUKI, T. ; FUJIKAKE, H. ; NOMOTO, T.: Millimeter-wave Beam Former Using Liquid Crystal. In: *Proc. 34th European Microwave Conf.* 3 (2004), October, pages 1141–1144

[KLV08] KROP, D.C.J. ; LOMONOVA, E.A. ; VANDENPUT, A.J.A.: Application of Schwarz-Christoffel Mapping to Permanent-Magnet Linear Motor Analysis. In: *Magnetics, IEEE Transactions on* 44 (2008), March, Nr. 3, pages 352–359

[KMR09] KOH, Kwang-Jin ; MAY, J.W. ; REBEIZ, G.M.: A Millimeter-Wave (40-45 GHz) 16-Element Phased-Array Transmitter in 0.18-μm SiGe BiCMOS Technology. In: *Solid-State Circuits, IEEE Journal of* 44 (2009), May, Nr. 5, pages 1498–1509

[KO89] KOC, C.K. ; ORDUNG, P.F.: Schwarz-Christoffel transformation for the simulation of two-dimensional capacitance [VLSI circuits]. In: *Computer-Aided Design of Integrated Circuits and Systems, IEEE Transactions on* 8 (1989), September, Nr. 9, pages 1025–1027

[KS95] KAPOOR, S. ; SCHNEIDER, J.B.: Characterization of microstrip discontinuities using conformal mapping and the finite-difference time-domain method. In: *Microwave Theory and Techniques, IEEE Transactions on* 43 (1995), November, Nr. 11, pages 2636–2639

[KW93] KHOO, Iam-Choon ; WU, Shin-Tson ; LTD., World Scientific Publishing Co. P. (Ed.): *Optics And Nonlinear Optics Of Liquid Crystals*. World Scientific Publishing Co. Pte. Ltd., 1993

[Kyo] KYORCERA: *SINGLE CRYSTAL SAPPHIRE*. Brochure,

[LB82] LI, Shihe ; BOSISIO, Renator G.: Composite Hole Conditions on Complex Permittivity Measurements Using Microwave Cavity Perturbation Techniques. In: *Microwave Theory and Techniques, IEEE Transactions on* 82 (1982), January, Nr. 1, pages 100–103

[LKS+98] LEE, Hyoung-Kwan ; KANAZAWA, Akihiko ; SHIONO, Takeshi ; IKEDA, Tomiki ; FUJISAWA, Toru ; AIZAWA, Masao ; LEE, Bong: All-Optically Controllable Polymer/Liquid Crystal Composite Films Containing the Azobenzene Liquid Crystal. In: *Chemistry of Materials* 10 (1998), Nr. 5, 1402-1407

[LL92] LANGE, K. (Ed.) ; LÖCHERER, K.-H. (Ed.): *Taschenbuch der Hochfrequenztechnik*. Springer, 1992

[LLMS93] LACKNER, A. M. ; LIM, K. C. ; MARGERUM, J. D. ; SHERMAN, E.: Microtubule particle dispersion in liquid crystal hosts. In: *Liquid Crystals* 14 (1993), Nr. 2, 351–359

[LM92] LIM, K. C. ; MARGERUM, J. D.: Liquid-crystal optical properties and applications in the millimeter-wave range. In: *Proceedings of SPIE* 1815 (1992), October, pages 99–105

[LML93a] LIM, K. C. ; MARGERUM, J. D. ; LACKNER, A. M.: Liquid crystal millimeter wave electronic phase shifter. In: *Applied Physics Letters* 62 (1993), March, Nr. 10, pages 1065–1067

[LML+93b] LIM, K. C. ; MARGERUM, J. D. ; LACKNER, A. M. ; MILLER, L. J. ; SHERMAN, E. ; SMITH, W. H.: Liquid crystal birefringence for millimeter wave radar. In: *Liquid Crystals* 14 (1993), Nr. 2, 327–337

[LP02] LYNCH, Michael D. ; PATRICK, David L.: Organizing Carbon Nanotubes with Liquid Crystals. In: *Nano Letters* 2 (2002), Nr. 11, 1197-1201

[MH97] MOULSON, A.J. ; HERBERT, J.M.: *Electroceramics - Materials - Properties - Applications*. London : Chapman & Hall, 1997

[MJM+01] MAJUMDER, S. B. ; JAIN, M. ; MARTINEZ, A. ; KATIYAR, R. S. ; KEULS, F. W. V. ; MIRANDA, F. A.: Sol–gel derived grain oriented barium strontium titanate thin films for phase shifter applications. In: *Journal of Applied Physics* 90 (2001), Nr. 2, 896-903

[Mül07] MÜLLER, Stefan: *Grundlegende Untersuchungen steuerbarer passiver Flüssigkristall-Komponenten für die Mikrowellentechnik*, Technische Universität Darmstadt, Diss., 2007

[MLP+03] MARTIN, Noham ; LAURENT, Paul ; PRIGENT, Gaetan ; GELIN, Philippe ; HURET, Fabrice: Improvement of an Inverted Microstrip Line-Based Microwave Tunable Phase-Shifter Using Liquid Crystals. In: *Proc. 34th European Microwave Conf.* 3 (2003), October, pages 1417–1420

[MNS98] MASUDA, Shin ; NOSE, Toshiaki ; SATO, Susumu: Optical Properties of a Polymer-Stabilized Liquid Crystal Microlens. In: *Japanese Journal of Applied Physics* 37 (1998), Nr. Part 2, No. 10B, L1251-L1253

[MO06] MCFEETORS, G. ; OKONIEWSKI, M.: Distributed MEMS analog phase shifter with enhanced tuning. In: *Microwave and Wireless Components Letters, IEEE* 16 (2006), Jan., Nr. 1, pages 34–36

[MSK+00] MIRANDA, F.A. ; SUBRAMANYAM, G. ; KEULS, F.W. van ; ROMANOFSKY, R.R. ; WARNER, J.D. ; MUELLER, C.H.: Design and development of ferroelectric tunable microwave components for Ku- and K-band satellite communication systems. In: *Microwave Theory and Techniques, IEEE Transactions on* 48 (2000), July, Nr. 7, pages 1181–1189

[MSW+04] MUELLER, Stefan ; SCHEELE, Patrick ; WEIL, Carsten ; WITTEK, Michael ; HOCK, Christian ; JAKOBY, Rolf: Tunable Passive Phase Shifter for Microwave Applications using Highly Anisotropic Liquid Crystals. In: *IEEE MTT-S International Microwave Symposium Digest* 2 (2004), Juni, pages 1153–1156

[Neo] NEOTEXX: *Datenblatt NdFeB*. Datasheet, http://www.neotexx.de/extras/Grad.pdf. `http://www.neotexx.de/extras/Grad.pdf`

[NKG+06] NATARAJAN, A. ; KOMIJANI, A. ; GUAN, Xiang ; BABAKHANI, A. ; HAJIMIRI, A.: A 77-GHz Phased-Array Transceiver With On-Chip Antennas in Silicon: Transmitter and Local LO-Path Phase Shifting. In: *Solid-State Circuits, IEEE Journal of* 41 (2006), Dec., Nr. 12, pages 2807–2819

[NSYH06] NOSE, T. ; SAITO, S. ; YANAGIHARA, S. ; HONMA, M.: Potential applications of nematic liquid crystal materials in the millimeter wave region. In: *Liquid Crystal Materials, Devices, and Applications XI* 6135 (2006), Nr. 1, 61350A

[Oxb07] OXBORROW, M.: Traceable 2-D Finite-Element Simulation of the Whispering-Gallery Modes of Axisymmetric Electromagnetic Resonators. In: *Microwave Theory and Techniques, IEEE Transactions on* 55 (2007), June, Nr. 6, pages 1209–1218

[OYK+07] OH-E, M. ; YOKOYAMA, H. ; KOEBERG, M. ; HENDRY, E. ; BONN, M.: THz time-domain spectroscopy of liquid crystal colloids. In: *Society of Photo-Optical Instrumentation Engineers (SPIE) Conference Series* Bd. 6487, 2007 (Presented at the Society of Photo-Optical Instrumentation Engineers (SPIE) Conference)

[PC03] PEDRO, José C. ; CARVALHO, Nuno B.: *Intermodulation Distortion in Microwave and Wireless Circuits*. Artech House, 2003

[PMS+04] PENIRSCHKE, Andreas ; MUELLER, Stefan ; SCHEELE, Patrick ; WEIL, Carsten ; WITTEK, Michael ; HOCK, Christian ; JAKOBY, Rolf: Cavity Perturbation Method for Characterization of Liquid Crystals up to 35 GHz. In: *Proc. 34th European Microwave Conf.* 2 (2004), October, pages 545–548

[Poz04] POZAR, David M.: *Microwave Engineering*. Wiley, 2004

[PP07] PAN, C.-L. ; PAN, R.-P.: Liquid-crystal-based electrically tunable THz optical devices. In: *Society of Photo-Optical Instrumentation Engineers (SPIE) Conference Series* Bd. 6487, 2007 (Presented at the Society of Photo-Optical Instrumentation Engineers (SPIE) Conference)

[Reb03] REBEIZ, Gabriel M.: *RF MEMS - Theory, Design, and Technology*. Wiley-Interscience, 2003

[RMC80] REITZ, John R. ; MILFORD, Frederick J. ; CHRISTY, Robert W.: *Foundations of Electromagnetic Theory*. 3rd. Addison-Wesley, 1980

[RPP+08] RUTKOWSKA, J. ; PERKOWSKI, P. ; PIECEK, W. ; RASZEWSKI, Z. ; KEDZIERSKI1, J.: Dielectric relaxation behaviour of liquid crystals with opposite orientation of -COO ester group in molecular core. In: *Opto-Electronics Review* 16 (2008), Nr. 3, pages 262–266

[RSGK96] ROZANSKI, Stanislaw A. ; STANNARIUS, Ralf ; GROOTHUES, Herbert ; KREMER, Friedrich: Dielectric properties of the nematic liquid crystal 4-n-pentyl-4'-cyanobiphenyl in porous membranes. In: *Liquid Crystals* 20 (1996), Nr. 1, 59–66

[SBD+06] SAIB, A. ; BEDNARZ, L. ; DAUSSIN, R. ; BAILLY, C. ; LOU, Xudong ; THOMASSIN, J.-M. ; PAGNOULLE, C. ; DETREMBLEUR, C. ; JEROME, R. ; HUYNEN, I.: Carbon nanotube composites for broadband microwave absorbing materials. In: *Microwave Theory and Techniques, IEEE Transactions on* 54 (2006), June, Nr. 6, pages 2745–2754

[SBR+83] SEN, Sushmita ; BRAHMA, Pradip ; ROY, Subir. K. ; MUKHERJEE, D. K. ; ROY, S. B.: Birefringence and Order Parameter of Some Alkyl and Alkoxycyanobiphenyl Liquid Crystals. In: *Molecular Crystals and Liquid Crystals* 100 (1983), 327–340

[Sch07] SCHEELE, Patrick: *Steuerbare passive Mikrowellenkomponenten auf Basis hochpermittiver ferroelektrischer Schichten*, Technische Universität Darmstadt, Diss., 2007

[SDD98] SAITO, R. (Ed.) ; DRESSELHAUS, M. S. (Ed.) ; DRESSELHAUS, G. (Ed.): *Physical Properties of Carbon Nanotubes*. World Scientific Pub. Co., 1998

[SDPN+05] SPIRITO, M. ; DE PAOLA, F.M. ; NANVER, L.K. ; VALLETTA, E. ; RONG, Bifeng ; REJAEI, B. ; VREEDE, L.C.N. de ; BURGHARTZ, J.N.: Surface-passivated high-resistivity silicon as a true microwave substrate. In: *Microwave Theory and Techniques, IEEE Transactions on* 53 (2005), Nr. 7, pages 2340–2347

[SF63] SUCHER, M. (Ed.) ; FOX, J. (Ed.): *Handbook of Microwave Measurements*. Bd. II. 3rd. New York : Polytechnic Press, 1963

[SL03] SCHINZINGER, Roland ; LAURA, Patricio A. A.: *Conformal Mapping, Methods and Applications*. Courier Dover Publications, 2003

[SLS+07] SCALIA, Giusy ; LAGERWALL, Jan P. F. ; SCHYMURA, S. ; HALUSKA, M. ; GIESSELMANN, F. ; ROTH, Siegmar: Carbon nanotubes in liquid crystals as versatile functional materials. In: *physica status solidi (b)* 244 (2007), Nr. 11, pages 4212–4217

[Som06] SOMALINGAM, Somakanthan: *Verbesserung der Schaltdynamik nematischer Flüssigkristalle für adaptive optische Anwendungen*, Technische Universität Darmstadt, Diss., 2006

[SS74] STEPHEN, Michael J. ; STRALEY, Joseph P.: Physics of Liquid Crystals. In: *Rev. Mod. Phys.* 46 (1974), Nr. 4, pages 617–697

[ST07] SALEH, B. E. A. ; TEICH, M. C.: *Fundamentals of Photonics*. Wiley, 2007

[Sva92] SVACINA, Jiri: Analysis of Multilayer Microstrip Lines by a Conformal Mapping method. In: *IEEE Transactions on Microwave Theory and Techniques* 40 (1992), April, Nr. 4, pages 769–772

[SWJC88] SHIH, C. ; WU, R.-B. ; JENG, S.-K. ; CHEN, C.H.: A full-wave analysis of microstrip lines by variational conformal mapping technique. In: *Microwave Theory and Techniques, IEEE Transactions on* 36 (1988), Mar, Nr. 3, pages 576–581

[THI+05] TAKATOH, Kohki ; HASEGAWA, Ray ; ITOH, Nobuyuki ; KODEN, Mitsuhiro ; SAKAMOTO, Masanori: *Alignment Technologies and Applications of Liquid Crystal Devices*. Taylor & Francis, 2005

[TOY+07] TANAKA, S. ; OKADA, Y. ; YAMAMOTO, K. ; TAKANISHI, Y. ; TANI, M. ; ISHIKAWA, K. ; HANGYO, M. ; TAKEZOE, H.: Effect of permanent dipole moments perpendicular to the molecular long axis on the terahertz absorption in liquid crystals. In: *Society of Photo-Optical Instrumentation Engineers (SPIE) Conference Series* Bd. 6487, 2007 (Presented at the Society of Photo-Optical Instrumentation Engineers (SPIE) Conference)

[Tre79] TREFETHEN, Lloyd: Numerical Computation of the Schwarz-christoffel Transformation / Computer Science Department, Stanford University. 1979. – Technical report

[TWQL08] TSELEV, Alexander ; WOODSON, Michael ; QIAN, Cheng ; LIU, Jie: Microwave Impedance Spectroscopy of Dense Carbon Nanotube Bundles. In: *Nano Letters* 8 (2008), Nr. 1, 152-156

[VBB+07] VELU, G. ; BLARY, K. ; BURGNIES, L. ; MARTEAU, A. ; HOUZET, G. ; LIPPENS, D. ; CARRU, J.-C.: A 360° BST Phase Shifter With Moderate Bias Voltage at 30 GHz. In: *Microwave Theory and Techniques, IEEE Transactions on* 55 (2007), Feb., Nr. 2, pages 438–444

[VCJ02] VIVEIROS, Jr. D. ; CONSONNI, D. ; JASTRZEBSKI, A.K.: A tunable all-pass MMIC active phase shifter. In: *Microwave Theory and Techniques, IEEE Transactions on* 50 (2002), August, Nr. 8, pages 1885–1889

[Wei05] WEILAND, T.: *Skriptum zur Vorlesung Elektromagnetisches CAD*. Fachgebiet Theorie Elektromagnetischer Felder, 2005

[WGS06] WILKERSON, J.R. ; GARD, K.G. ; STEER, M.B.: Electro-Thermal Passive Intermodulation Distortion in Microwave Attenuators. In: *Microwave Conference, 2006. 36th European*, 2006, pages 157–160

[WHB+07] *Chapter* Expanded Polytetrafluoroethylene Membranes and Their Applications. In: WIKOL, Michael ; HARTMANN, Bryce ; BRENDLE, Joseph ; CRANE, Michele ; BEUSCHER, Uwe ; BRAKE, Jeff ; SHICKEL, Tracy: *Filtration and Purification in the Biopharmaceutical Industry*. Informa HealthCare, 2007, pages 619–640

[Whe64] WHEELER, H.A.: Transmission-Line Properties of Parallel Wide Strips by a Conformal-Mapping Approximation. In: *IEEE Transactions on Microwave Theory and Techniques* 12 (1964), Nr. 3, pages 280–289

[Whe65] WHEELER, H.A.: Transmission-Line Properties of Parallel Strips Separated by a Dielectric Sheet. In: *Microwave Theory and Techniques, IEEE Transactions on* 13 (1965), March, Nr. 2, pages 172–185

[WL97] WU, Mount-Learn ; LEE, Ching-Ting: Quasistatic analysis of arbitrary coplanar waveguide structures by combination of conformal mapping and finite-difference methods. In: *Microwave and Optical Technology Letters* 16 (1997), Nr. 3, 149–154

[WMS+03] WEIL, Carsten ; MUELLER, Stefan ; SCHEELE, Patrick ; BEST, Peter ; LUESSEM, Georg ; JAKOBY, Rolf: Highly-anisotropic liquid-crystal mixtures for tunable microwave devices. In: *Electronics Letters* 39 (2003), November, pages 1732 – 1734

[YS03] YANG, Fuzi ; SAMBLES, John R.: Determination of the permittivity of nematic liquid crystals in the microwave region. In: *Liquid Crystals* 30 (2003), Nr. 5, 599–602

[YW06] YANG, D.-K. ; WU, S.-T. ; LOWE, Anthony C. (Ed.): *Fundamentals of Liquid Crystal Devices*. John Wiley & Sons Ltd., 2006

[ZB98] ZINKE, Otto ; BRUNSWIG, Heinrich ; VLCEK, Anton (Ed.) ; HARTNAGEL, Hans L. (Ed.) ; MAYER, Konrad (Ed.): *Hochfrequenztechnik II: Elektronik und Signalverarbeitung*. Springer, Berlin, 1998

[ZB00] ZINKE, Otto ; BRUNSWIG, Heinrich ; VLCEK, Anton (Ed.) ; HARTNAGEL, Hans L. (Ed.) ; MAYER, Konrad (Ed.): *Hochfrequenztechnik I: Hochfrequenzfilter, Leitungen, Antennen*. Springer, Berlin, 2000

[Zel82] ZELLER, H. R.: Dielectric Relaxation and the Glass Transition in Nematic Liquid Crystals. In: *Physical Review Letters* 48 (1982), February, pages 334–337

[ZK08] ZHANG, Shanju ; KUMAR, Satish: Carbon Nanotubes as Liquid Crystals. In: *Small* 4 (2008), Nr. 9, 1270–1283

[ZM95] ZHANG, Xiang ; MIYOSHI, T.: Optimum design of coplanar waveguide for $LiNbO_3$ optical modulator. In: *Microwave Theory and Techniques, IEEE Transactions on* 43 (1995), March, Nr. 3, pages 523–528

[ZS08] ZHENG, You ; SAAVEDRA, C.E.: An Ultra-Compact CMOS Variable Phase Shifter for 2.4-GHz ISM Applications. In: *Microwave Theory and Techniques, IEEE Transactions on* 56 (2008), June, Nr. 6, pages 1349–1354

Own Publications

[1] F. Goelden, A. Gaebler, M. Goebel, A. Manabe, S. Mueller, and R. Jakoby. Tunable Liquid Crystal Phase Shifter for Microwave Frequencies. *Electronics Letters*, 45(13):686–687, 2009.

[2] A. Gaebler, F. Goelden, S. Mueller, and R. Jakoby. Investigation of High Performance Transmission Line Phase Shifters Based on Liquid Crystal. In *European Microwave Conference*, 2009.

[3] A. Gaebler, F. Goelden, S. Mueller, and R. Jakoby. Direct Simulation of Material Permittivities by using an Eigen-Susceptibility Formulation of the Vector Variational Approach. In *International Instrumentation and Measurement Technology Conference*, 2009.

[4] A. Gaebler, A. Moessinger, F. Goelden, A. Manabe, M. Goebel, R. Follmann, D. Koether, C. Modes, A. Kipka, M. Deckelmann, T. Rabe, B. Schulz, P. Kuchenbecker, A. Lapanik, S. Mueller, W. Haase, and R. Jakoby. Liquid Crystal-Reconfigurable Antenna Concepts for SpaceApplications at Microwave and Millimeter Waves. *International Journal of Antennas and Propagation*, 1:1–7, 2009.

[5] O.H. Karabey, Y. Zheng, A. Gaebler, F. Goelden, and R. Jakoby. A Synthesis Technique for Multiband Tunable Impedance Matching Networks with Optimized Matching Domain. In *German Microwave Conference*, 2009.

[6] F. Goelden, A. Gaebler, S. Mueller, A. Lapanik, W. Haase, and R. Jakoby. Liquid-crystal Varactors With Fast Switching Times for Microwave Applications. *Electronics Letters*, 44:480–481, 2008.

[7] F. Goelden, A. Lapanik, A. Gaebler, S. Mueller, W. Haase, and R. Jakoby. Characterization and Application of Liquid Crystals at Microwave Frequencies. *FREQUENZ*, 3-4:57, 2008.

[8] A. Gaebler, F. Goelden, S. Mueller, and R. Jacoby. Triple-Mode Cavity Perturbation Method for the Characterization of Anisotropic Media. In *Proc. 38th European Microwave Conference*, 2008.

[9] A. Gaebler, F. Goelden, S. Mueller, and R. Jakoby. Efficiency Considerations of Tuneable Liquid Crystal Microwave Devices. In *German Microwave Conference*, 2008.

[10] A. Gaebler, F. Goelden, S. Mueller, and R. Jakoby. Modeling of Electrically Tunable Transmission Line Phase Shifter Based on Liquid Crystal. In *IEEE International Symposium on Antenna and Propagation*, 2008.

[11] S. Mueller, A. Moessinger, R. Marin, F. Goelden, A. Gaebler, M. Koeberle, and R. Jakoby. Liquid Crystal Phase Shifters for Electronically Steerable Antenna Systems. In *IEEE Int. Microwave Symposium*, 2008.

[12] S. Mueller, M. Koeberle, A. Moessinger, F. Goelden, A. Gaebler, and R. Jakoby. Liquid Crystal Based Electronically Steerable 4x4 Antenna Array with Single Horn Feed at Ka-Band. In *IEEE International Symposium on Antennas and Propagation*, 2008.

[13] F. Goelden, A. Lapanik, S. Mueller, A. Gaebler, W. Haase, and R. Jakoby. Investigations on the Behavior Of Ferroelectric Liquid Crystals at Microwave Frequencies. In *Proc. European Microwave Conference*, pages 106–109, 2007.

[14] F. Goelden, A. Lapanik, A. Gaebler, S. Mueller, W. Haase, and R. Jakoby. Systematic Investigation of Nematic Liquid Crystal Mixtures at 30 GHz. In *IEEE LEOS Summer Topical Meeting*, 2007.

[15] F. Goelden, A. Lapanik, A Gaebler, S. Mueller, V. Lapanik, V. Bezborodov, W. Haase, and R. Jakoby. Tunable Microwave Phase Shifter using Thin Layer Ferroelectric Liquid Crystals. In *11th International Conference on Ferroelectric Liquid Crystals, Sapporo, Hokkaido, Japan, 3-8. September*, 2007.

[16] R. Marin, A. Moessinger, F Goelden, S. Mueller, and R. Jakoby. 77 GHz Reconfigurable Reflectarray with Nematic Liquid Crystal. In *2nd European Conference on Antennas and Propagation*, 2007.

[17] P. Scheele, A. Giere, Y. Zheng, F. Goelden, and R. Jakoby. Modeling and Applications of Ferroelectric-Thick Film Devices with Resistive Electrodes for Linearity Improvement and Tuning-Voltage Reduction. *IEEE Transactions on Microwave Theory and Techniques*, 55, No. 2:383–390, 2007.

[18] F. Goelden, S. Mueller, P. Scheele, M. Wittek, and R. Jakoby. IP3 Measurements of Liquid Crystals at Microwave Frequencies. *Proc. 36th European Microwave Conf.*, pages 971–974, 2006.

[19] S. Mueller, F. Goelden, P. Scheele, M. Wittek, C. Hock, and R. Jakoby. Passive Phase Shifter for W-Band Applications Using Liquid Crystals. *Proc. 36th European Microwave Conf.*, pages 306–309, 2006.

[20] A. Penirschke, S. Mueller, F. Goelden, A. Lapanik, V. Lapanik, V. Bezborodov, W. Haase, and R. Jakoby. Cavity Perturbation Method for Temperature Controlled Characterization of Liquid Crystals at 38 GHz. In *GeMiC 2006 German Microwave Conference Karlsruhe, Germany, 28.-30. March*, 2006.

Supervised Diploma Thesis

- Entwurf und Realisierung eines passiven steuerbaren Anpassnetzwerks auf Basis von Flüssigkristallen
  Diplomarbeit D 2114, Darmstadt 2006

Lebenslauf

Persönliche Daten

Name:	Felix Gölden
Geburtsdatum:	18. September 1977
Geburtsort:	Darmstadt

Schulausbildung

1984-1988:	Rehbergschule (Grundschule) in Rossdorf b. Darmstadt
1988-1997:	Ludwig-Georgs-Gymnasium, Darmstadt

Ersatzdienst

1997-1998:	Arbeiter-Samariter-Bund, Darmstadt

Studium

1998-2004:	Studium der Elektrotechnik an der Technischen Universität Darmstadt, Vertiefungsrichtung Nachrichtentechnik

Berufstätigkeit

05/2004-03/2005:	Entwicklungsingenieur bei Diehl Avionik Systeme GmbH, Frankfurt
04/2005-10/2009:	Wissenschaftlicher Mitarbeiter am Fachgebiet Mikrowellentechnik der Technischen Universität Darmstadt
seit 11/2009:	Wissenschaftlicher Mitarbeiter am Fachgebiet Mikrowellentechnik der Technischen Universität Berlin